Computational Methods for Enhancing Sensitivity to MRI Cell-Tracking Agents

Thesis
submitted in partial fulfillment of the requirements
for the degree of
Doctor of Philosophy
in the Department of Biological Sciences

Parker H. Mills

Advised by
Eric T. Ahrens, Ph.D.

Thesis Committee
Chien Ho, Ph.D.
William F. Eddy, Ph.D.
Russell S. Schwartz, Ph.D.
Fernando E. Boada, Ph.D. (Visiting Member)

Mellon College of Science
Carnegie Mellon University
Pittsburgh, PA, USA

April 22, 2011

Contents

Abstract

New methods for programming cells to perform desired functions *in vivo* promise to enable new diagnostic tools and therapies. To develop, confidently deploy, and routinely use these emerging cellular therapies, it is necessary to have the ability to non-invasively detect and monitor transplanted cells, or those that have been genetically-modified *in situ*. MRI offers non-invasive high-resolution imaging within deep tissues without the use of ionizing radiation. In order for cells of interest to appear in MR images, they are labeled with iron oxide contrast agent (CA), genetic instructions to produce their own CA, or with fluorine-based tracer agents. Regardless of the type of label used, it is a challenge to achieve sufficient MR image signal and contrast in order to differentiate labeled cells from background tissue or image noise, especially when they reside in inhomogeneous tissue, or when scan time is limited. Improvements in sensitivity to labeled cells are needed for their ready detection and quantification.

Cells labeled with iron oxide CA appear in conventional proton (^{1}H) MR images as hypointense spots or regions within the organ or anatomy being imaged. To facilitate cell-tracking that employs iron-oxides, we present three methods: The first, called the Two-Compartment T2 Contrast Model (T2CM), is a model for predicting the relationship between iron oxide CA concentration and expected image contrast. The second method, called Phase Slope Magnitude Imaging (PSM), highlights arbitrary distributions of iron oxide CA in tissue. The third method, called Phase Map Cross-Correlation Detection and Quantification (PDQ), detects isolated magnetic dipoles that indicate the presence of an iron oxide-labeled cell or cell cluster. PDQ then measures the magnetic moment of each dipole and registers its location for the purpose of cell-tracking and 3D visualization.

Cells labeled with fluorine-based tracer agents appear in fluorine (^{19}F) MR images as hyperintense spots or regions against a background of only image noise. The background is devoid of anatomical features, since tissue fluorine concentration is insignificant relative to that within labeled cells – distinguishing fluorine tracer from anatomical tissue features is not an issue. However, fluorine-based tracer agents often have a sparse spatial distribution and produce low levels of MRI signal, so it is often difficult to distinguish labeled cells from background image noise, especially when scan times are limited during *in vivo* experiments. To facilitate cell-tracking that employs fluorine-based tracers, we implemented and evaluated compressed sensing acquisition and reconstruction. This method generates 3D images with higher signal-to-noise ratios than conventional methods, allowing for 3D fluorine acquisitions with higher resolutions or shortened scan times.

Overall these methods for enhancing sensitivity to cells labeled with iron oxide CAs and fluorine tracer agents will help enable MRI as a platform for detecting and tracking cells in living subjects. Improved MRI cell monitoring will help researchers understand how normal and diseased cells behave and migrate inside living systems, and will help to determine the efficacy of new cellular therapies.

Acknowledgements

I am tremendously grateful to my colleagues for the support and opportunities they provided over the past six years. Without their talent and efforts the following works would not have been possible.

I thank my advisor, Eric T Ahrens, for his guidance, ideas, and valuable critiques. Eric provided me with a relentless series of opportunities, and generous latitude to pursue independent investigations.

I thank my thesis committee members: Chien Ho, Fernando Boada, William Eddy, and Russell Schwartz, for their incisive critiques of my research direction, valuable experimental suggestions, and generosity with their time whenever I sought orientation through committee gatherings or office visits.

Many thanks to all collaborators for great research experiences and help with my professional development. From Carnegie Mellon: T. Kevin Hitchens, Yi-Jen Wu, Lesley Foley, and Qing Ye; Magee Womens Research Center: Carlos Castro, Gerald Schatten, John Ozolek; University of Pittsburgh: J. Richard Chaillet, Steven DeKosky, and Patrick Kochanek; Johns Hopkins University: Jeff Bulte, Thomas Link, Clifford Weiss, and Wesley Gilson; Los Alamos National Lab: Joseph Thompson; University of Illinois at Urbana-Champaign: Zhi Pei Liang and Hien Nguyen; and Vanderbilt University: Kathie Eagleson.

Many thanks to all members of the Ahrens Lab for their advice, friendship, and assistance: Clint Robison, Jelena Janjic, Won-Bin Young, Ulrike DeMarco, Hongyan Xu, Michael Patrick, Lisa Pusateri, Jia Zhong, Laurel Farmer, and my fellow graduate students Mangala Srinivas, Bistra Iordanova, and Deepak Kumar Kana Kadayakkara.

I thank those in the Pittsburgh NMR Center for Biomedical Research for their support, ideas, cooperation, and levity: Michelle Waters, Virgil & Elena Simplaceanu, Don Bennett, Lisa McGaw, Haosen Zhang, Greg Chen, John Williams, Baiyu Tang, and Frank Yeh.

Also many thanks to those in the Carnegie Mellon Department of Biological Sciences: Ena Miceli, Al Scheuring, Carol Lee, Cynthia Davis, Donya Parker, and V. Emily Stark. For generosity with time and instruction during my academic lab rotations and teaching: Robert Murphy, Gordon Rule, and Frederick Lanni.

Finally special thanks to my family for their support, upbringing, and workable genetic material: Ann, Ernest, Benjamin, Mary, and Rhea.

Various groups provided support for this work, including the National Institutes of Health (R01-EB005740, P41-EB001977, P01-HD047675, and P50-ES012359), and the National Institute of Neurological Disorders and Stroke (NS38087 and NS30318). The transition from Physics to Biology was facilitated by Stephen Garoff, Kunal Ghosh, and Amy Burkert's referral to Ahrens Lab. Fellowship support was provided by the Carnegie Mellon Dept. of Biological Sciences.

Preface

The works within this thesis share a common investigatory thread – enhancing MRI's sensitivity to cells labeled with contrast agent in order to improve cell detection, tracking, and visualization. While these investigations were taking place, I also had the pleasure of engaging in three major collaborative projects, performing 3D magnetic resonance microscopy (MRM) on dozens of biological samples and maximizing the value of the resulting images through 3D measurements, registrations, and visualizations. I also had the privilege of authoring sections related to magnetic resonance within these manuscripts. These collaborative projects included:

1. 3D MRM of teratomas derived from pedigreed nhpESCs with Carlos Castro, Ahmi Ben-Yehuudah, and John Ozolek, published July 2010 in the journal Stem Cell Research under the title "Semiquantitative histopathology and 3D magnetic resonance microscopy as collaborative platforms for tissue identification and comparison within teratomas derived from pedigreed primate embryonic stem cells" [1].

2. 3D MRM of mice with inadequate maintenance of genomic imprints (Dnmt1o-deficient) with Marc Toppings, Carlos Castro, Bonnie Reinhart, J. Richard Chaillet, and Jacquetta Trasler, published January 2008 in the journal Human Reproduction under the title "Profound phenotypic variation among mice deficient in the maintenance of genomic imprints" [2].

3. 3D MRM of mice with disrupted *Foxg1* expression with Kathie Eagleson, Lisa Schlueter Mcfadyen-Ketchum, Mark Does, and Pat Levitt, published June 2007 in the journal Neuroscience under the title "Disruption of *Foxg1* Expression by Knock-In of Cre Recombinase: Effects on the Development of the Mouse Telencephalon" [3].

Each project was also a great learning experience, thanks to generous collaborator explanations to my many questions.

List of Abbreviations

χ	Volume Magnetic Susceptibility
γ	Gyromagnetic ratio
μ	Permeability (electromagnetic)
$\mu_0 = 4\pi \times 10^{-7}$ H/m	Permeability of free space
B_0	Primary magnetic field strength
BW	Bandwidth
CA	Contrast Agent
CNR	Contrast-to-Noise Ratio
DFT	Discrete Fourier Transform
FOV	Field Of View
FWHM	Full Width Half Maximum
GRE	Gradient-Recalled echo
m	Magnetic moment
M	Bulk magnetization
MPIO	Micron-sized Paramagnetic Iron-Oxide
MRI	Magnetic Resonance Imaging
MRM	Magnetic Resonance Microscopy
NMRC	Pittsburgh NMR Center for Biomedical Research
PCE	Perfluoro-15-crown-5-ether
PFC	Perfluorocarbon
PFPE	Perfluoropolyether
PS	Pulse Sequence
RF	Radiofrequency
SE	Spin Echo
SNR	Signal-to-Noise Ratio
SPIO	Superparamagnetic Iron-Oxide
T_1	Longitudinal (spin-lattice) proton relaxation time
T_2	Transverse (spin-spin) proton relaxation time
T_2-WI	T_2-Weighted Image
T_2^*	T_2 dephasing (meas.) from magnetic field inhomogeneity
TA	Tracer Agent
TBI	Traumatic Brain Injury
TE	Echo Time
TR	Repetition Time

List of Figures

List of Tables

Chapter 1

Summary

1.1 Enhancing Sensitivity to SPIO CAs

1.1.1 Two-Compartment T_2 Contrast Model (T2CM)

The rational development of new generations of MRI contrast agents (CAs) requires a scheme for predicting contrast enhancement. Previous contrast predictions have been based largely on empirical results in specific systems. Here, we presented a general theoretical model for evaluating the minimum concentration of T_2 CA required for satisfactory image contrast. This analytic contrast model is applicable to a wide range of T_2-type agents and delivery scenarios, and requires only a few readily-evaluated parameters. We demonstrated the model by predicting contrast produced by superparamagnetic ferumoxide and the iron storage protein, ferritin. We then experimentally verified the predictions using suspensions of Feridex and ferritin in phantoms. The model was also used to compare the contrast efficacy of the metal ions in two clinically approved T_1- and T_2-type CAs. In the Appendix, we present a numerical formalism that is useful for relating image contrast and agent concentration when gradient-echo (GRE) T_2^*-weighted (T_2^*-W) pulse sequences are used.

1.1.2 Phase Slope Magnitude Imaging (PSM)

Iron oxide-based MRI contrast agents (CAs) are increasingly being used to non-invasively track cells, target molecular epitopes, and monitor gene expression *in vivo*. Detecting regions of CA accumulation can be challenging if resulting contrast is subtle relative to endogenous tissue hy-

pointensities. A post processing method is presented that yields enhanced positive-contrast images from the phase map associated with T_2^*-weighted MRI data. As examples, the method was applied to an agarose gel phantom doped with superparamagnetic iron-oxide (SPIO) nanoparticles and *in vivo* and *ex vivo* mouse brains inoculated with recombinant viruses delivering transgenes that induce overexpression of paramagnetic ferritin. The method was also applied to a mouse thigh that had been injected with SPIO-labeled dendritic cells (DCs), and to an APP/PS1 transgenic Alzheimer model mouse brain burdened by iron-containing amyloid-β plaques. Overall, this approach generates images that exhibit a 1- to 8-fold improvement in contrast-to-noise ratio in regions where paramagnetic agents are present compared to conventional magnitude images. Importantly, this approach can be used in conjunction with conventional T_2^* pulse sequences, requires no pre-scans or increased scan time, and can be applied retrospectively to previously-acquired data.

1.1.3 Phase Map Cross-Correlation Detection and Quantification (PDQ)

Understanding how individual cells behave inside living systems will help enable new diagnostic tools and cellular therapies. Superparamagnetic iron oxide (SPIO) particles can be used to label cells and theranostic capsules for non-invasive tracking using MRI, and are increasingly being used to non-invasively track cells, target specific molecules, and monitor gene expression *in vivo*. Contrast changes from SPIO are often subtle relative to intrinsic sources of contrast, presenting a detection challenge. Here we describe a versatile post-processing method, Phase map cross-correlation Detection and Quantification (PDQ), that automatically identifies localized deposits of SPIO, estimating their volume magnetic susceptibility and magnetic moment.

PDQ was applied to over a half-dozen different classes of datasets: We first investigated the theoretical detection limits of PDQ using a simulated dipole field. We then applied PDQ to 3D MRI datasets of agarose gel containing isolated dipoles, and *ex vivo* transplanted allogenic rat hearts infiltrated by numerous iron-oxide labeled macrophages as a result of organ rejection. The simulated dipole field showed this method to be robust in very low signal-to-noise ratio images. Analysis of agarose gel and allogenic rat heart show this method can automatically identify and count dipoles while visualizing their biodistribution in 3D renderings. In the heart, this information was used to calculate a quantitative index that may indicate its degree of cellular infiltration. Next, PDQ was used to detect and characterize SPIO-labeled magnetocapsules implanted in porcine liver

and suspended in agarose gel. PDQ magnetic measurements were SNR-invariant for images with SNR>11. PDQ was also applied to mouse brains infiltrated by MPIO-labeled macrophages following traumatic brain injury (TBI); longitudinal, *in vivo* studies tracked individual MPIO clusters over three days, and tracked clusters were corroborated in *ex vivo* brain scans. Finally, we applied PDQ to rat hearts infiltrated by MPIO-labeled macrophages in a transplant model of organ rejection. Comparisons between PDQ and other cell-counting methods were also performed: PDQ was compared with ImageJ dark spot counting in TBI model mouse brains, and was compared with histological ED1+ cell counting and Manual dark spot counting in the rat heart chronic rejection model.

PDQ was designed to be practical - it works on previously-acquired data and can be used with conventional high-SNR gradient-echo pulse sequences, requiring no extra scan time. The method is useful for visualizing biodistribution of cells and theranostic magnetocapsules, and for measuring their relative iron content.

1.2 Detection and Quantification of Sparse ^{19}F-based Tracers with Low SNR

1.2.1 Enhancing Sensitivity to Fluorine-19 Tracer Agents

When imaging sparse fluorine-based tracer agents, low intrinsic signal can cause fluorine-labeled cells or other deposits to appear indistinguishable from image noise. Recently, compressed sensing methods have been used to accelerate MRI acquisition when resulting images are expected to be 'sparsely-representable.' MR images of cells labeled with fluorine tracer agent are sparse in the image pixel domain, making compressed sensing directly applicable to imaging these agents, promising a distinct SNR/t advantage over conventional imaging methods. Here we simulate compressed sensing image reconstruction by undersampling already-acquired MR data of a perfluoro-15-crown-5-ether ^{19}F phantom. We then test compressed sensing fluorine-19 imaging by using a custom Bruker pulse sequence that directly undersamples 3D k-space. We applied this undersampling pulse sequence to the same ^{19}F phantom used in simulations, and to a rat brain injected with 9L glioma cells labeled with a perfluoro-15-crown-5-ether emulsion. Overall, acquisition of 3D sparse

19F images were accelerated by 4×-8× with little qualitative degradation in image quality.

1.3 Contributions

1.3.1 Publications

Manuscripts

- Mills PH, Hitchens TK, Foley LM, Ye Q, Weiss C, Thompson JD, Gilson W, Eytan D, Arepally A, Melick JA, Kochanek PM, Ho C, Bulte JW, Ahrens ET. Automated detection and characterization of SPIO-labeled cells and capsules using magnetic field perturbations. Magnetic Resonance in Medicine 2011; In press.
- Mills PH, Ahrens ET. Enhanced positive-contrast visualization of paramagnetic contrast agents using phase images. Magnetic Resonance in Medicine 2009; 62:1349-1355.
- Mills PH, Wu YL, Ho C, Ahrens ET. Sensitive and automated detection of iron-labeled cells using phase image cross-correlation analysis. Magnetic Resonance Imaging 2008; 26:618-628.
- Mills PH, Ahrens ET. Theoretical MRI contrast model for exogenous T_2 agents. Magnetic Resonance in Medicine 2007; 57:442-447.
- Castro CA, Ben-Yehudah A, Ozolek JA, Mills PH, Redinger CJ, Mich-Basso JD, McFarland DA, Oliver SL, Ahrens ET, Schatten GP. Semiquantitative histopathology and 3D magnetic resonance microscopy as collaborative platforms for tissue identification and comparison within teratomas derived from pedigreed primate embryonic stem cells. Stem Cell Research 2010; 5:201-211.
- Toppings M, Reinhart B, Castro C, Mills PH, Ahrens ET, Schatten GP, Chaillet JR, Trasler J. Profound phenotypic variation among mice deficient in the maintenance of genomic imprints. Human Reproduction 2008; 23:807-818.
- Eagleson KL, McFadyen-Ketchum LJ S, Ahrens ET, Mills PH, Does M, Nickols J, Levitt P. Disruption of Foxg1 expression by knock-in of cre recombinase: effects on the development of the mouse telencephalon. Neuroscience 2007; 148:385-99.
- Simerly C, McFarland D, Castro CA, Lin C, Redinger C, Jacoby E, Mitch-Basso J, Orwig K, Mills PH, Ahrens ET, Navara C, Schatten GP. Interspecies chimera between primate embryonic stem cells and mouse embryos: Monkey ESCs engraft into embryos, but not post-implantation fetuses. [Submitted 4/2010].

Abstracts and Presentations

- Hitchens TK, Mills PH, Foley LM, Melick JA, Kochanek PM, Ahrens ET, Ho C. In-vivo tracking of single phagocytic cells in mouse brains following traumatic brain injury using micron-sized iron-oxide particles. International Society for Magnetic Resonance in Medicine 2010, Stockholm, Sweden.
- Chen C, Ozolek JA, Castro CA, Mills PH, Rohde G. Relating MRI to Histology through Machine Learning. Biomedical Engineering Society Annual Fall Meeting 2009, Pittsburgh, PA, USA.

- Mills PH, Thompson JD, Gilson W, Arepally A, Bulte JW, Ahrens ET.Facilitated Detection and Quantification of Theragnostic Magnetocapsules by Analyzing MRI Susceptibility Perturbations. International Society for Magnetic Resonance in Medicine 2009, Honolulu, Hawaii.
- Mills PH, Ahrens ET. Sensitive positive contrast imaging of paramagnetic contrast agent distributions by visualizing phase gradients. International Society for Magnetic Resonance in Medicine 2007, Berlin, Germany.
- Mills PH, Ahrens ET. Sensitive and automated detection of iron-oxide labeled cells using phase image cross-correlation analysis. International Society for Magnetic Resonance in Medicine 2007, Berlin, Germany.
- Castro CA, Mason NS, Mills PH, Lopeta B, Ahrens ET, Schatten GP. 3D MRI reconstruction, μPET and immunohistochemistry. Embryology and Teratomas in Stem Cell Research, Clinica Universidad Fundacin Favaloro 2006, Buenos Aires, Argentina.
- Mills PH, Ahrens ET. Enhanced detection of paramagnetic contrast agents in magnetic resonance images via phase image cross-correlation analysis. IEEE Symposium on Biomedical Imaging 2006, Washington, DC, USA.
- Mills PH, Ahrens ET. Modeling MRI contrast enhancement using exogenous T2 and T2* agents. International Society for Magnetic Resonance in Medicine 2006, Seattle, WA, USA.
- Castro CA, Mills PH, Ozolek JA, Ahrens ET, Schatten GP. In utero and embryonic NHP imaging, Stem cell teratomics. Environmental Epigenomics, Imprinting, and Disease Susceptibility 2005, Durham, NC, USA.
- Castro CA, Mills PH, Ozolek JA, Ahrens ET, Schatten GP. In utero NHP imaging and monkey fetus imaging. NIH Interdisciplinary Symposium on Women's Health Research 2005, Washington, DC, USA.
- Castro CA, Mills PH, Park JH, Ozolek JA, Ahrens ET, Schatten GP. Comparative analysis between diploid and tetraploid stem cell-derived teratomas using MRI and histopathology. American Society for Cell Biology 2005, San Francisco, CA, USA.

1.3.2 Codes and Pulse Sequences

- Modified Bruker MSME, RARE, and FISP pulse sequence methods to create four new methods for use on Bruker scanner:
  - MSME-DIFF: A diffusion-weighted spin-echo.
  - CS_RARE_PHM: A fast spin-echo with compressed sensing k-space acquisition.
  - CS_FISP_PHM: A balanced steady-state free precession sequence with compressed sensing k-space acquisition.
  - FISP_PHM: A balanced steady-state free precession sequence with keyhole imaging k-space acquisition.
- MATLAB codes for the following methods:
  - T2CM contrast prediction

- PSM image generation
- PDQ dipole detection
- Image reconstruction from data acquired using compressed sensing pulse sequences (CS_RARE_PHM and CS_FISP_PHM)
- 19F noise correction and signal quantification

Core selections of code for the PSM and PDQ methods can be found in Appendix 1 of this thesis. Complete codes for all of the above methods, which include many required subroutines, is available on the website for the Pittsburgh NMR Center for Biomedical Research.

Chapter 2

Introduction

2.1 Cell Tracking for Monitoring Disease and Therapy

In vivo cell tracking within mammalian deep tissues offers insights into cell behavior, disease progression, and informs the development of new cell-based therapies. Numerous animal studies and a growing set of human trials have labeled stem cells, antigen-primed immune cells, or genetically-engineered cells with MRI contrast agents (CA) *ex vivo*, then implanted these cells and monitored them using MRI. Phagocytic cell types such as macrophages can alternatively be labeled *in situ* by *i.v.* administration of CA. The type of cell that is implanted or monitored is chosen for its propensity for repairing damaged tissue, replacing lost cell types, priming the immune system to fight cancer or infection, or treat other diseases [4]. Before implantation, cells can be genetically engineered to secrete different molecules, such as growth factors, cytokines, or other chemokines, which alter the behavior of tissues and local immune cells. Successful monitoring of these different types of CA-labeled cell requires sensitive detection and differentiation from the anatomical background present in MR images. Techniques for enhancing tracking sensitivity will facilitate deployment of these exciting applications.

Optimization of cell therapy protocols requires the ability to monitor cells after implantation. Optimizations include determining the appropriate cell delivery route, implantation site, dosage, dose scheduling, and optimal time for implantation during the course of a disease or injury. After cell implantation, accurate delivery of cells must then be verified, as correct placement is critical to therapeutic success [5]. In one study, MR verification of cell delivery revealed that dendritic

cells had accidently been misinjected by ultrasound-guided, experienced radiologists in 40-50% of patients, with injected cells appearing in the tissues surrounding the targeted lymph node [6, 7]. For this therapeutic model, accurate injection into lymph nodes was essential for dendritic cells to stimulate the desired therapeutic immune response. After cell delivery is verified, cells must then be monitored for properties such as survival, cell death, and response to administered drugs, and behaviors such as differentiation and division must be noted. If cells migrate in response to inflammation or chemokines, their movements and biodistribution require tracking. Some cell types move quickly – multipotent neuroblasts can move 100 μm per hour *in vivo* [8]. Cell movements can also be correlated with the severity of disease [4, 9]. Overall, sensitive monitoring of the effects following current cell therapy protocols will be necessary for informing the development of new ones.

Tracking cells using MRI requires they be labeled with an adjuvant contrast agent (CA) so they impart contrast in MR images. Successful tracking depends on which CA is employed, as they have varied composition, particle size, and coatings which can all alter cell uptake and retention of the agent. CA can also affect cell behavior. For example, mesenchymal stem cells have reduced migratory potential if loaded with ~100 1.63-μm diameter SPIO particles, possibly since internalizing too many particles interferes with their actin cytoskeletons [10]. Reduced synthesis of proteins for cartilage development has also been reported following cell labeling with SPIO particles [11]. Cell labeling may also alter cell differentiation, immune response [6], cell motility, and gene expression profiles [11]. Although labeled cells retain label for weeks, if they are prone to proliferation and mitotic division, their label can become diluted, splitting either symmetrically or asymmetrically between daughter cells. For example, macrophages that are not activated can undergo mitotic division after labeling by SPIO, doubling cell numbers in 24 hours [12]. Also, upon death of a labeled cell, the label may be taken up by phagocytic cells, which might then migrate and appear as if they are the originally-labeled cell type. Overall these and other factors need to be considered when choosing an appropriate cell labeling agent, and when interpreting tracking results.

Deployment of cellular therapies and monitoring in humans requires addressing CA safety. To be used in human cell-tracking applications, CAs must have minimal or manageable immunogenic, toxic, genotoxic, or toxic reproductive effects. In general, minimizing CA concentration and dose is desirable, so long as it still affords satisfactory image contrast and cellular detectability. Low

concentrations of CA help to minimize side-effects that are difficult to predict, such as prescription drug interactions, immune reactions, and organ accumulation, as the physiological effects upon CA retention are not known [4]. Recently, FDA-approved gadolinium-based contrast agents (GBCAs) have been implicated in nephrogenic systemic fibrosis in patients with severe renal insufficiency [13, 14]. Mild and severe systemic allergic reactions have also been reported to GBCAs. Other CAs based on iron oxide particles are often coated with polymers such as dextran, carboxydextran, or siloxane, which may minimize CA effects on cell function, but strategies for mitigating potential iron toxicity remains an important consideration.

Notwithstanding all the concerns and challenges related to MRI cell tracking, human studies using these methods are being reported. One study labeled neural stem cells with SPIO then injected them into humans following traumatic brain injury, tracking cell migration [15]. Neural stem cells that migrate toward trauma or demyelinated lesions may repair these tissues by differentiating into neurons, myelinating oligodendrocytes, or other types of supportive glial cell [16]. In animal models, labeled neural stem cells have been tracked longitudinally for 6 weeks *in vivo* [17]. Endogenous adult neural stem cells, which originate in the subgranular and subventricular zones, also exhibit capacity to generate new neurons and are viable targets for MR tracking. More generally, embryonic stem cells (ESCs) are being considered for their ability to propagate and differentiate into all cell types. Unmodified ESCs have a heightened potential for teratoma formation after implantation, making them an important cell type for accurate monitoring. In a second human study, cadaveric pancreatic islet cells were grafted into patients with Type 1 diabetes and were monitored using MRI. Islets were transplanted through portal vein injection after labeling with SPIO and appeared as hypointense spots in the liver, while patients no longer required insulin injections [18]. A third human study allowed monitoring of dendritic cell (DC) delivery in melanoma patients to provoke a therapeutic immune response. In this study DCs were injected into the lymph node and were successfully monitored, and migration to other local lymph nodes was observable [7]. Future human trials will be assisted by addressing ongoing technical cell tracking challenges and concerns.

Immune system activity can also be monitored without the need for *ex vivo* labeling and implantation of cells. Phagocytic cell types can be labeled *in situ* by direct i.v. injection of CAs. Circulating and tissue-resident phagocytes endocytose injected CA particles, causing them to accumulate sufficient label for MR detection. Using this concept, immune cell progression has been

non-invasively monitored during rejection of solid organs including heart, kidney, and lung [19, 20]. The quantity and biodistribution of labeled immune cells in tissue provides important information. For example, in cardiac tissue undergoing immune rejection, macrophage numbers reflect different stages of rejection[19] and might be useful for titrating the dosage of, and monitoring the efficacy of, immunosuppressive therapy [4]. *In situ* labeling has also been used for detection of cancer metastasis in lymph nodes. Injected CA is taken up by circulating and resident macrophages, causing normal lymph nodes to darken in an MR image, while lymph nodes with metastasis do not darken as they have less available space within the node for labeled phagocytic cells to reside. A hybrid *ex vivo-in situ* labeling method called magnetovaccination involves *ex vivo* labeling of antigenic cancer cells with CA, followed by cancer cell irradiation and subsequent injection into a subject. Antigen and CA from these cancer cells are taken up *in situ* by antigen-presenting cells, which can then be observed to migrate and accumulate in lymph nodes. This monitoring was sensitive enough to detect increased antigen-presenting cell migration elicited by a chemical adjuvant [21]. Other pathologies that exhibit macrophage accumulation in damaged or diseased tissues are amenable to detection via *in situ* labeling methods, including CNS lesions, ischemic brain injury, and atherosclerosis.

Overall, cellular therapies will improve as cell tracking methods improve. These improvements will come in many forms, and here we focus on the development of new CAs, and CA detection. New CAs will generate more contrast with less agent concentration, enhancing cell detectability while reducing body and cellular side effects, and new sensitive computational methods will enable tracking of cell distributions and individual cells.

2.2 Advantages of MRI as an Imaging Modality

MRI has many advantages when compared to other imaging modalities. MR has no ionizing radiation and offers excellent soft tissue contrast, unlike CT, PET, and SPECT, since it measures the radiofrequency response of protons in water, fat, and biomolecules [4]. MRI is non-invasive and can image deep tissues. This ability has made MRI the most commonly used modality for *in vivo* tracking of stem cells [5]. MRI has no dependence on radioactive isotopes that decay, allowing for prolonged longitudinal studies [5]. Finally, as of 2005, no imaging modality besides MRI can

simultaneously image a whole body and detect single cells [22]. MRI also carries a few disadvantages relative to other imaging modalities, most notably its inability to image sub-cellular details when imaging mammalian subjects, and the overall expense of facility procurement and maintenance.

2.3 Cell Tracking with SPIO Contrast Agents (^{1}H)

Superparamagnetic iron oxide (SPIO) particles are used extensively for cellular MRI due to their biocompatibility and strong contrast efficacy. SPIO particles in tissue create microscopic static magnetic field perturbations that extend 10-50 times the diameter of the particle, thereby reducing the T_2 and T_2^* of nearby water protons [23]. This inhomogeneity causes nearby protons to rapidly dephase, leading to a dramatic reduction in the T_2 and T_2^* relaxation times. T_2^*-weighted magnitude images are particularly sensitive to these effects, often exhibiting regions of hypointensity indicating SPIO accumulation.

For preclinical research, a wide variety of SPIO particles have been used with different sizes, compositions, and functional surface coatings, such as peptides or antibodies for molecular epitope detection [24, 25, 26, 27, 28]. Unmodified SPIO nanoparticles, such as Resovist$^{\text{TM}}$and Feridex$^{\text{TM}}$, are used for liver lesion detection and for distinguishing between normal and cancerous lymph nodes [29]. Histologically, SPIO presence in tissue has been verified using electron microscopy, iron staining, or immunohistochemistry [4]. Many cell types have been labeled by SPIO [20], either *ex vivo* or *in situ* [4]. Different cell types have been shown to endocytose SPIO particles on the order of 1.6 μm to 5.8 μm in diameter [20, 30]. Non-phagocytic cells can also be labeled *ex vivo* via the use of transfection agents [31], electroporation [32], sonoporation [33], receptor-mediated binding, or receptor-mediated endocytosis [34]. Numerous studies have investigated the impact of SPIO labeling on cell viability and function [35, 24, 36, 37, 38], and the empirical detection limits of SPIO-labeled cells have been investigated [37, 39, 22]. Clinical translation of SPIO-based cell tracking has also been demonstrated [6, 7].

Iron-oxide CAs also encompass intracellular labeling approaches that image gene expression by utilizing genetically-encoded metalloproteins [40, 41, 42, 43, 44, 45]. In these approaches, metalloproteins, particularly from the ferritin family, are selectively overexpressed in specific host tissues. These iron storage proteins effectively become a paramagnetic CA by sequestering endogenous iron

from the organism, thereby imparting exogenous MRI contrast to transduced tissues.

Distinguishing SPIO-induced image hypointensity from intrinsic contrast is a common challenge when imaging these agents using T_2 and T_2^*-weighted scans, especially if their contrast is subtle or biodistribution is not known beforehand. False positives can originate from intrinsic contrast sources, for example, from tissue interfaces, blood vessels, necrosis, hemorrhage, or low proton density. To help address this challenge, investigators have developed image acquisition methods that generate positive contrast images highlighting SPIO. These methods include, for example, differential imaging before and after agent delivery, specialized weighted contrast methods [46], spectrally-selective excitation [47, 48, 49], gradient dephasing [50, 51], quantum coherence imaging [52], and ultrashort TE image subtraction [53]. These techniques generate positive contrast images that complement anatomical magnitude images, but may also carry limitations. For example, several methods require foreknowledge of the magnitude of the field disturbances caused by SPIOs, and this information is used to configure scan parameters such as excitation frequency, bandwidth, selective RF pulse shape [47], echo time, slice thickness, and rephasing gradient amplitude [50]. Additionally, some of these techniques demand high-end or customized hardware [53] or additional anatomical scans that result in prolonged acquisition times [47, 48, 50]. Positive contrast methods tend to diminish the signal-to-noise ratio (SNR) per unit scan time compared to conventional magnitude images in order to reap the benefits of positive contrast. Alternatively, one can highlight SPIO by using conventional acquisition methods, followed by generation of positive-contrast images using MRI phase images. Applying high-pass filters to phase images has been shown to accentuate spatial magnetic field variations due to SPIO deposits [54, 55].

Overall, positive-contrast methods for imaging SPIO assume unknown or arbitrary distributions of agent. However, if SPIO is distributed in a known geometry, this can be exploited to computationally estimate the total number of SPIO deposits, and the volume magnetic susceptibility and iron concentration of each deposit. Previously, phase images have been used to assay these quantities for macroscopic objects such as cylinders [56] or spheres [57]. An *in vivo* study quantified iron by modeling a localized tissue injection of SPIO as a sphere [58]. Other studies quantify clusters of SPIO labeled cells by measuring local signal loss [59] or proton relaxation rates [60]. Analyzing magnitude signal loss around SPIO deposits generally leads to quantification results that correlate with echo time or sample orientation [58].

Also, to generate useful images, CAs must accumulate in cells or tissues in adequate concentrations. Too high of a concentration, particularly when agents are used intracellularly, can be disadvantageous due to potential cytotoxicity and immunogenicity concerns. Therefore, models for relating iron concentration to MR image contrast can help for minimizing CA concentrations or for CA development.

2.4 Cell Tracking with Sparse Fluorine-19 Based Tracer Agents (^{19}F)

Achieving sufficient signal and image quality when imaging sparse fluorine tracers is a challenge when developing novel cell-tracking methods. Sometimes low signal can necessitate long scan times, leading to prohibitively long *in vivo* imaging sessions, as well as possible false-negative results when signal is buried beneath image noise levels. Since mammals have low endogenous fluorine concentrations in their tissues, one can acquire ^{19}F MR images of fluorine-labeled cells inside of a subject and encounter no confounding sources of fluorine-signal background. Locations where fluorine agent has accumulated can be determined with near-absolute certainty and require no disambiguation. One can take advantage of this property by overlaying ^{19}F images onto ^{1}H images of the same subject to visualize the anatomical distribution of fluorine-labeled cells.

Previously, sparse ^{19}F MRI tracers have been used to image the mouse gastrointestinal tract [61] and perform quantitative immuno-targeting of fibrin within atherosclerotic plaque [62, 63, 64]. Tracers have also been used for tracking and quantifying various cell types including dendritic cells [65], diabetogenic T-cells [66], and stem cells[67]. Multiple cell populations have been tracked in the same subject by using multiple ^{19}F labels [67]. Direct i.v. injection of ^{19}F tracer agent emulsions allow for detection of organ rejection within rat models of allografted heart and kidney tissue [68]. In these models, rat monocytes and macrophages are labeled *in situ* by circulating ^{19}F tracer, which then migrate to tissue undergoing rejection [68]. ^{19}F MR spectroscopy has been used to study fluorine-based drug metabolism [69, 70] and to determine partial oxygenation of tissues since some perfluorocarbon (PFC) compounds have a spin-lattice relaxation time (T1) that is proportional to the PFC's partial oxygenation (pO_2) [71, 72]. Perfluorinated microcapsules (i.e., perfluorocapsules) have been synthesized that incorporate ^{19}F tracer agent into spheroids of alginate [73].

Fluorine-19 is a spin-$\frac{1}{2}$ nucleus like hydrogen-1. It has a gyromagnetic ratio that differs from ^{1}H by ∼6%, and each ^{19}F nucleus has a sensitivity in MRI ∼ 0.83 that of ^{1}H, so the minimum number of fluorine spins per voxel that can be detected using conventional MRI is on the order of 10^{18} spins [65, 5]. Therefore, imaging of this nucleus can be performed using conventional ^{1}H MRI procedures after adjusting imaging parameters. Because of this sensitivity requirement, lack of fluorine signal in a ROI does not indicate the absence of fluorine-labeled cells in that region. Imaging of single cells is not feasible using ^{19}F MRI. The ideal ^{19}F agent exhibits resonance at a single, narrow frequency band, with each molecule consisting predominantly of fluorine atoms [74]. A commonly-used perfluorocarbon (PFC) is perfluoro-15-crown-5-ether (PCE), which is a crown-ether with a longitudinal relaxivity of $T_1 \approx 1.0 \pm 0.2$ seconds at 7.0 Tesla [75].

Methods utilizing fluorine-based tracers for *in vivo* cell tracking involve labeling of cells with nanoparticles containing tracer agent such as perfluoropolyether (PFPE) or perfluorocarbon (PFC) [4]. In these methods, cells are typically labeled *ex vivo* by encouraging them to take up a fluorine-based compound, usually by coincubation. PFCs are chemically and biologically inert organic molecules [74]. They have highly stable carbon-fluorine bonds, and biologically undergo no degradation within lysosomes, or metabolism by any known enzymes [74]. Loading cells with PFC on the order of 10^{11} – 10^{13} spins/cell shows no overt cellular toxicity [74]. When analyzing T-cells labeled with PFPE emulsion, NMR spectra for intracellular PFPE were observed to show no sign of chemical shift or change in line shape, suggesting PFPE is not being metabolized [66]. Dendritic cells (DCs) labeled *ex vivo* have been shown uptake PFPE efficiently with little effect on DC function [65]. These cells were tracked with ^{19}F MRI, and when pelleted and analyzed by NMR, their ^{19}F spectrum will show a single resonance peak with a FWHM of ∼150 Hz. Like T-cells, dendritic cells also have not had any observed change in their PFPE NMR line shape [65].

In general, using reported cell-labeling and imaging methods, as few as ∼7,500 ^{19}F-labeled cells per voxel are detectable *in vitro*, and ∼28,000 cells per voxel detectable *in vivo* [66, 65, 67]. Other studies report that as few as ∼6,100 cells per voxel can be detected in *ex vivo* cell pellets [67]. Estimates of the number of fluorine spins per labeled cell range from 5.2×10^{12} spins per cell in DCs (0.25 ng PFPE) to 2.2×10^{13} spins/cell [66, 65].

Typical MR imaging methods for ^{19}F acquisitions use spin-echo [65, 68] or fast-spin echo [66, 75] pulse sequences to avoid spin-dephasing effects present when using gradient-echo pulse sequences.

Depending on ^{19}F tracer agent concentration and voxel size, the number of signal averages required for a satisfactory image can range from 4 averages to as high as 1024 averages. When imaging PCE, TE values will typically range from TE = 6.4 – 15 ms and TR values range from TR = 1000 – 1200 ms, since the T_1 of PCE is $\sim 1.0 \pm 0.2$ s at a field strength of B_0=7 T [75]. Fast spin echo pulse sequences will tend to employ 4 – 8 echoes within each TR period. In general, in order to obtain adequate SNR when performing ^{19}F imaging, acquisitions have a lower resolution than anatomical proton images, and can require hundreds of signal averages. SNR, resolution, averages, and total acquisition time must be balanced or sacrificed in order to avoid prohibitively long imaging sessions.

Different methods have been proposed to increase the SNR per unit time (SNR/t) when performing ^{19}F imaging. Specifically, the use of multi-echo pulse sequences can increase SNR/t because signal is repeatedly acquired while the fluorine nuclei undergo longitudinal relaxation. Small tip-angle pulse sequences and steady-state gradient-echo pulse sequences also have the potential to increase SNR/t, as these sequences preserve longitudinal magnetization, enabling the use of short TR values (i.e., TR$\ll$T1). When modeled by fundamental signal equations, fast imaging pulse sequences provide more SNR/t than conventional spin-echo [76]. However, fast sequences based on gradient echoes also are susceptible to magnetic inhomogeneity within a sample or the image field of view, especially at high field strengths, which can lead to a loss of already-low ^{19}F signal. Pulse sequences based on spin echoes however, such as fast spin echo (i.e., RARE), refocus dephased spins, avoiding this source of signal loss. Fast imaging sequences also often require high-end MR acquisition hardware in order to generate strong and rapidly-switching magnetic field gradients. Gradient hardware will typically be limited by maximum gradient strength (units mT/m) and maximum duty cycle (D_c), which represents the time-averaged gradient intensity. Duty cycle must remain below a gradient-specific level so that hardware does not sustain damage from accumulated waste heat. Assuming that a pulse sequence is running for a sustained period of time (i.e., 3 s), for each separate gradient (i.e., X-, Y-, Z-axes), the duty cycle is defined as

$$D_c = \sum_{t=0}^{\mathrm{TR}} \frac{G}{G_{max}} \Delta t \tag{2.1}$$

where G is gradient strength during time period Δt, G_{max} is maximum gradient strength, and Δt represents each time period during which G has a new value during the period from $t = 0$ to

t = TR.

As an alternative to implementing these different fast imaging techniques, ^{19}F tracer agents can be doped to increase SNR/t. Gd-DTPA has previously been used to shorten ^{19}F tracer agent longitudinal relaxation (T_1), thereby enabling the use of pulse sequences with shorter TR times, accelerating signal acquisition, and increasing SNR/t [77]. Other alternatives for increasing SNR/t include image denoising algorithms and methods that sparsely sample k-space using conventional pulse sequences, such as keyhole imaging or compressed sensing MRI.

2.5 Differences Between Using ^{1}H Versus ^{19}F MRI for Cellular Imaging

When performing MRI cell-tracking, there are advantages and disadvantages to using ^{19}F tracer agents versus ^{1}H SPIO CAs:

1. SPIO CA imaging has a sensitivity advantage over ^{19}F tracer imaging. SPIO contrast results from shortening T_2 of nearby protons, which are already abundant in living tissues, while ^{19}F imaging requires a sufficiently-high concentration of fluorine atoms to acquire a relatively weak MR signal. Therefore, on a per-atom basis, fewer iron atoms are need than fluorine atoms to obtain satisfactory image contrast when imaging labeled cells. Single-cell imaging of fluorine tracer-labeled cells is not feasible, while single-cell imaging of iron-containing cells has been demonstrated [22, 19] and requires an intracellular iron mass on the order of 1 pg[Fe] [78].

2. Image contrast is unambiguous when using fluorine tracer because fluorine is present in mammals at trace concentrations. When using SPIO however, image contrast due to CA can sometimes be ambiguous due to other sources of hypointense MR image contrast, potentially leading to false-positive and false-negative results.

3. Because the only sources of image intensity in fluorine images are fluorine nuclei and Gaussian/Rician image noise, noise can be statistically characterized and differentiated from fluorine signal. Working with and eliminating ^{1}H image noise can be more difficult than in ^{19}F imaging because it is combined with, and dependent on, different sources of proton signal and endogenous tissue contrast.

4. Quantification of ^{19}F tracer or tracer-labeled cells can be done by integrating fluorine signal, whereas SPIO quantification or SPIO-labeled cell counts rely on various subject-dependent parameters, including R_2 relaxivity and local magnetic field inhomogeneity [66].

Chapter 3

Theory

3.1 MRI Signal

Nuclear species with unpaired protons or unpaired neutrons have a spin quantum number, I, which is related to their total angular momentum (intrinsic angular momentum and orbital momentum) of all their nucleons, $\overrightarrow{J}$ [79]. The spin states for a nucleus with spin quantum number I can be enumerated as $m_I = [I, I-1, ..., -I+1, -I]$, resulting in a total of $2I+1$ possible spin states [79]. Nuclei with a value of $I \neq 0$ have a net nuclear spin. Hydrogen-1 has a net nuclear spin due to a single unpaired proton, giving it a spin quantum number of $I = \frac{1}{2}$ and 2 spin-states: $[\frac{1}{2}, -\frac{1}{2}]$. Fluorine-19 also has a net nuclear spin due to a single unpaired proton, giving it a spin quantum number of $I = \frac{1}{2}$ and $[\frac{1}{2}, -\frac{1}{2}]$ spin states. Other nuclei that have a net nuclear spin have been imaged for research purposes and include the following: sparse physiological nuclei [^{13}C, ^{15}N, ^{17}O], physiological nuclei [^{23}Na, ^{32}P], and hyperpolarized nuclei [^{3}He, ^{129}Xe] [80]. ^{1}H is the most commonly-imaged nucleus in MRI since the human body is approximately 60% mobile water.

Because each unpaired proton has an intrinsic electric charge and angular momentum, it generates an electromagnetic field, giving its nucleus a magnetic dipole moment. The magnetic dipole moment for ^{1}H and ^{19}F nuclei are:

$$\mu_{[^{1}\mathrm{H}]} = 2.792847 \cdot \mu_N \tag{3.1}$$

$$\mu_{[^{19}\mathrm{F}]} = 2.628868 \cdot \mu_N \tag{3.2}$$

where μ_N is the nuclear magneton constant, which has a dipole moment value of $\mu_N = 5.051 \times 10^{-27}$ J/T [81]. When a nucleus with a magnetic dipole moment is placed in an external magnetic field ($\overrightarrow{B}_0$), it freely precesses when not parallel to the axis of that field ($\overrightarrow{B}_0$). The angular frequency of precession, the Larmour frequency ω, about the axis of B_0 is

$$\omega = \gamma B_0 \tag{3.3}$$

where γ is the gyromagnetic ratio of the nucleus being imaged [82]. This ratio represents the ratio of magnetic dipole moment to angular momentum. Combining Eqs. (3.1)-(3.3), the gyromagnetic ratios for hydrogen and fluorine are

$$\gamma_{^1\mathrm{H}} = \frac{\mu_{[^1\mathrm{H}]}}{I\hbar} = 267.513 \, \frac{\mathrm{rad}}{s \cdot T} = 42.5764 \, \frac{\mathrm{MHz}}{\mathrm{T}} \tag{3.4}$$

$$\gamma_{^{19}\mathrm{F}} = \frac{\mu_{[^{19}\mathrm{F}]}}{I\hbar} = 251.662 \, \frac{\mathrm{rad}}{s \cdot T} = 40.0745 \, \frac{\mathrm{MHz}}{\mathrm{T}} \tag{3.5}$$

where $\hbar$ is derived from Planck's constant ($\hbar = \frac{h}{2\pi} = 1.0546 \times 10^{-34} J \cdot s$). Larmor precession frequencies for different nuclei can be altered due to their local molecular environment, causing a "chemical shift" in the resonance frequency of the nuclei. Chemical shift tends to be on the order of a few ppm in ^{1}H [82].

When the bulk of nuclei are at equilibrium within a voxel, their total longitudinal spin-magnetization is:

$$M_{0,z} = \frac{4\pi^2 \gamma^2 \hbar^2 I(I+1) B_0 N_S}{3KT_S} \tag{3.6}$$

which simplifies in our case of spin-$\frac{1}{2}$ nuclei to:

$$M_{0,z} = \frac{4\pi^2 \gamma^2 \hbar^2 B_0 N_S}{4KT_S} \tag{3.7}$$

where N_S represents the total number of spins contained in the voxel, K is the Boltzmann constant ($1.38 \times 10^{-23} J/K$), and T_S represents the spin system's temperature in Kelvin, which for mammalian *in vivo* scenarios is typically 310 K. [83].

According to the classical description of nuclear spin precession, applying an RF electromagnetic wave that matches the precession frequency of a nucleus (ω) will cause the nucleus to steadily rotate away from the axis of the primary magnetic field ($\overrightarrow{B}_0$) when observed in the rotating frame of reference. While the nucleus is precessing around the axis of the primary magnetic field it produces a weak electromagnetic wave that can be detected as a signal voltage by detection coils (by Faraday's Law of Induction). Pulse sequences encode these signals so that proton densities can be mapped onto a 2D or 3D grid, with discrete dimensions and discrete volume regions represented by volumetric pixels (voxels). When performing ^{1}H or ^{19}F imaging, image voxel intensity values depend on many intrinsic tissue and molecular parameters beyond just proton density (ρ), including the spin-lattice (longitudinal) relaxation time (T_1), spin-spin relaxation time (T_2), molecular movement (e.g. diffusion), chemical shift, and magnetic susceptibility effects (T_2^*). Voxel intensity values also depend on the pulse sequence that is used and its related parameters (most commonly TE and TR).

When nuclei stop being excited by RF energy, they will dissipate this energy into their surrounding environment. The spin-lattice relaxation rate ($R_1 = 1/T_1$) describes how quickly nuclei will return to equilibrium magnetization M_0 along the axis of the primary magnetic field (Eq. (3.7)). T_1 primarily depends on the size of molecules in the lattice and their temperature [84]. T_1 relaxation also tends to be faster with smaller molecule size and when molecule rotation frequency is closer to the Larmour frequency [84].

3.2 MRI Noise

Signal detected from precessing nuclei is corrupted by statistical noise that comes primarily from Johnson white noise, which arises from thermal agitation of electrons within subject tissue and from the apparatus receiver coil and its associated electronics [85]. Johnson noise intensity values are approximately modeled by a Gaussian probability distribution of the form:

$$G(x, \mu, \sigma) = \frac{1}{\sigma\sqrt{2\pi}} e^{-\frac{(x-\mu)^2}{2\sigma^2}} \tag{3.8}$$

where x is the sampled noise value, μ is the average noise value, and σ is the standard deviation of the distribution. Johnson noise in MRI signals has a zero mean value, simplifying Eq. (3.8) to

become

$$G(\sigma, x) = \frac{1}{\sigma\sqrt{2\pi}} e^{-\frac{x^2}{2\sigma^2}} \tag{3.9}$$

This zero-mean Gaussian Johnson noise is present in both real μ_R and imaginary μ_I parts of the MRI signal, with both noise signals uncorrelated and independent of one another. When these signals are converted into real and imaginary images using a 2D Fourier transform, the noise retains its zero-mean Gaussian identity. Conventional MRI images are formed by calculating the magnitude of the real and imaginary image components of a complex-data MRI image using the relation $I = \sqrt{\mu_R^2 + \mu_I^2}$ and are called "magnitude images." After this operation, the noise distribution in the generated magnitude images is no longer modeled as Gaussian, and instead follows a Rayleigh distribution. Specifically, if X and Y are two Gaussian random variables with $X \sim N(0, \sigma^2)$ and $Y \sim N(0, \sigma^2)$, then the random variable $R = \sqrt{X^2 + Y^2}$ follows a Rayleigh distribution. The Rayleigh distribution has a more general form called the Rice (Rician) distribution, which has been used to describe noise in MRI [86]. Gudbjartsson and Patz [86] define M as measured pixel intensity in a magnitude image and A as actual pixel intensity before noise addition, leading to the following probability distribution for magnitude images:

$$p_M(M) = \frac{M}{\sigma^2} e^{-(M^2+A^2)/2\sigma^2} I_0 \frac{A \cdot M}{\sigma^2} \tag{3.10}$$

.

where I_0 is the modified zeroth order Bessel function of the 1st kind and σ represents the standard deviation of image noise assumed to be the same value in both real and imaginary channels. Often noise in magnitude MRI images is modeled as Gaussian, which can result in significant noise underestimation (60% reduced noise power) [86]. However, this probability distribution, Eq. (3.10) can be approximated as Gaussian in the limit of $A/\sigma > 3$ as follows:

$$\begin{cases} p_M(M) \approx \frac{1}{\sqrt{2\pi\sigma^2}} e^{-(M-\sqrt{A^2+\sigma^2})^2/2\sigma^2} & \text{if } A/\sigma > 3 \\ \overline{M} = \sqrt{A^2 + \sigma^2} \\ \sigma_M^2 = \sigma^2 \end{cases}$$

and in the limits of $A = 0$ (no signal, just noise):

$$\begin{cases} p_M(M) = \frac{M}{\sigma^2} e^{-M^2/2\sigma^2} & \text{if } A = 0 \\ \overline{M} = \sigma\sqrt{\pi/2} \\ \sigma_M^2 = (2 - \pi/2)\sigma^2 \end{cases}$$

3.3 MRI Contrast

The signal-to-noise ratio (SNR) in an image region (compartment) can be described as

$$\text{SNR} = \left|\bar{I}/\bar{N}\right| \tag{3.11}$$

where $\bar{I}$ represents mean image intensity in the compartment and $\bar{N}$ represents mean image noise.

The contrast-to-noise ratio (CNR) between a region, A, against a background, B, can be expressed as the difference between their respective SNRs:

$$\text{CNR} = \left|(\bar{I}_A - \bar{I}_B)/\bar{N}\right| \tag{3.12}$$

where $\bar{I}_A$ and $\bar{I}_B$ are the respective mean image intensities in compartments A and B, and $\bar{N}$ is the mean image noise intensity. CNR is often determined by differences in proton density and relaxation times T_1, T_2, and T_2^* between the two compartments.

Contrast in T_2-weighted images (T_2-WI) can be enhanced by introducing a T_2-reducing agent that changes the effective transverse relaxation time to become T_2' according to the relation

$$\frac{1}{T_2'} = \frac{1}{T_2} + r_2[M] \tag{3.13}$$

where T_2 is the transverse relaxation time within a compartment in the absence of agent, r_2 is the transverse relaxivity of the agent, and $[M]$ is its concentration.

Similarly, for T_1 agents,

$$\frac{1}{T_1'} = \frac{1}{T_1} + r_1[M] \tag{3.14}$$

3.4 MRI Phase Images

MR images are typically reconstructed from a series of echoes acquired in k-space using a multi-dimensional Fourier transform, with each voxel in the reconstruction having a real and imaginary component (i.e., $I = a + bi$, $i^2 = -1$). The magnitude image, given by $|I| = \sqrt{\mu_R^2 + \mu_I^2}$ is typically displayed, where μ_R and μ_I represent real and imaginary signal components, respectively. Phase angle information, given by $\phi = tan^{-1}(\mu_I/\mu_R)$, is typically discarded. Phase maps have been studied extensively [46, 87, 88, 89]. Generally, a voxel's phase value is proportional to the magnetic field at its location. MRI phase maps have been successfully used to quantify magnetic field inhomogeneity and bulk material susceptibility [89, 90, 5, 88, 91], enhance contrast among tissues with different susceptibilities [46], quantify iron in the brain [87], classify chemical shifts [92], enhance vascular contrast [88, 93], identify magnetic particles based on how they appear [94], and undistort MR images [95]. The measured phase angle (ϕ) in each voxel of a phase map can be simplified as

$$\phi = \phi_{low-f} + \phi_{\text{SPIO}} + \phi_{high-f} \quad [-\pi \leq \phi \leq \pi] \tag{3.15}$$

where ϕ_{low-f} represents low-spatial-frequency contributions to the phase angle, ϕ_{SPIO} represents contribution from nearby SPIO, and ϕ_{high-f} represents other, non-SPIO high-spatial-frequency contributions (e.g., material/tissue interfaces). The uncertainty in the measured phase angle is given by [96]

$$\sigma_\phi = 1/\text{SNR}_{ROI}. \tag{3.16}$$

where σ_ϕ is the standard deviation in the phase angle in a region of interest (ROI) and SNR_{ROI} is the SNR in the conventional magnitude image in the same ROI. In phase images, we define the phase contrast-to-noise ratio (CNR_ϕ) between an ROI and its background as

$$\text{CNR}_\phi = (\phi_{ROI} - \phi_{BKG})/\sigma_{\phi,\text{ROI}} = \text{SNR}_{\text{ROI}}(\phi_{ROI} - \phi_{BKG}) \tag{3.17}$$

where ϕ_{ROI} is the measured phase angle for our ROI and ϕ_{BKG} is the background phase angle near the ROI containing no paramagnetic deposits.

When working with a single gradient-recalled echo (GRE) image, the phase image must first be 'unwrapped' to remove phase discontinuities when crossing from $-\pi$ to $+\pi$ over the image field of view before one can distinguish the desired ϕ_{SPIO} component in Eq. (3.15). These $-\pi$ / $+\pi$ boundaries can be eliminated using unwrapping algorithms that determine the multiple of 2π that must be added or subtracted from the phase angle to obtain a discontinuity-free phase map. After unwrapping, we eliminate ϕ_{low-f} by applying a high-pass filter to the unwrapped phase map, resulting in a phase-offset image, with each voxel represented by

$$\Delta\phi = \phi_{\text{SPIO}} + \phi_{high-f} \tag{3.18}$$

The resulting phase-offset image contains only phase contributions from SPIO and other high-spatial-frequency sources. A voxel's intensity in the phase-offset image ($\Delta\phi$) is proportional to that voxel's deviation in magnetic field (ΔB_Z) relative to its surrounding background material, i.e.,

$$\Delta\phi = \gamma \cdot \text{TE} \cdot \Delta \text{B}_Z(r, \theta) \tag{3.19}$$

where γ is the proton gyromagnetic ratio and TE is echo time. This relationship between $\Delta\phi$ and ΔB_Z (Eqs. (3.18) and (3.19)) will be used extensively during the derivation of theory for the chapter on the PSM method and the chapter on the PDQ method.

3.4.1 Noise Effects on Phase Angle

Conventional phase images have a noise distribution in each voxel's phase angle that approximately follows a zero-mean Gaussian distribution (Eq. 3.9) when SNR>3 [86]. Specifically,

$$p_{\Delta\theta}(\Delta\theta) \approx \begin{cases} \frac{1}{\sqrt{2\pi(\sigma/A)^2}} \exp\left[\frac{-\Delta\theta^2}{2(\sigma/A)^2}\right] & \text{if } A/\sigma > 3 \\ \frac{1}{2\pi} & \text{if } A = 0 \text{ and } (-\pi < \Delta\theta < \pi) \end{cases} \tag{3.20}$$

where the standard deviations for $\Delta\phi$ are:

$$\sigma_{\Delta\theta} = \begin{cases} \frac{\sigma}{A} & \text{if } A \gg \sigma \\ \sqrt{\frac{\pi^2}{3}} & \text{if } A = 0 \end{cases} \tag{3.21}$$

where A represents image pixel intensity in the absence of noise [86].

3.4.2 Inaccuracies introduced by phase unwrapping algorithms

Phase unwrapping algorithms eliminate $-\pi$ / $+\pi$ boundaries to obtain a discontinuity-free phase map by adding a multiple of 2π to every phase angle value. Between any two pixels, phase can go through the entire unit circle (2π) multiple times, and a phase unwrapping algorithm will not have enough information to decide on the correct multiple of 2π to add or subtract, making the phase unwrapping problem an underdetermined one. In many scenarios, rapid phase changes that confound phase unwrapping algorithms are arguably non-physical, since phase maps represent static magnetic field which can be represented by a smooth, continuous function. However, MRI phase map data are discrete, and when resolution is not sufficient for properly sampling phase, unwrapping algorithms can introduce errors if phase is spatially undersampled (i.e., two adjacent pixels have an actual phase difference greater than π) [97].

Phase unwrapping is used for our different computational methods (i.e., PDQ and PSM), so errors introduced by the process will propagate and create errors in results generated by our computational methods. The unwrapping algorithm used for most of our work [98] has an error rate of 0.4% when SNR = 2.5 [98], but SNR $<$ 2.5 is common at the center of dipoles, where signal-free pixels contain random phase values [58]. To mitigate this effect, one may weigh or mask out pixels with SNR $<$ 2.5 to deemphasize these in our different analyses [58]. Alternatively, one can acquire phase maps using multi-echo GRE pulse sequences that replace phase unwrapping with 'temporal unwrapping' [99, 100, 58]. In general there are two different temporal unwrapping (rapid phase-mapping) approaches. The first approach is to modify a conventional GRE pulse sequence to have two echoes instead of one [99]. The two echoes are spaced apart by a short time of about 7 ms. Two different 2D/3D phase maps are calculated from the first and second echoes. The phase map voxel values of the first echo are then subtracted from the phase map values of the second. The result represents how much phase angle changes at every voxel in the sample volume over a short 7 ms time period. Short inter-echo times tend to produce small phase angle changes at each voxel that allow one to determine the change's magnitude and sign with higher confidence than when using conventional single-echo GRE coupled with phase-unwrapping algorithms. Although dual-echo GRE sequences do not completely eliminate the possibility of phase-angle wrapping, it does ensure that phase angle changes are sufficiently small so that the correct multiple of 2π to add

or subtract from a specific voxels phase angle value is chosen with a higher confidence than when using conventional methods. The second approach to rapid phase-mapping is to use an 8-echo GRE pulse sequence with reversed gradient polarities [100]. This GRE echo train uses eight echoes with a linearly increasing delay between each echo. As few as three echoes can be used, but greater field-mapping accuracy results from more echoes [100]. A typical acquisition can be made with a first echo at 1.2 ms, initial echo spacing of 0.7 ms, and an incremental echo spacing increase of 0.2 ms [100]. By incrementing echo spacings, the phase angle has a quadratic dependence on echo number, which allows second-derivative minimization to be used. This in turn enables accurate inference of the phase wrapping jump of $\pm 2\pi$ that may occur in a fraction of voxels. This method, coined "temporal unwrapping," doesn't propagate spatial errors like time-consuming unwrapping algorithms may do in areas of high-frequency phase angle wrapping [100].

Chapter 4

Two-compartment T_2 Contrast Model (T2CM)

The majority of this thesis chapter has previously been published under the title "Theoretical MRI contrast model for exogenous T_2 agents" in the scientific journal Magnetic Resonance in Medicine [101]. *The journal is the copyright holder for this previously-published material.*

4.1 Introduction

There is a great interest in developing new generations of MRI contrast agents (CAs) that can be used for diagnostic purposes, therapeutic monitoring, and to further our understanding of diseases. New generations of agents can often provide MRI contrast for specific cell types, detect the presence of specific molecules, such as enzymes and nucleic acids [44, 40, 45], and be responsive to physiology.

For useful images to be generated, CAs must accumulate in cells or tissues in adequate concentrations. Moreover, too high of a concentration, particularly when agents are used intracellularly, can be disadvantageous because of potential cytotoxicity concerns. In this chapter a general theoretical model is presented to evaluate the minimum concentration of a T_2 CA required for satisfactory MRI contrast. This model provides an *in silico* alternative to empirical determination in specific *in vivo* systems, and should be viewed as an important component to an overall rational design strategy. Previous work along these lines includes general [102] and sparse [63] models for T_1 CAs. Our model requires only a few readily evaluated parameters. For practicality, we provide a set of simple analytic expressions to address the specific uptake and activation mechanisms used by vascular, extracellular, and intracellular agents. The model is demonstrated by predicting contrast produced by Feridex, a clinically-approved CA, and by ferritin, a superparamagnetic protein. Model predic-

tions are then tested using phantoms. As an additional example of the applicability of the contrast model, we compare the contrast efficacy of the metal ions in two clinically approved T_1- and T_2-type CAs. Finally, in an Appendix within this chapter we discuss a general numerical formalism that can help relate the contrast and agent concentration when working with T_2^*-weighted (T_2^*-W) gradient-echo (GRE) methods.

4.2 Theory

The CNR of a region, A, against a background, B, is described by Eq. (3.12). One can enhance contrast in T_2-W images by introducing a T_2-reducing agent as described by Eq. (3.13).

4.2.1 Contrast from Spin Echo and Gradient-Recalled Echo

Our model considers both the spin-echo (SE) and gradient-recalled-echo (GRE) pulse sequence. For the spin-echo (SE) pulse sequence, signal intensity in a voxel is given by

$$I_{\mathrm{SE}} = k \cdot [1 - 2e^{-(\mathrm{TR}-\mathrm{TE}/2)/T_1} + e^{-\mathrm{TR}/T_1}]e^{-\mathrm{TE}/T_2} \tag{4.1}$$

where k is the proton density ($M_{z,0}$ from Eq. (3.7)) scaled by a system-specific that reflects the signal sensitivity of the MRI apparatus (k_0) [103]. In a T_2-WI, TR $\gg T_1$, which reduces the SE intensity equation (Eq. (4.1)) to

$$I_{\mathrm{SE}-T_2} \approx k \cdot e^{-\mathrm{TE}/T_2} \tag{4.2}$$

We note that Eq. (4.2) has the same form for a GRE sequence when TR $\gg T_1$ and the RF excitation tip angle is $\theta = 90°$, except that T_2^* is substituted for T_2. (See the Appendix at the end of this chapter to address cases of GRE with short TR values and small tip angles). To model the contrast between compartments A and B, we combine equations (3.12) and (4.2), which gives

$$\mathrm{CNR} = \frac{k}{\bar{N}}|e^{-\mathrm{TE}/T_{2A}} - e^{-\mathrm{TE}/T_{2B}}| \tag{4.3}$$

We define the parameter $\lambda = k/\bar{N}$, which is specific to an imaging system and its subject. We find λ empirically by acquiring a T_2-WI and using the relation

$$\lambda = k/\bar{N} = \bar{I}/\bar{N}e^{-\mathrm{TE}/T_2} \tag{4.4}$$

4.2.2 Two-Compartment T_2 Contrast Model

We find the optimum TE value that maximizes CNR by taking the derivative of Eq. 4.3 with respect to TE and equating the derivative to zero [96]:

$$\mathrm{TE}_{\mathrm{opt}} = \ln(T_{2A}/T_{2B}) \cdot T_{2A}T_{2B}/(T_{2A} - T_{2B}) \tag{4.5}$$

Substituting $\mathrm{TE}_{\mathrm{opt}}$ for TE in Eq. (4.3) gives

$$\mathrm{CNR} = \lambda(\alpha^{\alpha/(1-\alpha)} - \alpha^{1/(1-\alpha)}), \qquad \text{where} \qquad \alpha = T_{2A}/T_{2B} \tag{4.6}$$

To ensure that contrast is easily discernible between the two compartments, we assume that a value of $\mathrm{CNR} \geq 5$ is required [102]. We solve Eq. (4.6) for α by setting $\mathrm{CNR} = 5$ and performing a numerical fit ($R^2 = 0.99$) for a realistic range of λ values ($40 < \lambda < 600$), which yields

$$\alpha = -10.5\lambda^{\lambda/(1-\lambda)} + 0.642\lambda^{1/(1-\lambda)} + 0.36 \tag{4.7}$$

To generalize Eq. (4.7) for different values of CNR, substitute λ with $\lambda_{\mathrm{NEW}} = \lambda(5/\mathrm{CNR}_{\mathrm{NEW}})$. Now, we allow Eq. (3.13) to have different CA concentrations in compartments A and B, which can be written as

$$\alpha = \frac{T'_{2A}}{T'_{2B}} = \frac{1 + r_{2B}[M]_B T_2}{1 + r_{2A}[M]_A T_2} \tag{4.8}$$

Using forms of Eq. (4.8) expressed in terms of the numerical solution for α (Eq. (4.7)), we classify CAs into four categories as described below:

1. Functional agents. CA is present in both compartments at equal concentrations ($[M]_A = [M]_B$), and the T_2 relaxivity of the agent in the target region of interest, compartment A, is

modified *in situ* by some active means. The minimum concentration required becomes:

$$[M]_A = \frac{1-\alpha}{T_2(\alpha \cdot r_{2A} - r_{2B})} \tag{4.9}$$

2. Selective or targeted agents. CA has a fixed T_2 relaxivity, but accumulates in or binds to region A at higher concentrations than background region B:

$$[M]_A = \frac{1-\alpha}{\alpha \cdot r_2 \cdot T_2} + \frac{[M]_B}{\alpha} \tag{4.10}$$

3. Highly localized agents. CA has a fixed T_2 relaxivity and is introduced into region A by direct injection or implantation of labeled cells. No agent is present in background region B:

$$[M]_A = \frac{1-\alpha}{\alpha \cdot r_2 \cdot T_2} \tag{4.11}$$

In categories 1-3, $[M]_A$ is the minimum CA concentration needed to obtain CNR=5. To use the scenarios in Eqs. (4.9) – (4.11), we empirically measure λ (Eq. (4.4)) for the particular MRI scanner and subject, and then calculate α (Eq. (4.7)). We then substitute α, the agent-free T_2, and the agent r_2 into the scenario equation.

4.2.3 Ferritin Relaxivity

Ferritin is a special contrast case because its relaxivity is strongly dependent on the amount of Fe contained in the apoferritin shell, and thus it requires additional modeling. The number of Fe atoms per shell is called its loading factor (LF), which varies between 0 and 4000 [104]. When $LF > 100$, the T_2 relaxivity of ferritin is approximately linearly proportional to both LF and magnetic field strength up to field strengths of at least 11.7 T, and we model this as [105]

$$r_2 = 0.2055(\mathrm{LF})\mathrm{B}_0 + 13 \quad \text{for} \quad (100 < \mathrm{LF} < 3500) \tag{4.12}$$

where r_2 has units of s^{-1} mM^{-1} (protein shells), B_0 is in Tesla, and 37 °C is assumed [106]. When LF < 60, however, ferritin T_2 relaxivity varies nonlinearly with both the LF and field strength, and

exhibits different relaxivity regimes. We parameterized these regimes by fitting data previously acquired by Vymazal *et al.* [107] at $B_0 < 1.5$ T to obtain

$$r_2 = 4(\mathrm{LF}) + 13 \quad \text{for} \quad (0 < \mathrm{LF} < 13) \tag{4.13}$$

$$r_2 = 130e^{-\mathrm{LF}/6} + 5.11\mathrm{B}_0 + 26.9 \quad \text{for} \quad (13 < \mathrm{LF} < 60) \tag{4.14}$$

where r_2 has units of s^{-1} mM^{-1} (protein shells), and B_0 is in Tesla. Using Eqs. (4.12) and (4.13) – (4.14) for the r_2 of ferritin, one can apply the contrast model scenarios presented in Eqs. (4.8)-(4.9).

4.3 Methods

4.3.1 Contrast Model Verification

As a simple test of this model, images were acquired in phantoms containing the different contrast agents in H_2O. The agents tested were Feridex® (Berlex Imaging, Wayne, NJ) and purified horse spleen ferritin (Sigma-Aldrich, St. Louis, MO). The horse spleen ferritin was used to approximate the contrasting behavior of intracellular recombinant ferritins expressed via transgenes. Its iron content was measured by spectrophotometric assay using Ferene-S reagent (3-(2-Pyridyl)-5,6-di(2-furyl)-1,2,4-triazine-5',5"). Normalizing iron content to protein content then gave LF = 720 ± 20. First, r_2 values of the two agents were measured using three concentrations of each agent at 11.7 T and 37 °C. We imaged capillaries containing the agents using a 20-echo Carr-Purcell-Meiboom-Gill (CPMG) pulse sequence, with TE/TR=9/7000 ms. The average image intensity for each capillary was computed. The intensities exhibited mono-exponential decay with increasing TE. Because ferritin and Feridex® have relatively small diameters, 12 nm and 50-150 nm respectively, r_2 should not depend on the choice of inter-echo time TE [108]. Using the measured r_2 values and λ calculated from Eq. (4.4), three capillary tubes of dilute Feridex® or ferritin solutions were prepared in concentrations where the model predicts a CNR = 2, 5, and 8. Fe concentrations used were 15 μM, 56 μM, and 86 μM for Feridex and 0.63 mM, 1.7 mM, and 3.0 mM for ferritin. Tubes were imaged at 37 °C using an 11.7 T, Bruker AVANCE micro-imaging system. T_2-weighted SE images were acquired for capillary pairs using a FOV=1 cm, a 4 mm slice thickness, a 256×256 image

matrix and TR=10 s. TE was set to TE_{opt} (Eq. 4.5), which ranged from 22-25 ms in Feridex® and 24-25 ms in ferritin. Although efforts were made to maintain identical imaging conditions, empirical λ varied between 90-140 in our apparatus, leading to CNR values that systematically differed from the theoretically predicted values of CNR = 2, 5, and 8 in the prepared phantoms. In order to compare our experimental results, actual λ values were calculated post-experiment, and these values were used for testing the predictive abilities of this model independent of these apparatus fluctuations.

4.4 Results

4.4.1 Contrast Model Predictions

To demonstrate our contrast model, we analyzed several contrast agents. Figure 4.1 panels a-b display the minimum Fe concentrations of Feridex® and ferritin, respectively, needed to obtain images with CNR = 5. These calculations assume a localized agent distribution (Eq. 4.11). For Feridex® we assumed an r_2 of 172 s^{-1} mM^{-1} (Fe) at 11.7 T and 144 s^{-1} mM^{-1} (Fe) at 1.5 T, an H_2O background with T_{20}=47 ms at 11.7 T, T_{20}=63 ms at 1.5 T, and 37 °C. Figure 4.1 panel a shows that concentrations on the order of 10–35 μM Fe at 1.5 T and 12–38 μM Fe at 11.7 T are required for realistic values of λ. Interestingly, a higher iron concentration is required when going from 1.5 T to 11.7 T. Figure 4.1 panel b models ferritin concentrations needed for high LF ($\sim$ 900) and low LF ($\sim$10) using Eqs. (4.12), (4.13) and (4.14), respectively. These calculations assume a localized agent distribution (Eq. (4.11)), a ferritin r_2 of 1900 s^{-1} mM^{-1} (protein) at 11.7 T and 244 s^{-1} mM^{-1} (protein) at 1.5 T, a H_2O background, and 37 °C. Figure 4.1 panel c shows the same calculation, but normalized per ferritin molecule. Interestingly, for low-LF, T_2 relaxivity per Fe atom is greater, and thus one requires significantly less total Fe ($< 70\%$) to achieve adequate contrast compared to more Fe-laden ferritin cores (Fig. 4.2 panel b) [109]. At high magnetic field strengths, concentrations in the range of 0.5 – 2.3 mM Fe or 0.8 – 3.0 μM holoferritin are required to achieve satisfactory contrast (Fig. 4.1 panels b–c).

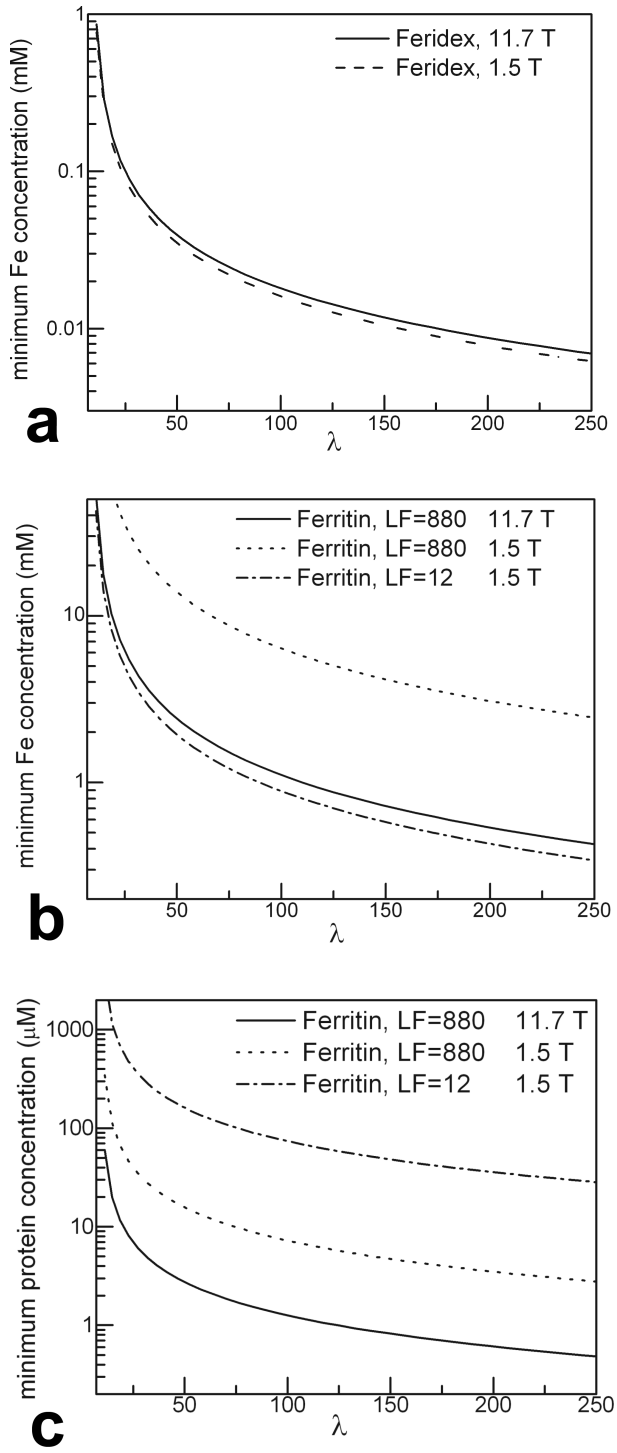

Figure 4.1: Minimal T_2 contrast agent concentration required to achieve CNR = 5.
Concentration curves are for (a) Feridex® and (b-c) ferritin. Panel (a) shows that Feridex® concentrations on the order of 10-40 μM Fe are required for realistic λ values in our simulated system. Panel (b) shows that for low LF ferritin, the T_2 relaxivity per Fe atom is maximized. Panel (c) shows that at high magnetic field strengths the ferritin concentration needed to provide useful contrast diminishes significantly. For LF=880 ferritin at 11.7 T, one requires only ∼0.1 times the concentration needed at 1.5 T ($\lambda = 100$). All simulations assumed a H_2O background at 37 °C. *(Figure taken from Fig. 1 of Mills and Ahrens [101])*

4.4.2 Contrast Model Verification

As an experimental confirmation of the accuracy of the contrast model, capillary tubes containing dilute aqueous solutions of Feridex and purified horse spleen holoferritin were imaged at 11.7 T. Figure 4.2 displays the experimental CNR results overlaid on the model-predicted CNR for each concentration tested. Predicted CNR values are within 2–13% of the empirically observed CNR.

There are many potential sources of error in these measurements, such as pipetting error when measuring the concentrated contrast agent, RF inhomogeneity of the birdcage coil across the image field of view, and imperfect shimming. Because of these confounding factors, we believe that a $< 13\%$ error is a reasonable expectation. Overall, in our experimental system, the model predicts that in order to obtain satisfactory T_2-weighted contrast (i.e. CNR = 5), one requires a minimum concentration of 15 μM Fe using Feridex or 1.2 μM ferritin protein. These calculations assume a highly-localized agent in H_2O with T_{20}=47 ms (Eq. (4.11)), optimal TE (Eq. (4.5)), B_0 = 11.7 T, 37 °C, and the measured r_2 of Feridex® and ferritin equal to 172 ± 9 s^{-1} mM^{-1} (Fe) and 1900 ± 200 s^{-1} mM^{-1} (protein), respectively. In our experiments the empirical parameter λ ranged from 90-140 when calculated via Eq. (4.4), where the pure water capillary was used as the background reference.

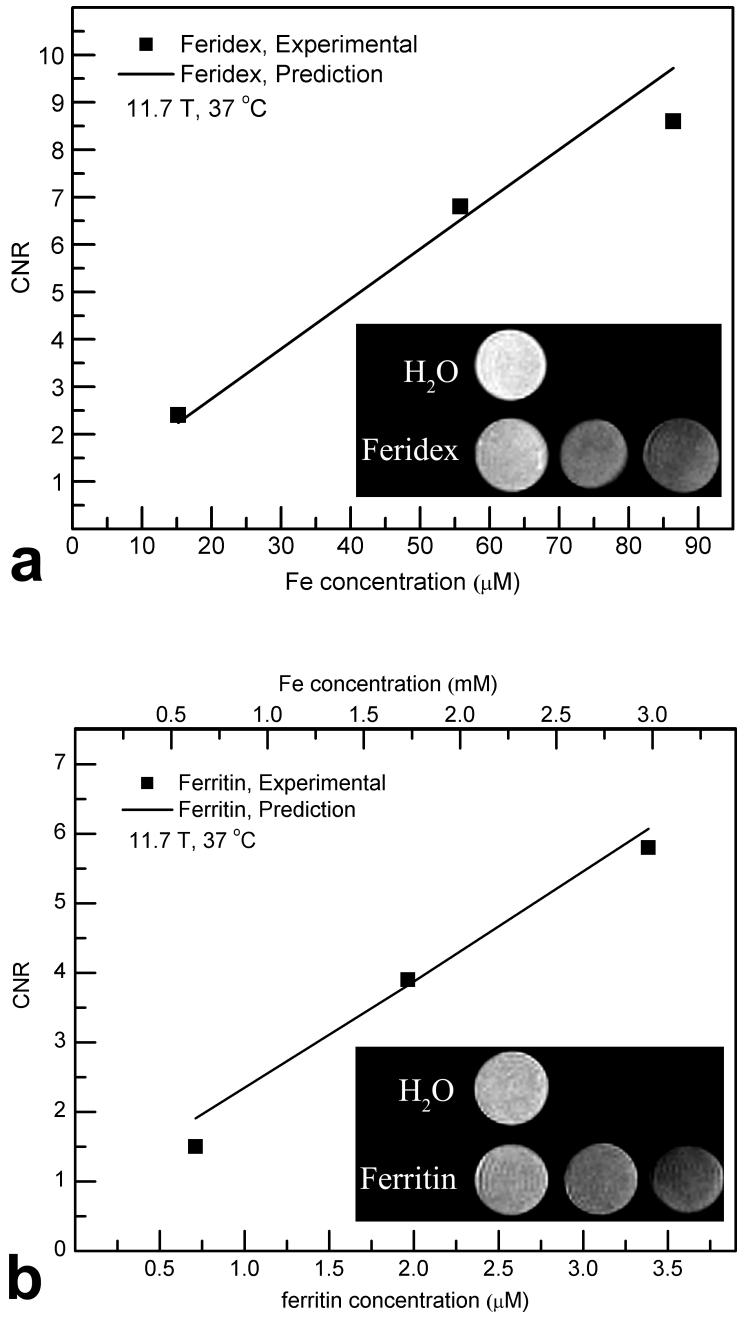

Figure 4.2: Experimental and model-predicted CNR for different T_2 contrast agent concentrations. Data points show the experimentally observed CNR in phantoms for three different concentrations of (a) Feridex® and (b) ferritin, while solid lines show model-predicted CNR for a highly-localized contrast agent (Eq. (4.11)). The capillary tube images (insets) show pure H_2O and the respective concentrations of Feridex® and ferritin. Model-predicted CNR values are within 2–13% of observed values. Data were acquired at 37 °C and 11.7 T. *(Figure taken from Fig. 2 of Mills and Ahrens [101])*

4.4.3 Contrast Model Predictions for comparing T_2 and T_1 CAs

As an additional application of the contrast model, we simulate the contrast efficacy of the metal ions in two clinically-approved T_1- and T_2-type contrast agents with the help of a T_1 contrast model previously described [102]. We compare the Fe^{2+}/Fe^{3+} in Feridex® and Gd^{3+} in GdHP-DO3A (ProHance, Bracco Diagnostics, Princeton, NJ) at two different field strengths (1.5 T and 11.7 T). For our simulation we set the background tissue to be gray matter of the central nervous system and rely on published values of relaxation times in humans at 1.5 T [108] and in mice at 11.7 T [110, 111]. For gray matter, we used T_1/T_2 = 1900 / 31.4 ms at 11.7 T [108], and T_1/T_2 = 1200 / 80 ms at 1.5 T [109]. For GdHP-DO3A, we use a T_1 relaxivity value at 37 °C given by 3.7 mM^{-1} s^{-1} (Gd) at 1.5 T [112], and we measured a value of 3.40 s^{-1} mM^{-1} (Gd) at 11.7 T. The high-field value was measured using an inversion recovery sequence at 15 different TI times and three dilute agent concentrations on an 11.7 T NMR spectrometer. Figure 4.3 displays the calculated results; on a per metal ion basis, Fe in ferumoxide is significantly more effective at enhancing MRI contrast compared to the Gd-based agent at typical clinical magnetic field strengths. For example, at 1.5 T and for λ=100, approximately 63% less metal ion is needed to produce satisfactory contrast. Interestingly, at 11.7 T the two ions differ by only 15%, where lower amounts of the Gd-agent are required. The T_1 relaxivity of both ferumoxide and GdHP-DO3A change only slightly from 1.5 T to 11.7 T [112, 113], thus some of this high-field behavior can be attributed to the increase in gray matters T_1/T_2 ratio.

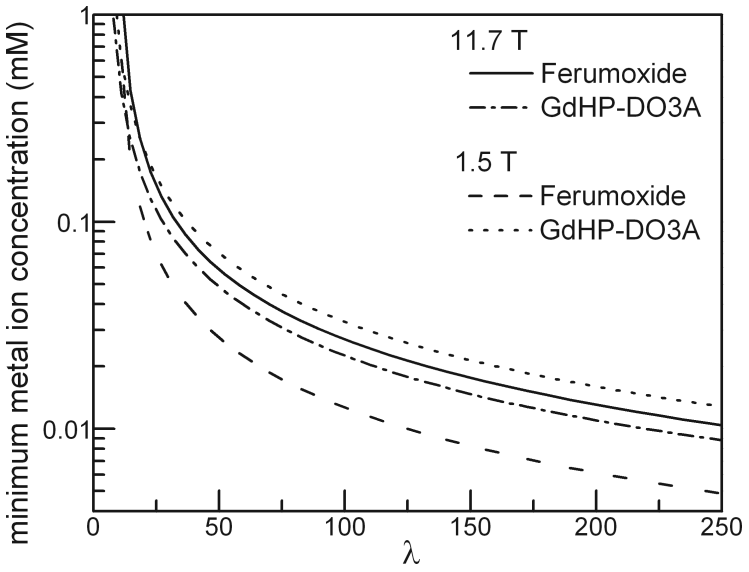

Figure 4.3: Comparison between contrast produced by GdHP-DO3A (ProHance®) and Ferumoxide (Feridex®) on a per metal-ion basis.
The simulation assumes *in vivo* gray matter of the central nervous system as a background tissue. For Feridex, approximately 63% less metal ion is needed compared to Gd to produce satisfactory contrast at 1.5 T (λ=100). However, at 11.7 T and the same λ, the concentration of ions provides the same level of contrast differ by only 15%, where lower amounts of the Gd-agent are required. Predictions for the Gd-based agent are based on the T_1 model described by Ahrens *et al.* [102]. *(Figure taken from Fig. 3 of Mills and Ahrens [101])*

4.5 Discussion

The development of new contrast agents requires an understanding of the minimum agent concentration needed to provide satisfactory contrast as part of an overall design strategy, and our contrast model can quantitatively address this issue. Furthermore, the model can be used to avoid excess agent concentrations, which may result in adverse biological effects such as cytotoxicity. The model can be used in a wide range of applications; four different application categories are defined that depend on the expected *in vivo* behavior of the agent and its mode of delivery. The model requires a minimum number of parameters, such as the relaxivity of the agent and regional T_2 in the absence of agent. It is simplified via the introduction of an empirical parameter, λ, that is independent of agent type and essentially describes the overall sensitivity of the MRI system with the subject. The λ parameter is readily evaluated (Eq. 4.4) empirically from an MR image and the measured regional T_2 value in the absence of agent. Our model predictions were tested using T_2-weighted SE images of aqueous phantoms containing dilute concentrations of an SPIO agent

and holoferritin, and reasonable agreement was found. In other analyses, we used the model to compare the contrast efficiency of the metal ions in T_1 versus T_2 agents. We note that a comparable model for T_1-type agents has been previously described [102], and has been effective, for example, in predicting the contrast enhancement of enzyme-activated functional contrast agents *in vivo*.

4.5.1 Accuracy and Applicability

There are many factors that limit the overall accuracy and applicability of this contrast model. First, it assumes that T_1 weighting effects are minimal (i.e., TR $\gg T_1$). However, as long as TR $> T_1$, this assumption is estimated to decrease the accuracy of the model predictions by only about 3–25%, depending on the intrinsic tissue T_1 in the model system. Second, our model assumes that the average contrast over a region of interest is comprised of numerous voxels. However, when using certain cellular contrast agents such as micron-sized SPIO agents [19, 30] *in vivo* contrast may be highly localized and punctate. This may offer improved detectability, and the contrast model may underestimate contrast in these cases. A third limitation is in our analysis of ferritin, which relies on *in vitro* T_2 relaxivity values of purified protein; there are likely to be significant differences between *in vitro* and *in vivo* holoferritin relaxivity values [114]. In addition, r_2 values *in vivo* may be tissue-type dependent, and thus high-accuracy contrast modeling may need to account for these differences. Overall, the intent of this contrast model is not to provide highly accurate predictions in specific tissues and organs *in vivo*, but rather, to numerically simulate the performance of agents, which is particularly important in their early development stages.

4.5.2 Implications for Ferritin

The modeling results for ferritin (Fig. 4.1 panels b-c) have interesting consequences for experiments that express holoferritin protein via transgenes [40, 41]. First, since ferritin has a pronounced linear T_2 relaxivity increase with increasing field strength, significantly less transgene expression is needed at high fields for contrast detection. For example, at 11.7 T the required concentration of LF=880 ferritin is only ≈0.1 times the concentration required at 1.5 T (for λ=100). Finally, we speculate that transgene-expressed ferritins are most often in the low-LF regime *in vivo*; strong molecular-genetic promoters can rapidly produce high copy numbers of intracellular ferritin, and *in vivo* iron loading of apoferritin is the rate-limiting step. Importantly, in the low-LF regime the T_2 relaxivity

per Fe is maximal, which works to the advantage of an investigator when using these technologies. Overall, the contrast model can aid in the design of molecular-genetic strategies incorporating ferritin reporters.

4.6 Conclusions

Emerging cellular-molecular MRI methods often utilize T_2 contrast agents for *in vivo* detection. We present a general theoretical model to predict minimal contrast agent concentration requirements. This model can be used to aid the development of new generations of contrast agents and their applications, and may be an effective alternative to empirical concentration determinations in phantoms or *in vivo*. It is applicable to a wide range of T_2-type agents and delivery scenarios, requiring only a few readily-evaluated parameters.

4.7 Appendix: Contrast Modeling when Using Short-TR, Small-tip-angle GRE

A general description of contrast agent concentration requirements for GRE T_2^*-weighted images is presented. Above, we considered the GRE sequence only in the limit of TR $\gg T_1$ and $\theta = 90°$. More generally, contrast between regions A and B of a spoiled GRE sequence is given by [103]

$$\mathrm{CNR_{GRE}} = \sqrt{\mathrm{NEX}}\frac{k}{\overline{N}}\sin(\theta) \quad \left[\frac{1-e^{-\mathrm{TR}/T'_{1B}}}{1-e^{-\mathrm{TR}/T'_{1B}\cos(\theta)}}e^{-\mathrm{TE}/T'_{2B}}\right] - \left[\frac{1-e^{-TR/T'_{1A}}}{1-e^{-\mathrm{TR}/T'_{1B}\cos(\theta)}}e^{-\mathrm{TE}/T'_{2A}}\right] \tag{4.15}$$

$$\text{where } \frac{1}{T'_{\{1:2\}\{A:B\}}} = \frac{1}{T_{\{1:2\}\{A:B\}}} + r_{\{1:2\}}[M]_{\{A:B\}}$$

In regions A or B, $T_{\{1:2\}\{A:B\}}$ are the agent-free T_1 or T_2 values, $r_{\{1:2\}\{A:B\}}$ are contrast agent T_1 or T_2 relaxivities, and $[M]_{\{A:B\}}$ are the agent concentrations. Analyzing the relationship between concentration and contrast in the generalized situation is made complex by introducing T_1-weighting

and the tip angle θ. To use Eq. (4.16), one can fix CNR = 5, fix TR, then computationally search Eq. (4.16) for the minimal agent concentration and optimal TE and θ. In general, one can run a minimization function of the form

$$\{[M]_A, \mathrm{TE}_{opt}, \theta_{opt}\} = f(\mathrm{CNR}, \mathrm{TR}, r_1, r_2, T_1, T_2, \lambda) \tag{4.16}$$

to obtain the minimal contrast agent concentration. In this approach the minimum concentration $[M]_A$, TE, and θ are varied and returned by the minimization method, and CNR, r_1, r_2, T_1, T_2, and λ are known input parameters. The minimization can be done using a standard "Simplex" algorithm [115]. This method is appropriate for Eq. (4.16) because only one optimal TE and θ, and minimal concentration exist and partial derivatives need not be known explicitly [115]. Using a "brute-force" method to optimize TE and θ is also reasonable since the search space is small.

To demonstrate this minimization, we ran a spoiled-GRE simulation for ferritin in mouse brain gray matter at 11.7 T and 37 °C. Assuming that ferritin accumulates in region A, but not in region B, the simulation parameters were λ=100, T_1=1800 ms, T_2^*=28 ms [111], and r_2=1900 s^{-1} mM^{-1} (protein). Constants were passed to a brute-force MATLAB function to minimize the concentration given by Eq. (4.16), and we calculated the results for the range TR=10–2000 ms. Figure 4.4 shows the resulting minimal concentration, optimal TE and θ required for CNR=5 in our simulated tissue system. This general numerical approach can be used for other pulse sequences. By combining the analytical intensity equations for a pulse sequence (i.e., in the form of Eq. (4.1)), and combining these equations with Eq. (3.12) to obtain a CNR function, one can computationally minimize concentration. For example, one can model contrast for steady-state free-precession sequences by using appropriate analytical signal intensity equations [116].

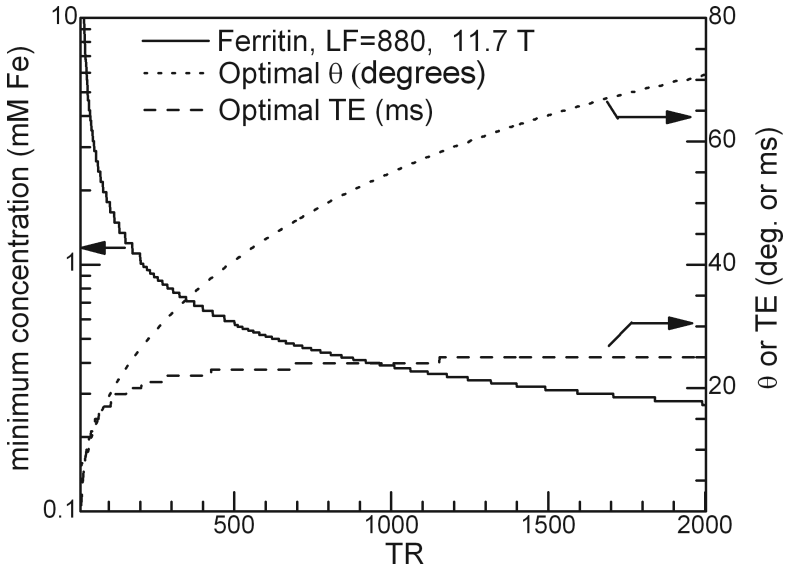

Figure 4.4: Plot of minimum Fe concentration, optimal tip angle, and optimal TE required for CNR = 5 in a simulated small-tip-angle GRE experiment.
The solid line denotes minimal concentration (left axis), while the other lines show optimal parameter values (right axis). The TE varies rapidly in the short-TR domain and levels off as TR $> T_1/2$. The optimal tip angle approaches 90° as TR increases. The simulation assumes a highly-localized distribution of LF=880 ferritin in a gray matter background. We assume 11.7 T, 37 °C, and λ=100. *(Figure taken from Fig. A1 of Mills and Ahrens [101])*

Chapter 5

Phase Slope Magnitude (PSM) Imaging

The majority of this thesis chapter has previously been published under the title "Enhanced positive-contrast visualization of paramagnetic contrast agents using phase images" in the scientific journal Magnetic Resonance in Medicine [55]. *The journal is the copyright holder for this previously-published material.*

5.1 Introduction

Distinguishing SPIO-induced image hypointensity from intrinsic contrast is a common challenge when imaging iron-oxide contrast agents using T_2 and T_2^*-weighted scans, especially if their contrast is subtle or biodistribution is not known beforehand. False positives can originate from intrinsic contrast sources, for example, from tissue interfaces, blood vessels, necrosis, hemorrhage, or low proton density. To help address this challenge, investigators have developed image acquisition methods that generate positive contrast images highlighting SPIO. Positive contrast methods tend to diminish the signal-to-noise ratio (SNR) per unit scan time compared to conventional magnitude images in order to reap the benefits of positive contrast. An alternative approach for addressing this common challenge is to highlight SPIO by generating positive-contrast images from MRI phase images [117, 54]. Because phase image pixel values correlate with local magnetic field, applying high-pass filters to phase images has been shown to accentuate spatial magnetic field variations (i.e., paramagnetic CA deposits). Importantly, post-processing of phase images does not require altering image acquisition procedures, as is required for many of the prior art methods, as discussed above. In one study, a smoothing high-pass filter was applied to phase images of an air-water phantom and *in vivo* brain tissue [54]. The filter used in this study, however, results in images with an

effective resolution roughly two times lower than the original image [54]. In a second study, a high-pass filter that does not reduce effective resolution was applied to phase images of bovine muscle tissue [117]. More recently, the linear component of phase spatial variation was visualized by performing quadratic fits to k-space phase shifts [118]. This method uses a variable-size sliding-window approach that avoids potential phase-unwrapping errors, but sacrifices image resolution as a result of partial-voluming.

These studies [117, 54, 118] provide strong visual evidence for enhanced sensitivity to magnetic susceptibility disturbances among tissues when using filtered phase maps. However, these studies either do not quantify sensitivity gains, or sacrifice spatial resolution during the image generation process. This study aims to simultaneously preserve image resolution while quantifying sensitivity improvements that result from high-pass filtering phase images. Our resulting Phase Slope Magnitude (PSM) images emphasize spatial magnetic field variations. The PSM image contrast-to-noise ratio (CNR) was calculated in regions surrounding paramagnetic CA distributions and compared against CNR values from conventional magnitude images. Initially, using PSM we analyzed an agarose gel phantom doped with SPIO particles. PSM analysis was also performed on a fixed mouse brain that had been stereotaxically inoculated in one hemi-segment of the striatum with a replication-defective adenovirus (AdV). The AdV contained transferrin receptor (TfR-1) transgenes; overexpression of TfR in transduced cells upregulates ferritin, a paramagnetic cellular iron storage protein that produces a weak contrasting effect in T_2 and T_2^*-weighted MRI scans [40, 119]. PSM analysis was also performed using *in vivo* data acquired in a mouse brain that had been inoculated with AdV containing transgenes for ferritin subunits. These transgenes cause the formation of paramagnetic holoferritin as brain cells sequester endogenous iron from the organism [40]. The paramagnetic disturbance from ferritin is weaker compared to SPIO, and PSM images may make the difference between seeing, and not seeing, a targeted CA. Finally, we applied the PSM algorithm to *in vivo* MRI data acquired in an anesthetized mouse with its quadriceps inoculated with primary dendritic cells (DCs) that had been labeled with SPIO *ex vivo*.

Overall, PSM images exhibit a significant 1– to 8–fold CNR improvement in regions where paramagnetic agent is present compared to conventional magnitude images. A method for thresholding PSM images to eliminate noise from phase measurements is also described. Additionally, a few variations of PSM images are presented. The PSM method does not require extra MRI scans

because it relies on phase images that are a by-product of conventional MRI scans; it can be used retrospectively on previously-acquired data. PSM image generation requires no prior knowledge about the magnitude of the field disturbance created by arbitrary CA distributions, and can be used in conjunction with any T_2^*-weighted MRI pulse sequence.

5.2 Theory

5.2.1 Phase Slope Magnitude (PSM) Image Generation

The intensity of a voxel in the phase-offset image ($\Delta\phi$ from Eq. (3.19)) is proportional to the deviation in magnetic field (ΔB_Z) within that voxel relative to its surrounding background material. To accentuate perturbations in phase due to paramagnetic agent deposits, we first calculate the mathematical gradient of the phase-offset image (Eq. (3.19)), which results in a vector field:

$$\Delta\phi_{\text{Offset}} = \sum_{i=1}^{n} \frac{d\phi_{\text{Offset}}}{dx_i}\hat{x}_i \tag{5.1}$$

In Eq. 5.1, n indicates the number of dimensions for comparison (e.g., $n = 3$ for 3D volumes). Using the vector field from Eq. (5.1), we set the magnitude of each vector as a pixel value in our final PSM image product:

$$I(x, y, z) = \|\Delta\phi_{\text{Offset}}(x, y, z)\| \tag{5.2}$$

where x, y, z represent image grid coordinates, and I represents PSM image pixel intensity. Additional computational details used in generating PSM images are described in the Methods section.

5.2.2 PSM Image Noise Thresholding

Pixel intensity values in PSM images are generated from phase maps as described by Eqs. (3.18),(5.1), and (5.2). Phase maps also contain an underlying probabilistic noise intensity that is inversely proportional to their corresponding magnitude images signal-to-noise ratio (SNR) [80, 86]. One can eliminate likely noise pixels in PSM images by applying the following statistical criterion. First, we assume that the phase offset images from which PSM images are generated (Eq. (3.18)) have corresponding magnitude images with regional SNR>3 [86]. This allows the phase image noise

distribution to be approximated as Gaussian [86], and one can calculate the standard deviation of noise values (σ) in the phase-offset images using the relation:

$$\sigma_\phi = \sigma / \sqrt{\overline{M}^2 - \sigma^2} \tag{5.3}$$

where $\overline{M}$ is the average intensity of the magnitude image in this ROI and σ is the standard deviation of the real or imaginary Gaussian noise in this same region [86]. Alternatively, σ can be estimated by:

$$\sigma^2 = \sigma_N^2 / (2 - \pi/2) \tag{5.4}$$

where σ_N is the noise standard deviation in a region devoid of proton signal [86]. Combining Eqs. (5.3) and (5.4) gives the relation:

$$\sigma_\phi = 1.5264 \cdot \sigma_N / \sqrt{\overline{M}^2 - 2.33 \cdot \sigma_N^2} \tag{5.5}$$

Since Eq. (5.5) provides the noise level in phase-offset images (Eq. (3.18)), we can use this to calculate noise in PSM-images by considering Eq. (5.2). Specifically, along each spatial dimension, (i.e., dx, dy, or dz) noise values in the PSM image will also follow a Gaussian distribution, with a new standard deviation of

$$\sigma_{\phi_{dx}} = \sigma_{\phi_{dy}} = \sigma_{\phi_{dz}} = \sqrt{\sigma_{\phi A}^2 + \sigma_{\phi B}^2} = \sqrt{2} \cdot \sigma_\phi \tag{5.6}$$

where $\sigma_{\phi A}$ and $\sigma_{\phi B}$ represent standard deviation in two adjacent voxels, and σ_ϕ is found using Eq. (5.5). Since this distribution is Gaussian, 95% of its values are expected to fall within the range $[-2\sqrt{2}\sigma_\phi, 2\sqrt{2}\sigma_\phi]$. Thus, when generating 2D or 3D PSM images using Eqs. (5.1) and (5.2), one can optionally threshold out values of dx, dy, or dz that are within this range, thereby removing a significant number of 'false-positive' pixels from our final PSM image product that likely represent random phase angle noise variations.

5.2.3 Direction-Weighted and Higher-Order Derivative PSM Images

PSM images are generated by calculating the spatial 3D first derivative (i.e., 3D gradient) of phase images. The contributions from the x-, y-, and z-dimension are all equal in magnitude, and a user may desire to weigh these components separately when looking to accentuate certain magnetic disturbances in phase-offset images. For example, a sphere in a magnetic field creates a dipole-shaped magnetic field disturbance. When visualized with conventional PSM images, the dipolar shape has bright intensity at its poles and around its center. If the center of the dipole is visualized using an x-dimension-weighted PSM image, only the poles have high intensity, whereas using a y-dimension-weighted PSM image, one only sees high intensity around the center of the dipole. The differences between these different phase-slope images may make them useful for detection of different geometrical distributions of SPIO.

Also, higher-derivative images that look at the curl of the phase-offset image in the x-, y-, and z-dimension will exhibit different contrast mechanisms that may accentuate certain desirable characteristics of a phase image. In the datasets we applied this to, there were no notable benefits of using higher-derivatives to visualize phase images.

5.2.4 Phase Slope Coherence (PSC) Images

The phase gradient in a phase-offset image often has a uniform directionality (angle of slope) when surrounding objects of interest. Other areas that do not surround objects of interest often have large phase gradient values in them, but these gradients are not uniformly oriented in the same direction (e.g., noise, tissue boundaries). In some cases, it may be beneficial to generate images that use both the phase slope magnitude (PSM) component from Eq. (5.2), and a 'phase slope angle' component, which quantifies the local coherence of the direction in which the phase gradient has its largest rate of change. We call these images Phase Slope Coherence images, and they tend to deemphasize tiny phase variations, while instead emphasizing the multi-voxel phase patterns which tend to be produced by any arbitrary coherent distribution of superparamagnetic contrast agent. The two types of PSC images that consider directional consistency were weighted by:

(i) Average neighbor difference: Every pixel in PSM image is divided by sum of differences in phase slope direction between it and its neighbors:

$$\mathrm{PSC}_P = \mathrm{PSM}_P \left| \sum_{n \in \mathrm{Neighbors}(p)} (\mathrm{PSD}_n - \mathrm{PSD}_p) \right|^{-1} \tag{5.7}$$

(ii) Greatest neighbor difference: Every pixel in PSM image divided by maximum difference in phase slope direction between that pixel and its neighbors.

$$\mathrm{PSC}_P = \mathrm{PSM}_P \left| \max_{n \in \mathrm{Neighbors}(p)} (\mathrm{PSD}_n - \mathrm{PSD}_p) \right|^{-1} \tag{5.8}$$

where for these two weighting approaches, PSC_P is the intensity of pixel P in the resulting PSC image, PSM_P is the phase slope magnitude value for pixel P in the phase slope vector field calculated using Equation (5.2), and PSD_P is the phase slope direction value (i.e., angle) for pixel P, and PSD_n is the phase slope direction of one of the neighbors of pixel P.

5.3 Methods

5.3.1 Gel Phantom

A gel phantom was constructed using a 3 mL syringe filled with 2% agarose that was lightly doped with 1.6 μm-diameter macroscopic paramagnetic iron-oxide (MPIO) particles (Bangs Laboratories, Fishers, IN). The phantom was imaged using an 11.7 T, 89-mm vertical-bore Bruker AVANCE micro-imaging system (Bruker BioSpin, Billerica, MA). We used a 25-mm diameter birdcage coil and a standard 3D GRE pulse sequence with parameters TE/TR=7/1500 ms, $\theta \approx 90^\circ$, and 40 μm isotropic resolution. Raw echo data were reconstructed to create phase images, as described below.

5.3.2 Mouse Brains Expressing Transferrin and Ferritin Transgenes

Adult 20 g female C57B1/6J mice (Harlan) were anesthetized using an intraperitoneal cocktail of ketamine and xylaxine and placed in a head stereotaxic device. Animals were injected with a recombinant, replication-defective adenovirus (AdV) carrying either the transferrin receptor (TfR-1) gene or a 1:1 mixture of the light and heavy subunits of ferritin (LF and HF, respectively), as described in Reference [40]. Inoculations were made into the right striatum with a 32-gauge needle (total of 1.6×10^9 plaque-forming units). A control AdV containing the β-galactosidase reporter

(LacZ) was injected into the contralateral hemisphere. Animals were monitored until recovered and housed with a normal diet and water *ad libitum*. In the AdV-TfR-1 transduced brain, at day 5 post-injection, the mouse was perfused and fixed in 4% paraformaldehyde, and the brain removed. The brain was suspended in 1% agarose in a plastic tube prior to imaging. Samples were imaged at 11.7 T using acquisition parameters TE/TR=6.4/50 ms, $\theta \approx 30°$, 51 μm isotropic voxels, $512 \times 256 \times 256$ image points, and 16 averages. The LF- and HF-AdV inoculated mouse was imaged *in vivo*. At day 5 after injection, the mouse was anesthetized using isoflurane in air and imaged as above except using a motion-gated gradient-echo pulse sequence with acquisition parameters TE/TR=7.7/175ms, 98 μm isotropic voxels, 256×256 image points, and 4 averages. Additional experimental details about these procedures and materials are described elsewhere [40]. All animal experiments were performed in accordance with the Carnegie Mellon Institutional Animal Care and Use Committee guidelines and the U.S. National Institutes of Health Guide for the Care and Use of Laboratory Animals.

5.3.3 Mouse Thigh Injected with SPIO-labeled DCs

PSM was applied to *in vivo* MRI data acquired in an anesthetized mouse with its quadriceps inoculated with primary dendritic cells (DCs) that had been labeled with SPIO *ex vivo*. Dendritic cells (DCs) were SPIO-labeled, injected into a mouse quadriceps, and imaged. Briefly, fetal skin-derived DCs from a stable cell line [120] were incubated with SPIO particles conjugated to a CD11c antibody (Miltenyi Biotec Inc., Auburn, CA). These ∼50 nm-sized SPIO particles were endocytosed by the DCs using a receptor-mediated endocytosis mechanism [24]. A detailed description of the cell culture methods used in this experiment is described elsewhere [24]. A 20-g male (DBA/2 × C57BL/6) F1 mouse (Jackson Laboratory) was anesthetized with isoflurane in air, intubated, and connected to a mechanical ventilator (150 strokes/min, 300 μl/stroke); isoflurane (1.25%) in an oxygen/nitrous-oxide mixture (70% / 30%) was administered. DCs (1×10^7 cells) in 0.1 mL PBS were slowly injected intramuscularly into the right quadriceps using a 27-gauge syringe. Afterwards, the mouse was positioned, with hind legs extended, in a cradle inside a 30 mm diameter birdcage RF resonator. The mouse temperature was regulated at 37 °C. The mouse was then positioned in an 11.7 T micro-imaging system (as above). Multiple contiguous axial slices were acquired through the lower extremities of the mouse using a standard spin-echo imaging sequence. Images were

T_2-weighted with TE/TR=30/1500 ms, 256×256 points, a 2.5 cm field of view, and a 0.6 mm slice thickness. Both legs were imaged simultaneously, and the uninjected (left) leg served as a control. Experiments were performed at the Pittsburgh NMR Center for Biomedical Research at Carnegie Mellon University, and all animal procedures were approved by the Institutional Animal Care and Use Committees at the University of Pittsburgh and Carnegie Mellon University.

5.3.4 APP/PS1 Transgenic Alzheimer Mouse Brain

Alzheimer disease pathology is typified by amyloid-beta ($A\beta$) plaques that in many cases will contain iron in the form of hemosiderin. MR microscopy has demonstrated the ability to resolve individual amyloid plaques in *ex vivo* mouse and human brain samples to determine amyloid burden in 3D volumes, non-invasively. Because iron in amyloid tangles may be paramagnetic, PSM was tested on an elderly mouse brain excised from a APP/PS1 dual-transgenic mouse to see if the method would increase sensitivity to iron deposits in this disease model.

5.3.5 PSM Image Construction

For all MRI data sets, raw echo data were reconstructed into 2D and 3D phase images. A cost minimization-based phase-unwrapping algorithm was applied to each image or 3D image stack [121]. Phase-unwrapped data were then imported into MATLAB and filtered with a high-pass filtering kernel designed to exclude the lowest 10% of frequencies. These operations resulted in a series of 2D phase-offset images, as described by Eq. (3.18). The phase gradient vector field from Eq. (5.1) was constructed by calculating $d\phi/dx$, $d\phi/dy$, and $d\phi/dz$ in each voxel of the phase-offset image and then expressing these three components as a single vector. PSM images were visually rendered in grayscale to show the magnitude of each vector in the phase gradient vector field, as described by Eq. (5.2).

5.3.6 PSM Image Contrast-to-Noise Ratio Analysis

To evaluate the efficacy of PSM image enhancement compared to conventional magnitude images, we measured the mean CNR surrounding each ROI containing presumed CA deposits in both image types. Image CNR was calculated using the formula:

$$\mathrm{CNR} = |I_A - I_B|/\sigma \tag{5.9}$$

where I_A represents the average image intensity around the presumed CA deposit, I_B represents the average image intensity of the background substance surrounding the ROI (e.g., agarose gel or tissue), and σ represents the background substances pixel-wise standard deviation. PSM image thresholding was not performed before CNR analysis. Specifically, using Eq. (5.9), the CNR was calculated for the following samples as described below:

1. Agarose gel phantom doped with MPIO. For the gel phantom, an arbitrary 2D slice through the volume was selected for CNR analysis. A small area containing four apparent dipolar perturbations was selected from the slice. The average intensity of each dipole (i.e., I_A in Eq. (5.9)) was calculated from a 6×6 voxel cluster, of $240 \times 240 \times 40$ μm total size, centered on each dipole. A 32×32 voxel background region, devoid of apparent dipoles, was used to measure the average background intensity (i.e., I_B in Eq. (5.9)) and background noise (σ). In addition, we also calculated the maximum, single-pixel CNR for each region of interest by substituting I'_A for I_A in Eq. (5.9), where I'_A represents the single voxel in the 6×6 voxel cluster exhibiting the largest deviation from the background I_B value.

2. *Ex vivo* mouse brain. For the mouse brain, a region centered on the site of AdV inoculation was segmented manually from the 3D mouse brain volume. Slice-by-slice, this region's average intensity (I_A in Eq. (5.9)) was calculated from a 20×20 voxel region of total volume $1 \times 1 \times 0.25$ mm^3. A comparable 32×32 voxel region on the contralateral side was also segmented, where AdV-LacZ control vector was injected; this region was used to measure average background intensity, I_B, via Eq. (5.9). Background noise (σ) was measured using a 32×32 voxel region from the homogeneous agarose gel embedding the brain. Image CNR was calculated using Eq. (5.9) on a slice-by-slice basis, five slices total, for both PSM and magnitude image types. In addition to analysis of the average regional CNR, we also calculated the maximum, single-pixel CNR slice-by-slice for this region by substituting I'_A for I_A in Eq. (5.9), where I'_A represents the single pixel in the 20×20 pixel transduced brain region exhibiting the largest deviation from the average background I_B value. The 3D PSM result was volume-rendered and made semi-transparent using the software package Amira (Mercury Computer Systems, Chelmsford, MA).

3. *In vivo* mouse brain. A region centered on the site of AdV inoculation was segmented manually from the mouse brain slice. The average intensity of this region (I_A in Eq. (5.9)) was calculated from a 9×15 voxel region of total volume 0.9×1.5 mm^2. A comparable 16×16 voxel region on the contralateral (AdV-LacZ) side was also segmented to measure average background intensity, I_B, via Eq. (5.9). Background noise (σ) was measured using the same 16×16 voxel homogeneous background region. Image CNR was calculated using Eq. (5.9) for both PSM and magnitude image types. In addition to analysis of the average regional CNR, we also calculated the maximum, single-pixel CNR for this region by substituting I'_A for I_A in Eq. (5.9), where I'_A represents the single pixel in the 9×15 pixel transduced brain region exhibiting the largest deviation from the average background I_B value.

4. Mouse Thigh Injected with SPIO-labeled DCs. For the *in vivo* mouse thigh, a region containing the site of DC inoculation was segmented manually from the mouse quadriceps volume. Slice-by-slice, the average intensity of this 33×37 pixel region (I_A in Eq. (5.9)) was calculated. A 32×32 pixel region in the contralateral quadriceps (control) was chosen to measure average background intensity (I_B) and background noise (σ). Each slice's CNR was calculated for both image types using (5.9). In addition to analysis of average regional CNR, we also calculated maximum, single-pixel CNR slice-by-slice for this region by substituting I'_A for I_A in Eq. (5.9), where I_A represents the single pixel in the 33×37 implanted-DC region exhibiting the largest deviation from I_B.

5.4 Results

PSM images were generated from a variety of diverse data sets to assess efficacy at highlighting CA deposits. None of the presented PSM images underwent the regional noise thresholding procedure, but we found that applying the procedure results in nearly noise-free PSM-images suitable for effective visualization of CA distribution. To compare PSM images to conventional magnitude images, the CNR was measured in both images in regions encompassing the CA deposits.

5.4.1 Gel Phantom

Table 5.3 summarizes the numerical CNR analysis for the MPIO-doped agarose gel phantom; Figure 5.1 shows the PSM and magnitude images used to obtain the results in Table 5.3. In the gel phantom, PSM images were found to exhibit a 2- to 8-fold CNR improvement over magnitude images in regions containing the MPIO deposits.

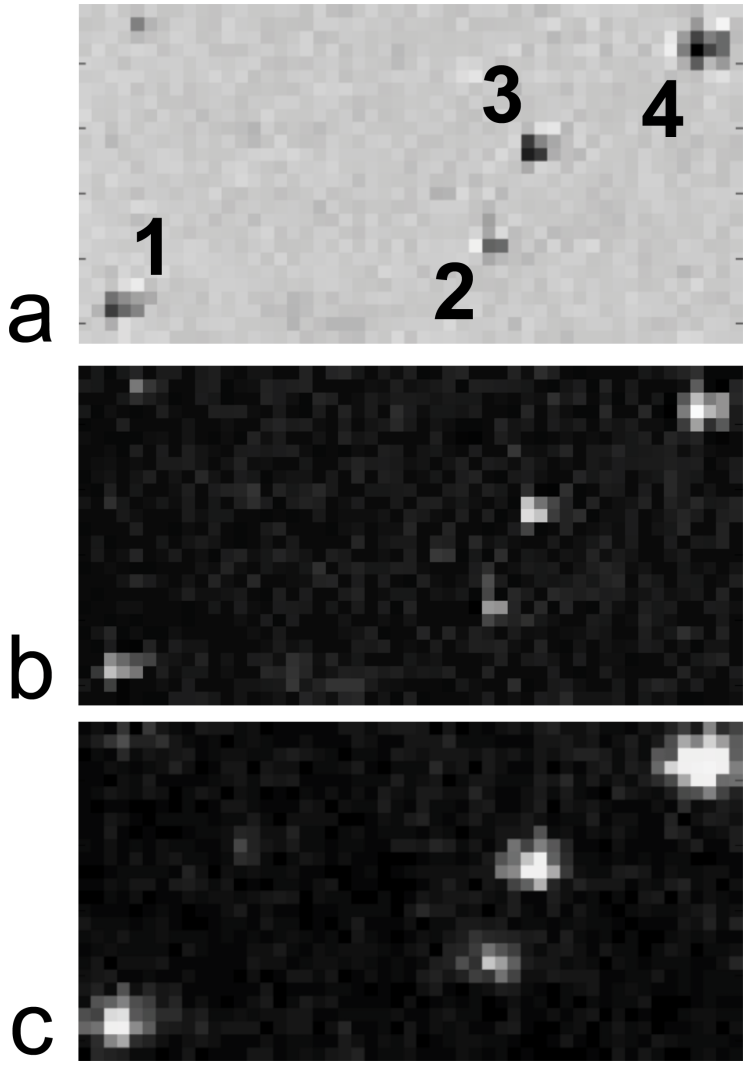

Figure 5.1: Three different image types formed from the same region of SPIO-doped agarose gel phantom.
Images include: (a) conventional magnitude image, (b) inverted magnitude image, and (c) positive-contrast PSM image. In panel (a), the four paramagnetic dipoles are labeled "1" through "4," corresponding to the same four dipoles enumerated in the gel dipole CNR improvement analysis (Table 5.3). In regions where SPIO is present, the PSM image exhibits CNR values $2-8\times$ greater than the conventional magnitude image. The inverted magnitude image in panel (b) is provided for comparison with the PSM result in panel (c). This comparison demonstrates that the PSM method does not just create simple positive contrast visuals it generates additional contrast that spatially extending around and accentuating CA. *(Figure taken from Fig. 1 of Mills and Ahrens [55])*

5.4.2 Mouse Brains Expressing Transferrin and Ferritin Transgenes

The analysis results for the AdV-TfR inoculated mouse brain are shown in Table 5.1, where Figure 5.2 shows the associated PSM and magnitude images. Figure 5.3 shows several views of a 3D volumetric rendering of this entire mouse brain using 3D PSM data.

Figure 5.2: Mouse brain transduced with TfR-1 transgenes via an AdV-vector injected into the striatum.
The TfR-1 upregulates paramagnetic ferritin, leading to iron accumulation in transduced cells and enhanced paramagnetism. Three image slices are shown comparing (a) positive-contrast PSM images generated using our described approach and (b) conventional magnitude images. These three sections correspond to the slices analyzed in Table 5.1. Arrows indicate where AdV/TfR-1 was injected, while the contralateral side was injected with an AdV/LacZ control and shows no contrast. In regions where ferritin is present, PSM images exhibit CNR values $1 - 5\times$ greater than the conventional magnitude images, (b). *(Figure taken from Fig. 2 of Mills and Ahrens [55])*

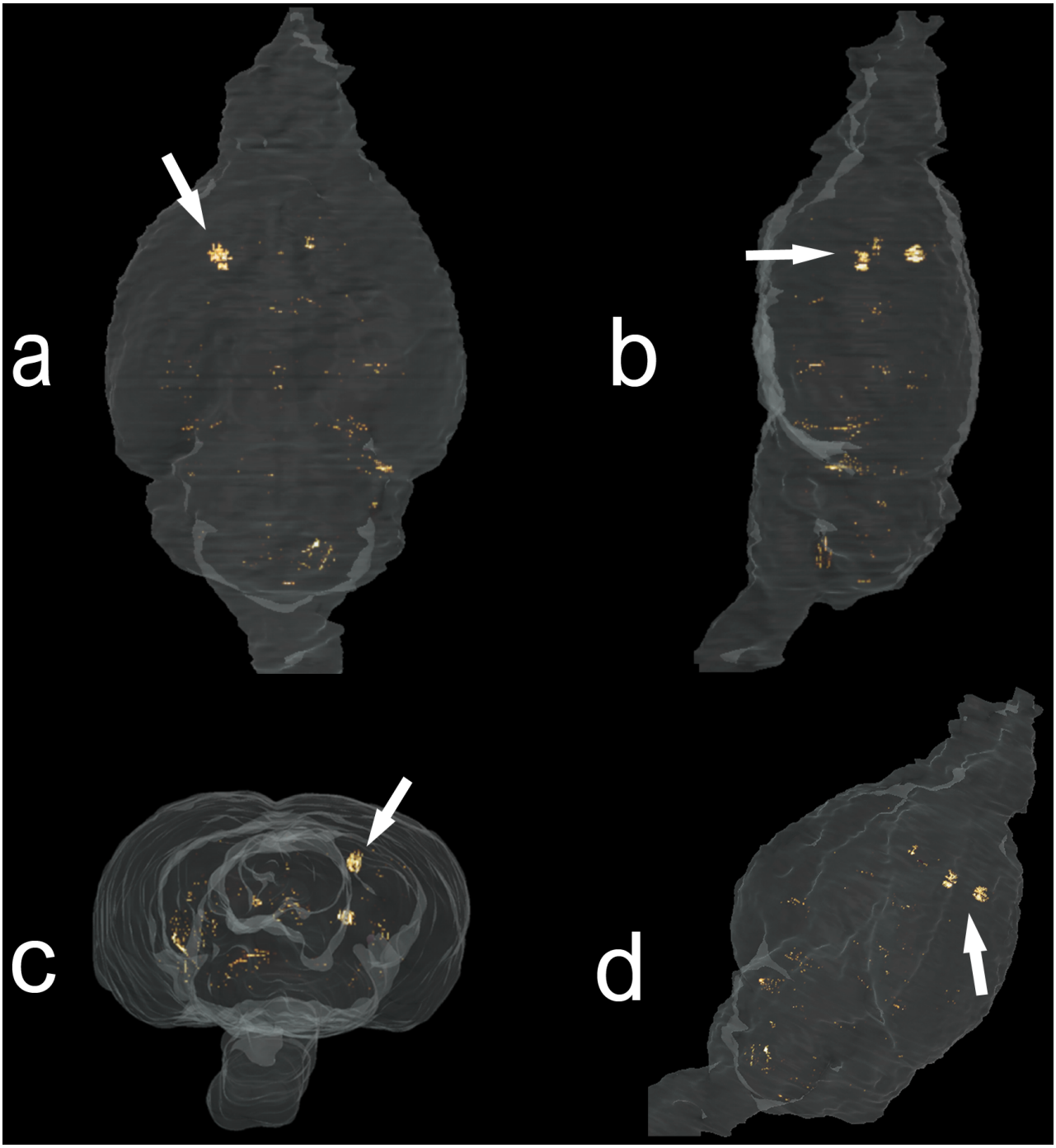

Figure 5.3: PSM 3D volume rendering of the mouse brain inoculated with AdV/TfR-1 into the striatum.

The panels show (a) dorsal, (b) lateral, (c) cranial, and (d) oblique views. The arrows indicate the site of AdV-TfR-1 injection, while the contralateral side was injected with AdV-LacZ control. These 3D PSM images are easily able to distinguish the paramagnetic deposits induced by the TfR-1 transgene. This is the same brain shown in Table 5.1 and Figure 5.2. *(Figure taken from Fig. 3 of Mills and Ahrens [55])*

Measurement	Section # 1	#2	#3	#4	#5
Average PSM CNR	1.9	3.0	3.9	4.2	4.5
Average MAG CNR	2.2	1.9	2.5	3.2	3.3
PSM improvement	**0.9**×	**1.6**×	**1.6**×	**1.3**×	**1.4**×
Maximum PSM CNR	28.0	56.7	50.7	72.0	127.4
Maximum MAG CNR	10.2	11.0	13.1	23.2	24.6
PSM improvement	**2.7**×	**5.2**×	**3.9**×	**3.1**×	**5.2**×

Table 5.1: PSM analysis results for the mouse brain transduced with TfR-1 transgenes.
Shown is a comparison between the CNR present in the PSM and MAG images. *(Table taken from Table 2 of Mills and Ahrens [55])*

Results for the LF/HF-AdV inoculated mouse brain are displayed as PSM and magnitude images in Figure 5.4. PSM images exhibited a 1- to 5-fold CNR improvement at sites of AdV injection (Table 5.1). Inspection of Figs. 5.2 and 5.4 support this finding, where transduced cells are significantly more apparent in the PSM images (Figs. 5.2, 5.4a) compared to the magnitude images (Figs. 5.2b, 5.4b). Importantly, Fig. 5.3 shows that full-brain visualization of the transgene distribution is feasible and efficacious, despite the presence of several regions of endogenous PSM contrast throughout the volume.

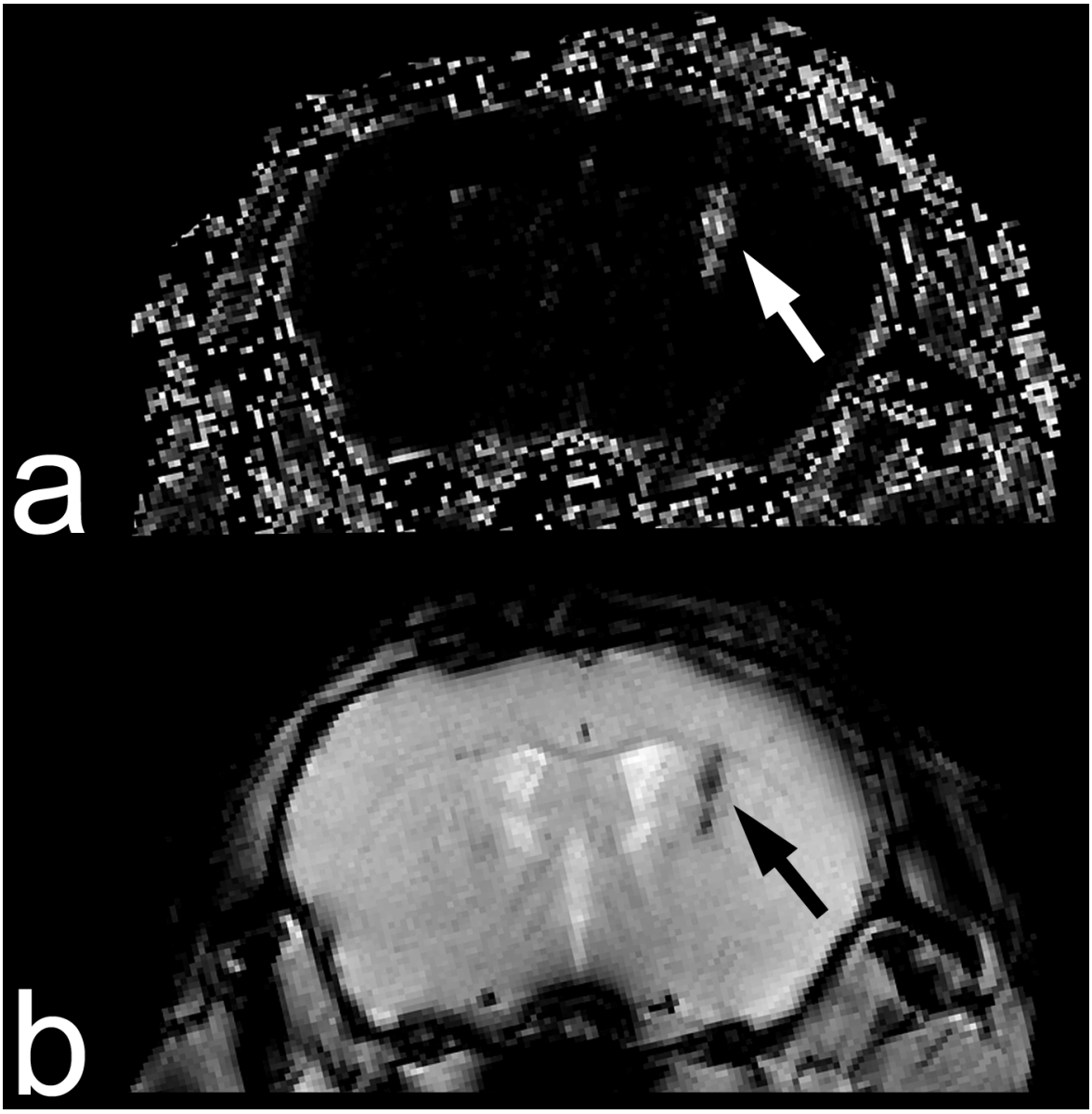

Figure 5.4: *In vivo* MRI of mouse brain transduced with HF and LF transgenes via an AdV-vector injected into the striatum.
The coronal section shown compares (a) positive-contrast PSM image and (b) conventional magnitude image. Arrows indicate the LF/HF-AdV mix injection site, while the contralateral side injected with the AdV-LacZ control shows no contrast. In the ferritin-transduced region, the PSM image exhibits CNR values $1.6 - 1.8\times$ greater than the conventional magnitude image. *(Figure taken from Fig. 4 of Mills and Ahrens [55])*

5.4.3 Mouse Thigh Injected with SPIO-labeled DCs

Figure 5.5 shows the PSM and magnitude images for the *in vivo mouse* quadriceps injected with SPIO-labeled DCs, while Table 5.2 summarizes the numerical analysis for this image. The PSM

images exhibited a 3- to 8-fold CNR improvement at the DC injection site (Table 5.2). This is significant since this biological sample of interest was imaged *in vivo* in a low-SNR regime, where adequate contrast is sometimes difficult to achieve.

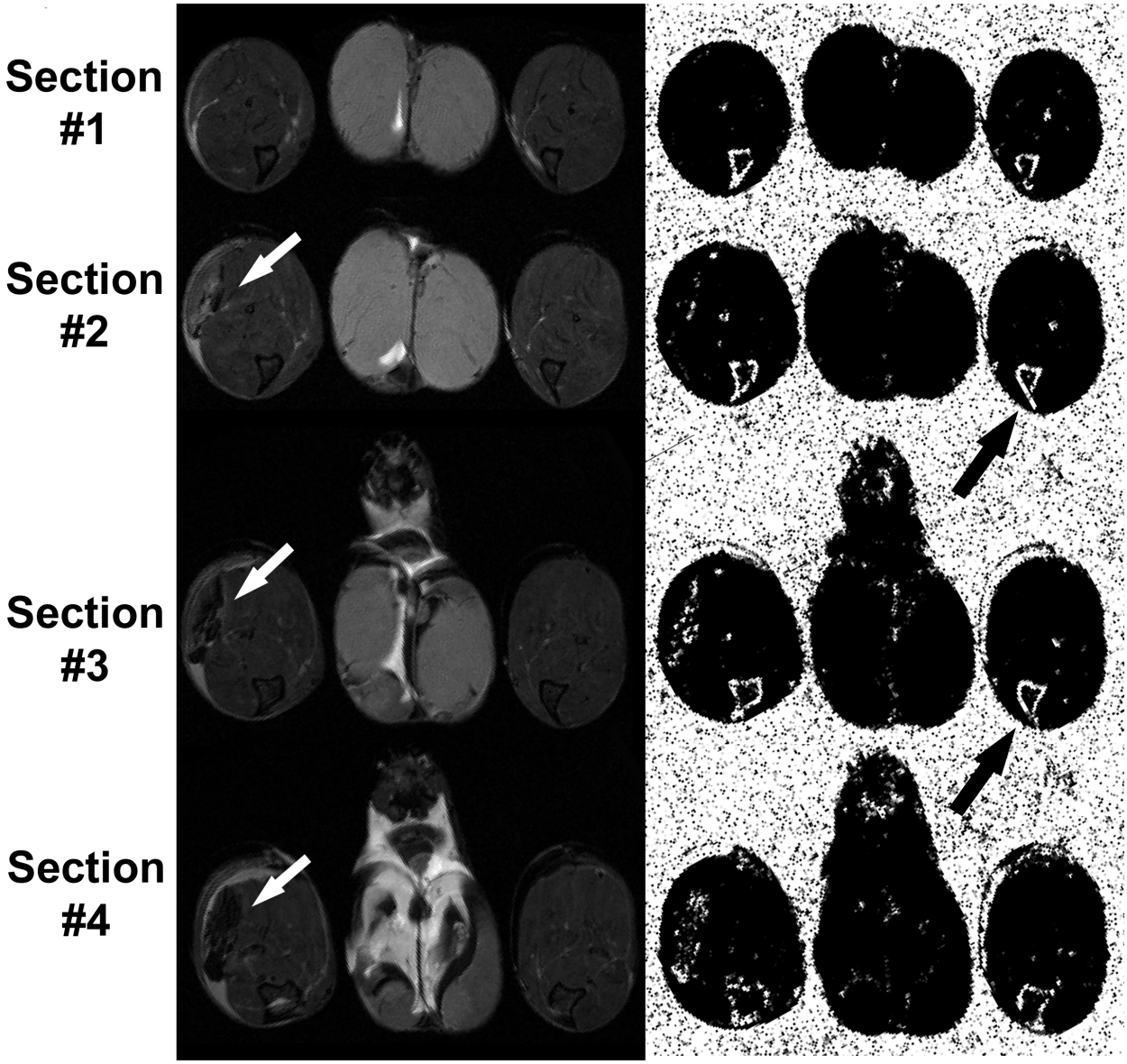

Figure 5.5: Conventional magnitude and PSM images generated from mouse quadriceps injected with SPIO-labeled DCs.

Four different 0.6 mm-thick sections are shown to compare conventional magnitude images (left panel) against PSM images generated using our described methods (right panel). These four sections are labeled numerically, corresponding to the sections enumerated in the mouse quadriceps CNR improvement analysis (Table 5.2). White arrows (left panel) indicate where DCs were injected into mouse thigh, while the contralateral thigh acts as a no-injection control. Black arrows (right panel) indicate the significant tissue interface that is highlighted by the PSM method between muscle and bone in the mouse thigh. The positive-contrast PSM images (right panel) exhibit CNR values 3–8× greater than the conventional magnitude images (left panel) when analyzing the region where SPIO-labeled DCs were injected. Images have an isotropic resolution of 100 μm.

Measurement	Section # 1	#2	#3	#4
Average PSM CNR	2.8	2.3	2.8	2.9
Average MAG CNR	0.3	0.2	0.9	1.0
PSM improvement	**8.5**×	**12.2**×	**3.1**×	**2.9**×
Maximum PSM CNR	47.8	47.0	41.5	46.8
Maximum MAG CNR	14.9	10.9	10.7	14.9
PSM improvement	**3.2**×	**4.3**×	**3.9**×	**3.1**×

Table 5.2: PSM analysis results for mouse quadriceps injected with SPIO.
Comparison between contrast-to-noise ratio (CNR) present in phase slope magnitude (PSM) and conventional magnitude (MAG) images. *(Table taken from Table 3 of Mills et al. [55])*

5.4.4 APP/PS1 Transgenic Alzheimer Mouse Brain

Finally, PSM images did not show contrast enhancement compared to conventional magnitude images when applied to an *ex vivo* elderly mouse brain excised from a dual-transgenic (APP/PS1) model of Alzheimer disease. However, interestingly, phase offset images formed during the PSM image-generation process were found to significantly increase contrast from individual amyloid plaques (Fig. 5.6). In the phase-offset image for these APP/PS1 dual-transgenic mice, the regional CNR due to each plaque deposit is enhanced, and many plaques appear that are not visible in the conventional magnitude image.

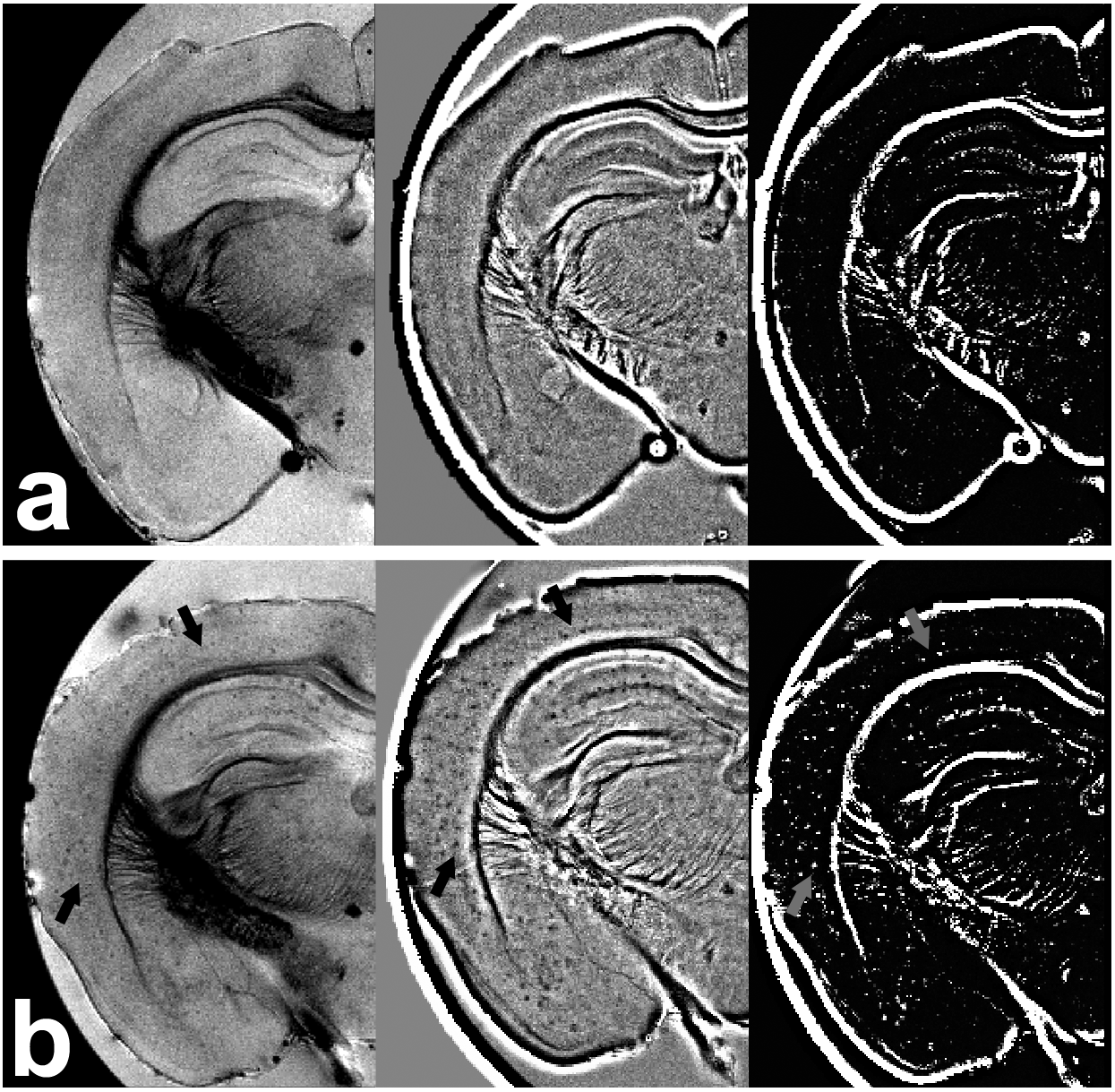

Figure 5.6: Conventional magnitude and phase-offset images generated from (a) PS1 (control) and (b) APP/PS1 dual-transgenic brains of elderly mice.
For both APP/PS1 and PS1 samples, three image types are shown: magnitude image (left panel), phase-offset image (center panel), and inverted phase-offset image (right panel). A large number of hypointense punctate plaques are detected in the APP/PS1 sample (b), but not in the PS1 sample (a). Arrows for the APP/PS1 sample (b) indicate locations where hypointense spots are faint or very difficult to detect in the magnitude image (left panel), while these same plaques appear prominent in the phase-based images (b, center and right panels). Also the many punctate spots that are detectable by eye in the APP/PS1 magnitude image (b, left panel), tend to be more easily detected when viewing the phase-offset images (b, center and right panels). Image resolution is 25 μm isotropic.

Overall, these results demonstrate the efficacy of our PSM-image generation methods for highlighting arbitrary distributions of paramagnetic agents in the context of *in vivo* cell tracking appli-

cations.

Measurement	Dipole # 1	#2	#3	#4
Average PSM CNR	11.6	5.3	12.0	28.5
Average MAG CNR	1.6	1.3	2.1	3.4
PSM improvement	**7.1**×	**4.0**×	**5.7**×	**8.3**×
Maximum PSM CNR	57.5	31.4	66.0	143.4
Maximum MAG CNR	3.1	2.8	3.3	3.5
PSM improvement	**2.9**×	**2.1**×	**2.9**×	**5.5**×

Table 5.3: PSM analysis results for the gel phantom doped with MPIO.
Shown is a comparison between the CNR present in PSM and conventional magnitude (MAG) images. *(Table taken from Table 1 of Mills and Ahrens [55])*

5.5 Discussion

In this chapter we describe how paramagnetic CA distributions can be highlighted using PSM images. Visualizing phase slope with PSM images provides a sensitive picture of magnetic field disturbances. In our pilot experiments the PSM images exhibit a 1- to 8-fold CNR improvement in CA-containing regions compared to conventional magnitude images. No loss in CNR was found in any images studied. We show that PSM images can be generated in 3D to visualize arbitrary agent distributions, and that these images help differentiate hypointense image regions due to CA, leading to improved detectability. Indeed, we find that when analyzing samples that show a weak paramagnetic effect, PSM images can make the difference between detecting, and not detecting, magnetic disturbances (Fig. 5.2, panels 1 and 3). We also show that PSM is effective for *in vivo* applications. However, acquired images should be relatively free from motion artifacts. By superimposing PSM images onto magnitude images, one can reap the benefits of increased sensitivity to magnetic susceptibility effects while retaining the critical anatomical backdrop.

5.5.1 Limitations

There are several limitations to the PSM method. First, an inherent limitation is its potential inability to distinguish between some tissue interfaces and regions containing CA. Both the agarose gel phantom and mouse brains had relatively homogeneous backgrounds for testing PSM image

generation and resulting CNR measurements. PSM image methods applied to tissues or interfaces of high magnetic susceptibility heterogeneity may not be as effective at distinguishing paramagnetic CA deposits from background. Furthermore, PSM-image generation may introduce computational artifacts if highly relaxative CAs generate rapid spatial changes in phase angle [122]. If image resolution is too low to sample these rapid phase changes, undersampling occurs, which can potentially cause phase unwrapping algorithms to choose an incorrect multiple of 2π to add to each phase image pixel. Any incorrect choice will propagate through the PSM image generation process, generating false-positive or negative pixel results. To mitigate this effect, one might acquire phase maps using multi-echo GRE pulse sequences which employ 'temporal unwrapping' in order to determine phase angle values with greater certainty [99, 100]. The detection limit of PSM images is primarily determined by phase image SNR. The outlined PSM image regional thresholding method can be used to identify all PSM image pixels that have a $\sim$95% certainty of representing a true susceptibility disturbance.

5.5.2 Optimizing Image Acquisition

Although the PSM method was designed to be used retrospectively on any acquired T_2^*-weighted MR data, the method may exhibit superior contrast if MR acquisition parameters are chosen beforehand while considering the PSM method. When using a conventional T_2^*-weighted GRE pulse sequence, phase disturbances spanning multiple voxels can be emphasized by maximizing the echo-time scanning parameter, TE. This stems from the fact that a voxel in a T_2^*-weighted GRE phase image has a phase-offset value proportional to:

$$\phi_{\text{offset}} \propto \quad \Delta \mathrm{B}_Z \cdot \mathrm{TE} \tag{5.10}$$

where $\Delta \mathrm{B}_Z$ represents the average magnetic field perturbation within the voxel. Applying Eq. (5.2) to calculate a single PSM image pixel intensity value from two neighboring ϕ_{offset} values, labeled A and B, yields a result directly proportional to TE:

$$I(A,B) = \phi_{\text{offset}}(A) - \phi_{\text{offset}}(B) \propto [\Delta B_z(A) - \Delta B_z(B)] \cdot \mathrm{TE} \tag{5.11}$$

In addition to increasing PSM image intensity values, increasing TE generally makes param-

agnetic field disturbances grow in apparent size (i.e., the 'blooming effect'). However, as TE is increased in a T_2^*-weighted GRE sequence (i.e., TR $\gg T_1$, T_2), the phase noise standard deviation, σ_ϕ, also increases according to the relation

$$\sigma_\phi \propto 1/e^{(-\mathrm{TE}/T_2)} \tag{5.12}$$

Therefore, in order to maximize $\mathrm{SNR_{PSM}}$ when using a GRE sequence, one would choose a value of TE empirically while considering these two opposing effects. Calculation of a TE value that optimizes global $\mathrm{SNR_{PSM}}$ would generally be impractical, since it would require foreknowledge of multiple pixel $\Delta \mathrm{B}_Z$ values and MR apparatus-specific signal sensitivity behavior.

5.6 Conclusion

Emerging cellular-molecular MRI applications can benefit from improved sensitivity to paramagnetic CA distributions. The PSM approach generates positive contrast images that help to differentiate CAs from endogenous sources of tissue hypointensity. Unlike many other positive contrast imaging methods, PSM-image generation requires no prior knowledge of magnetic agent strength or distribution, no special pulse or gradient sequences, no extra scan time, and can be applied retrospectively to already-acquired data. Finally, these image generation methods can be made into an automated routine with few or no input parameters.

Chapter 6

Phase map cross-correlation Detection and Quantification (PDQ)

Some sections from this thesis chapter have previously been published under the title "Sensitive and automated detection of iron-labeled cells using phase image cross-correlation analysis" in the scientific journal Magnetic Resonance Imaging [123]. *Other sections are in press for publication under the title "Automated detection and characterization of SPIO-labeled cells and capsules using magnetic field perturbations" in the scientific journal* Magnetic Resonance in Medicine [In Press]. *These two journals are the copyright holders for these sections of previously-published material.*

6.1 Introduction

Here we describe a post-processing method, called Phase map cross-correlation Detection and Quantification (PDQ), that uses phase images to automatically identify and count spherical SPIO deposits [123] and estimate their volume magnetic susceptibility and magnetic moment. We demonstrate the utility of the PDQ algorithm in several diverse MRI data sets.

First, we investigated theoretical detection limits using a simulated dipole field, which demonstrated the robustness of the PDQ algorithm in very low SNR images (< 4). At all levels of SNR tested in the simulation, the PDQ method was $\sim$90% accurate.

As a further test, three-dimensional (3D) data were acquired in an agarose gel phantom lightly doped with MPIO. When analyzing this homogeneous agarose phantom, the PDQ method found 94% of the dipoles that were identified by visual inspection of MR phase-offset images.

Next, we analyzed *ex vivo* 3D MRI data from transplanted allogenic rat heart specimens that were infiltrated with macrophages as a result of acute organ rejection; the macrophages were *in situ* labeled with MPIO nanoparticles using techniques described elsewhere [19]. The resulting 3D

positive contrast images starkly highlighted labeled cells and other magnetic dipoles. Dipoles were automatically counted by computer and their spatial biodistribution visualized using 3D renderings. In the heart data, this information was used to calculate a quantitative index of MPIO accumulation that potentially reflects the severity of immune cell infiltration (i.e., an "infiltration index") and the stage of organ rejection. Overall, when analyzing heterogeneous heart tissue, the PDQ method found 79% of the dipoles that were also observed by visual inspection of MR phase-offset images.

We then applied PDQ to detect magnetocapsules implanted in porcine liver. Magnetocapsules are spheres of alginate crosslinked with SPIO that are permeable to metabolites but not native antibodies, thereby encapsulating and immunoisolating therapeutic cells [124]. The PDQ analysis was validated in MRI phantoms containing magnetocapsules. Moreover, superconducting quantum interference device (SQUID) magnetometry was used to validate the magnetostatic quantification abilities of the PDQ method.

Subsequently, we applied PDQ to an *in vivo* mouse model of traumatic brain injury (TBI) to analyze inflammation-associated MPIO-labeled macrophage infiltration. TBI is a leading cause of death and disability in children and young adults. The inflammatory response following brain injury repairs damaged tissue and can cause secondary injury [125]. Many of the inflammatory mechanisms involved in repair and secondary injury are mediated by contributions from activated microglia/macrophages, among other cell types including neutrophils, astrocytes, and neurons [125]. In brief, unactivated microglia reside in brain tissue and perivascular microglia reside by brain blood vessels. After CNS injury, perivascular microglia release IL-1β and TNFα, which induce expression of adhesion molecules that increase infiltration of circulating macrophage and leukocytes through the endothelial wall (i.e., diapedesis). The IL-1β and TNFα also activate microglia in brain tissue, stimulating them and endothelial cells to secrete chemokines to attract leukocytes to the injury site [126]. Additionally, some blood-monocyte-derived macrophages directly enter the brain through damaged vasculature (i.e., extravasation though disrupted BBB). In both mice and humans, there is robust macrophage accumulation at $\sim$72 hours post-TBI that increases through 96 hours post-TBI in rats [127, 128]. The ability to monitor macrophage behavior is important since these cells are involved in many disease processes. Macrophages have been shown to migrate and accumulate in sites of inflammation, solid organ transplant rejection, atherosclerosis, renal ischemia, renal nephropathies, autoimmune neuritis, and in EAE (experimental autoimmune encephalomyelitis)

provided the BBB or BSB is disrupted [20, 4]. In the TBI model, PDQ longitudinally tracked individual MPIO clusters over three days *in vivo*.

Finally, PDQ was applied to rat hearts infiltrated by MPIO-labeled macrophages as a result of chronic transplant organ rejection.

Overall, we show that using PDQ it is feasible to detect and quantify thousands of individual MPIO-labeled cells or magnetocapsules throughout tissue volumes in an automated fashion, with significant discrimination capacity against endogenous tissue contrast. The PDQ algorithm can help to reduce false positive and negative results when SPIO deposits are localized, can be used in conjunction with conventional high-SNR imaging pulse sequences, requires no extra scan time and can be applied retrospectively to previously acquired data.

6.2 Theory

The intensity of a voxel in the phase-offset image ($\Delta\phi$ from Eq. (3.19)) is proportional to the deviation in magnetic field ($\Delta \mathrm{B}_Z$) within that voxel relative to its surrounding background material. In our analysis, we exploit how phase images describe the magnetic field to analyze the distortions caused by localized spheroidal deposits of paramagnetic agents in tissue. $\mathrm{B}_Z(r,\theta)$ for a spherical deposit of a paramagnetic or diamagnetic substance will cause a dipolar magnetic field perturbation of the form [80]

$$\Delta \mathrm{B}_Z(r,\theta) = \frac{\Delta\chi \cdot \mathrm{B}_0}{3}\left(\frac{a}{r}\right)^3\left(3\cos^2\theta - 1\right) \tag{6.1}$$

where $\Delta\chi$ is the difference in magnetic susceptibility between the sphere and its surroundings, B_0 is background field strength, a is the sphere radius, r is distance from its center, and θ is the angular deviation from the direction of B_0. Notably, the sphere has a maximum $\mathrm{B}_Z(r,\theta)$ field deviation at its poles given by

$$\Delta \mathrm{B}_{Z,max} = 2 \cdot \Delta\chi \cdot \mathrm{B}_0/3. \tag{6.2}$$

This characteristic dipole shape is rendered as a 3D isosurface in Fig. 6.1.

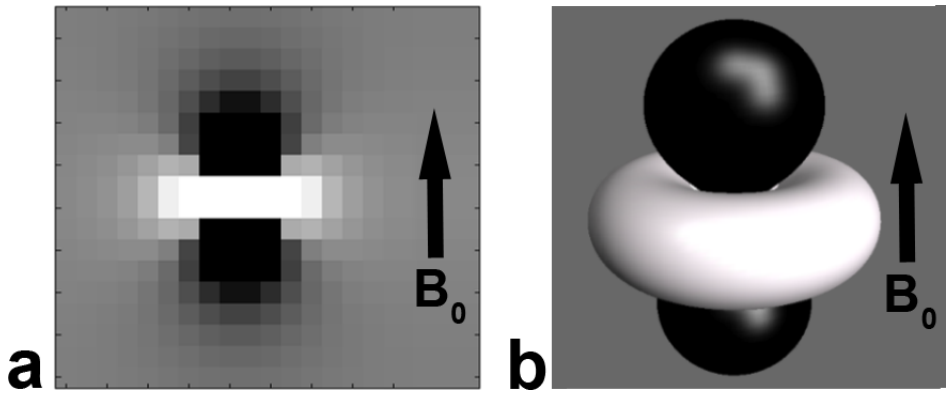

Figure 6.1: Visual representations of magnetic dipole in (a) 2D and (b) 3D.
For both representations, dark areas generate a negative phase offset and bright areas a positive phase offset. These templates were computed using Eq.(6.1). *(Figure taken from Fig. 2 of Mills et al. [123].)*

Substituting an estimated radius, a, for an SPIO deposit into Eqs. (3.19) and (6.1), allows one to calculate the mean $\Delta\chi$ of the deposit by sampling many of its surrounding phase-offset ($\Delta\phi$) values. From $\Delta\chi$, one can calculate a representative, uniform magnetic susceptibility, χ_A, for an SPIO deposit, provided the background susceptibility (χ_B) is known, using:

$$\chi_A = \Delta\chi + \chi_B \tag{6.3}$$

Note that in the case of magnetocapsules, we assume SPIO is homogeneously distributed throughout the volume of each capsule.

The radius parameter, a, is measured by optical microscopy for each batch of magnetocapsules, and ranges from 230–330 μm. In the case of SPIO-labeled cells, we assume each cell is spherical and a approximates the cell radius. Since cells are sub-voxel-sized, details of the actual intracellular SPIO distribution are inconsequential for this analysis.

Common values for χ_B (unitless) include water at 37 °C ($\chi = -9.051 \times 10^{-6}$) [80], agarose ($\chi \approx \chi_{water}$) [51], human tissues ($-11.0 \times 10^{-6} < \chi < -7.0 \times 10^{-6}$), liver ($\chi = -8.8 \times 10^{-6}$), deoxygenated whole blood ($\chi = -7.9 \times 10^{-6}$), and air ($\chi = +0.36 \times 10^{-6}$) [80]. Even in tissues with severe pathological iron loading (e.g., hemochromatosis), it has been estimated that $\chi \approx 0.0$; thus, the most extreme natural tissue susceptibility value in organs is only a few ppm more paramagnetic than water [80].

After finding χ_A for an SPIO deposit, this can be used to estimate the bulk volume magnetiza-

tion of the deposit using

$$\overrightarrow{M}_A = \chi_A \left(\frac{1}{\mu_0} \overrightarrow{B} - \overrightarrow{M}_A \right) \tag{6.4}$$

where $\overrightarrow{M}_A$ is the volume magnetization of the sphere (in units $A \cdot m^{-1}$), $\mu_0 = 4\pi \times 10^{-7}\ \ T \cdot m \cdot A^{-1}$, and $\overrightarrow{B}$ is the surrounding magnetic field strength (in T units) [129]. We model each SPIO deposit as a uniform sphere with a magnetic moment given by

$$\overrightarrow{m}_A = \frac{4}{3} \pi a^3 \overrightarrow{M}_A \tag{6.5}$$

where $\overrightarrow{m}_A$ is magnetic moment (in units $\mathrm{A \cdot m^2}$) and a is sphere radius in meters. Combining Eqs. (6.4) and (6.5) and substituting $\overrightarrow{B} = \overrightarrow{B}_0$, the magnetic moment for each deposit can be expressed as

$$\overrightarrow{m}_A = 10^{19} \cdot \overrightarrow{B}_0 \frac{a^3}{3} \left(\frac{\chi_A}{1 + \chi_A} \right) \tag{6.6}$$

where $\overrightarrow{m}_A$ is the magnetic moment (units $\mathrm{pA \cdot m^2}$) and χ_A is sphere susceptibility from Eq. (6.3).

Cells and magnetocapsules are predominantly water by volume. Thus, the uniform susceptibility for these deposits, χ_A, calculated from Eq. (6.3), represents both aqueous (χ_{water}) and anhydrous (χ_{an}) susceptibility components. If we assume that a spherical SPIO vehicle is almost entirely water by volume, and that its anhydrous content (e.g., SPIO) is of negligible volume (i.e., $v_{water} \gg v_{an}$), we can estimate the anhydrous susceptibility component of the SPIO deposit (χ_{an}) by subtracting the aqueous susceptibility component (χ_{water}) from the χ_A value of the deposit:

$$\chi_{an} \approx \chi_A - \chi_{water}. \tag{6.7}$$

By removing the susceptibility contribution from water, this aqueous SPIO deposit is modeled as a negligible volume of anhydrous material uniformly distributed throughout a spherical space with radius a. The magnetic dipole moment for this rarefied anhydrous sphere ($\overrightarrow{m}_{an}$) is calculated by substituting χ_{an} for χ_A in Eq. (6.6). Moreover, if the SPIO dominates χ_{an}, one can estimate iron content of the deposit using

$$m_{Fe} = \overrightarrow{m}_{an} / \overrightarrow{M}_{Fe} \tag{6.8}$$

where m_{Fe} is mass of iron, $\overrightarrow{m}_{an}$ is the magnetic moment of the SPIO deposit assuming χ_{an}, and $\overrightarrow{m}_{Fe}$ is the mass magnetization of the SPIO (units emu/g or A·m^2/kg).

An overview of the PDQ algorithm is shown in Fig. 6.2; this flowchart shows the progression from raw k-space data to a list of quantified magnetic dipoles (i.e., SPIO deposits). First, the phase image is unwrapped in 3D, which provides more information than 2D unwrapping, improves accuracy [97], and avoids phase-unwrapping errors in the Z-stack dimension [98]. The unwrapped phase data is high-pass filtered, resulting in the phase-offset image described by Eq. (3.18). The SPIO deposits are detected using templates generated from Eqs. (3.19) and (6.1) as a model function (i.e., template). Since many dipoles do not lie exactly on the Cartesian grid points of acquired MRI data, 27 templates are generated, representing dipoles that are offset [-0.4, 0.0, or +0.4] voxels from the Cartesian grid, in each of x-, y-, and z-dimensions. The search templates and the phase-offset data set are passed to a 3D normalized cross-correlation algorithm, which systematically overlays the search template onto every template-sized patch across the phase-offset image, calculating the similarity beween the template and each image patch while considering the average image intensity in a region. This results in a two-dimensional (2D) or 3D similarity matrix that can be visualized or used to pinpoint template matches using local maxima [130]. For the 2D case of normalized cross-correlation, cross-correlating 2D template T with 2D source image S gives the resulting image, R, given by [131]

$$R(u,v) = \frac{\sum_{x,y}[S(x,y) - \bar{S}_{u,v}][T(x-u,y-v) - \bar{T}]}{\left[\sum_{x,y}[S(x,y) - \bar{S}_{u,v}]^2 \sum_{x,y}[T(x-u,y-v) - \bar{T}]^2\right]^{1/2}} \tag{6.9}$$

where $\bar{T}$ is the mean pixel value of the template, $\bar{S}_{u,v}$ is the mean pixel value of the image patch that is compared with the template, (u,v) is the position of the template on the image, and each summation runs over the template-sized image region that is currently being compared with the template. The result is a similarity matrix "image" that contains bright areas where the template matches the image being analyzed (i.e., magnetic dipoles), gray areas where there is no similarity, and dark areas where the template is dissimilar to the analyzed image.

The algorithm output is a set of 27 template similarity (TS) matrices, where each voxel contains a TS value between [–100%, 100%], representing the likelihood that a voxel in the phase image represents the center of a magnetic dipole (i.e., SPIO deposit).

A 3D peak-finding algorithm is applied to each TS matrix to pinpoint the center of each dipole. To reduce the chance of detecting false-positive dipoles, peak locations with TS $< 30\%$ are discarded and deemed deviant from Eq. (6.1) theory, since many false-positive peaks with a TS $< 30\%$ are found in random noise. To measure $\Delta\chi$ for each SPIO deposit, a 3D least-squares fit is performed between the phase-offset image impression and its search template. The uniform magnetic susceptibility of the dipole, χ_A, is calculated from user-provided χ_B via Eq. (6.3) and its magnetic moment from Eq. (6.6). If the spherical volume of the SPIO deposit is predominantly water, Eq. (6.7) is used to calculate χ_{an}. If the SPIO mass magnetization (i.e., g/emu) is known, Eq. (6.8) can be used to estimate the iron content of the SPIO deposit.

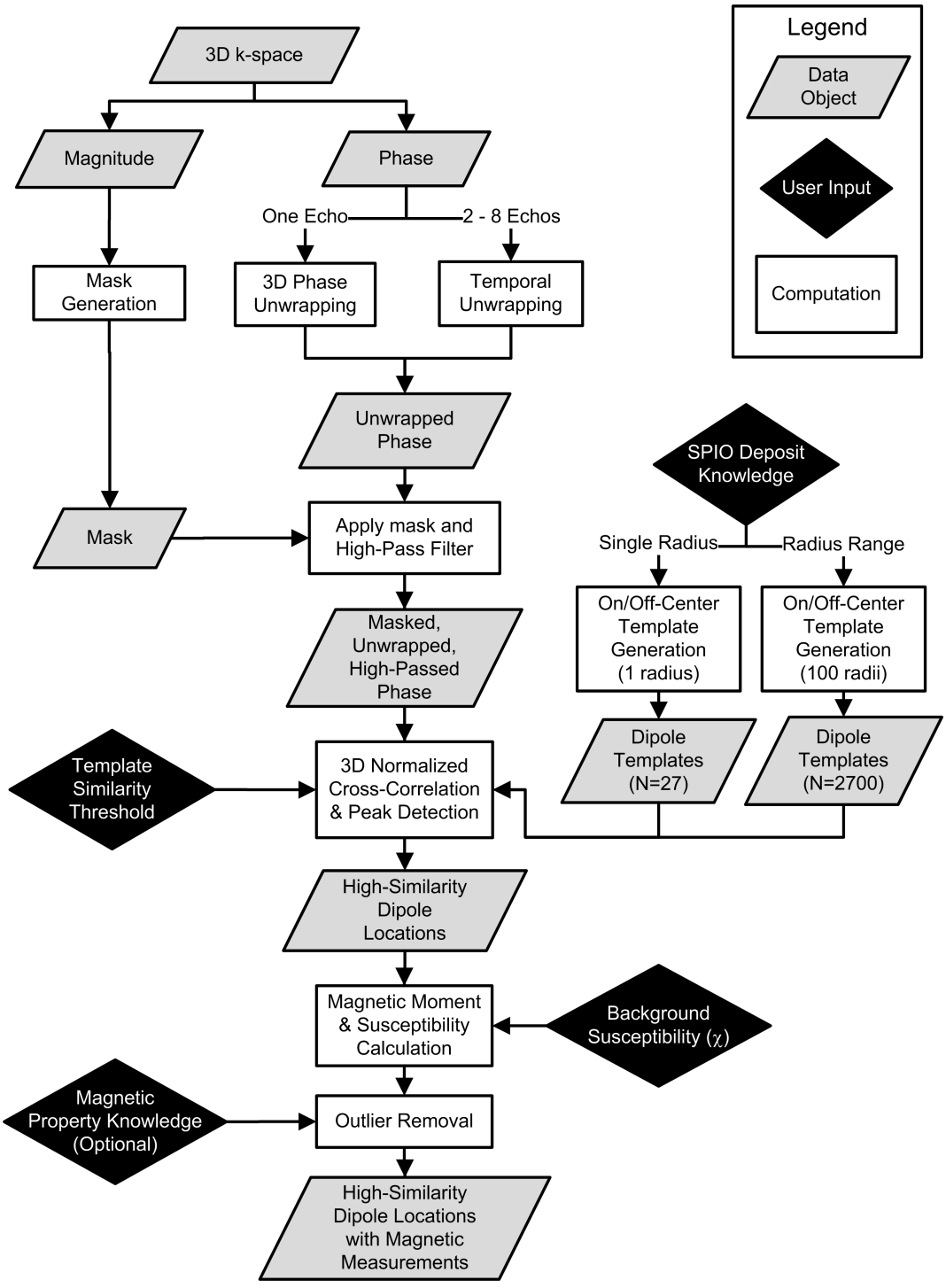

Figure 6.2: PDQ algorithm flowchart.
The process turns raw k-space data into a list of suspected SPIO deposits (i.e., magnetic dipoles), along with their locations and magnetic measurements. The process is automated except for user-provided estimates of SPIO deposit radius (a), the magnetic susceptibility of the background media surrounding the SPIO deposits (χ_B), and a template similarity (TS) threshold. Optionally, if magnetic properties of SPIO deposits are known and provided to PDQ beforehand, this information is used to discard false-positive dipoles. *(Figure taken from Fig. 1 of Mills et al., In Press, Magnetic Resonance in Medicine.)*

6.3 Materials and Methods

6.3.1 MPIO Gel Phantoms

We acquired MR images of a 2% agarose gel phantom that was lightly doped with 1.6 μm-diameter MPIO particles (Bangs Laboratories, Fishers, IN) to generate localized dipolar field perturbations. Phantoms were imaged using an 11.7 T Bruker AVANCE micro-imaging system using a standard 3D gradient-echo pulse sequence with TE/TR=7/1500 ms and an isotropic resolution of 40 μm. Raw echo data were reconstructed to create a volume phase image. A cost minimization-based phase-unwrapping algorithm was applied to each 2D sagittal section in the 3D volume [121]. Phase unwrapped data were then imported into MATLAB and high-pass filtered with a kernel that excluded the lowest 10% of frequencies. The theoretical dipole phase pattern (Eq. (6.1)) was used to generate 2D and 3D dipole templates for the cross-correlation analysis. Two different templates having dimensions of 8 and 16 voxels per side were used; these corresponded to image distances of 0.3 mm and 0.7 mm, respectively. When analyzing this relatively homogeneous gel phantom, only template sizes of 3×3 and smaller resulted in a large number of false positives. For templates larger than 3×3, the number of false positives was independent of template size. MATLAB's 2D normalized cross-correlation function was then applied between the phase offset image of the phantom and both templates separately. A 3D implementation was used for 3D normalized cross-correlation analysis, which is similar to Eq. (6.9), but extended to three dimensions (3-D).

The similarity matrices resulting from this 2D cross-correlation were automatically thresholded to locate each dipole. The threshold was determined by applying the cross-correlation to both the plane orthogonal to B_0 and then to the plane parallel to B_0. Theoretically, the cross-correlation analysis should find zero dipoles in the orthogonal plane, while the parallel plane analysis should identify many dipolar patterns. Using this property, the similarity matrix cutoff threshold for both images was systematically increased iteratively by the computer until the ratio of dipoles found in the parallel plane, to dipoles found in the orthogonal plane, was maximized. A global maximum was found for this ratio by sampling all threshold values since this relationship had a few local maxima in our analysis. Optionally, adjusting the threshold manually is straightforward by visually inspecting an image because the similarity matrix response to dipoles is robust and highly selective.

The thresholded similarity matrix was used to generate the final 'pinpoint' images showing the locations of apparent dipoles. The dipoles were counted automatically using a MATLAB (The MathWorks Inc., Natick, MA) connected-region-counting function and volume-rendered in 3D using Amira software (Mercury Computer Systems, Chelmsford, MA). On our 2.4 GHz Intel Pentium 4 platform, the computing time for the 2D/3D cross-correlation takes on the order of minutes for a high-resolution 3D data set, and dipole counting is instantaneous.

Performance of the 3D PDQ method was estimated by a four step process: (i) a multi-slice volume from a central region of the gel phantom (∼10% of total volume) was selected to be representative of a 3D PDQ analysis on the entire sample; (ii) dipoles found by visual inspection in the phase image for that volume were tabulated; (iii) the number of dipoles that appeared both in the 3D PDQ pinpoint image and by visual inspection were counted; and (iv) the number of apparent dipoles marked in the pinpoint image that were not detected by visual inspection (i.e., false positives) were also counted.

6.3.2 Detection Limits using Low-SNR Simulated Dipole Field

To investigate how the PDQ algorithm performs with noisy data, it was applied to a synthetic dataset where noise was systematically varied. The synthetic dataset consisted of a phase-offset image containing 40 virtual paramagnetic particles against a uniform diamagnetic background. The 40 particles consisted of 8 dipoles from each of the following template sizes: 3×3, 8×8, 12×12, 16×16, and 20×20. The templates listed corresponded to the unitless susceptibility values 1, 2, 3, 4, and 5, respectively. Without any noise added, the system started with $\mathrm{CNR}_\phi = 7.0$ for all dipole sizes. To systematically reduce the phase image signal-to-noise ratio, CNR_ϕ , Gaussian noise was added to the real and imaginary components of the Fourier transform of the image to generate CNR_ϕ levels of 0.23, 0.25, 0.27, 0.29, 0.32, 0.35, 0.39, 0.45, 0.5, 0.58, 0.7, 0.88, 1.17, 1.75, and 3.5. At each noise level, a 2D normalized cross-correlation was performed between the simulated image and each of the two templates, sized 8×8 and 16×16 voxels. These two template sizes were chosen because they were slightly smaller and larger, respectively, than the median dipole in the simulated image, and thus it is expected that they will produce a different cross-correlation response. Our aim was to explore the sensitivity to dipole detection for different template sizes, with the systematic addition of noise. A serial application of the cross-correlation analysis was performed; the small

template was first applied to obtain a high-sensitivity similarity matrix. Next, the response of the large template was used to further reduce false positives and filter out any dipoles that the small template may have detected in random noise. For SNR simulations the resulting similarity matrices for each noise level were not thresholded automatically and a single confidence cutoff threshold for all simulations was determined by eye; this was accomplished by increasing the cutoff until only well-defined peak-valued pixels remained in the original, noiseless image. PDQ performance on the noisy synthetic data using the two-template approach was scored by comparing the resulting pinpoint images with prior knowledge of the simulated dipole locations. This comparison allowed us to extract two important measurements for each level of CNR_ϕ. First, we extracted the probability that a pinpoint (single dot) is actually a dipole by calculating P=(# of dots marking a dipole)/(total # of dots). Second, we extracted the probability that any given dipole is found by calculating P=(# dipoles marked by dot)/(total # of dipoles). These probabilities were plotted for every level of CNR_ϕ tested. The dual template method was not needed for either the agarose gel phantom analysis or the allograft heart analysis (below). Two templates were tested in the synthetic dataset only to evaluate the maximum performance ability of PDQ when confronted with data sets with exceedingly high noise levels.

6.3.3 MPIO-Labeled Macrophages in Rat Heart Acute Rejection Model

We investigated intact *ex vivo* rat hearts that had been infiltrated by MPIO-labeled macrophages. The hearts are from an allogenic heart rejection model, and the details of this model are described by Wu *et al.* [19]. Briefly, for allogeneic transplantation, the heart from a Dark Agouti rat was transplanted to the abdominal region of a Brown Norway rat, whereas, for syngeneic transplantation, the heart from the same strain was used. When MPIO is injected intravenously (i.v.), the particles are endocytosed by resident macrophages, effectively labeling these cells *in situ* [19]. Because macrophages play a crucial role in early organ rejection, they will infiltrate engrafted tissues in a number that has been observed to be proportional to the severity of organ rejection [19]. The MPIO, consisting of 0.9 μm polymer-coated microspheres with a magnetite core (Bangs Laboratories, Fishers, IN), was injected i.v. four days after organ transplant. After 24 hours, the rat was sacrificed, perfused, and the intact heart tissues were fixed in a 4% paraformaldehyde and 1% gluteraldehyde solution and then placed in PBS. Data were also acquired in control isogenic rat

heart transplants that do not undergo rejection. All animals received humane care in compliance with the Guide for the Care and Use of Laboratory Animals, published by the National Institutes of Health, and the animal protocol was approved by our University's Institutional Animal Care and Use Committee.

High-resolution 3D T_2^*-weighted, gradient-echo images of the intact organ were acquired at 11.7 T with TE/TR=8/500 ms and a resolution of $40 \times 40 \times 80$ μm. Before PDQ analysis, data were zero-filled to generate approximately isotropic voxels. After reconstructing and unwrapping the phase images, a 2D cross-correlation analysis was performed on each image slice of the 3D data stack using only the 16×16 template. When analyzing this relatively inhomogeneous heart tissue, template sizes of 8×8 and smaller resulted in a large number of false positive results. For templates larger than 8×8, the number of false positive results was not found to vary with template size. The slice plane was chosen to be parallel to B_0. A 3D analysis was also performed, where the confident cutoff threshold of the similarity matrix was automatically determined using the same B_0-parallel versus B_0-orthogonal slice comparison as described for the gel phantom (above). Once the threshold parameter was determined computationally, it was applied globally throughout the volume. The dipoles in the tissue volume were counted using a connected-region-counting algorithm in MATLAB. Images were rendered for 3D visualization, and method accuracy and sensitivity were calculated using the same analysis procedure described for the gel phantom (above).

6.3.4 Magnetocapsules in Agarose Gel

PDQ was initially evaluated in a set of phantoms, each containing 103 magnetocapsules suspended in 13 ± 3 mL of 2% agarose gel (~70 capsules/mL). In brief, magnetocapsules were synthesized by crosslinking alginate with poly-L-lysine and 2.5%, 5%, or 10% v/v Feridex SPIO (11.2 mg [Fe]/ml, Berlex Laboratories, Montville, New Jersey). A coating layer of alginate was added to the surface of the initial capsules. Capsules had uniform Feridex labeling and a diameter of 570 $\pm$ 60 μm (preparation details described elsewhere [124]).

MRI data were acquired for 12 agarose gel phantoms containing suspended 2.5%, 5%, and 10% v/v Feridex magnetocapsules (n=3, 5, and 4, respectively). A typical magnetocapsule phantom is shown in 6.3 All samples were imaged using a 4.7 T, 40 cm horizontal bore Bruker AVANCE AVI scanner (Bruker BioSpin, Billerica, MA) using a 3D GRE pulse sequence with imaging parameters:

TE/TR=1.2/300 ms, averages = 18, and 280 μm isotropic resolution.

Figure 6.3: Typical Magnetocapsule Phantom.
A concentration of 10% v/v Feridex magnetocapsules are suspended in 10mL of 1% agarose gel within a 50mL centrifuge tube. Magnetocapsule density followed a gentle gradient from lower density at the top of the suspension to a higher density at the bottom.

The accuracy of PDQ magnetic measurements in low-SNR images was also tested. One 10% v/v Feridex magnetocapsule phantom was imaged with decreasing scan times to generate images with SNR = 29, 18, 14, and 11. Addition of Gaussian noise to the datas real and imaginary components simulated images with SNR = 4.5 and 2.5. PDQ was run on each image to count the detected magnetocapsules and calculate apparent magnetic properties.

6.3.5 Magnetocapsule Magnetometry

The magnetic moment of the magnetocapsules was measured using SQUID magnetometry. Triplicate samples were prepared, each containing 100 dehydrated 10% Feridex v/v magnetocapsules. Dehydration was performed via immersion in 100% ethanol followed by desiccation under vacuum for 10 minutes. To ensure that this process did not degrade the magnetocapsules, samples were challenged with ethanol immersion for 72 hours, resulting in no noticeable loss of integrity.

For magnetometry, desiccated magnetocapsules were counted (100 ± 1) and placed into an empty two-piece gelatin capsule. Each gelatin capsule sample was held in a plastic drinking straw by a small amount of quartz wool and placed into a SQUID magnetometer (Quantum Design, San Diego, CA). Measurements were made at 310 K as a function of magnetic field ranging from 0–7 T; magnetic moment values were averaged across the three samples and corrected for the diamagnetic contributions from the gelatin capsule and quartz wool.

6.3.6 Magnetocapsules in Porcine Liver

Using a porcine model, PDQ was used to analyze 10% v/v Feridex magnetocapsules lodged in the vasculature of a porcine liver. Approximately 1.4×10^5 magnetocapsules were injected via portal vein into a swine using methods described elsewhere [124]. On the same day as transplant the swine was sacrificed, the liver was harvested, and a 58 cm^3 section was fixed in 4% paraformaldehyde for *ex vivo* imaging. A 3D GRE image of the liver section was acquired at 4.7 T with TE/TR=3.5/200 ms, averages = 5, and a resolution of 180×280×140 μm.

6.3.7 MPIO-Labeled Macrophages in Murine Traumatic Brain Injury Model

PDQ was used to analyze macrophage infiltration in mouse brains following TBI induced by a controlled cortical injury (CCI). Male C57BL/6J mice (Charles River Laboratories, Wilmington, MA) aged between 11-15 weeks were anesthetized and injected with 4.5 mg [Fe]/kg of 0.9 μm-diameter microspheres containing 62% magnetite (w/w) and fluorescein-5-isothiocyanate dye cross-linked within polystyrene/divinylbenzene (Bangs Laboratories, Fishers, IN). These MPIO particles are endocytosed by circulating monocytes and macrophages, thereby labeling these cells in situ [19]. Control mice received no MPIO injection. Between 24–48 hours after MPIO injection a CCI was delivered as previously described [125]. Mice were imaged 24 and 96 hours post-TBI using a 7 T, 21 cm horizontal bore Bruker AVANCE AV3 system using a standard 3D GRE pulse sequence with parameters: TE/TR = 7/100 ms, averages = 4, and a resolution of 58×79×79 m. After the final *in vivo* session mice were perfused, fixed with 4% paraformaldehyde, and the brains excised. 3D volume images were acquired in the fixed brains using an 11.7 T, 89-mm vertical bore Bruker AVANCE micro-imaging system with parameters: TE/TR=6/500 ms, averages=4, and 58×39×39 μm resolution.

6.3.8 MPIO-Labeled Macrophages in Rat Heart Chronic Rejection Model

PDQ investigated MPIO-labeled macrophages infiltrating cardiac tissue in a working-heart model of chronic cardiac rejection. In this model, the heart and lung from a PVG.1U rat are transplanted en bloc into the abdomen of a PVG.R8 rat, where the experimental details are described elsewhere [132]. One day before transplant, or 1-5 weeks after transplant, each of the 27 transplant recipients was injected i.v. with 4.5 mg [Fe] per rat of 0.9 μm-diameter MPIO (Bangs). These 0.9-μm-diameter MPIO have a blood half-life of 1.2 $\pm$ 0.6 minutes in Brown Norway rats [132]. At different time points after transplantation (2-26 weeks), rats were sacrificed, perfused, and the intact heart tissues were fixed in 4% paraformaldehyde. Hearts were imaged at 11.7 T using a standard 3D GRE pulse sequence with parameters TE/TR = 8/500 ms, averages = 2, and an isotropic resolution of 40 μm. All animal experiments throughout this methods section were approved by the Carnegie Mellon Institutional Animal Care and Use Committees (IACUC), or the Johns Hopkins IACUC, and animals received care in compliance with the National Institute of Health Guide for the Care and Use of Laboratory Animals.

6.3.9 10 μm-diameter SPIO Particles in Agarose Gel

A 2% w/v agarose gel phantom was doped with a high concentration of large SPIO particles, in order to challenge the PDQ algorithm with a high spatial density of dipole impressions. The SPIO particles have a 10 μm-diameter and are composed of 90% magnetite by weight (Bangs Laboratories, Fishers, IN). A typical phantom for this type of iron oxide is shown in Figure 6.4. The phantom was imaged at 11.7 T using a standard 3D gradient-echo pulse sequence with TE/TR = 5/75 ms, $\theta \approx 90°$, Averages = 44, and an isotropic resolution of 40 μm.

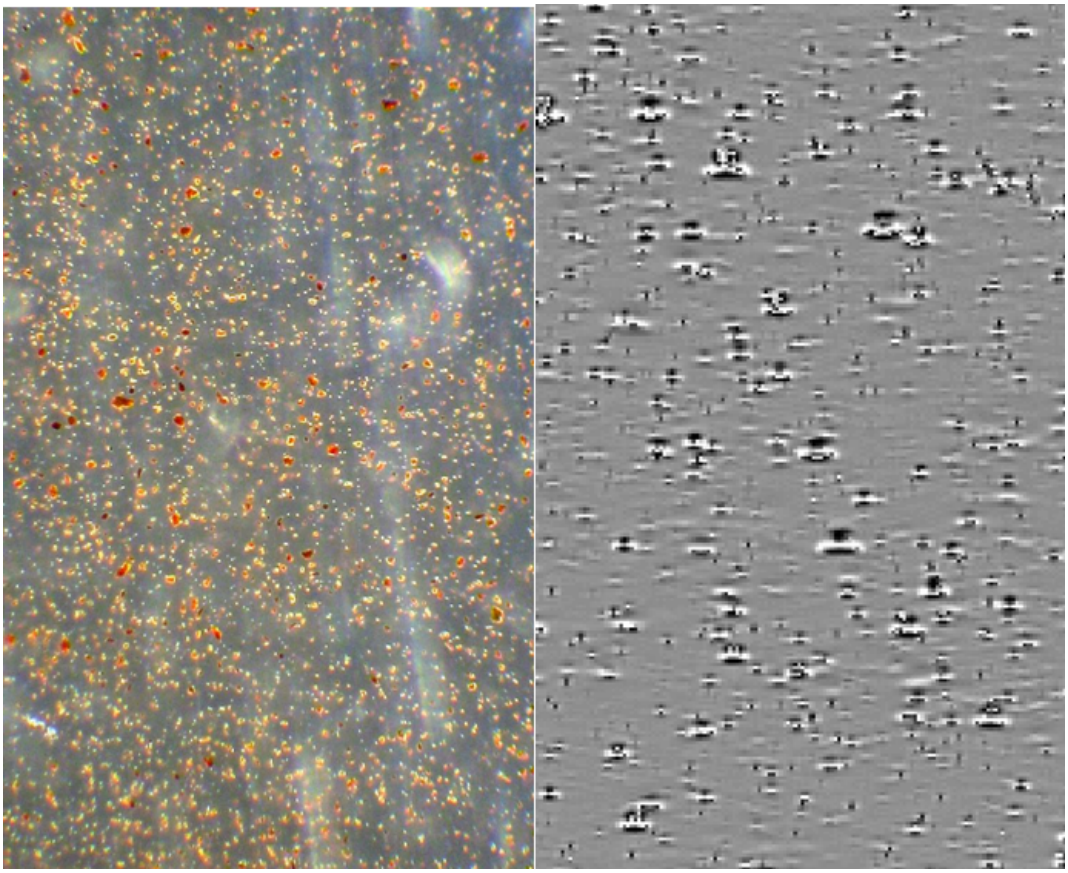

Figure 6.4: Typical 10μm-diameter SPIO agarose phantom.
Light micrograph (left) and MRI phase image (right) of mixed-size SPIOs with an average diameter of 10μm. Particles are 90% magnetite by weight.

6.3.10 PDQ Data Analysis

An overview of the PDQ algorithm is displayed in Fig. 6.2, and the details are described below. First, PDQ reconstructed the raw k-space data into magnitude and phase images, where unwrapping of the 3D phase data was performed using PRELUDE [98]. Phase-unwrapped data were imported into MATLAB (The MathWorks, Inc., Natick, MA) and high-pass filtered with a kernel designed to exclude the lowest 10% of frequencies, which is the smallest percentage of frequencies that must be removed in order to eliminate large-scale magnetic inhomogeneity, as described by Eq. (3.18). As described above, Eqs. (3.19) and (6.1) were used to generate 27 templates, sized $7 \times 7 \times 7$ voxels, with each template representing dipoles shifted [–0.4, 0.0, or +0.4] voxels in x-, y-, and z-dimensions. 3D normalized cross-correlation was applied between each of the 27 templates and

the high-passed phase data, resulting in 27 similarity matrices. A 3D peak detection algorithm was applied to the non-shifted similarity matrix to pinpoint the location of each dipole. To account for dipole shifts off the Cartesian grid, each dipole was assigned its maximum TS value from the 27 shifted similarity matrices, and peaks with TS $\leq 30\%$ were discarded.

$\Delta\chi$ for SPIO deposits with TS $\geq 70\%$ was measured using a 3D least-squares fit between the phase-impression in the high-passed phase image and a dipole template. The 70% TS threshold is used since PDQ was found to underestimate magnetic moments by >15% when applied to dipoles with TS $< 70\%$, (see Results). The χ_A of each dipole was calculated from user-provided χ_B using Eq. (6.3) and its magnetic moment from Eq. (6.3). For each SPIO deposit, we calculated χ_{an} using Eq. (6.7), $\overrightarrow{m}_{an}$ using Eq. (6.6), and $\overrightarrow{m}_{Fe}$ using Eq. (6.8). The final result of the PDQ process is a list of high-confidence SPIO deposit locations and their magnetic and iron measurements.

PDQ analyzed the experimental datasets assuming the following χ_B parameters: Magnetocapsules or SPIO in agarose $\chi_B = -9.05 \times 10^{-6}$ [80, 51], magnetocapsules in liver $\chi_B = -8.8 \times 10^{-6}$ [80], and macrophages in mouse brain and rat heart $\chi_B = \chi_{water} - 9.05 \times 10^{-6}$ [80]. The PDQ radius parameter for macrophage was assumed to be a ≈ 8.5 μm [133].

6.3.11 Dipole Density versus Distance from Injury in Murine TBI Model

The distribution of SPIO-labeled cells in a tissue volume may be a biomarker for different disease conditions. For example, in cardiac tissue undergoing immune rejection, macrophages have been observed to progress from pericardium to endocardium at different stages of rejection. PDQ analyzed a mouse brain infiltrated by MPIO-labeled macrophages as a result of a controlled cortical impact traumatic brain injury (TBI). The TBI region (damaged brain tissue) was segmented from the rest of brain tissue and designated as a region-of-interest (ROI). The number of dipoles were plotted as a function of distance from this ROI to investigate whether there exists a density gradient of MPIO-labeled cells (i.e., macrophages) in the tissue surrounding the area of injured tissue.

6.3.12 Comparison between PDQ and ImageJ Dark Spot Counting in Murine TBI model

To compare the results from PDQ to the current standard for automated hypointense spot counting, MPIO-labeled macrophages were counted using ImageJ software in 15 different *ex vivo* mouse

brains following TBI. Methods for obtaining the high-resolution *ex vivo* TBI mouse brain datasets are described above. PDQ was applied to the same samples analyzed by ImageJ, and macrophage counts from PDQ were compared against the ImageJ counts. The ImageJ "analyze particles" feature was used to perform the automatic hypointense spot counting, using parameters that searched for spots 4–50 pixels in size with a circularity of 75–100%. PDQ parameters were run assuming a macrophage radius of $a = 8.5$ μm and a template similarity (TS) of TS $> 45\%$. Both PDQ and ImageJ analyzed the entire heart volume, providing 100% coverage of the tissue samples.

6.3.13 Comparison between PDQ, ED1+ Cell Counts, and Manual Dark Spot Counts in Rat Heart Chronic Rejection Model

Three different cell quantification methods were compared by applying them to datasets for 21 rat hearts undergoing chronic rejection (see above methods for rejection model details). Eight of the 21 rat heart samples were categorized as incompletely-perfused, as they had numerous instances of blood in vessels following the perfusion process. This blood appears as hypointense spots, regions, or lines in the magnitude image of the heart tissue. Figure 6.5a and 6.5b shows typical heart samples that are incompletely-perfused. Of the 21 rat heart samples, 13 were categorized as completely-perfused, since they are nearly devoid of blood in vessels following tissue perfusion (seen in Figure 6.5c and 6.5d).

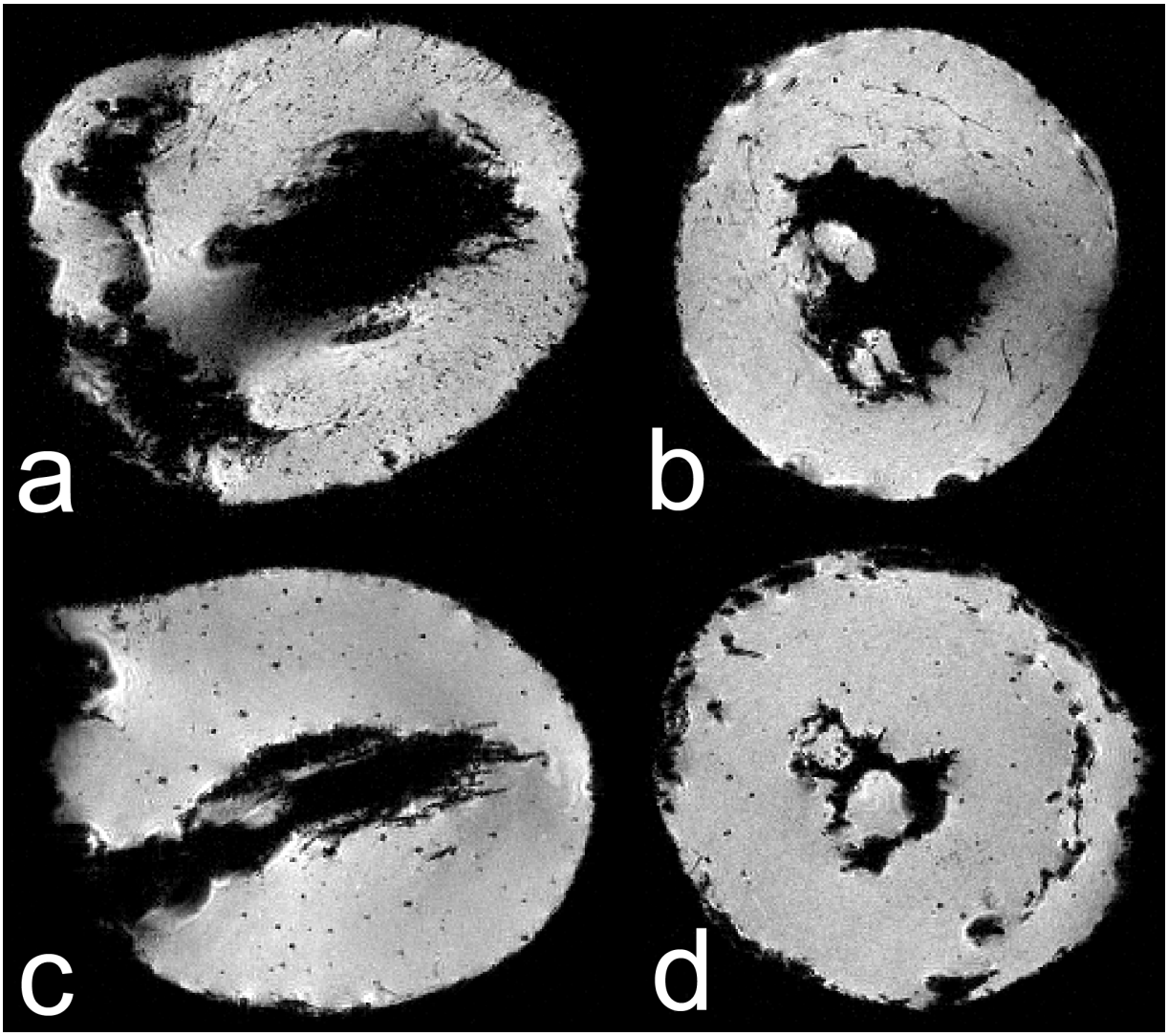

Figure 6.5: MR images of four rat hearts undergoing chronic rejection that were analyzed by three different cell quantification methods: PDQ, manual dark spot counting, and ED1+ cell counting. Shown are (a) sagittal view of incompletely-perfused heart P48, (b) axial view of incompletely-perfused heart P27, (c) sagittal view of completely-perfused heart P30, and (d) axial view of completely-perfused heart P41. Incompletely-perfused heart samples show hypointense spots and regions that confound manual cell counting in these 3D heart tissue volumes. The completely-perfused heart samples show a few large-scale artifacts, but dark spots that indicate the presence of MPIO-labeled macrophages or macrophage clusters are isolated and able to be distinguished from tissue features by manual inspection.

The first quantification method was PDQ counting of magnetic dipoles within the phase image of each heart sample. Only dipoles with a template similarity (TS) value of TS $> 45\%$ were counted, so as to include only those that had a high similarity to the dipole pattern expected for a spherical deposit of MPIO (i.e., individual MPIO-labeled cell).

The second quantification method was manual counting of ED1+ cells within an 8-μm thick

histological section from the center of each heart sample. Figure 6.6 shows one of these histological sections. This ED1+ cell count represented a total area of 2.89 mm^2 within the histological section, and was performed by summing the cells counted within five disparate 0.578 mm^2 tissue regions. Calculating the number of ED1+ cells per mm^2 of heart tissue is straightforward, but estimating a volumetric value of ED1+ cells per mm^3 of heart tissue is desirable for comparison with the PDQ method, which reports cell counts normalized to tissue volume (i.e., dipole count per mm^3 of heart tissue). To estimate the density of ED1+ cells per mm^3 of heart tissue, we make two assumptions about the spatial arrangement of macrophages in tissue. First, we assume that rat macrophages have a diameter of 19 ± 4 μm [133]. Second, we assume that at least 4 μm of the cell body diameter of a macrophage must be present within an 8 μm-thick histological section for a successful ED1+ immunostaining. Using these assumptions, an isolated 8 μm-thick histological section will detect macrophages whose centers are located within $\pm$ 9.5 μm of the center of the section. Hence, we estimate an 8 μm-thick histological section detects macrophages present within a 19 μm-thick slab of tissue in the slice-stack dimension. Using this detection estimate, we further estimate that the 2.89 mm^2 region that we inspect for each heart sample, will detect ED1+ cells present within a total tissue volume of 0.055 mm^3.

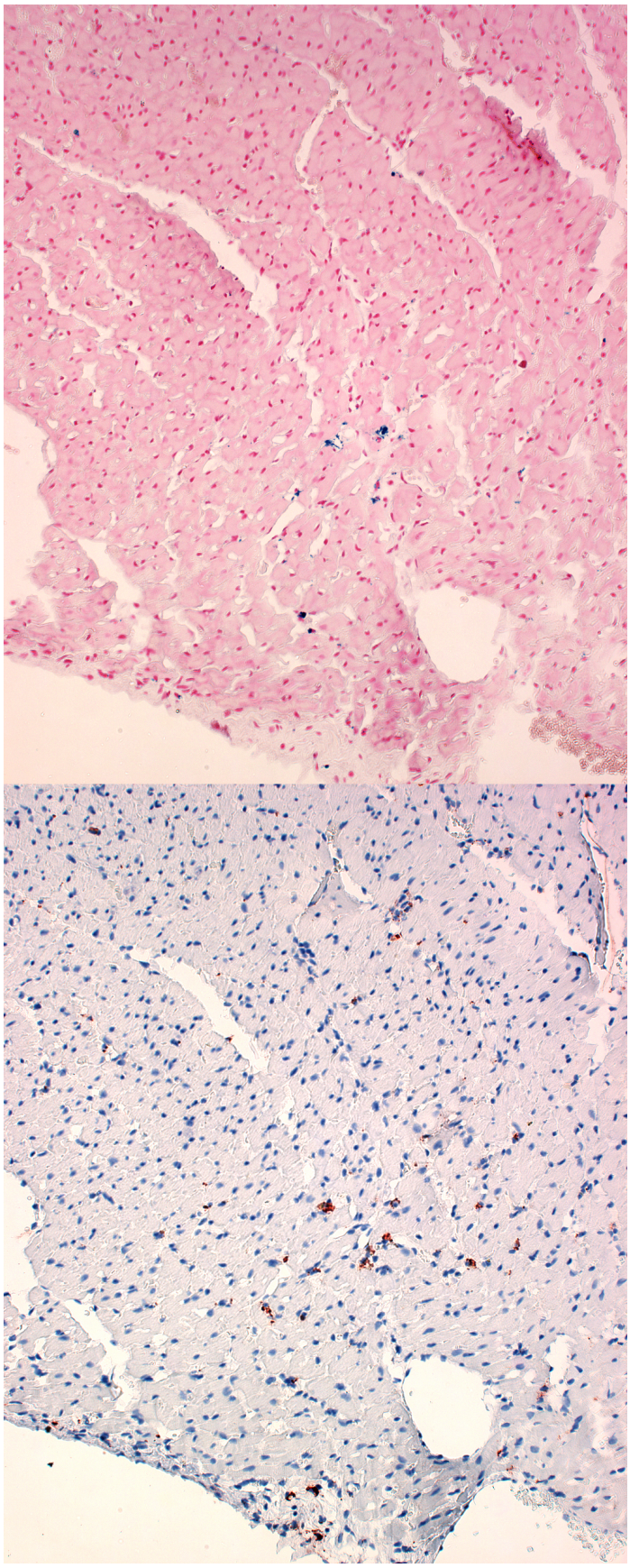

Figure 6.6: Adjacent histological sections of rat cardiac tissue undergoing chronic immune rejection.
The (left) panel highlights cell nuclei using a DAPI stain (blue) and ED1+ cells (activated microglia/macrophages/monocytes) using an ED1 immunostain (brown). The (right) panel shows an adjacent section stained with hematoxylin and eosin (H&E) and Prussian blue iron stain to highlight 0.9-μm diameter MPIO particles. In this field of view, there are many instances where MPIO particles and ED1+ cells colocalize. Some ED1+ cells appear to contain no MPIO particles. Registration uncertainty between these two sections exists since since these two sections are adjacent, not identical. Some ED1+ cells are clustered with one or more other ED1+ cells. (Histological images courtesy of Qing Ye).

The third quantification method was hypointense spot counting within magnitude images of each heart sample. For each heart, 6 sections displaying the axial plane were selected along the long axis of the heart. Each section consisted of three contiguous 40 μm-thick slices, resulting in a total of 18 manually-inspected slices per heart (approximately 10% heart volume coverage). Within each inspected slice, hypointense spots that indicate the presence of an MPIO-labeled macrophage (or macrophage cluster) were counted, with care taken to exclude hypointensities due to other apparent structures (e.g., blood vessels).

To compare these three different quantification methods, linear fits were performed between the results of each quantification method.

6.3.14 Longitudinal *in vivo* multi-dipole tracking in Mouse TBI Model

To test the feasibility of PDQ for *in vivo* serial longitudinal tracking of MPIO-labeled cells, the method was applied to mouse brains at different time points following TBI. Male C57Black/6J mice aged between 11–15 weeks were anesthetized with isoflurane in N_2O:O_2 (1:1), intubated, and mechanically ventilated; a femoral venous catheter was then surgically placed for MPIO injection (4.5 mg[Fe]/kg). Mice were injected with 0.96 μm-diameter MPIO (Bangs Labs, Fishers, IN). The mouse controlled cortical impact (CCI) model was used as previously described [125]. Mice were imaged at different time points using a Bruker 7-Tesla/21-cm AVANCE AV3 scanner equipped with a 35 mm mouse birdcage coil or a 2-cm T/R surface coil. High resolution T_2^*-weighted 3D images were obtained with the following parameters: TE/TR=7/100 ms, Averages = 4, and a resolution of $70 \times 95 \times 95$ μm (volume coil) or $58 \times 79 \times 79$ μm (surface coil). After the final MRI session, brains were perfused, fixed with 4% paraformaldehyde and imaged with MRM at 11.7-T with a resolution of $58 \times 39 \times 39$ μm, as described previously [125]. Dipole moments were calculated assuming a radius of $a = 7.5$ μm for each MPIO-labeled phagocyte.

To track individual dipoles between scans performed on different days, each time point for a particular mouse brain was registered in the same coordinate system using an iterative rigid body transformation. A rigid transformation assumes that the brain stays the same shape and volume, but severe tissue deformations are present at the site of injury (Fig. 6.27), and mild deformations of tissue geometry occur in the area surrounding the site of injury. Because the injury is at a controlled depth of 1 mm, an estimated 70-90% of tissue did not undergo deformation

exceeding one voxel (25-50μm), allowing for rigid transformation to be used as an approximate method to register brain volumes. Registration error may be present when registering pre-TBI brains with post-TBI brains, causing a dipole exhibit apparent movement upon rigid registration if it is present near the region where the controlled cortical impact is delivered. In this scenario, dipole registration would report a detected dipole movement, while instead only tissue moved. However, rigid registration performance between the same brain post-TBI posed no confounding tissue deformations as the injury healing process progressed. Over time period exceeding the scale of this study (maximum of 96 hours), it is possible that progressive healing of the brain injury may deform brain tissues sufficiently for non-rigid transformation to provide more accurate dipole-tracking results. To register dipoles between two time points, a cost value was calculated between all detected dipoles at the earlier time point (M dipoles at t=t_1) and all dipoles at the later time point (N dipoles at t=t_2). The cost value between dipole m at t=t_1 and dipole n at t=t_2 was calculated as: $cost_{mn} = r/r_{max} + \Delta m/\Delta m_{max}$ where r represents the distance between the two dipoles, r_{max} represents the maximum possible distance that a dipole is expected to travel, Δm represents the difference in magnetic moment between the two dipoles, and Δm_{max} represents the maximum possible change in the magnetic moment value measured by PDQ. Dipole pairs with $r > r_{max}$ or $\Delta m > \Delta m_{max}$ were discarded. For this experiment, the parameter r_{max} was set to be 480 μm for 24 hours (assumes a maximum movement speed of 20 μm per hour) and the parameter Δm_{max} was set to be $0.4pA \cdot m^2$. Dipoles were then matched using the Hungarian algorithm, which calculates the optimal assignment between all dipoles at $t = t_1$ and all dipoles at $t = t_2$, given the above constraints.

6.4 Results

6.4.1 MPIO Gel Phantoms

As an initial evaluation of the PDQ method, we performed 3D imaging studies of an agarose gel phantom doped with MPIO particles to generate localized dipolar field perturbations. A magnitude MR image slice of the phantom (Fig. 6.7a) shows numerous hypointense spots that are consistent with the presence of MPIO particles, microscopic air bubbles, and perhaps undissolved agarose particles. Figures 6.7b-c show the phase image of the same slice before and after phase unwrapping,

respectively. Applying a high-pass filter to the slice reveals numerous dipolar magnetic field patterns (Fig. 6.7d). Most dipoles are due to localized paramagnetic entities (e.g., MPIO or air bubble), however a few dipoles appear diamagnetic (Fig. 6.7d, white arrows). We speculate that these diamagnetic dipoles could possibly be small crystals of undissolved agarose, since these would be more diamagnetic than the aqueous agarose gel.

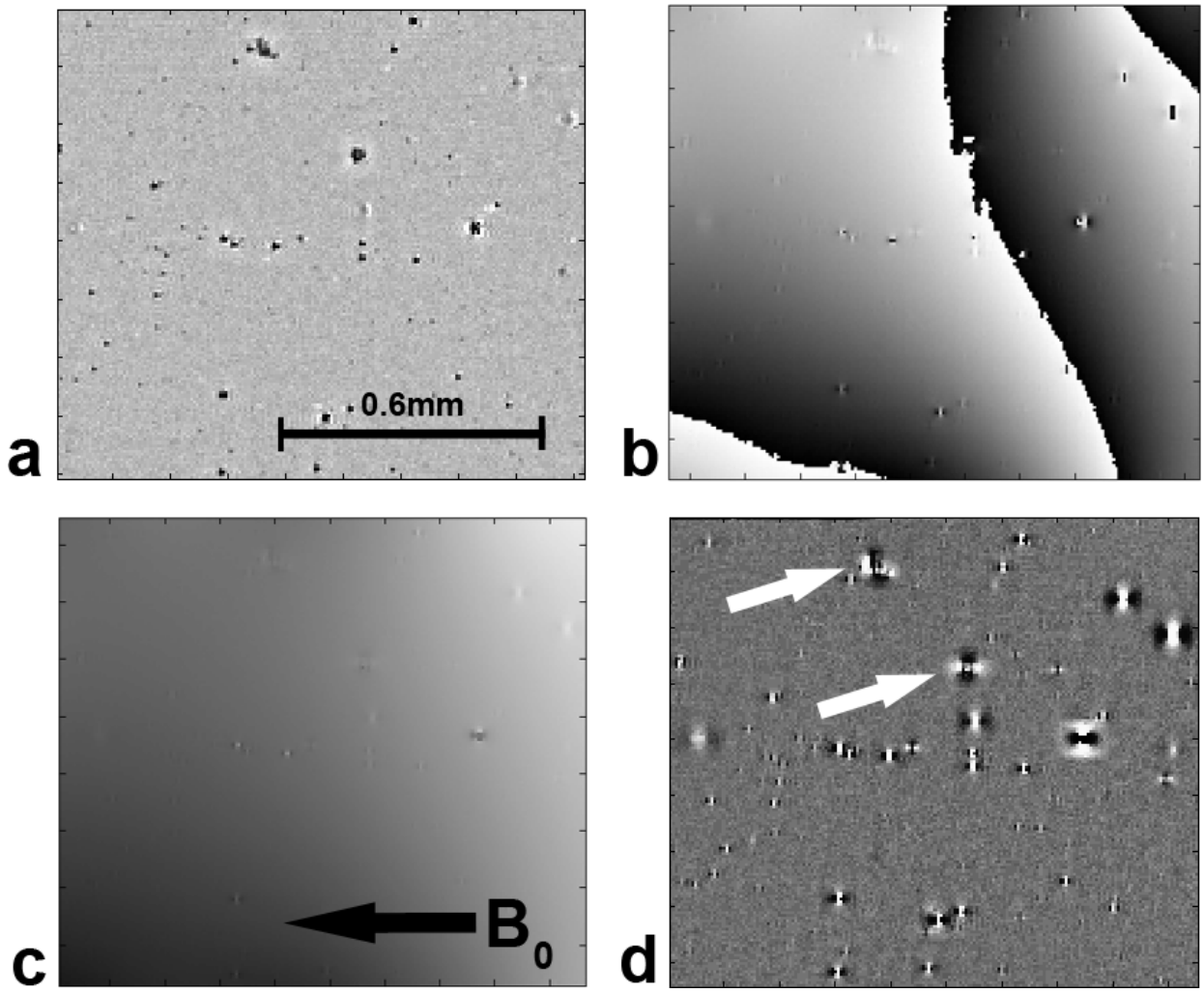

Figure 6.7: Various representations of the same MR image of a gel phantom containing a mixture of MPIO particles, air bubbles, and undissolved agarose crystals.
The image types displayed include (a) magnitude image, (b) phase image, (c) unwrapped phase image, and (d) phase offset image. Arrows indicate diamagnetic dipoles. Each dipole in the magnitude image (a) appears as a dark spot against the background while those in the phase offset image (d) have a clear dipolar impression. *(Figure taken from Fig. 1 of Mills et al. [123])*

The templates used for the cross-correlation analysis were calculated using Eq. (6.1), where Fig. 6.1a shows a 16×16 voxel 2D template, and Fig. 6.1b shows a generic 3D version. Figure

6.8 shows portions of a phase MR image of six different dipolar profiles found in the gel phantom, along with a one-dimensional cross section through the similarity matrix response following a 8×8 and 16×16 template cross-correlation serial analysis. The larger dipole template is insensitive to noise (Fig. 6.8a). The smaller dipole template is more sensitive to small and weak dipoles (Figs. 6.8b-c), but is more likely to generate false-positives when cross-correlated against noise. The large response of the 3D template alone was used to generate the final PDQ output (Fig. 6.13a).

We note that cross-correlating either template with the diamagnetic particle (Fig. 6.8e) resulted in a strong negative response in the similarity matrix; thus, the PDQ method can provide stringent differentiation between paramagnetic and diamagnetic dipoles, a feature not offered by conventional magnitude images.

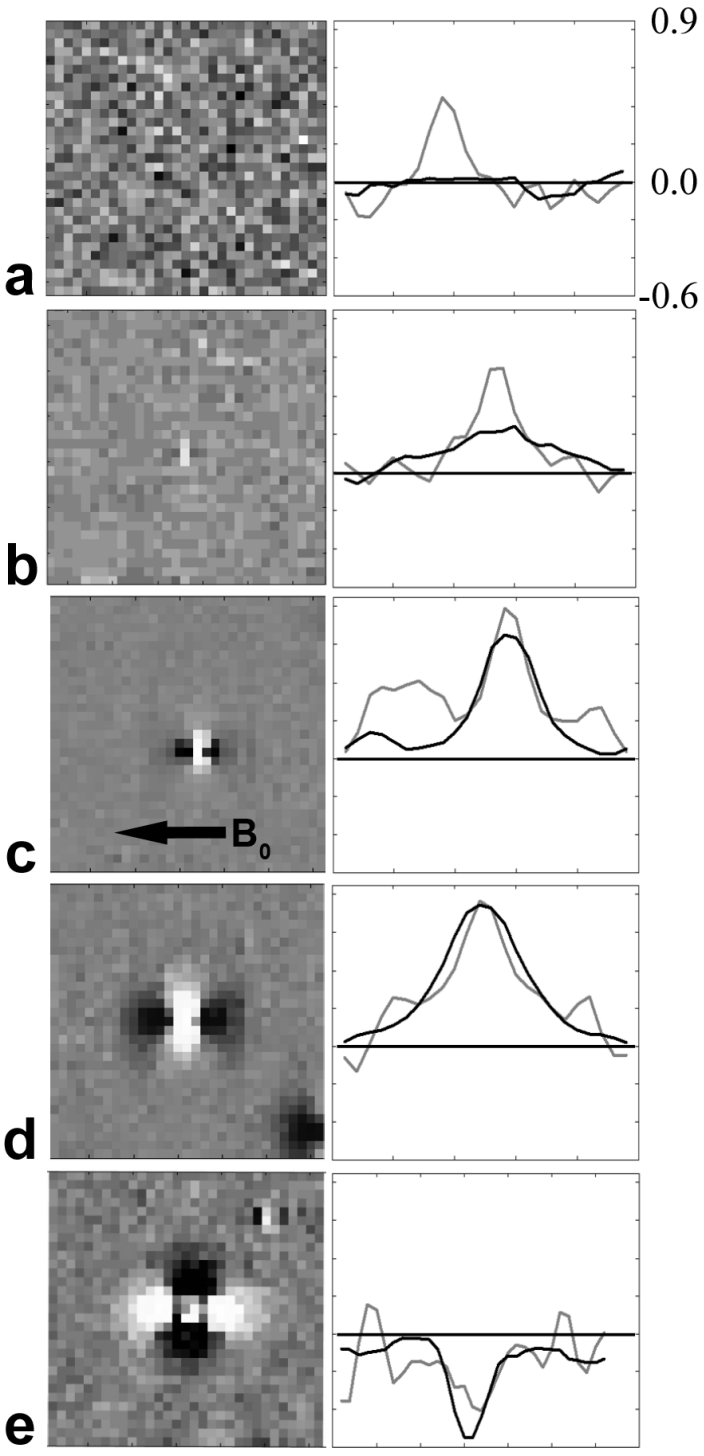

Figure 6.8: Normalized cross-correlation analysis applied to various dipole impressions found in the gel phantom phase offset images.

The gray and black lines are the maximum similarity when an 8×8 and 16×16 template, respectively, are cross-correlated with- (a) region of noise, (b-d) paramagnetic objects of various strengths, and (e) unidentified diamagnetic object. The larger dipole template is impervious to noise (a), while the smaller dipole template detects noise but is more sensitive to small, weak dipoles (b-c). Note that cross-correlating the template with the diamagnetic object (e) results in a strong negative response. *(Figure taken from Fig. 3 of Mills et al. [123])*

A summary of results showing the efficacy of the PDQ method when compared to visual inspection is tabulated in Table 6.1. The 3D cross-correlation methods showed no statistically significant improvement over a 2D analysis, implying that imperfectly-shaped dipoles in the sample may be a limiting factor when using this method against homogeneous backgrounds such as agarose. Using a representative sample size of 625 mm^3 of agarose gel, the dipole density was calculated in Table 6.1 under the heading "infiltration index."

Dataset	Dipoles found by visual inspection	Dipoles found by PDQ	Dipoles missed	Infiltration Index (dipoles/mm^3)
Gel Phantom	50	47	6%	12.8
Heart Allograft	29	23	21%	7.36
Heart Isograft	31	28	10%	3.22

Table 6.1: Results applying 3D PDQ to the gel phantom and allograft and isograft heart tissues. Visual inspection was performed by manually searching for dipolar patterns in MRI phase-offset images. 'Dipoles missed' represents the fraction of dipoles found by visual inspection that were missed by PDQ. The infiltration index represents the number of dipoles detected per unit tissue volume. *(Table taken from Table 1 of Mills et al. [123])*

Figure 6.13a shows the 3D-rendered distribution of dipoles using the 3D PDQ method in the gel phantom. Figure 6.13b shows the 3D-rendered distribution of false positive "dipoles" found by analyzing 2D slices through the volume orthogonal to B_0 at the same threshold; theoretically this field orientation should result in no detectable dipoles, however, several false positives are clearly visible.

6.4.2 Detection Limits Using Low-SNR Simulated Dipole Field

To test the robustness of the PDQ method in low SNR images, a simulated dipole field was analyzed. Figure 6.9a shows the noise-free synthetic phase image, and Figs. 6.9b-d show the effects of incrementally increasing noise. Smaller (i.e., weaker) dipoles are the first to be dropped from detection with the addition of noise. At $CNR_\phi = 0.3$, 50% of the large dipoles are still detectable by this method. To summarize the effect of noise, Fig. 6.10 plots the probability of finding a given dipole using the PDQ method in addition to the probability that a "positive" is actually a dipole. The figure shows detection accuracy remains between 85-95% for all values of CNR_ϕ studied. For values of $CNR_\phi > 1.5$, all dipoles are found. Notably, at $CNR_\phi = [0.23, 0.25, 0.29]$, even though the CNR_ϕ is held nearly constant, the probability that a single dot is a dipole varies by $\pm$ 0.05.

This variance appears because a different noise field is generated and imposed on the dipole field image for each value of CNR_ϕ. Therefore, two different noise fields can be generated for the same CNR_ϕ value, but the contrast of individual dipoles may vary between the two noise-field images, causing dipole detection probabilities to vary within a small range of values. This likely explains the drop in dipole detection probability at $CNR_\phi = 0.32$ (Fig. 6.10). The magnitude of this drop is comparable to the intrinsic probability variance of $\pm$ 0.05.

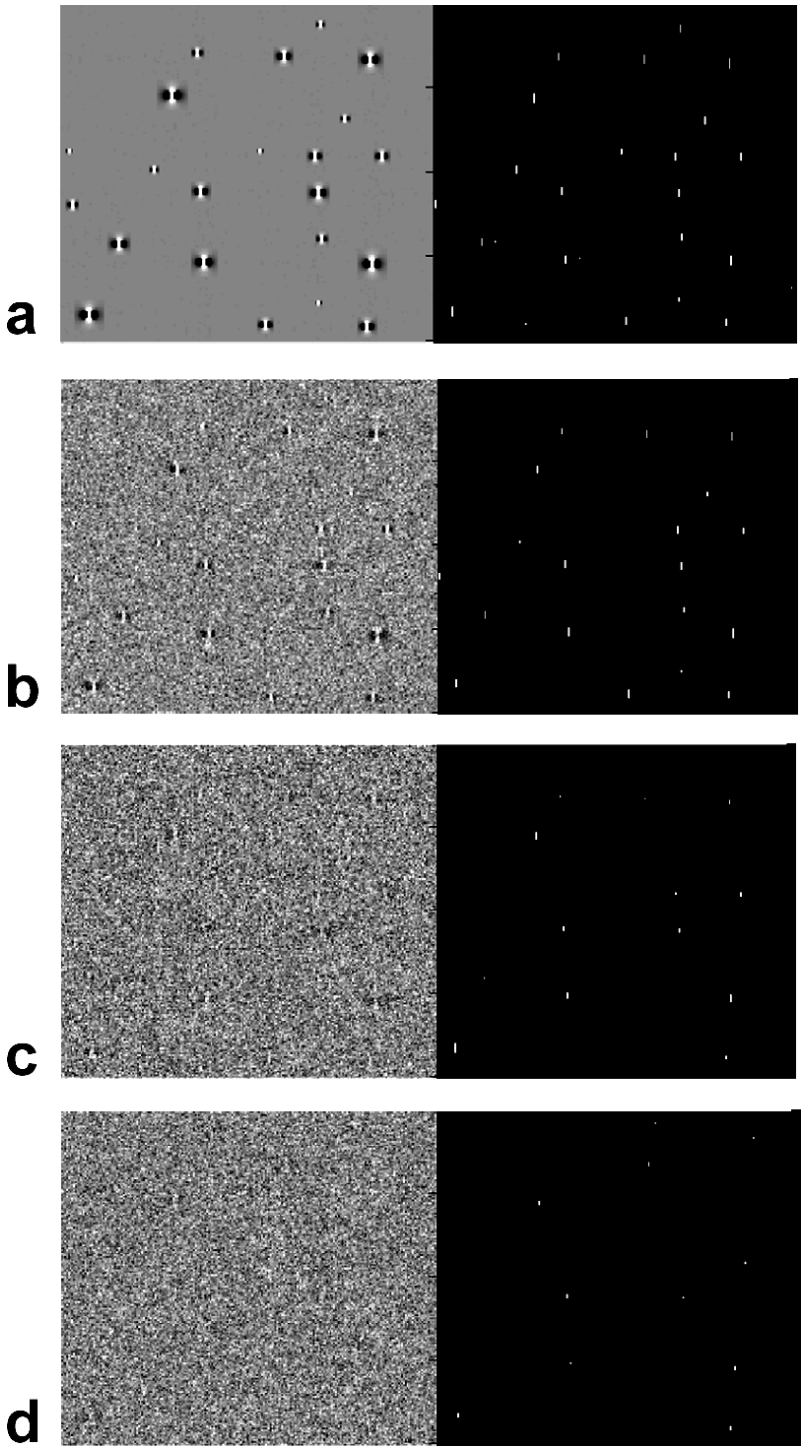

Figure 6.9: Synthetic dipole field images (left column) and the corresponding results of cross-correlation analysis with varying amounts of noise (right column).
Each dot indicates the location of a dipole. The same simulated image is analyzed at CNR_{ϕ}= (a) 7.0, (b) 0.7, (c) 0.35, and (d) 0.23. As noise increases, small dipoles drop from detection, but the largest dipoles remain detectable to the highest values of noise. At noise levels where dipoles are nearly undetectable by eye, the algorithm is able to locate half of dipoles present. *(Figure taken from Fig. 4 of Mills et al. [123])*

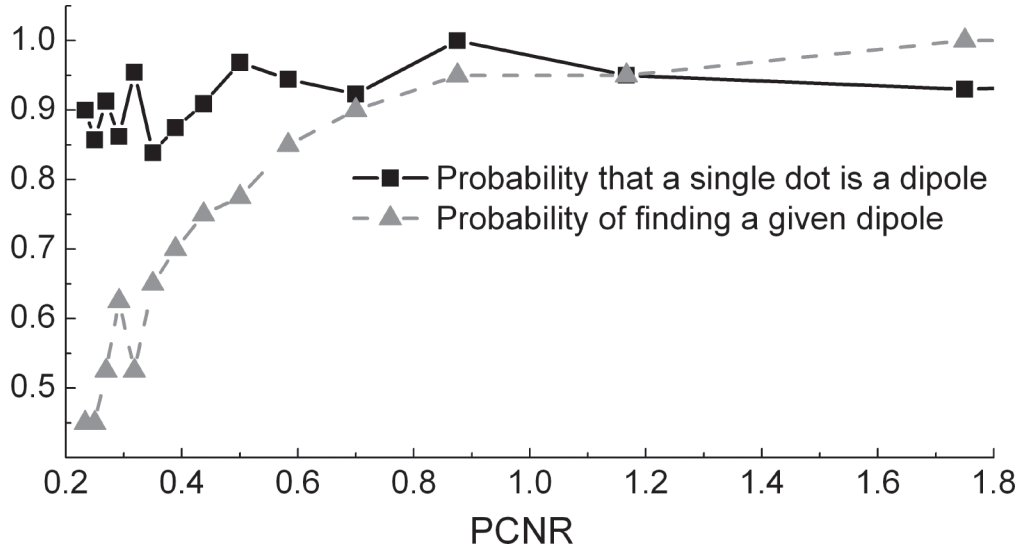

Figure 6.10: Plot of (i) probability of finding a given dipole in the synthetic dipole field when using PDQ analysis and (ii) probability that a dot in the similarity matrix image is a dipole. Both probabilities are plotted versus CNR_ϕ. At CNR_ϕ=0.3, 50% of the large dipoles are still detectable by this method. Detection accuracy remains between 85-95% for all noise values studied. For values of $CNR_\phi > 1.7$ (not shown) all dipoles are found. *(Figure taken from Fig. 5 of Mills et al. [123])*

6.4.3 MPIO-Labeled Macrophages in Rat Heart Acute Rejection Model

The PDQ method was found to be effective in detecting and quantifying magnetic dipoles in heterogeneous tissue, many of which represent MPIO-labeled cells and cell clusters. These experiments used an allogenic rat heart transplant that was excised and fixed following acute organ rejection. Prior to sacrificing the rat, its macrophages, destined to participate in the organ rejection, were labeled *in situ* with MPIO [19]. Figure 6.11 shows T_2^*-weighted magnitude slices (left column) and the corresponding phase offset images (right column) through the rejecting heart viewed from both orthogonal and parallel planes to B_0 (Figs. 6.11a-b, respectively). The characteristic 2D dipole impressions are scattered throughout the heart slice parallel to B_0 in the phase images (bottom, Fig. 6.11b), but are mostly absent in the slice orthogonal to B_0 (top, Fig. 6.11a). This property was used to automatically threshold the cross-correlation similarity matrix results; the PDQ algorithm minimizes false positives by choosing a similarity matrix threshold such that minimal dipoles appear in the B_0-orthogonal slices, while simultaneously maximizing the number of dipoles detected in the B_0-parallel slices.

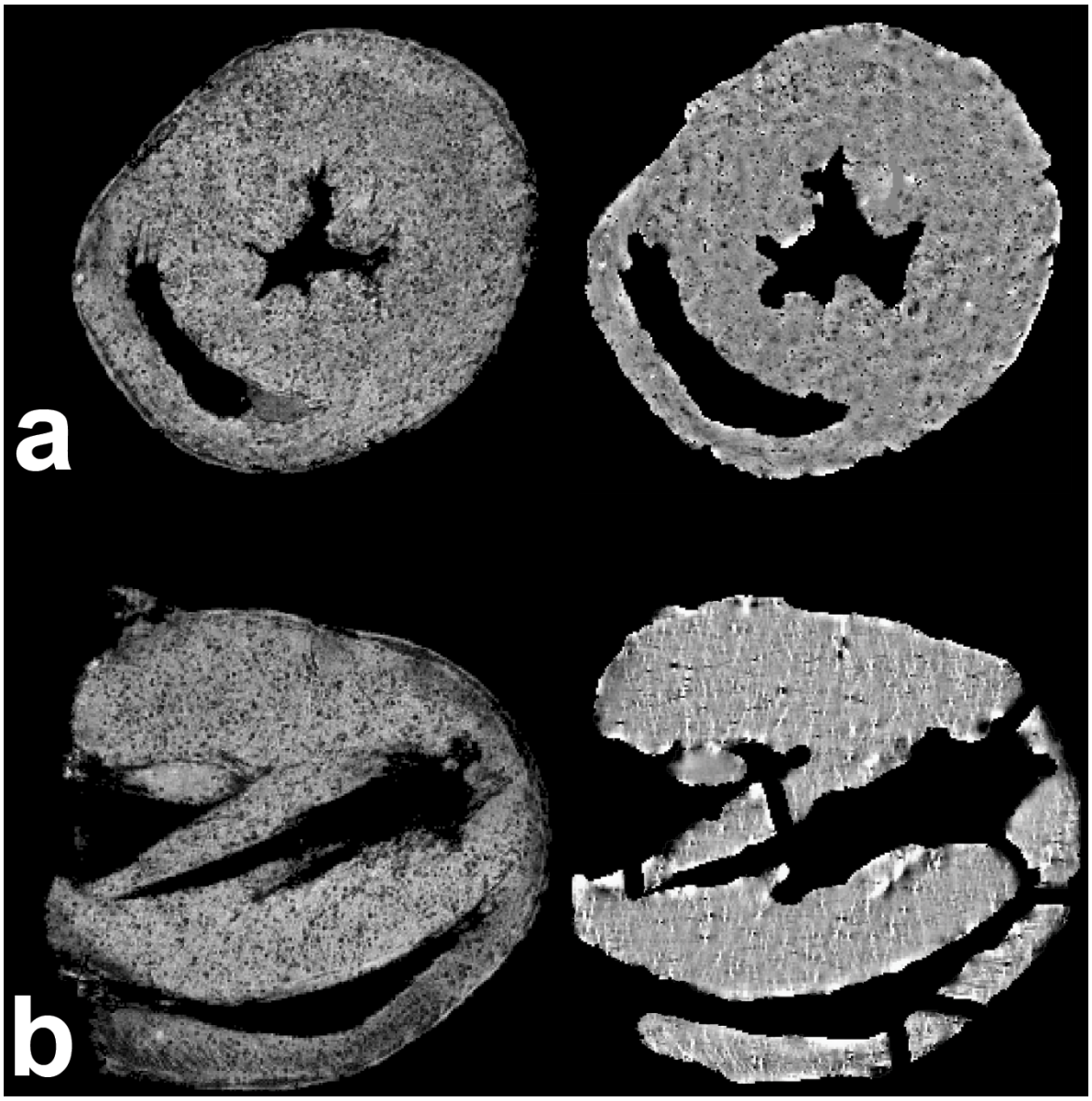

Figure 6.11: Magnitude images (left column) and phase offset images (right column) of the same heart allograft tissue sample when viewed from (a) a plane orthogonal to B_0 and (b) a plane parallel to B_0.
As predicted by Eq. (6.1), phase impressions matching the 2D dipole template are scattered throughout the slice parallel to B_0 (b), but are absent in the slice orthogonal to B_0 (a). *(Figure taken from Fig. 6 of Mills et al. [123])*

Figures 6.12a-b show allograft tissue with numerous macrophages infiltrating deep tissue as expected for this heart transplant model. Figure 6.12a shows putative macrophages labeled by 2D PDQ analysis (red dots) after analyzing a single 2D tissue section. Figure 6.12b shows the same slice after applying 3D PDQ analysis. A comparison between these 2D and 3D results indicate

that more dipoles are detected in the 3D analysis at the expense of only a few additional false positives. Thus, the additional redundancy provided by neighboring image slices improves the overall performance of the 3D PDQ method. As a control, the 3D PDQ method was applied to the heart isograft samples (Fig. 6.12c). As expected for this isogenic transplant, fewer dipoles are detected in tissue (Table 6.1). Histological assays of the transplanted tissues examining macrophage infiltration are qualitatively consistent with the results of the PDQ analysis for both the allograft and isograft tissues [19].

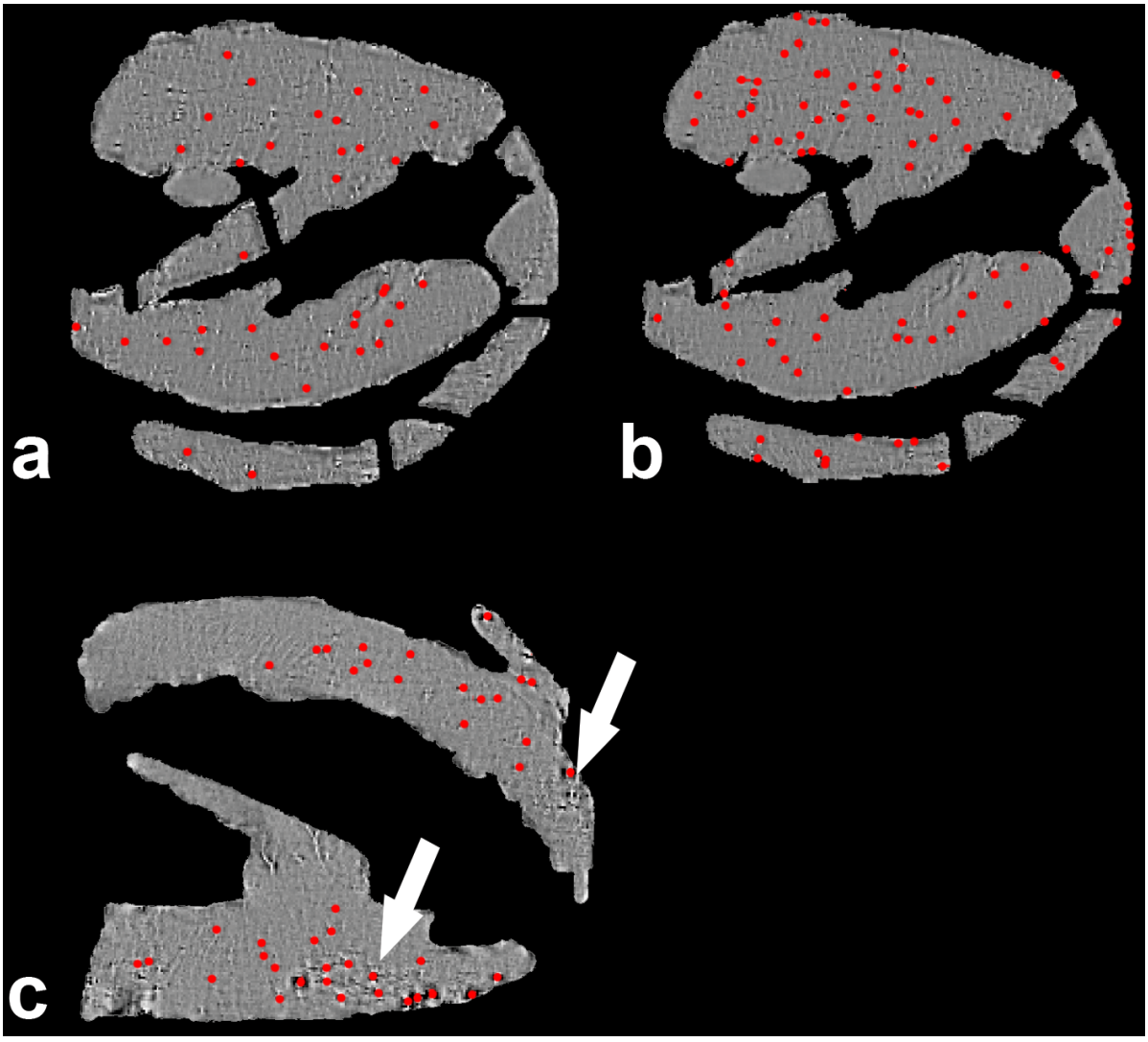

Figure 6.12: MPIO-labeled macrophages infiltrating heart tissue detected by (a) 2D and (b) 3D PDQ analysis on heart allograft tissue and (c) 3D PDQ analysis on heart isograft control.
Each red dot marks a dipole found. The white arrow shows an example of artifact highlighted by the PDQ method, which is presumed to be a blood vessel. Dipoles found in the allograft are dispersed throughout the myocardium, while the isograft control has a lower dipole density in tissue. *(Figure taken from Fig. 7 of Mills et al. [123])*

Unlike the dipoles detected in the gel phantom that appear mostly punctate after PDQ analysis (Fig. 6.13a), the 3D-rendered PDQ output for the entire allograft heart volume (Fig. 6.13c) often displays irregular and linear shapes, possibly indicating clusters of labeled macrophages, intra- or peri-vascular macrophage deposits, or perhaps residual blood in vessels.

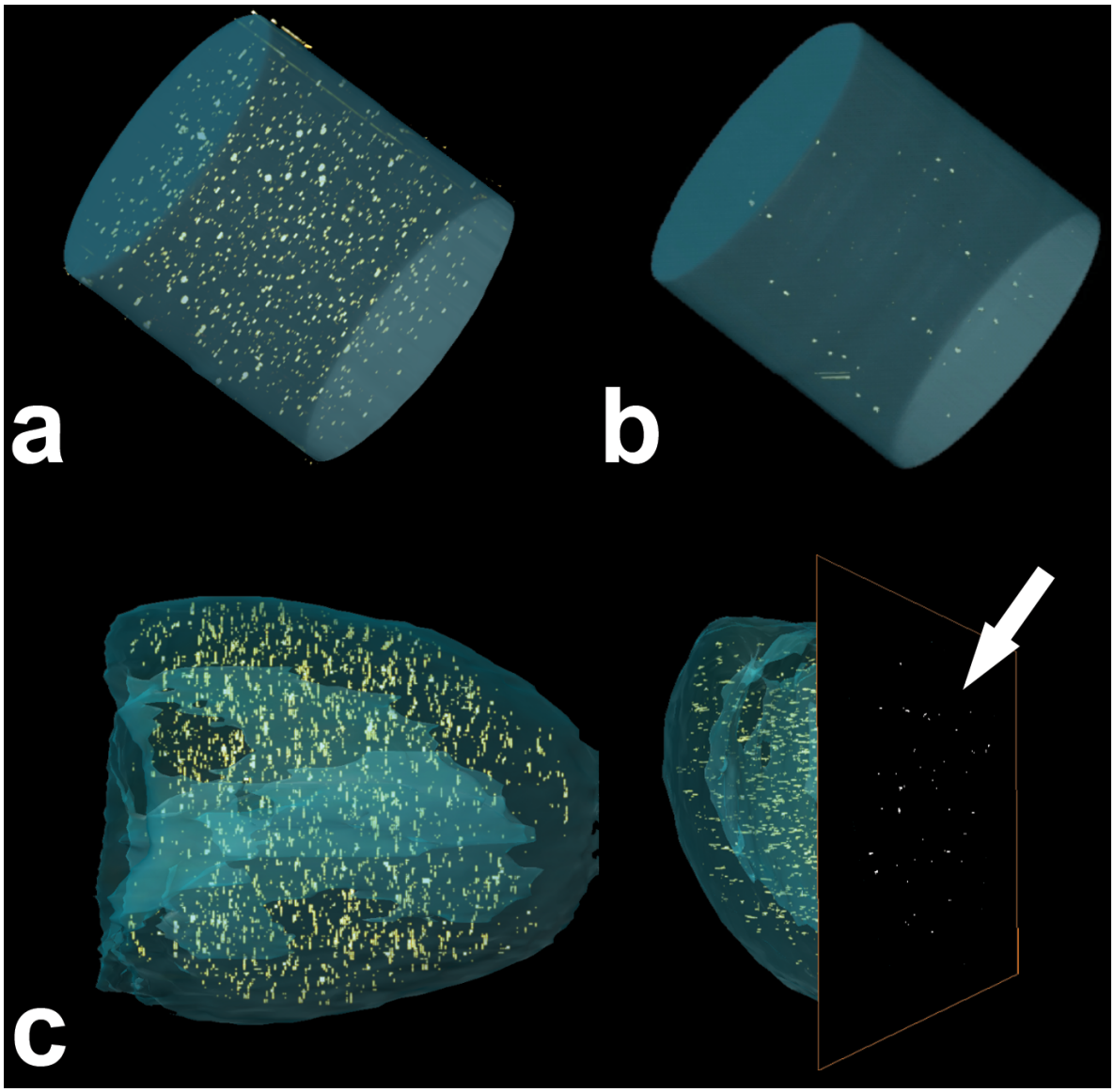

Figure 6.13: 3D renderings of PDQ-detected dipoles.
Shown is the gel phantom analyzed with (a) B_0-parallel slices and (b) B_0-orthogonal slices. Panel (c) shows the 3D PDQ analysis for the allograft rat heart infiltrated by MPIO-labeled macrophages. Gel and heart volumes are outlined in translucent blue, while dipoles are rendered as white spots. The arrow denotes dipoles found in a typical tissue slice. All dipole marks in the gel phantom appear spherical, but a fraction of marked areas in the heart tissue have linear shapes and may indicate curvilinear distributions of labeled macrophages or blood vessels with trajectory components parallel to B_0. *(Figure taken from Fig. 8 of Mills et al. [123])*

Table 6.1 shows the accuracy and sensitivity of the PDQ method, compared to visual inspection, when applied to the allograft and isograft heart tissue using representative sample sizes of 314 mm^3 and 288 mm^3 respectively. In the allograft heart, the dipole density, or the infiltration index, was calculated to be 7.36 dipoles/mm^3 (Table 6.1) and may represent the magnitude of macrophage infiltration in the heart tissue at this post-operational stage. A fraction of the dipoles counted are expected to be false positives (∼15%, see Methods). However, we note that since continuous regions in the PDQ output, such as due to blood vessels or edge artifact, will only be counted as a single dipole, thus these artifacts represent a small contribution to the total dipole count.

6.4.4 Magnetocapsules in Agarose Gel Phantoms

Figure 6.14a shows a magnitude and phase image of an agarose phantom containing a uniform distribution of magnetocapsules. Table 6.2 lists the PDQ calculated magnetic measurements derived from this data. Note that the 2.5% magnetocapsules are diamagnetic overall, due to their low SPIO content. Figure 6.15 shows a plot of the anhydrous magnetic moment ($\overrightarrow{m}_{an}$) calculated from Eqs. (6.6) and (6.6) versus template similarity for ∼2,000, 10% v/v Feridex magnetocapsules. Notably, the measured magnetic moment of the magnetocapsule is correlated to its template similarity (TS) value. Figure 6.16 shows estimated magnetic moments for ∼4,000 magnetocapsules with a TS ≥70%. Across all magnetocapsules, iron content estimated using Eq. (6.8) ranged from 15-125 ng. These iron estimates assume a saturation magnetization for Feridex of 68 emu/g [Fe] [134, 135].

SPIO Deposit Type	χ_B ($\times 10^{-6}$)	Number of Deposits	Sample Size	B_0 (T)	Deposit Radius (μm)	χ_A ($\times 10^{-6}$)	$\vec{m}_A$ (pA·m^2)	χ_{an} ($\times 10^{-6}$)	$\vec{m}_{an}$ (pA·m^2)
Isolated 10 μm diameter SPIO	−9.05	n=2192	2 Gels	11.7	5.0 ± 5	180 ± 70	0.9 ± 0.3	—	—
Rat macrophage in heart tissue	−9.05	n=7617	27 Hearts	11.7	9.5 ± 2	26 ± 13	0.9 ± 0.6	35 ± 13	1.2 ± 0.6
Mouse macrophage in CNS (*ex vivo*)	−9.05	n=1577	27 Brains	11.7	7.5 ± 2	54 ± 33	0.9 ± 0.6	63 ± 33	1.0 ± 0.6
Mouse macrophage in CNS (*in vivo*)	−9.05	n=60	12 Brains	7.0	7.5 ± 2	82 ± 19	1.4 ± 0.3	91 ± 19	1.4 ± 0.3
2.5% v/v Feridex magnetocapsule in agarose	−9.05	n=430	3 Gels	4.7	286 ± 11	-5 ± 2	-1700 ± 300	5 ± 2	1600 ± 300
5.0% v/v Feridex magnetocapsule in agarose	−9.05	n=1127	5 Gels	4.7	271 ± 32	3 ± 1	900 ± 400	12 ± 1	3700 ± 400
10% v/v Feridex magnetocapsule in agarose	−9.05	n=923	4 Gels	4.7	298 ± 19	8 ± 1	3300 ± 400	17 ± 1	7100 ± 400
Feridex magnetocapsule in porcine liver	−8.80	n=665	1 Lobe	4.7	247 ± 20	-2 ± 1	-600 ± 300	6 ± 1	1500 ± 300
10% v/v Feridex magnetocapsule (SQUID, Desiccated, 310K)	——	n=300	——	4.7	——	——	——	——	8100 ± 200

Table 6.2: PDQ-estimated magnetic moment and susceptibility for different types of SPIO deposit.
All values are measured at sufficiently high B_0 to ensure SPIO magnetic saturation. Dipoles with TS $\geq$ 70% were used for magnetic property estimates. *(Table taken from Table 1 of Mills et al. In Press within Magnetic Resonance in Medicine.)*

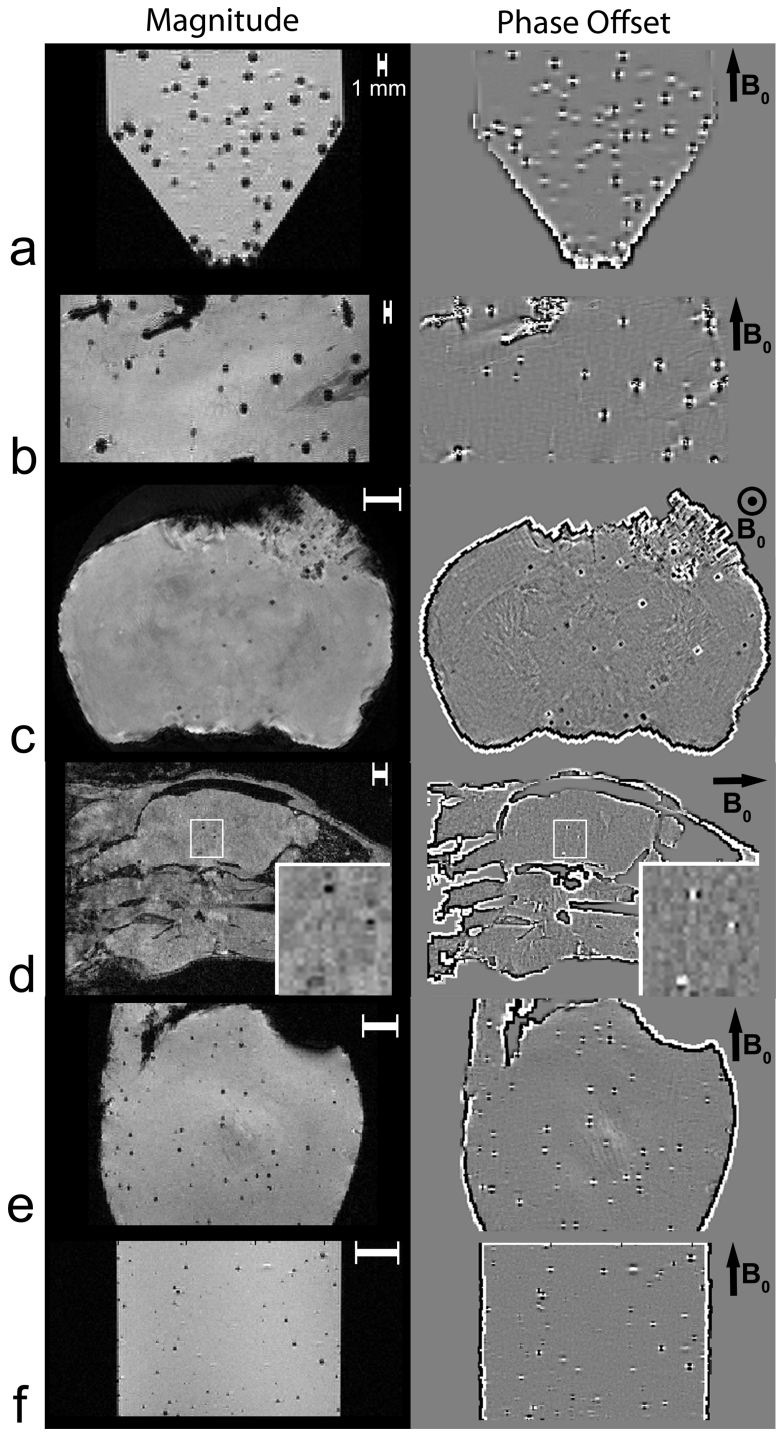

Figure 6.14: Magnitude and corresponding phase images of datasets analyzed by PDQ.
Shown are 10% Feridex v/v magnetocapsules in (a) agarose gel and (b) porcine liver; MPIO-labeled macrophages in mouse brain after TBI imaged (c) *ex vivo* (axial view) and (d) *in vivo* (para-sagittal view); (e) MPIO-labeled macrophages in rat cardiac tissue undergoing chronic rejection. In the phase image for each sample, many characteristic dipole shapes are present, each corresponding to a hypointense spot in the conventional magnitude images. PDQ counts instances of these dipole patterns, estimating their susceptibility and magnetic moment. *(Figure taken from Fig. 2 of Mills et al. In Press within Magnetic Resonance in Medicine.)*

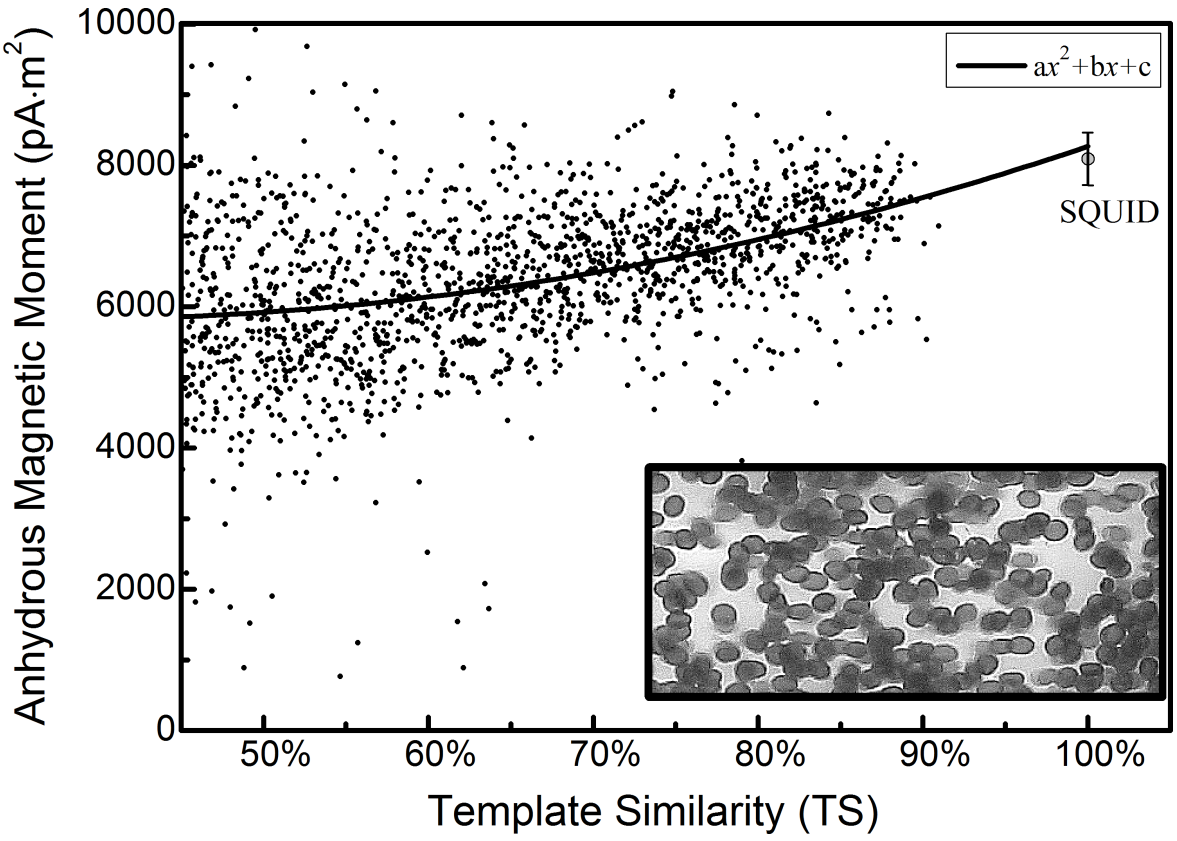

Figure 6.15: PDQ-measured anhydrous magnetic moment ($\overrightarrow{m}_{an}$) versus template similarity (TS) for ∼2000, 10% Feridex v/v magnetocapsules in agarose gel.
Magnetocapsules with greater TS values more closely match the theoretical phase impression for a magnetic dipole. The non-linear correlation between TS and magnetic moment is presumed to be related to magnetocapsule deviation from sphericity and long-axis orientation relative to B_0 (see inlay). The black line is a best-fit polynomial projection of this correlation. At TS=100%, the projection predicts a anhydrous magnetic moment of 8,300 pA·m^2 per magnetocapsule which is in reasonable agreement with the SQUID-measured dehydrated value of 8,100 ± 200 pA·m^2. At TS=50%, PDQ measures a mean magnetic moment of 5,900 ± 200 pA·m^2, which is 27% below the SQUID-measured value, suggesting that TS thresholding should generally be employed. *(Figure taken from Fig. 3 of Mills et al. In Press within Magnetic Resonance in Medicine.)*

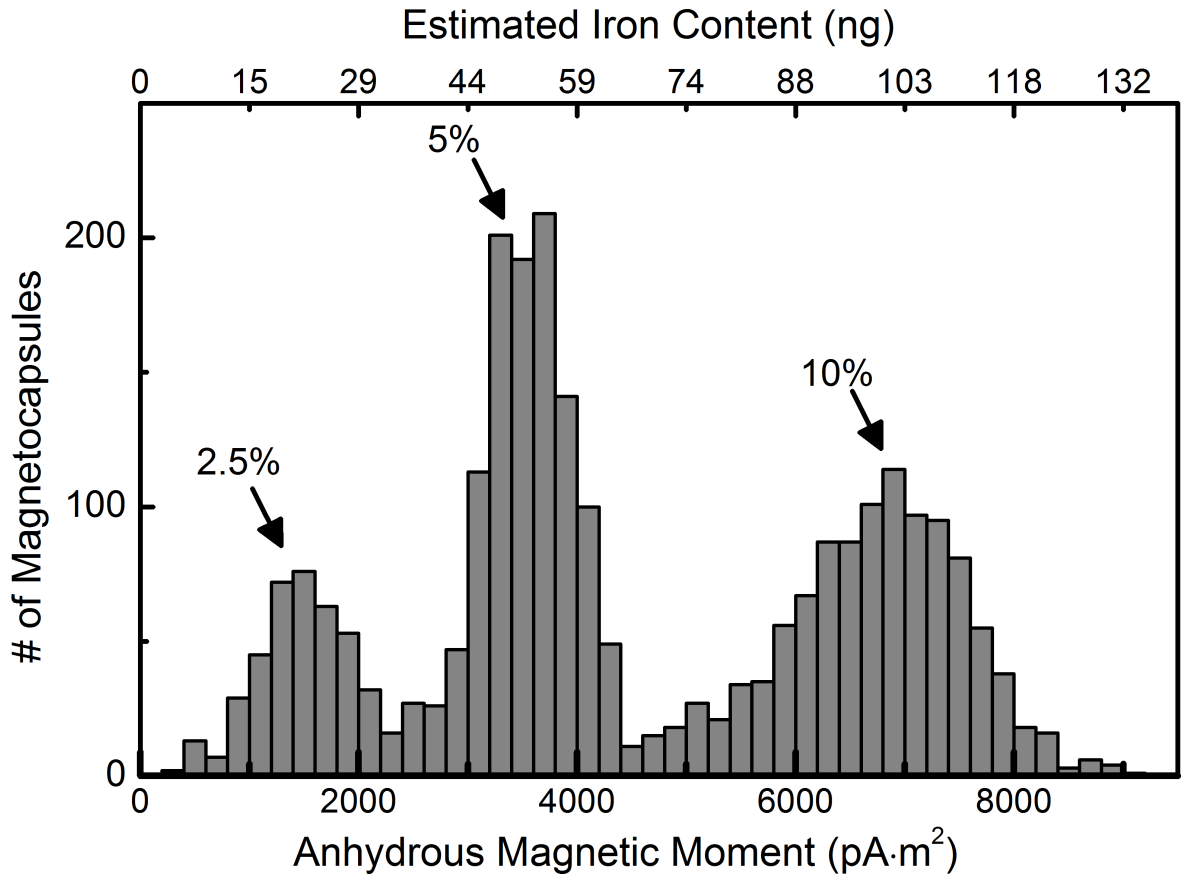

Figure 6.16: Distribution of magnetic moment results from all gel phantoms (n=12) containing magnetocapsules.
Plot shows the detection of ~4,000 magnetocapsules with a TS $\geq$ 70%. The magnetocapsules were suspended in 12 separate agarose gel phantoms imaged containing 2.5% (n=3), 5% (n=5), and 10% (n=4) v/v Feridex. The average magnetic moment values for these capsules are recorded in Table 6.2 and is strongly correlated with Feridex concentration. Estimated iron content (top axis) is calculated assuming a saturation magnetization for Feridex of 68 emu/g [Fe]. *(Figure taken from Fig. 4 of Mills et al. In Press within Magnetic Resonance in Medicine.)*

The PDQ-derived magnetocapsule magnetic moment was compared to values obtained from direct SQUID magnetometry measurements. Figure 6.17 shows the mean magnetic moment for 300 magnetocapsules as a function of applied magnetic field. As expected, above 3 T the magnetite in the magnetocapsules shows saturation. The mean magnetic moment, 8,100 $\pm$ 200 pA·m^2, was used to estimate the saturation magnetization of Feridex in units emu/g [Fe]; we substituted this value into Eq. (6.8) along with the Feridex iron concentration (11.2 mg [Fe]/ml) and the magnetocapsule radius (298 μm). The result gives a saturation magnetization of 65 $\pm$ 13 emu/g [Fe], in agreement with published magnetite magnetization values between 68-130 emu/g [Fe] [134, 135]. From PDQ, the magnetocapsule anhydrous magnetic moment was calculated to be 8,300 pA·m2 when the TS

value is extrapolated to 100%, which agrees with the SQUID-measured value (8,100 ± 200 pA·m2). At TS=50%, PDQ appears to underestimate the magnetic moment by 27% of the SQUID-measured value, whereas for TS ≥ 70%, PDQ underestimates the value by only 15%. We note that no similar accuracy trend with decreasing TS was found for sub-voxel-sized SPIO deposits in labeled cells (below), possibly implying that the magnetic moment underestimates are due to aspherical variations in magnetocapsule shape and partial magnetocapsule alignment along B_0 (see Fig. 6.15, inlay).

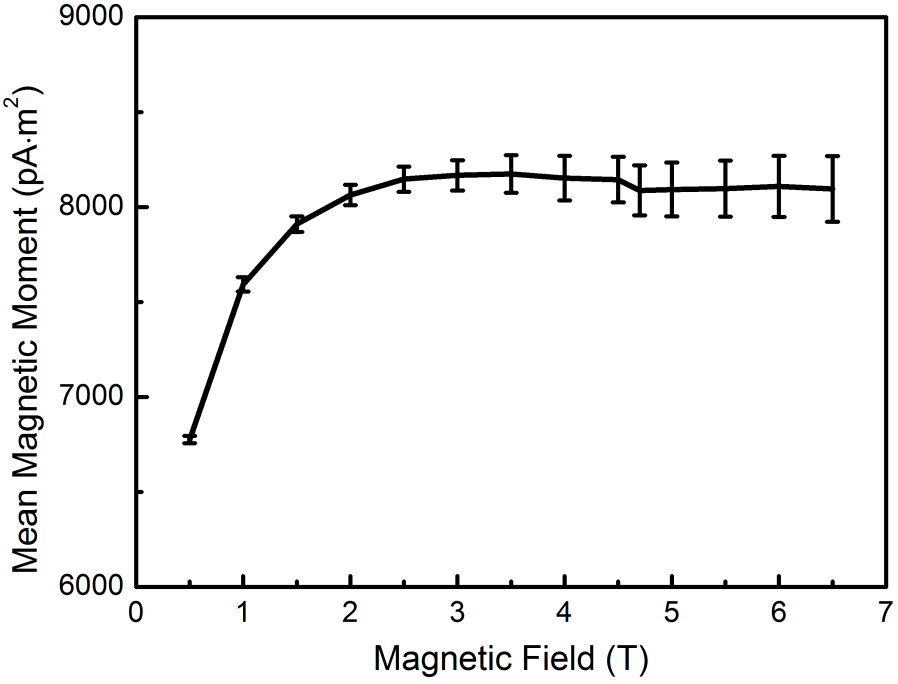

Figure 6.17: SQUID-based magnetic moment measurements for desiccated 10% v/v Feridex magnetocapsules.
The mean magnetic moment for 300 magnetocapsules is plotted as a function of the applied magnetic field. As expected, the magnetic moment of the magnetocapsules saturates above 3 T, yielding a value of 8,100 ± 200 pA·m^2 per magnetocapsule. All data were acquired at 310 K. Error bars represent contributions from both the standard deviation for measured samples (n=3) and the uncertainty introduced by diamagnetic correction. *(Figure taken from Fig. 5 of Mills et al. In Press within Magnetic Resonance in Medicine.)*

The PDQ magnetic measurement accuracy in low-SNR images was also tested using the 10% v/v Feridex magnetocapsule phantom. Table 6.3 lists the results of this test. For SNR > 11, magnetic susceptibility and moment measurements were stable and equivalent to the reference scan (SNR = 30). Magnetic measurements remain largely independent of noise levels since sampling 343 voxels surrounding each dipole deemphasizes noise error contributions. For SNR < 4.5, magnetic

measurements were erroneous (Table 6.3), even when averaged over 200-600 magnetocapsules. Also, the fraction of magnetocapsules detected decreased as SNR decreased, with 71% detected for SNR = 4.5 and 25% detected for SNR = 2.5. Previously, PDQ detection accuracy was analyzed for low-SNR 2-dimensional images and exhibited accuracy comparable to that found in this 3-dimensional analysis [123].

6.4.5 Magnetocapsules in Porcine Liver

PDQ was used to detect and analyze 10% v/v Feridex magnetocapsules implanted *in vivo* in the porcine liver via intraportal infusion. A portion of the resected liver was imaged, and PDQ detected ∼700 isolated magnetocapsules in a 58 cm^3 sample (12 isolated capsules/cm^3). Figure 2b shows representative magnitude and phase images of the liver lobe. We observed that numerous magnetocapsules clustered within the liver blood vessels with a curvilinear distribution. PDQ assigned low TS values to these strings of magnetocapsules, often excluding them from magnetic measurement, since the magnetic impression due to abutting magnetocapsules is dissimilar to that for an isolated sphere of SPIO. Histological analyses of similar porcine livers with portal vein injections of large numbers of magnetocapsules showed qualitatively similar results [124].

6.4.6 MPIO-Labeled Macrophages in Murine Traumatic Brain Injury Model

PDQ was used to analyze mouse brains (n=27) following TBI to detect MPIO in inflammation-associated macrophages that infiltrated lesioned areas. Macrophages migrate and accumulate both near the site of injury and elsewhere in the brain following TBI, and recruit other immune cells. Prior work in the same model [125] showed that the F4/80+ macrophages contain a variable number of 0.9 μm-diameter MPIO particles [125]. Figure 6.18 shows fluorescence microscopy of murine macrophages colocalized with these MPIO particles within the dorsal hippocampus following TBI. Control TBI mice with no injected MPIO had no dipole patterns present in MR images of their brain volume. Figures 6.14c-d show *ex vivo* and *in vivo* magnitude and phase images of mouse brains, and Table 6.2 lists the magnetic measurement results.

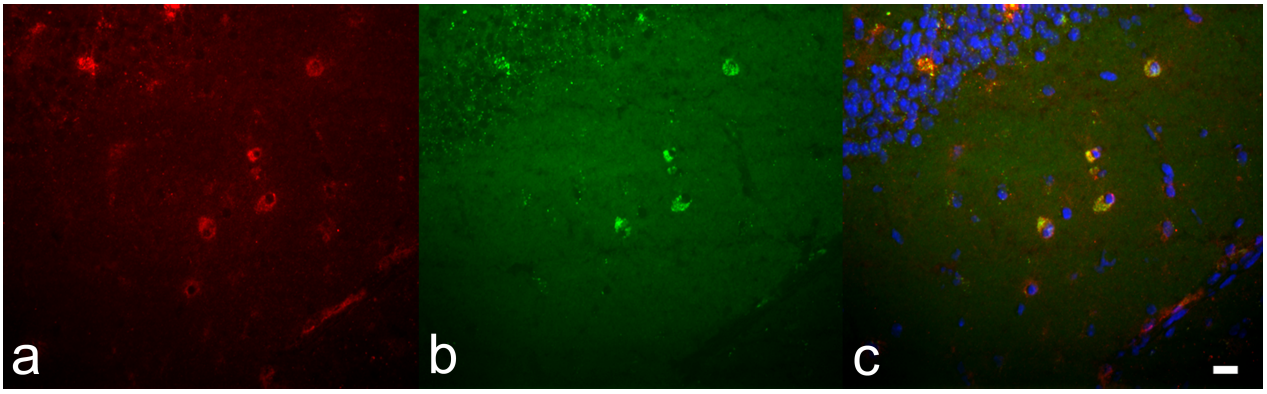

Figure 6.18: Fluorescence microscopy of mouse dorsal hippocampus beneath TBI contusion site. Image was taken following *in situ* macrophage labeling with 0.9 μm-diameter MPIO.
Shown are (a) labeling of murine macrophages with F4/80 antibody (red), (b) individual MPIO particles (Dragon Green), and (C) triple-labeling by overlaying DAPI nuclear stain (blue). In this field of view, most F4/80+ cells colocalize with many MPIO particles (10+), indicating that MPIO particles accumulate within these macrophages. Some F4/80+ cells contain few or no MPIO particles. Scale bar represents 40 μm. (Image courtesy of Lesley Foley and T. Kevin Hitchens; Published as Figure 6 in *Journal of Neurotrauma* 2009, 26:1509-1519).

Figure 6.19 shows the estimated magnetic moment for all macrophages detected in brains scanned *ex vivo*. Magnetic moments ranged from 0.2–2.7 pA·m^2, corresponding to an estimated iron content of 3–38 pg, assuming MPIO particles have a saturation magnetization of 68 emu/g [Fe] [134, 135]. This range of iron content is comparable to published values of *ex vivo* labeled macrophage, where rat or human macrophages incubated in media containing 0.9 μm or 1.6 μm-diameter MPIO internalize between 27–39 pg of iron [20, 78]. The wide distribution of magnetic moments shown in Figure 6.19 for these MPIO-labeled cells is presumably due to different numbers of internalized MPIO particles. Iron content can be used to estimate the number of MPIO particles within these cells, since each 0.9 μm-diameter MPIO particle contains on average $\sim$0.47 pg [Fe] (62% magnetite w/w). This implies that PDQ detected macrophages labeled with as few as $\sim$6 MPIO particles and as many as $\sim$76 MPIO particles. Also, there appears to be an inverse relationship between magnetic moment and the number of macrophages. Macrophages containing no or only a few particles have weak magnetic moments ($<$0.2 pA·m^2) and were not detected by the PDQ analysis.

Figure 6.20 shows the estimated magnetic moment for all macrophages detected in brains scanned *in vivo*. Magnetic moments ranged between 0.4–2.6 pA·m^2 per cell, corresponding to an estimated iron content of 5–38 pg or 10–76 MPIO particles under the same assumptions listed

above for the set of *ex vivo* brain scans. Fewer dipoles are detected *in vivo* due to reduced scan time, SNR, and resolution. Across all brain scans analyzed, only ~33% of dipoles are detected *in vivo* compared to *ex vivo* scans. Also, Fig. 6.20 shows that dipoles with magnetic moments below ~ 0.5 pA·m^2 were often too weak relative to image noise levels to be detected by PDQ *in vivo*. Therefore, although *ex vivo* scans show the number of dipoles increase as magnetic moment decreases below 0.5 pA·m^2, the opposite happens *in vivo* in this range – the number of dipoles detected decreases as magnetic moments decrease below 0.5 pA·m^2. This effect causes the average magnetic moment detected *in vivo* to be higher than that detected in the more-sensitive *ex vivo* scenario.

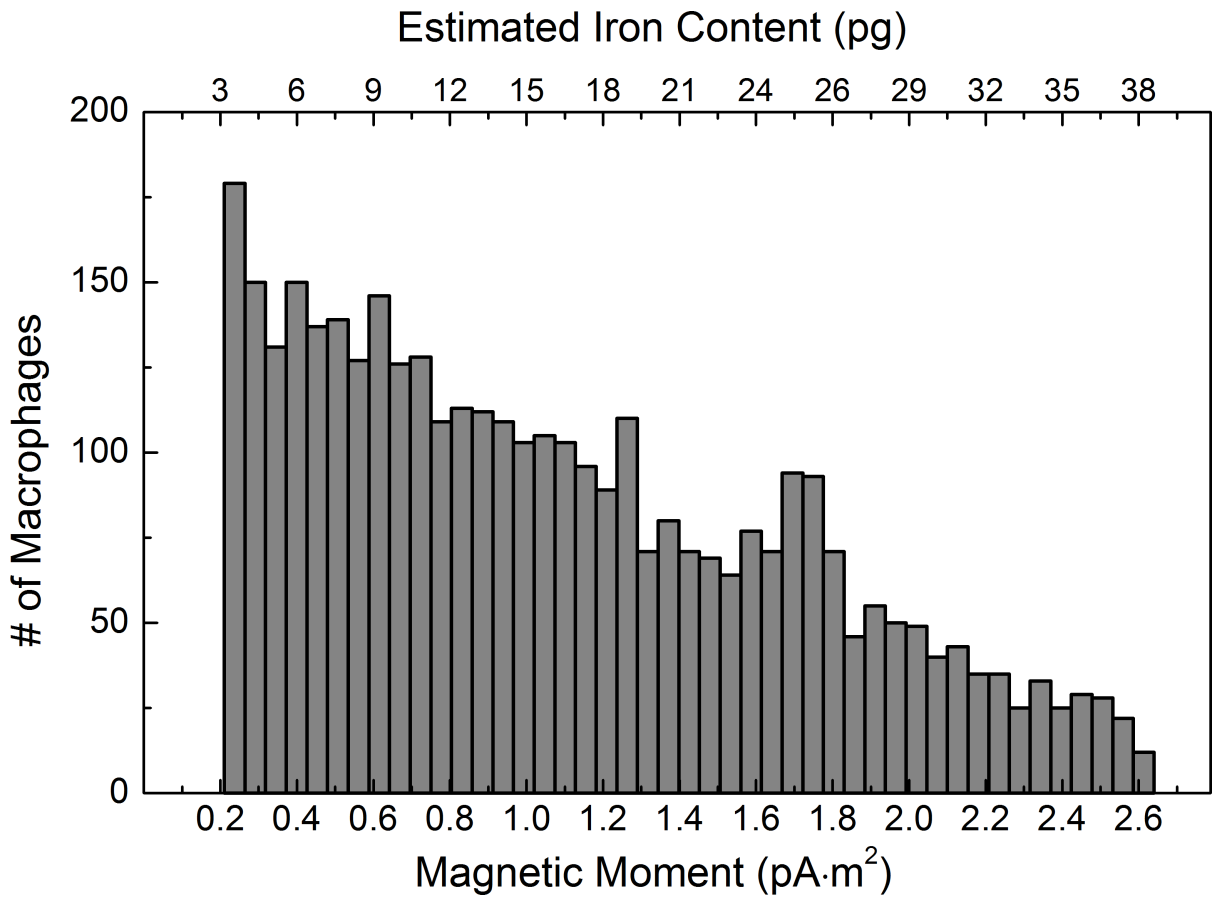

Figure 6.19: PDQ measured magnetic moment distribution for MPIO-labeled macrophages in mouse brain imaged *ex vivo* following TBI.
Shown are composite results from 27 brain samples imaged *ex vivo* and represent ~3,000 total macrophages. Magnetic moments ranged between 0.2-2.7 pA·m^2 per cell, corresponding to an estimated iron content of 3–38 pg (top axis) or 6–76 MPIO particles. The number of macrophages detected decreases linearly with increasing magnetic moment, suggesting that macrophages are more likely to internalize fewer MPIO particles. Dipoles below 0.2 pA·m^2 were too weak relative to image noise levels to be detected by PDQ. Dipoles shown have a TS > 40%. *(Figure taken from Fig. 6 of Mills et al. In Press within Magnetic Resonance in Medicine.)*

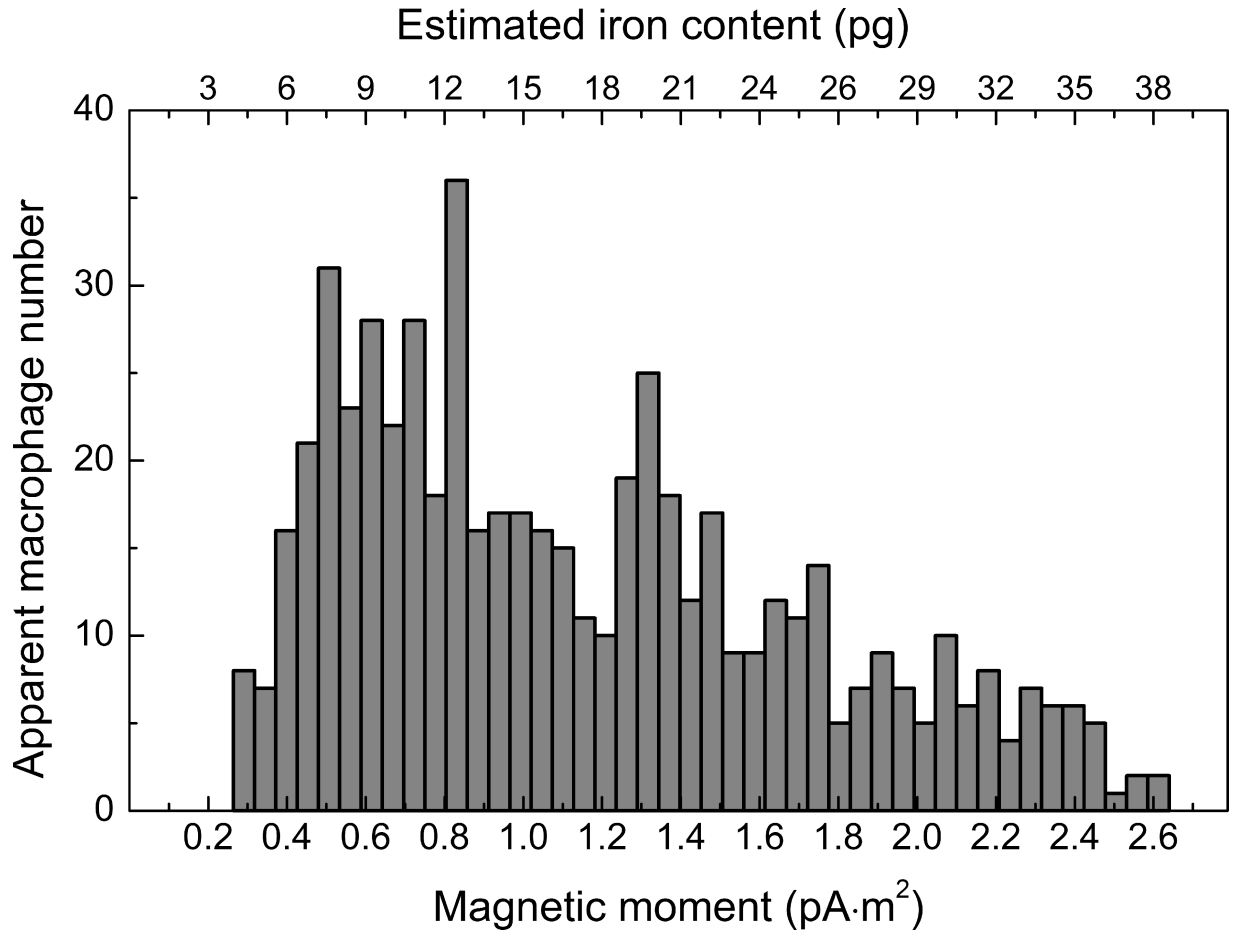

Figure 6.20: PDQ measured magnetic moment distribution for MPIO-labeled macrophages in mouse brain imaged *in vivo* following TBI.
Shown are composite results from 19 brain samples imaged *in vivo* and represent ∼600 total macrophages. Magnetic moments ranged between 0.4-2.6 pA·m^2 per cell, corresponding to an estimated iron content of 5–38 pg (top axis) or 10–76 MPIO particles. The number of macrophages detected decreases linearly with increasing magnetic moment, suggesting that macrophages are more likely to internalize fewer MPIO particles. Dipoles below 0.3 pA·m^2 were too weak relative to image noise levels to be detected by PDQ. Compared to *ex vivo* scans, fewer dipoles overall were detected per mouse brain sample, and dipoles below 0.5 pA·m^2 were more likely to go undetected by PDQ, thereby increasing the average measured magnetic moment. Dipoles shown have a TS > 40%.

PDQ was also able to detect and measure magnetic moments of MPIO-labeled macrophages *in vivo* in the TBI model. Comparing the same cohort of brains scanned *in vivo* and *ex vivo* (i.e., fixed), approximately 75% of labeled macrophages were detected *in vivo*. The *in vivo* scans were acquired with lower resolution and SNR than in the excised brains. *In vivo*, macrophages with low magnetic moments went undetected, and thus the average magnetic moment measured *in vivo* was greater than *ex vivo* (Table 6.2). When *in vivo* isotropic resolution was reduced further, from 63 μm to 100 μm, only 25% of labeled cells were detected, relative to *ex vivo*. Figure 6.21 shows

co-registrated images of a comparable slice acquired *in vivo* (Fig. 6.21a) and *ex vivo* (Fig. 6.21b); the slice contains two prominent MPIO clusters, presumed to be concentrated within macrophages or macrophage clusters. *In vivo*, the measured magnetic moments of these deposits where 1.1 and 1.2 pA·m^2 (top to bottom, respectively), while *ex vivo* PDQ measured 0.7 and 1.0 pA·m^2 for the same deposits. We note that this small discrepancy may be due to different background tissue susceptibilities between the live and fixed tissues. Figure 6.21c shows a second mouse brain imaged 24 and 96 hours following MPIO injection. Both images show a cell or cell cluster in the same anatomical location, with a magnetic moment of 2.5 and 2.4 pA·m^2 at 24 and 96 hours, respectively.

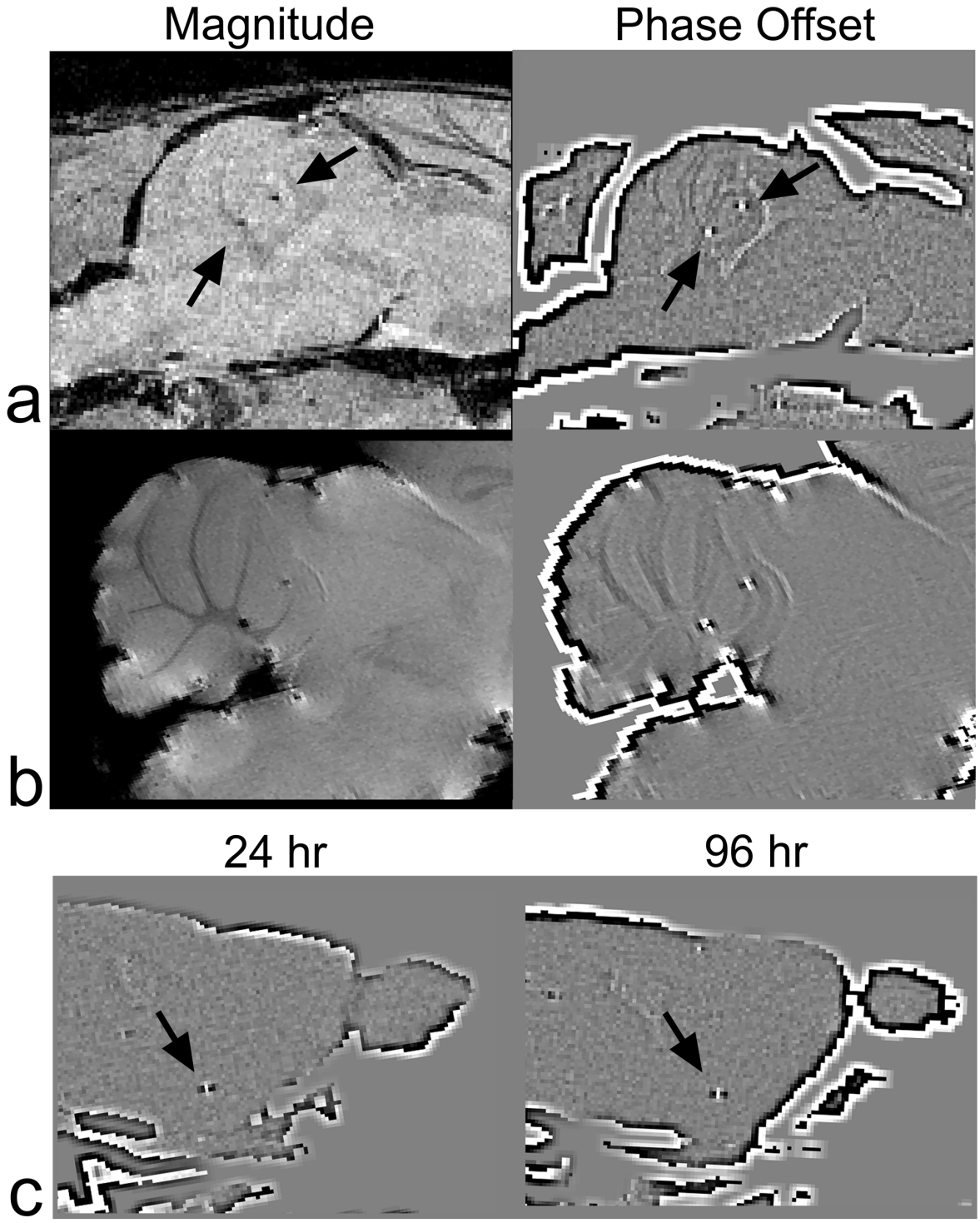

Figure 6.21: *In vivo* studies of MPIO-labeled macrophages infiltrating mouse brains following TBI. Registration was performed between (a) *in vivo* and (b) *ex vivo* magnitude and phase images of the same slice. Black arrows indicate two prominent MPIO clusters that may be concentrated within macrophages and/or macrophage clusters. *In vivo*, PDQ measured the two clusters to have magnetic moments (top to bottom) of 1.1 and 1.2 pA·m^2. *Ex vivo*, PDQ measured the same deposits as having magnetic moments of 0.7 and 1.0 pA·m^2, respectively. A second *in vivo* mouse brain, (c), demonstrates serial detection of the same clusters between scans performed 24 and 96 hours following TBI. In addition to being in the same anatomical location, the dipole had a similar measured magnetic moment of 2.5 and 2.4 pA·m^2 after 24 and 96 hours, respectively. *(Figure taken from Fig. 7 of Mills et al. In Press within Magnetic Resonance in Medicine.)*

6.4.7 MPIO-Labeled Macrophages in Rat Heart Chronic Rejection Model

PDQ investigated MPIO-labeled macrophages infiltrating cardiac tissue in a heterotopic working heart transplant model of chronic cardiac rejection. Macrophages are observed to migrate and accumulate in regions of solid organ rejection, often performing secretory and phagocytic functions [4, 20, 19]. In this experiment, macrophages were labeled in situ with 0.9 μm-diameter MPIO following i.v. injection. Figure 6.14e shows magnitude and phase images of macrophage-infiltrated heart tissue, where the corresponding magnetic measurements from PDQ are listed in Table 6.2. The mean (n=27) magnetic moment of MPIO-labeled macrophages in heart tissue was approximately equal to that measured for macrophages in mouse brains following TBI (see above). Both models label macrophages through i.v. injection of 0.9 μm-diameter MPIO.

SNR (A/σ_N)	Acquisition Time	Dipoles Detected	χ_A ($\times 10^{-6}$)	Magnetic Moment (pA·m^2)
30	18 min	829 (100%)	8 ± 4	3300 ± 600
18	5 min	769 (93%)	8 ± 4	3200 ± 800
14	1 min	706 (85%)	8 ± 4	3200 ± 900
11	18 s	638 (77%)	7 ± 4	2900 ± 700
4.5	Simulated	591 (71%)	4 ± 4	1400 ± 400
2.5	Simulated	224 (27%)	N/A	N/A

Table 6.3: Effect of noise on magnetic measurement estimates for 10% Feridex v/v magnetocapsules in agarose phantom.
Estimates remain stable when SNR > 11, since sampling 343 voxels surrounding each dipole deemphasizes noise error contributions. *(Table taken from Table 2 of Mills et al. In Press within Magnetic Resonance in Medicine.)*

6.4.8 10 μm-diameter SPIO Particles in Agarose Gel

A 2% w/v agarose gel phantom was doped with a high density of large SPIO particles, in order to challenge the PDQ algorithm with a high spatial density of dipole impressions. PDQ detected 2,192 dipole patterns from individual SPIO particles suspended within two agarose gel phantoms. SPIO particles were reported by the manufacturer to have an average diameter of 10 μm. Actual particle size was not measured, as the phantom was used primarily to challenge the PDQ method algorithms with an extremely high density of dipole impressions. A phase and magnitude image of a phantom is shown in Figure 6.14f. A few large artifacts were observed in each gel phantom, most likely due to contamination by a foreign particle or an air bubble. Artifacts were excluded from the aggregate estimated magnetic moment measurement of 0.9 ± 0.3 pA·m^2. Additional magnetic measurements

are in Table 6.2. Interestingly, this value is comparable to the average magnetic moment values found for MPIO-labeled macrophages in mouse brain and rat heart tissues. In those two models, macrophages were estimated to endocytose 10–76 MPIO particles with a diameter of 0.9-μm. These estimates suggest that each 10-μm diameter particle has a similar magnetic moment to cells labeled with 10–76 of the smaller 0.9 μm diameter MPIO particles. Because the size of these large SPIO particles varies considerably (Fig. 6.4), and was not measured independently, a full comparison between PDQ-measured magnetic moments for these two types of iron-oxide particle cannot easily be made.

6.4.9 Dipole Density versus Distance from Injury in Murine TBI Model

The distribution of SPIO-labeled cells in a tissue volume may be a biomarker for different disease conditions. PDQ plotted the dipole density versus distance from the site of injury in a mouse brain infiltrated by MPIO-labeled macrophages as a result of a controlled cortical impact traumatic brain injury (TBI). Figure 6.22 shows the number of dipoles versus distance from the traumatic brain injury ROI. When normalized for the geometry of the brain, no correlation was found between number of dipoles and distance from the TBI ROI. However, PDQ may be underestimating dipole number in the area directly around the injury site, due to confounding paramagnetic disturbances due to the presence of blood and disrupted tissue interfaces. Outside the injury region, this result implies that labeled cells are distributed evenly across the brain. Across multiple brain samples, however, a correlation may become apparent.

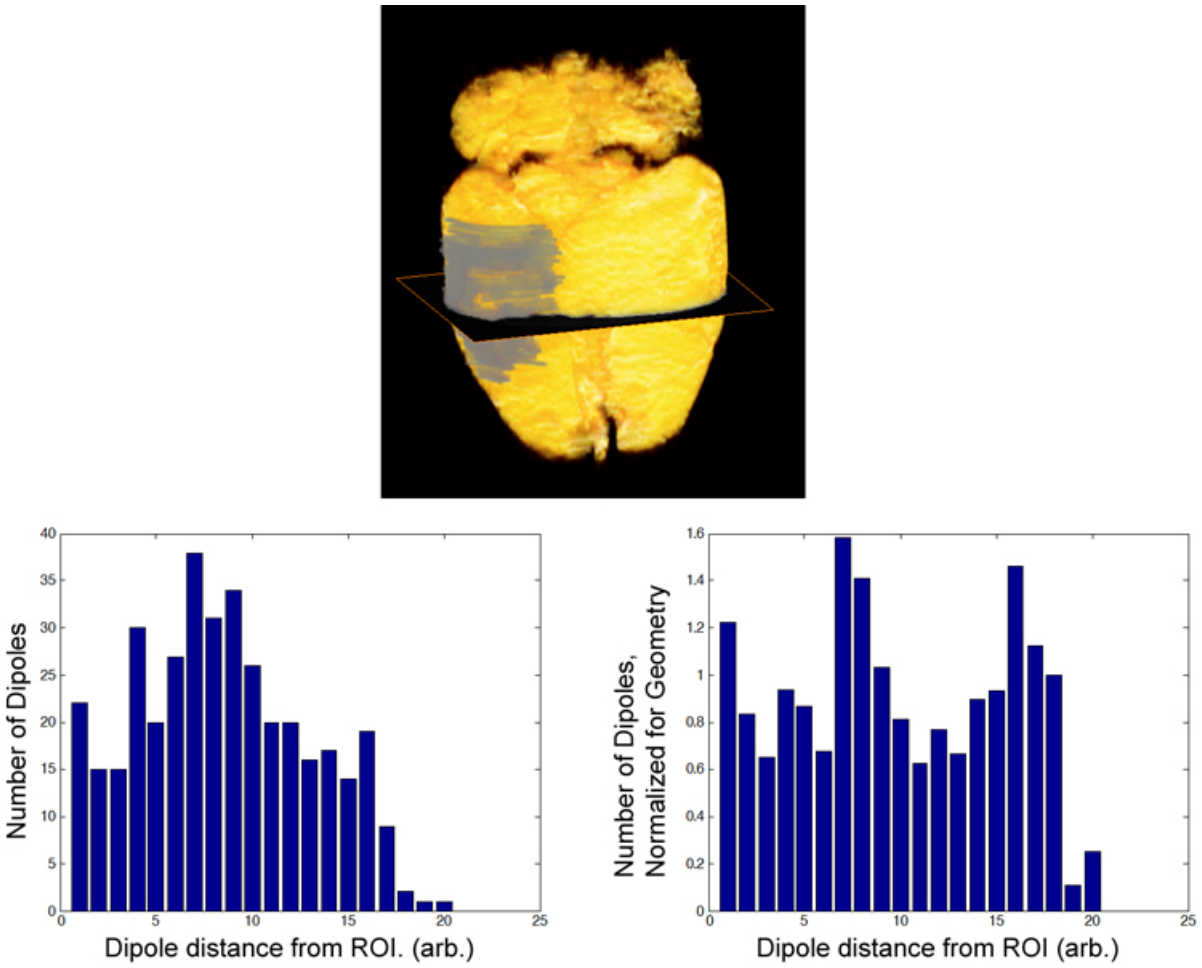

Figure 6.22: Number of Dipoles versus Distance from site of Traumatic Brain Injury in one mouse brain.
The top panel shows a 3D rendering of the mouse brain in yellow, with the brain injury ROI in gray. The left plot shows the number of dipoles present in mouse brain tissue as a function of distance from the TBI ROI. The right plot displays the same data, but with dipole numbers normalized to the amount of tissue present at each distance from the ROI. Each dipole represents a likely MPIO-labeled macrophage infiltrating the brain tissue. When normalized for the geometry of the brain tissue, no correlation was found between number of dipoles and distance from the TBI ROI. However, in the area directly surrounding and within the TBI region, dipole counts may be underestimated due to confounding distributions of paramagnetic blood and disrupted tissue interfaces.

6.4.10 Comparison between PDQ and ImageJ Dark Spot Counting in Murine TBI model

MPIO-labeled macrophages were counted using ImageJ software in 15 different *ex vivo* mouse brains following TBI. Each heart was searched for hypointense spots of a user-defined radius. PDQ was applied to the same samples and both methods analyzed the entire 3D heart volume (100% coverage). Figure 6.23 shows the results of this comparison between PDQ and ImageJ methods. For

all sample types, the number of dipoles detected by PDQ strongly correlated with the number found using ImageJ. PDQ counted significantly fewer dipoles than ImageJ across all sample types (Fig. 6.23). Because PDQ counts only dipoles that have a template similarity (TS) value of TS>45%, the method provides total counts that are $\sim 30\%$ the magnitude that ImageJ counts. On the other hand, we hypothesize that the dark-spot search performed by ImageJ is more likely than PDQ to have some false-positive counts, due to other intrinsic sources of hypointense spots. The ImageJ dark-spot counting method does not distinguish between spots due to MPIO or other sources of tissue contrast (e.g., blood vessels), while the PDQ dipole search excludes any objects that create a phase image impression that is $\leq 45\%$ similar to the theoretical impression for a perfect sphere of SPIO.

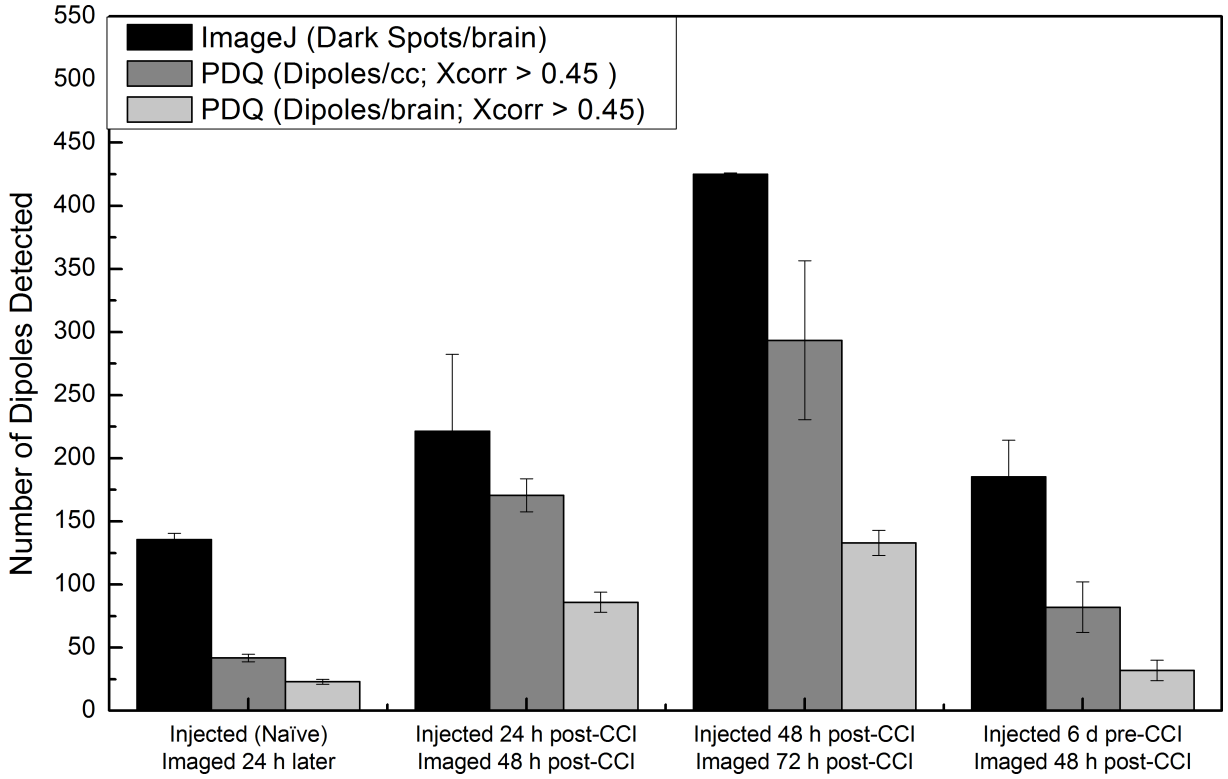

Figure 6.23: Dipoles counted by PDQ and ImageJ methods for different classes of macrophage-infiltrated mouse brain sample from TBI model experiments.
Four classes of mouse brain sample are shown, with each labeled with time of injection (top label) and time of imaging (bottom label) relative to the time of delivered Controlled Cortical Injury (CCI). The number of dipoles found by ImageJ and PDQ correlate across all four sample types tested. PDQ counts fewer dipoles for all sample types due to the discriminating 'Template Similarity' threshold (TS> 45%) used by the algorithm.

6.4.11 Comparison between PDQ, ED1+ Cell Counts, and Manual Dark Spot Counts in Rat Heart Chronic Rejection Model

Three different cell quantification methods were compared by applying them to 21 rat hearts undergoing chronic rejection: PDQ counting of magnetic dipoles, manual counting of ED1+ cells, and hypointense spot counting. Figure 6.24 shows the results of this comparison in the set of completely-perfused heart samples. Notably, there is a strong linear correspondence between ED1+ cell counts and PDQ dipole counts (Fig. 6.24a; R^2=0.79) and (Fig. 6.24b; R^2=0.79), even though ED1+ count represents only a small fraction of the heart volume, and the PDQ count represents only the small fraction of ED1+ cells that phagocytized a sufficient number of MPIO particles for MRI detection. Interestingly, the hypointense spot count also linearly corresponded with both ED1+ cell counts and PDQ dipole counts (Fig. 6.24c-d). The manual counts were not as correlative however (Fig. 6.24c; R^2=0.59) and (Fig. 6.24d; R^2=0.42), presumably due to the partial volume coverage of manual counting ($\sim$10%) and challenge of distinguishing MPIO-labeled cells from other endogenous sources of tissue hypointensity (Fig. 6.5). Overall, if ED1+ cell counts are taken as a gold standard, PDQ moderately outperforms hypointense spot counting methods.

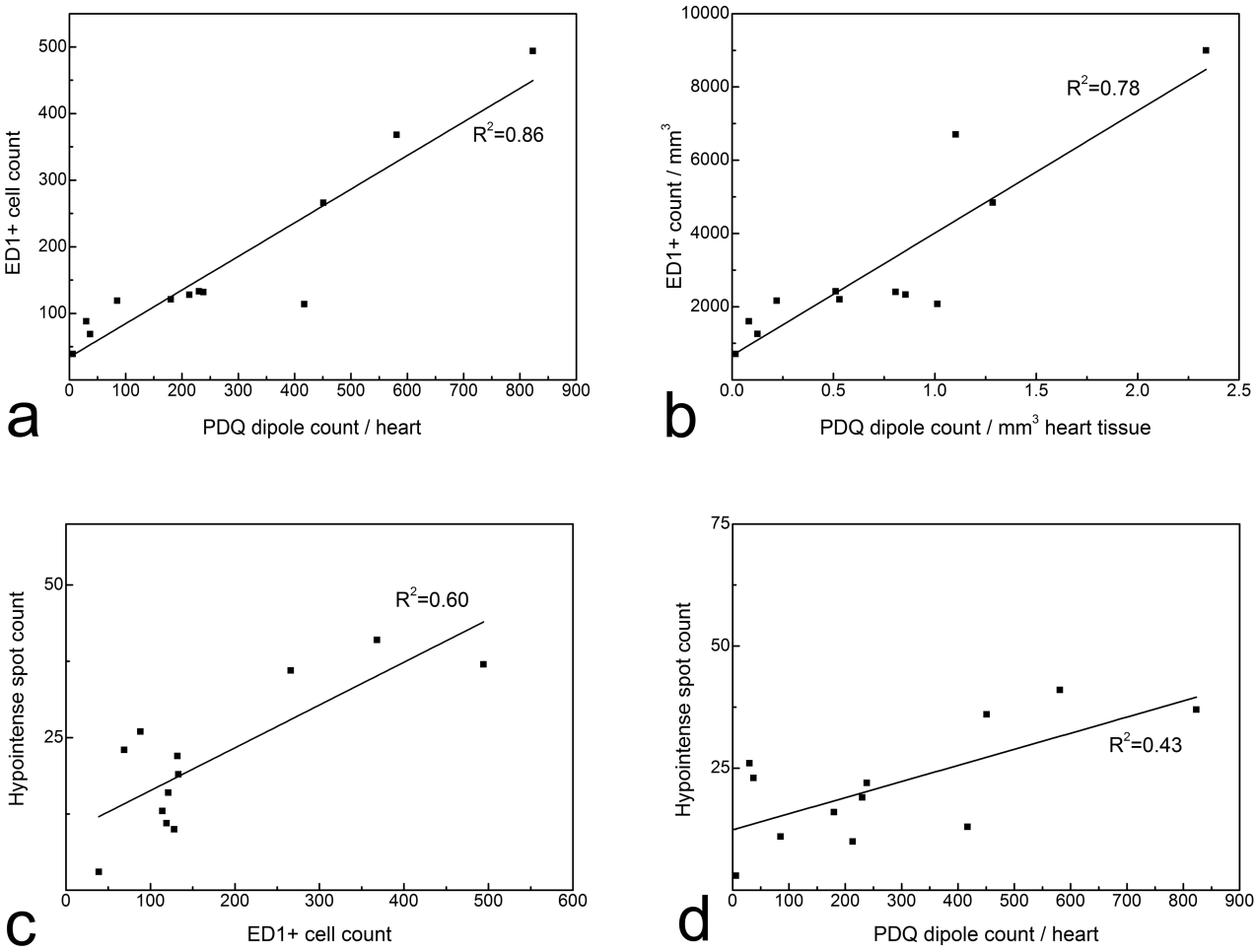

Figure 6.24: Comparison between three different cell quantification methods applied to 13 completely-perfused rat hearts undergoing chronic rejection.

Each panel shows a linear fit to 13 plotted points, each representing one of the 13 heart samples. Panel (a) shows ED1+ cell count versus PDQ dipole count. The ED1+ cell count was performed manually using a 2.89 mm^2 region of an 8-μm thick histological section from the center of each heart. The PDQ count was performed by detection of magnetic dipoles with TS>45% throughout the phase image of each heart volume. Panel (b) shows the same counts from (a), but normalized to mm^3 of heart tissue. Panel (c) shows hypointense spot count versus ED1+ cell count. The hypointense spot count was performed by manually inspecting ∼10% of the magnitude image for each heart volume. Panel (d) shows hypointense spot count versus PDQ dipole count. Notably, there is a strong linear correspondence between ED1+ cell counts and PDQ dipole counts (Panel a; R^2=0.87) and (Panel b; R^2=0.79), even though ED1+ count represents only a small fraction of the heart volume, and the PDQ count represents only the small fraction of ED1+ cells that phagocytized a sufficient number of MPIO particles for MRI detection. Interestingly, the hypointense spot count also linearly corresponded with both ED1+ cell counts and PDQ dipole counts (c-d). The manual counts were not as correlative however (Panel c; R^2=0.59) and (Panel d; R^2=0.42), presumably due to the partial volume coverage for manual counting (∼10%) and challenge of distinguishing MPIO-labeled cells from other endogenous sources of tissue hypointensity (Fig. 6.5).

Figure 6.25 shows the results of the quantification method comparison in the set of incompletely-perfused heart samples. Notably, there is a weaker linear correspondence between ED1+ cell counts and PDQ dipole counts (Fig. 6.25a; R^2=0.53) and (Fig. 6.25b; R^2=0.49), than when these methods

were used on completely-perfused hearts (Fig. 6.24). Interestingly, the hypointense spot count did not linearly correspond with either ED1+ cell counts or PDQ dipole counts (Fig. 6.25c; R^2=−0.16) and (Fig. 6.25d; R^2=−0.16). This is presumably due to difficulty distinguishing MPIO-labeled cells from other endogenous sources of tissue hypointensity in these incompletely-perfused hearts (Fig. 6.5). Overall, if ED1+ cell counts are taken as a gold standard, PDQ significantly outperforms hypointense spot counting methods in these incompletely-perfused heart samples, due to the ability of the method to distinguish dipoles from other sources that generate endogenous contrast.

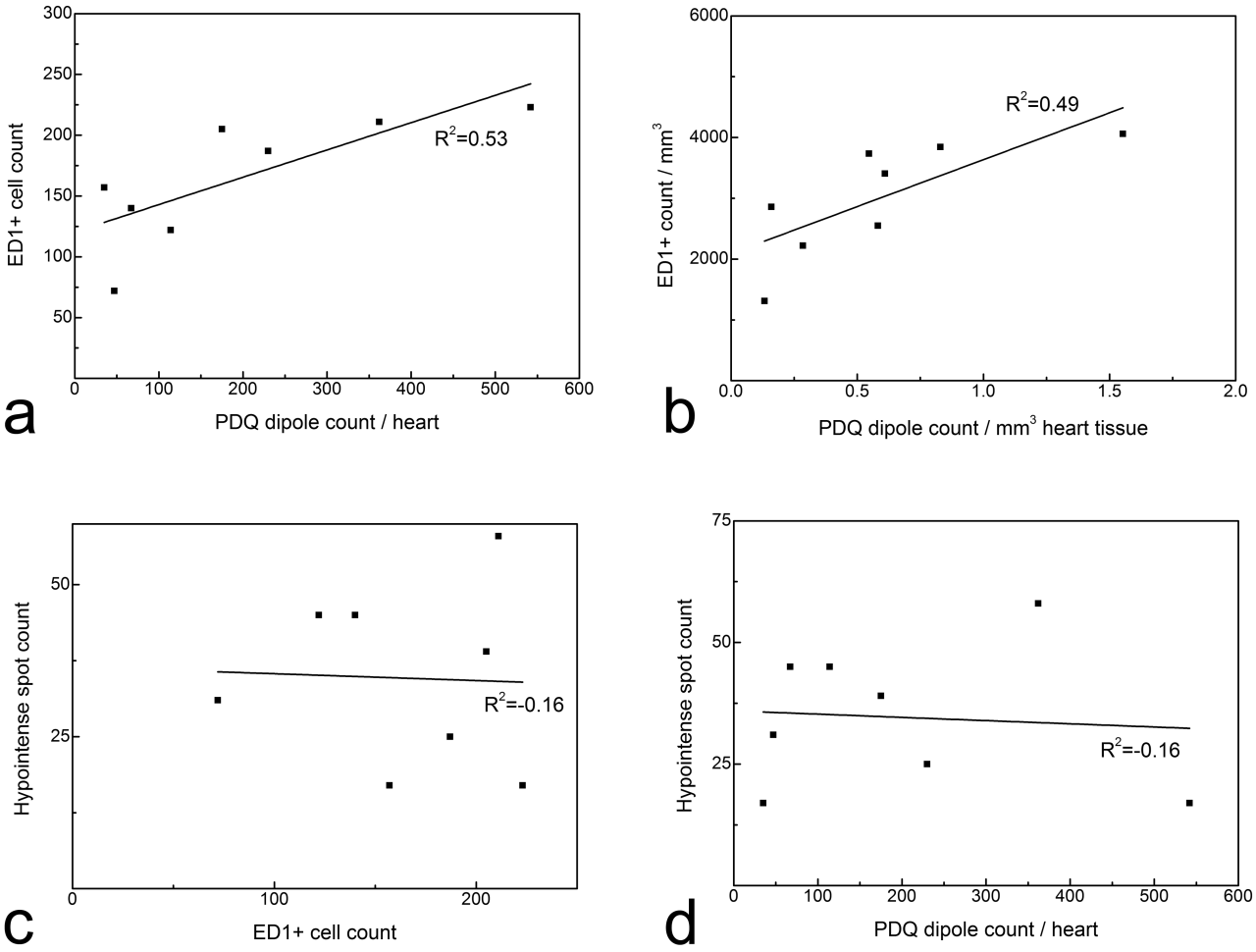

Figure 6.25: Comparison between three different cell quantification methods applied to 8 incompletely-perfused rat hearts undergoing chronic rejection.

Each panel shows a linear fit to 8 plotted points, each representing one of the 8 heart samples. Panel (a) shows ED1+ cell count versus PDQ dipole count. The ED1+ cell count was performed manually using a 2.89 mm^2 region of an 8-μm thick histological section from the center of each heart. The PDQ count was performed by detection of magnetic dipoles with TS>45% throughout the phase image of each heart volume. Panel (b) shows the same counts from (a), but normalized to mm^3 of heart tissue. Panel (c) shows hypointense spot count versus ED1+ cell count. The hypointense spot count was performed by manually inspecting ∼10% of the magnitude image of each heart volume. Panel (d) shows hypointense spot count versus PDQ dipole count. Notably, there is a weaker linear correspondence between ED1+ cell counts and PDQ dipole counts (Panel a; R^2=0.53) and (Panel b; R^2=0.49), than when these methods were used on completely-perfused hearts (Fig. 6.24). Interestingly, the hypointense spot count did not linearly correspond with either ED1+ cell counts or PDQ dipole counts (Panel c; R^2=−0.16) and (Panel d; R^2=−0.16). This is presumably due to difficulty distinguishing MPIO-labeled cells from other endogenous sources of tissue hypointensity in these incompletely-perfused hearts (Fig. 6.5).

Figure 6.26 shows the results of the quantification method comparison in the set of all heart samples, both those categorized as incompletely-perfused and completely-perfused. As expected for this union of these two sets, because all 21 heart samples are analyzed together (13 completely-perfused and 8 incompletely-perfused), the linear correspondences found between the three different

cell quantification methods are a moderation between the results for completely-perfused (Fig. 6.24) and incompletely-perfused (Fig. 6.25) heart sets.

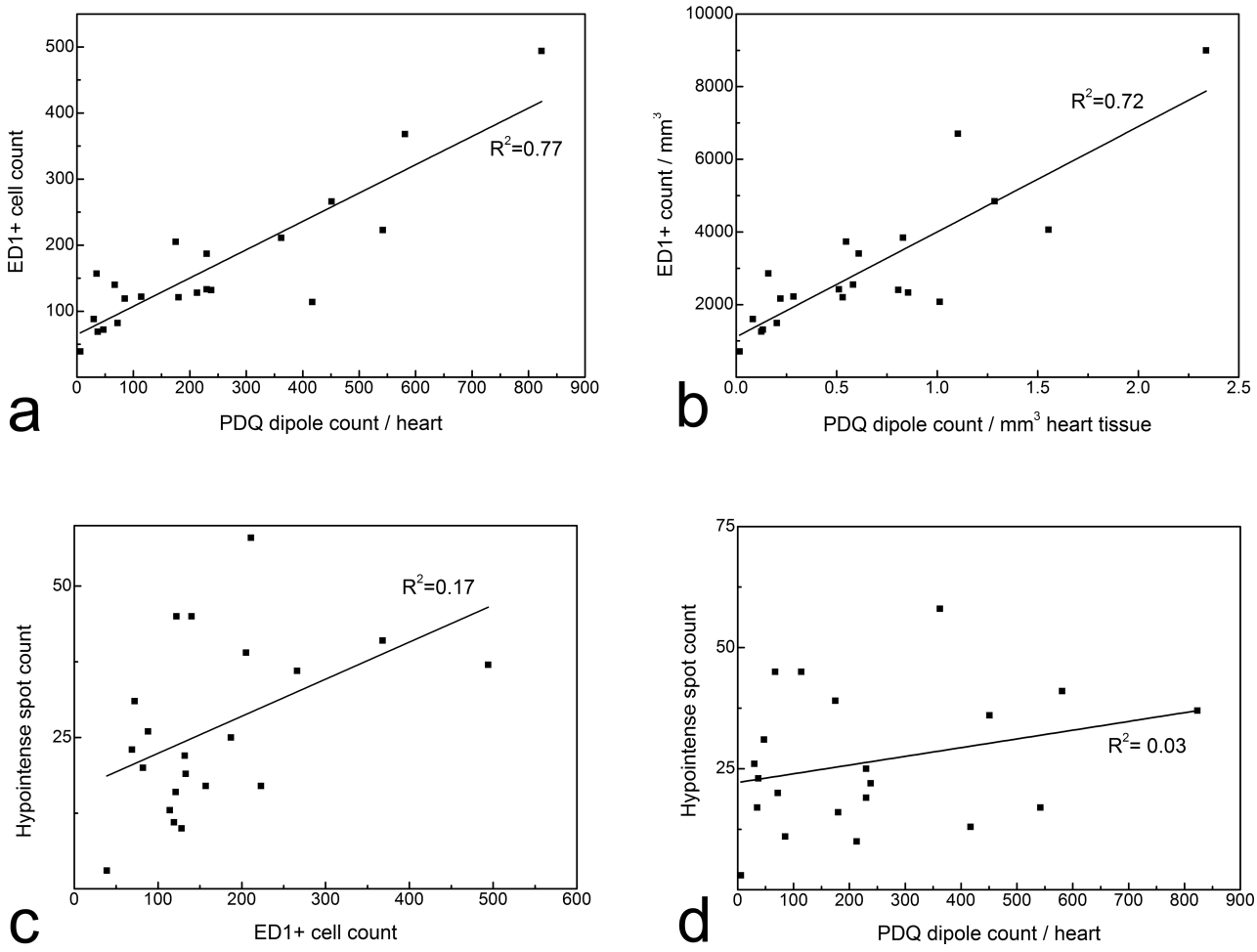

Figure 6.26: Comparison between three different cell quantification methods applied to the union of the 8 incompletely-perfused and the 13 completely-perfused rat hearts undergoing chronic rejection.

Each panel shows a linear fit to 21 plotted points, each representing one of the 21 heart samples. Panel (a) shows ED1+ cell count versus PDQ dipole count. The ED1+ cell count was performed manually using a 2.89 mm^2 region of an 8-μm thick histological section from the center of each heart. The PDQ count was performed by detection of magnetic dipoles with TS>45% throughout the phase image of each heart volume. Panel (b) shows the same counts from (a), but normalized to mm^3 of heart tissue. Panel (c) shows hypointense spot count versus ED1+ cell count. The hypointense spot count was performed by manually inspecting ∼10% of the magnitude image of each heart volume. Panel (d) shows hypointense spot count versus PDQ dipole count.

Interestingly, although PDQ counts ED1+ cells throughout each entire heart volume [(mean ± stdev) = 349 ± 80 mm^3], only a small fraction of these cells contain MPIO in quantities sufficient for detection by MRI. We estimate this fraction from Figure 6.26 to be ∼1 in 4,000 ED1+ cells are

labeled with MPIO sufficient for detection, or alternatively, ∼1 in 2,000 ED1+ cells are sufficiently labeled, if we assume that each dipole represents a cluster of on average 2.0 ED1+ cells). Conversely, the immunohistological ED1+ cell counting covers a single 8 μm-thick section of the central heart volume, but nearly every ED1+ cell is counted regardless of whether it contains sufficient MPIO for MRI detection. Because the PDQ cell count and ED1+ cell counts strongly correlate, this implies that because ED1+ cells are so sparsely-labeled, that a count performed by PDQ is actually representative of the number of ED1+ cells present in cardiac tissue undergoing chronic rejection. As a final consideration, manual counting methods (histological or hypointense spot counting) are time-consuming, with each heart image taking approximately 30 minutes to analyze. PDQ may offer significant time savings when quantifying heart rejection, as the method required $\sim$ 4 minutes per sample, and will see further time reductions as computer processors become increasingly capable.

6.4.12 Longitudinal *in vivo* Multi-Dipole Tracking in Mouse TBI Model

To test the feasibility of PDQ for *in vivo* longitudinal tracking of MPIO-labeled cells, the method was applied to mouse brains at different time points following TBI. Figure 6.27 shows image data acquired from one of these single-brain longitudinal studies. TBI-naive brains, which received no MPIO injection or brain injury, showed no hypointense spots in their magnitude image, and no dipole patterns in their phase image (Fig. 6.27). When PDQ was run on TBI-naive/MPIO-naive brains *in vivo*, the method detected on average 9 false-positive dipoles throughout each naive brain volume, usually at locations where blood vessels or phase-unwrapping artifacts were present. At 48 h post-TBI in MPIO-labeled mice, PDQ detected hundreds of dipoles within each brain volume (Fig. 6.27). Interestingly, at 92 h and 72 h post-TBI, PDQ often detected a reduced number of dipoles relative to the 48 h time point, which we might expect since the concentration of quinolinic acid produced by infiltrating macrophages has previously been found to begin declining 72 h post-injury [127].

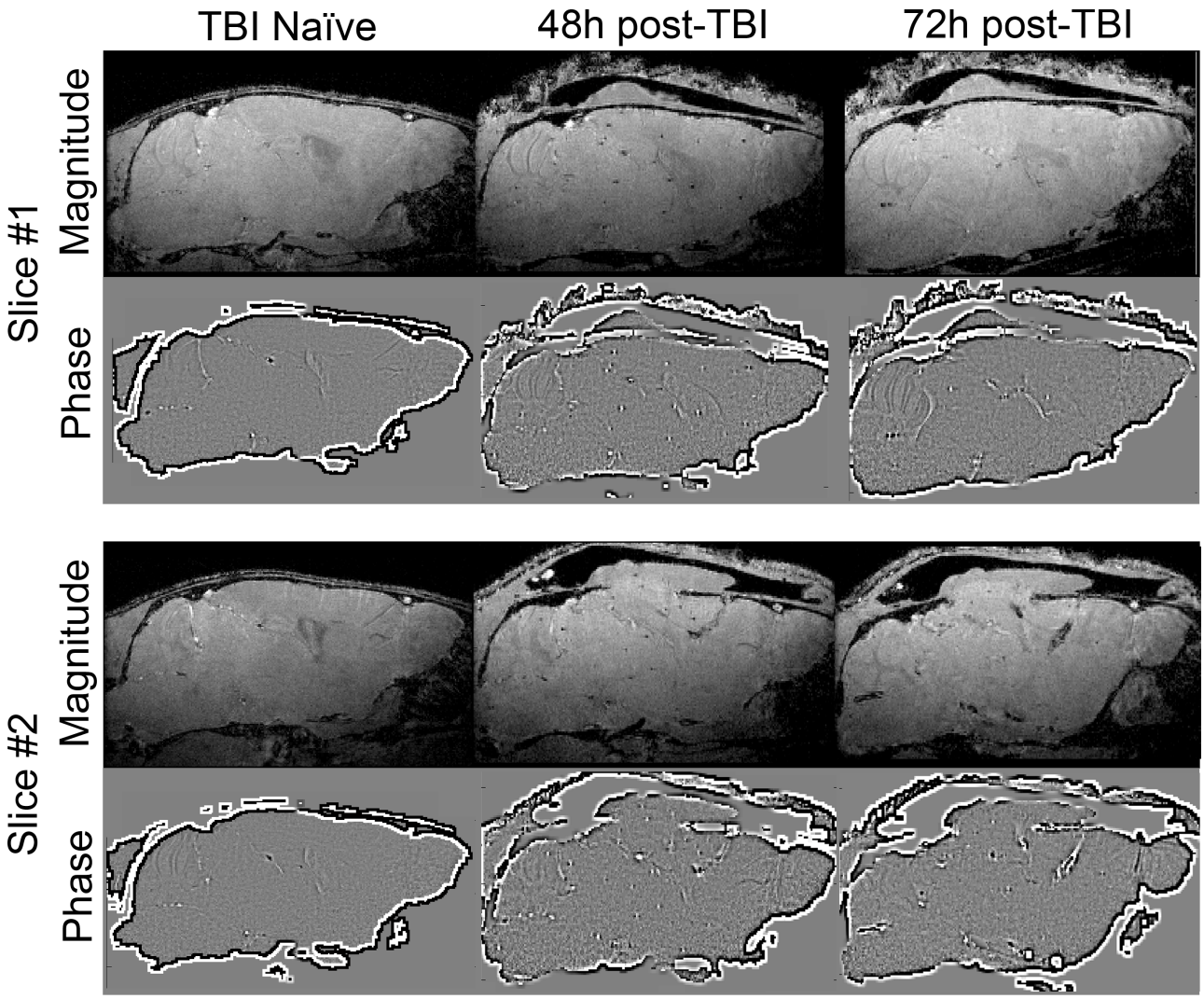

Figure 6.27: Longitudinal *in vivo* MR imaging of same mouse brain at three different time points: Before TBI, 48 h post-TBI, and 72 h post-TBI.
Shown are two sagittal slices from the same brain volume at different depths in the tissue (top panel set and bottom panel set). For each set, magnitude(top) and phase (bottom) images are displayed. These images were manually registered across the three time points. The first time point, TBI Naive, shows no hypointense spots in the magnitude image, and no dipole patterns in the phase image, since no MPIO particles have been injected. The second time point, 48 h post-TBI, shows many hypointense spots and dipole patterns in magnitude and phase images, respectively, with each representing an MPIO-labeled macrophage or macrophage cluster. The third time point, 72 h post-TBI, shows a reduced number of dipoles relative to the 48 h time point, which follows the expected progression following traumatic injury. PDQ automatically registers these datasets, allowing for preliminary cell tracking of the many MPIO-labeled macrophages or macrophage clusters present at 48 h and 72 h time points.

After applying PDQ to brain scans at different time points, the method was extended to attempt longitudinal tracking of individual dipoles from 48 h to 72 h post-TBI, and from 72 h to 96 h post-TBI. Figure 6.28 shows a 3D rendering that visualizes the results of this tracking experiment. 45%

of dipoles (57/127) coregistered between the 48 h and 72 h time points did not move > 5 voxels ($\Delta x > 360$ μm) during the 24 hours until the 72 h time point. These dipoles were considered to be stationary, given an expected registration error of ~ 2 voxels between brain time points. The change in magnetic moment measured by PDQ for these 'stationary' dipoles was a small value of $\Delta\vec{m} = 0.07 \pm .17$ pA·m^2. This represents a change in magnetic moment relative to the measured magnetic moment of only $7 \pm 27\%$ (i.e., $\Delta\vec{m} = .07 \cdot \vec{m}_{48\text{h}} \pm .17 \cdot \vec{m}_{48\text{h}}$). 55% of registered dipoles (70/127) moved between 5–34 voxels (360 μm $\leq \Delta x <$ 2448 μm). Notably, many dipoles appeared at 72 h that were not detected at 48 h. The dipoles that 'appeared' can be classified into two categories: dipoles with strong magnetic moments that truly appeared in tissue, and dipoles with weak magnetic moments that were actually present in tissue at 48 h, but missed detection by PDQ due to prevailing image noise levels combined with the PDQ template similarity (TS) threshold of TS>0.31. These apparent appearances are due to the PDQ algorithm missing the dipoles at 48 h. Similarly, many dipoles disappeared between 48 h and 72 h. Again, these disappearances can be classified as either dipoles with strong magnetic moments that truly disappeared from tissue, and dipoles with weak magnetic moments that did not really vanish between time points, they just were above the PDQ cutoff threshold at the earlier timepoint (detected), then were below the PDQ cutoff threshold at the later timepoint (not detected), causing apparent disappearance. Between 72 h and 96 h, more dipoles disappeared than appeared (Fig. 6.27). An additional consideration is the possibility that macrophages may proliferate (undergo mitotic division), as they have been observed to do provided they are not activated, in murine testes and lung tissue [136, 137]. Also, apparent moving dipoles in the area surrounding and within the traumatic brain injury may be due to tissue herniation as a result of injury, or tissue movement as a result of resolving inflammation processes. By using a non-rigid transformation to register brains between time points, instead of a rigid transformation, these potential errors might be mitigated. Overall, a way to address questions about cell movement, herniation, tissue movement, or cell appearance and disappearance would be to increasing the time resolution between scans. Fewer than 24 hours elapsed between scans may help resolve some of the questions about the dynamics of these MPIO-labeled macrophages.

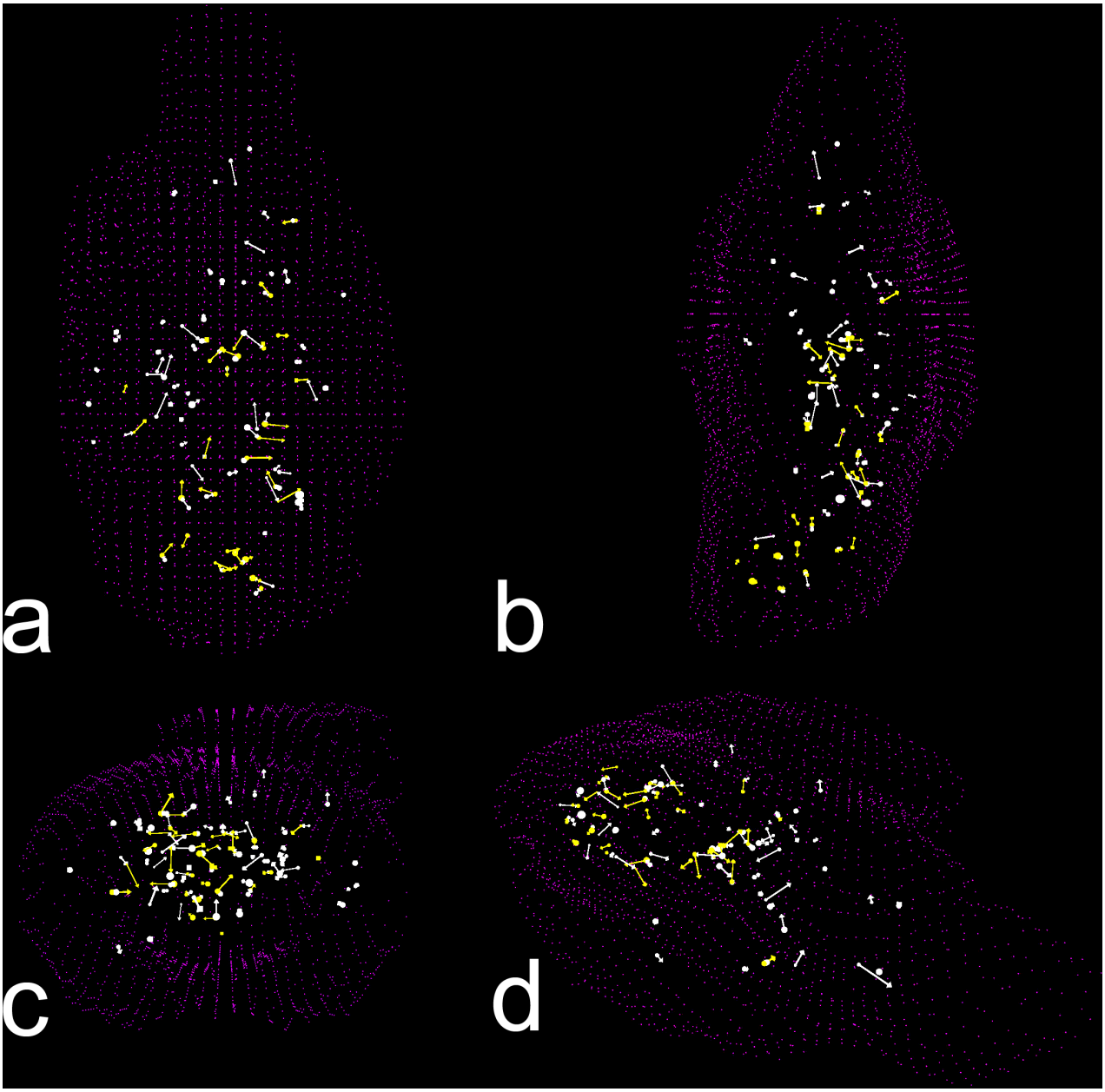

Figure 6.28: *In vivo* tracking of MPIO-labeled macrophages/macrophage clusters within same mouse brain imaged longitudinally at 48 h, 72 h, and 96 h post-TBI.
The 3D volume rendering panels show (a) dorsal, (b) lateral, (c) cranial, and (d) oblique views. White spheres represent magnetic dipoles detected at 48 h; sphere radius is proportional to the magnetic moment of the dipole. White arrows protruding from white spheres indicate suspected cell movements of the same cell between 48 h and 72 h. Yellow spheres indicate dipoles detected at 72 hours post-TBI, that were not detected at 48 h; sphere radius is proportional to the magnetic moment of the dipole. Yellow arrows protruding from yellow spheres indicate suspected cell movements between 72 h and 96 h. Hence, all spheres with no (or short) arrows are considered stationary. Substantial numbers of dipoles were found to appear, disappear, or move short distances. Some matches may be false-positives, for example, if between 48 h and 72 h, a dipole disappears, and a new dipole with a similar magnetic moment appears close-by, it might be displayed in this rendering as being the same dipole. Automatic dipole matches between timepoints were done under two constraints: dipoles must move less than 20 μm/hour and must have a magnetic moment that differs by ≤ 0.3 pA$\cdot$ m^2.

To test PDQ registration and tracking abilities, the same mouse brain 96 h post-TBI was scanned twice (*in vivo* then *ex vivo*) and run through the registration and tracking process using the same parameters used for the 48 h–72 h–96 h tracking experiment shown in Fig. 6.28. Figure 6.29 shows the result of this brain auto-registration. Notably, no dipole movements > 5 voxels (> 360 μm) were detected, implying that false positive dipole movements are not due to the registration and tracking process itself, but are due to either actual dipole movements, or false-positive movements when one dipole disappears and a different dipole with a dipole moment within ± 0.4 pA·m^2 appears within 2448 μm of the disappeared dipole.

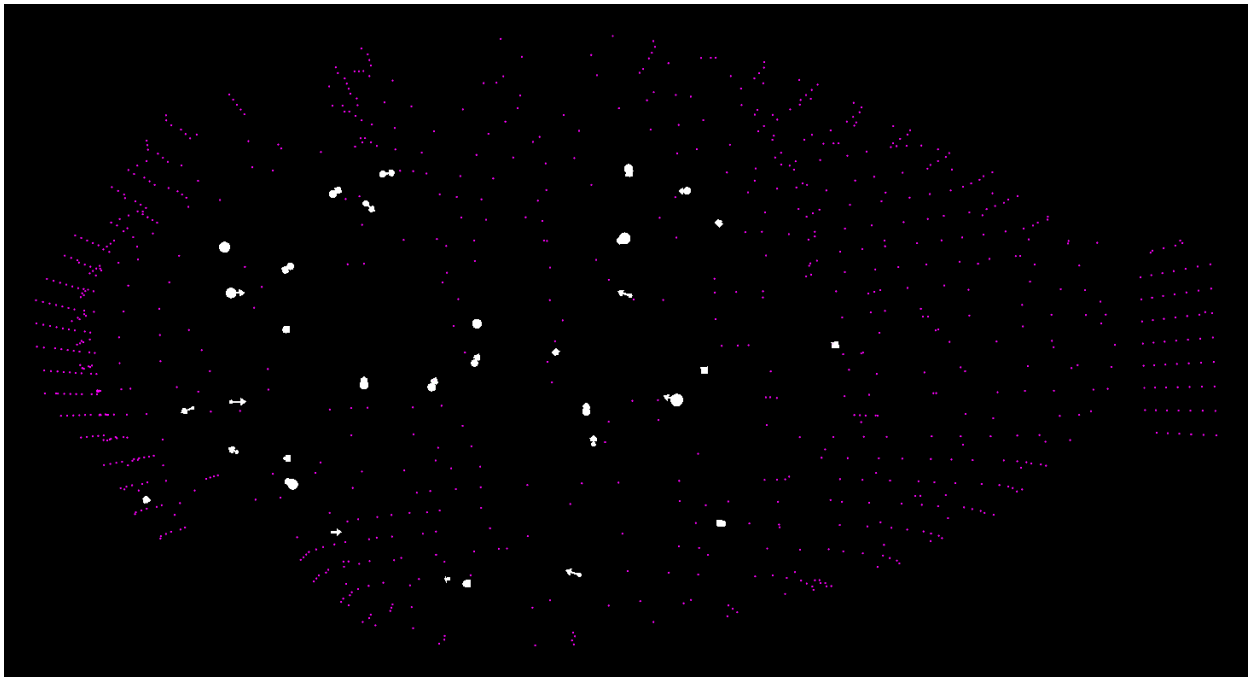

Figure 6.29: Control application of tracking system on MPIO-labeled macrophages/macrophage clusters within same mouse brain imaged *in vivo*, then *ex vivo*, at 96 h post-TBI.
The 3D volume rendering panels shows a dorsal view. White spheres represent magnetic dipoles detected *in vivo*; sphere radius is proportional to the magnetic moment of the dipole. White arrows protruding from white spheres indicate detected cell movements between *in vivo* scans and *ex vivo* scans. Because this is the same brain imaged twice, any detected movement is suspected to be due to algorithm error. Notably, large distance movements were not detected, implying that errors due to the registration and tracking process itself are small. Alternatively, error may be due to the *in vivo* brain being alive, whereas *ex vivo* brain was imaged following paraformaldehyde fixation. Automatic dipole matches between timepoints were done under two constraints: dipoles must move less than 20 μm/hour and must have a magnetic moment that differs by ≤ 0.3 pA·m^2.

6.5 Discussion

Here, we present a post-processing method that uses phase MR images to automatically identify and count spherical SPIO deposits and estimate their volume magnetic susceptibility and magnetic moment. The PDQ algorithm can automatically scan, detect and quantify individual MPIO-labeled cells, cell clusters or therapeutic magnetocapsules in tissue volumes, with significant discrimination capacity. Moreover, the PDQ algorithm provides an estimation of the volume magnetic susceptibility and magnetic moment of these detected paramagnetic deposits, which may enable greater discrimination against false positives.

The PDQ method can potentially improve the detection of spheroid deposits of paramagnetic agents in several ways. Like other positive contrast methods, this approach enhances the ability to detect and differentiate paramagnetic agents from intrinsic sources of hypointensity such as regions of short T_2 and T_2^*, low proton density, and susceptibility artifacts across interfaces. It can also improve the ability to detect smaller, weaker, or partial-volume deposits of contrast agent, and decrease the number of false negatives. Importantly, we show that the PDQ method remains robust when applied to low SNR images.

The PDQ method becomes useful for numerous applications where paramagnetic deposits are quantified and visualized in 3D. For example, in the heart rejection model, the number and spatial distribution of cellular infiltrates provides information about the degree to which the heart allograft is undergoing organ rejection [19]. The number of infiltrating macrophages is related to post-operative day (POD). Macrophages progress from pericardium to endocardium in the left ventricle of the heart, reaching different distances from the edge of the heart as the POD increases [19].

The utility of the PDQ algorithm is demonstrated in several diverse MRI data sets. We tested these methods in 3D using gel phantoms doped with isolated paramagnetic dipoles and apply the methods to simulated data to determine how much noise one can introduce before the method fails. We also test our methods in heterogeneous tissue; a 3D dataset from an *ex vivo* allograft rat heart infiltrated by numerous MPIO-labeled macrophages. The heart was part of a study that aims to develop a non-invasive MRI alternative to biopsy, which is the current gold standard for diagnosing and staging rejection after organ transplantation [19]. We demonstrate that it is feasible to derive quantitative markers based on the density of dipoles present in tissue, and we speculate that the

infiltration index may be a useful biomarker for quantifying the degree of cellular infiltration into tissue and thus the extent of organ rejection. PDQ magnetic measurements were performed in animal models of therapeutic magnetocapsule engraftment, TBI, and organ transplant rejection, both in fixed tissues and *in vivo*.

6.5.1 Sources of Error

There are a several sources of error in PDQ magnetic measurements. First, phase unwrapping can assign an incorrect multiple of 2π to a pixel, especially if phase is spatially undersampled (i.e., two adjacent pixels have an actual phase difference greater than π) [97]. The unwrapping algorithm used has an error rate of 0.4% when SNR = 2.5 [98], but SNR $<$ 2.5 is common at the center of dipoles, where signal-free pixels contain random phase values [58]. To mitigate this effect, one may weigh or mask out pixels with SNR $<$ 2.5 to deemphasize these in the PDQ analysis [58], or acquire phase maps using multi-echo GRE pulse sequences that replace phase unwrapping with 'temporal unwrapping.' Second, there is often imprecise knowledge of the background χ-values among different tissues. This fact was acknowledged in comparing magnetic moment values of the same paramagnetic deposit acquired *in vivo* versus in fixed tissue in the TBI model (Fig. 6.21); fixed, perfused brain specimens have the blood removed and undergo dehydration in the fixation process that may alter χ. Finally, in order for PDQ dipole counts to be comparable across different datasets, each must be acquired at similar resolution and SNR. Datasets with low resolution and/or SNR may have many dipoles omitted from final counts, due to thresholding of the TS parameter; in the analysis presented, dipoles with TS$<$30% were ignored. As expected, more false negatives and positives are found in heterogenous tissues than in homogeneous tissues, and more false results are found in any tissue, compared to gel phantoms.

6.5.2 Overlapping Dipole Impressions

If labeled cells or magnetocapsules are very close or touching, PDQ will detect these as a single entity yielding an aggregate magnetic susceptibility and moment. If cells or magnetocapsules are further apart, but within a template-sized region of one another, their phase image profiles overlap, and TS values will tend to decline. A possible extension of the algorithm could measure the magnetic properties of neighboring dipoles simultaneously. One can model dipoles as vertices ($v \in V$) in

a graph $G = (V, E)$, with edges ($e = (v_1, v_2) \in E$) representing dipole pairs that share the same $7 \times 7 \times 7$ voxel space. Then, for each connected subgraph of G, one would perform a least squares fit to account for all dipoles in that subgraph.

When considering neighboring magnetic dipoles, one may also consider how each neighboring field changes the effective B_0 experienced at the other location. Calculations using Eq. (6.1) show that this effect is very small for adjacent magnetocapsules ($\Delta B_0 = \sim$16ppm) and for adjacent MPIO-labeled cells ($\Delta B_0 = \sim$190 ppm). Other materials and SPIO configurations may have a larger effect requiring appropriate correction.

In the case of magnetocapsules, these paramagnetic objects are slightly oblong and are not perfect spheres. The PDQ method can be modified to consider arbitrary, non-spherical distributions of SPIO agent. This modification would require the replacement of the phase-offset template generated using Eq. (6.1) with one that models the magneto-static field of a specific paramagnetic geometry of interest. One way to generate these new composite templates would be to convolve Eq. (6.1) with a 2D image that represents the distribution of multiple spherical paramagnetic deposits.

6.5.3 Readout Dimension Spatial Shifts

SPIO deposits change the precession frequency of surrounding protons, distorting the phase image along its readout dimension. If scan parameters are not configured to minimize this effect, SPIO deposits will not exhibit the expected geometry for detection and measurement (e.g., Eq. (6.1)). Specifically, a proton spin experiencing a magnetic field deviation of ΔB_Z exhibits a spatial shift in the readout dimension in a phase image of amount [80]:

$$\Delta p = \frac{N_x \cdot \Delta B_Z}{FOV_x \cdot G_x} = \frac{N_x \cdot \gamma \cdot \Delta B_Z}{BW} \tag{6.10}$$

where Δp is the distance the proton is shifted in pixels, N_x is the number of pixels in the readout dimension, ΔB_Z is magnetic field deviation from B_0 (T), FOV_x represents readout field of view (m), G_x represents readout gradient amplitude (T/m), γ represents proton gyromagnetic ratio (Hz/T), and BW represents readout bandwidth (Hz/T). Equation (6.10) teaches that the spatial shift artifact is minimized by increasing bandwidth, which also reduces image SNR. Equations (6.1) and (6.10) can be used to calculate the minimum BW required to avoid image distortion.

6.5.4 Optimal Image Acquisition

In general, increased SNR and resolution will benefit PDQ: more dipoles should be detected as image SNR/CNR increases, and precision increases as image resolution increases, since a larger, more detailed cross-correlation template can be used. The echo time, TE, should be sufficiently long to allow for dephasing around SPIO deposits to occur, but not so long that SNR declines substantially. When dipoles are in highly heterogeneous backgrounds, dual-echo GRE scans may enable more accurate measurements than single-echo GRE scans [58]. In samples where SPIO deposits reside within homogenous tissue backgrounds (e.g., brain, liver) a single TE gradient-echo image is sufficient. Short-T_2 tissues (e.g., liver) may require higher cell-labeling contrast agent relaxivity or concentrations, since sub-voxel dephasing occurs rapidly in these organs, thereby reducing the CNR available for accurate dipole detection.

Template sizes should be larger than $3\times3\times3$ voxels, so that no dipoles are found in random noise (many 3-pixel-wide dipole-like arrangements are present in random noise). The template should be sized so that voxels on its periphery have a phase offset of greater magnitude than phase image noise. Oversized templates may start to overlap neighboring dipoles. Users must set a template similarity (TS) threshold above 30%, as lower thresholds generally detect dipoles in random noise. PDQ underestimates magnetic measurements when applied to SPIO deposits with different orientations or slightly aspherical geometries. Therefore to maximize magnetic measurement accuracy, one should measure dipoles with the highest TS values available for a particular dataset, or modify the templates generated by Eq. (6.1) to reflect non-spherical geometries.

6.5.5 Using PDQ with 2D Slice Stacks and 2D Slices

For a 2D MR image to be analyzed using PDQ, the in-plane orientation of the slice must have a significant parallel component to the applied magnetic field (B_0), as required by Eq. (6.1). If the slice orientation is orthogonal to the direction of B_0, the dipolar profile will appear circular in the phase offset image and will not exhibit the lobe pattern needed for a quality cross-correlation analysis. At lower magnetic field strengths, high-resolution images may be difficult to achieve and 2D slice thickness may also be larger. As the slice thickness increases so does partial-voluming, thereby reducing the impact of magnetic field disturbance in the phase map due to a dipole. The

PDQ method works ideally with a slice thickness no greater than the extent to which the magnetic field perturbation of a dipole is significant versus the background noise.

A potential pitfall of applying the PDQ method to 2D tissue slices is that blood vessels are often detected when they curve parallel to B_0. The detection of blood vessels may be reduced or eliminated by raising the template similarity (TS) threshold, but one risks eliminating the weakest dipoles present in the tissue. Alternatively, 3D PDQ analyses give improved blood vessel discrimination; vessels within 2D images have cross-sections that may be indistinguishable from iron-oxide labeled cells.

6.5.6 Future Applications

PDQ detects single cells or cell clusters *in vivo*, measuring magnetic moments as low as 0.8 pA·m^2 ($\sim$12 pg[Fe]) at 7 Tesla. Previously, single macrophages were detected when labeled with 100 pg [Fe] at clinical field strengths as low as 1.5 Tesla [78]. Magnetic measurements provided by PDQ, in addition to location data, may provide more certainty when identifying labeled cells at different time points in longitudinal studies. For *in vivo* PDQ, sufficient resolution is critical, as the magnetic field rapidly attenuates with distance from the center of an SPIO deposit ($\sim 1/r^3$). *In vivo* imaging also presents challenges including movement from breathing and cardiac function, as well as cellular motion. Many cells may migrate during multi-hour scans, confounding PDQ. For example, multipotent neuroblasts can move 100 μm/hour *in vivo* [8]. Problems can be avoided by performing sufficiently short scans so cells move no more than one voxel.

Tracking of single cells by PDQ should be increasingly feasible through motion correction, cell-registration methods, increased magnetic field strengths, and development of sensitive hardware and contrast agents. *In vivo* cell tracking studies may potentially be used to detect the arrival of immune cells at sites of disease, define optimal cell populations and delivery methods in the emerging field of cellular therapeutics, and understand basic biological phenomena *in vivo*. For example, in cardiac tissue undergoing immune rejection, macrophage numbers reflect different stages of rejection [19] and can be used to titrate dosage and monitor the efficacy of immunosuppressive therapy [4]. Magnetic moment measurement can also be used for theranostic magnetocapsule applications to assay magnetocapsule integrity (i.e., intact versus ruptured), which can be an important predictor of encapsulated pancreatic islet survival [124], for example. Moreover, labeling capsules

with different iron contents may allow for unambiguous magnetic moment signatures enabling, for example, identification of multiple encapsulated therapeutic cell types, or transplants occurring at different times.

6.6 Conclusion

Superparamagnetic MRI contrast agents are increasingly being used to label cells and theranostic vehicles for *in vivo* imaging applications. This study addresses an urgent need in this emerging field which is the analysis and quantification of the resulting MR images. The PDQ algorithm offers great sensitivity by specifically searching for localized SPIO deposits in phase images. After detecting SPIO deposits, PDQ measures their magnetic moment, which is a quantity that can be used to improve detection specificity, reducing false positives and negatives. PDQ-detected dipole locations can be rendered as positive-contrast images for overlaying onto conventional magnitude images to quickly highlight contrast agent deposits.PDQ is capable of detecting single cells and cell clusters *in vivo*, and provides reliable magnetic measurements.

Like other positive contrast methods, PDQ helps differentiate dark areas due to SPIO from other intrinsic sources of hypointensity, but unlike these methods it requires no prior knowledge of agent concentration or distribution, no special imaging pulse sequences, no extra scan time, only a few user-set parameters, and can be applied retrospectively to previously acquired data. PDQ may have future applications for monitoring therapies, measuring cellular iron content, and observing cell behaviors.

Chapter 7

Fluorine-19 imaging using Compressed Sensing

7.1 Introduction

When imaging sparse fluorine tracer agents, signal deposits can sometimes appear indistinguishable from image noise, or imaging may require MRI scan times that are prohibitively long for use during *in vivo* experiments. In order to maximize the utility of *in vivo* fluorine-labeled cell tracking and quantification methods, there is a need for MRI procedures that maximize sensitivity to fluorine tracer agents by increasing the SNR per unit time (SNR/t) when acquiring image data.

Recently, compressed sensing methods have been used to reduce MRI scan times, in situations where images that result from a scan are expected to be 'information-sparse' or 'sparsely-representable.' Compressed sensing is a modality-independent class of methods for digitally undersampling a subject in a fashion that takes into account the compressibility of the image that will be reconstructed. In other words, by knowing to what degree an image is compressible after acquisition (its "sparsity"), yet still retain all its salient features and integrity, one can reduce acquisition time by digitally undersampling and reconstruct the image in a fashion that takes its sparsity into account. Examples of sparse images in MRI include those that have a small fraction of voxels containing signal (e.g., ^{19}F or other sparse nuclei), dynamic MR images where each time point is expected to change little from its previous time point, and images that contain objects that have geometries known *a priori* (e.g., catheters).

Compressed sensing has been previously used for different MR applications, including: accelerated dynamic imaging (k-t imaging) [138]; mapping relaxation parameters T_1 and T_2 [139]; viewing

pixel-sparse flow patterns in microfluidic devices [140] and angiography [141]; increasing temporal resolution when visualizing catheters [142, 143]; accelerating 3D upper-airway MRI imaging [144]; rapidly acquiring hyperpolarized ^{3}He lung MR images [145]; and 3D ^{19}F chemical shift imaging [146]. Compressed sensing MRI has also been used in conjunction with parallel coil imaging methods (e.g., SENSE) to exploit hardware acceleration [147]. For most of these applications, the k-space undersampling pattern and image reconstruction constraints are customized for each application.

Notably, MR images of cells labeled with fluorine tracer agent are sparse in the image pixel domain. The number of voxels that contain fluorine signal is small relative to the total number of voxels in the image grid. Typically when ^{19}F images are acquired using a 3D large field of view to incorporate a subject's full body anatomy, only 0.5–3.0% of image voxels contain fluorine signal. As sparsity is a requirement for compressed sensing methods, it is directly applicable to imaging sparse distributions of fluorine tracer agents, and promises a distinct SNR/t advantage over conventional imaging methods. Compressed sensing also naturally denoises images, avoiding the need for a noise-removal following image formation.

Here, we simulate compressed sensing image reconstruction by undersampling MR data of a ^{19}F phantom that has already been fully acquired (100% k-space sampling). We also test fluorine-19 imaging using compressed sensing by employing a custom Bruker pulse sequence that directly undersamples 3D k-space. We apply this pulse sequence to the same fluorine phantom used for the simulations, as well as a rat brain injected with 9L glioma cells labeled with ^{19}F tracer agent. Overall, acquisition of 3D sparse ^{19}F images were accelerated by $4\times - 8\times$ with little qualitative degradation in resulting image quality.

7.2 Theory

The theoretical foundations for compressed sensing are described in full detail elsewhere [148, 149, 141]. Briefly, k-space is undersampled in a random fashion with variable density to include k-space lines with high SNR, while simultaneously avoiding the generation of spatially-coherent artifacts that occur when undersampling patterns are uniform. Reconstruction of the image is done by solving the following equation, involving the convex combination of L1-norm and TV-norm regularization:

$$\hat{\rho}_{TVL1} = \arg\min \ [\alpha|\rho|_{TV} + (1-\alpha)|\rho|_1] \quad s.t. \quad ||F\rho - d||_2^2 \leq \epsilon \tag{7.1}$$

where

$$|\rho|_{TV} = \sum_{p=1}^{P} \sqrt{|[D^h\rho]_p|^2 + |[D^v\rho]_p|^2} \tag{7.2}$$

and $|\rho|_1]$ represents the L-1 norm operation, F is the Fourier encoding matrix, d is the sampled data vector (k-space samples), ρ is the image of interest to be reconstructed, α is a weighting parameter between L1-norm and TV-norm constraints, ϵ is the threshold constraint on data consistency, and D^h and D^v represent the differential operators along horizontal and vertical dimensions, respectively. The sparsifying transform used here is the identity transform, since ^{19}F images are sparse in the pixel domain. Other sparsifying transforms can be used, including spatial finite differences and wavelet transforms. The L1-norm minimization constrains reconstruction under the assumption that the fluorine images can be represented by a small number of numerical values (i.e., few pixels actually contain significant fluorine spins). The Total Variation (TV) minimization constrains under the assumption that fluorine images have limited intensity variation between neighboring pixels (i.e., difference between pixel values between rows and columns of the fluorine image). The TV constraint naturally suppresses image noise, as random noise has a much higher local total variation than deposits of fluorine signal do.

When deciding what 3D image size to acquire and which k-space lines to sample when imaging ^{19}F with compressed sensing, it is generally desirable to maximize SNR/t. The signal-to-noise ratio (SNR) for a conventionally-acquired 3D image can be modeled as:

$$\text{SNR} = \frac{\rho}{\sigma}\sqrt{\frac{N_{\text{EX}} \cdot N_x \cdot N_y \cdot N_z}{\text{BW}}} \cdot \frac{\text{FOV}_x}{N_x} \cdot \frac{\text{FOV}_y}{N_y} \cdot \frac{\text{FOV}_z}{N_z} \tag{7.3}$$

where ρ represents average ^{19}F spin density, σ represents the standard deviation of measured image noise from the apparatus and sample, N_{EX} represents the number of excitations (repeated samplings of sampled k-space lines) performed, N_x, N_y, and N_z represent the number of samples acquired in the X-,Y-, and Z-dimensions of k-space respectively, FOV_x, FOV_y, and FOV_z represent the field of view in X-,Y-, and Z-dimensions respectively, and BW represents bandwidth of the readout

direction (X-dimension) [96]. The total imaging time (t_{acq}) required for a fast spin echo pulse sequence is:

$$t_{acq} = \mathrm{TR} \cdot N_{\mathrm{EX}} \cdot N_y \cdot N_z / N(s) \tag{7.4}$$

where TR is repetition time and $N(s)$ is the number of k-lines acquired per TR period. Combining Equations (7.3) and (7.4), SNR/t_{acq} can be expressed as:

$$\frac{\mathrm{SNR}}{t_{acq}} = \frac{\rho}{\sigma} \cdot \frac{N(s) \cdot \mathrm{FOV}_x \cdot \mathrm{FOV}_y \cdot \mathrm{FOV}_z}{\mathrm{TR} \cdot \sqrt{\mathrm{BW} \cdot N_x}} \cdot \frac{\sqrt{N_y \cdot N_z}}{N_y^2 \cdot N_z^2 \cdot \sqrt{N_{\mathrm{EX}}}} \tag{7.5}$$

Combining ρ, σ, $N(s)$, FOV, TR, BW, and N_x into a single constant (c_{scan}) that represents a specific subject, fluorine tracer agent, and apparatus,

$$c_{scan} = \frac{\rho}{\sigma} \cdot \frac{N(s) \cdot \mathrm{FOV}_x \cdot \mathrm{FOV}_y \cdot \mathrm{FOV}_z}{\mathrm{TR} \cdot \sqrt{\mathrm{BW} \cdot N_x}}, \tag{7.6}$$

This scan-specific constant allows us to simplify Equation (7.5) to represent only acquired k-space lines and signal averages:

$$\frac{\mathrm{SNR}}{t_{acq}} = c_{scan} \frac{\sqrt{N_y \cdot N_z}}{N_y^2 \cdot N_z^2 \sqrt{N_{\mathrm{EX}}}} \tag{7.7}$$

Finally, since we plan to undersample k-space lines within the Y-Z plane (i.e., $N_{samp} \neq N_y \cdot N_z$), we reduce N_y and N_z from Eq. (7.7) to a single term, N_{samp}, representing the total number of k-space samples acquired:

$$\frac{\mathrm{SNR}}{t_{acq}} = \frac{c_{scan}}{N_{samp}^{3/2} \cdot N_{\mathrm{EX}}^{1/2}} \tag{7.8}$$

From Equation (7.8) we see that in order to maximize SNR/t_{acq}, it is better to increase the number of excitations (N_{EX}), than to increase the number of k-line samples in either Y- or Z-dimensions. Therefore, when imaging low-SNR, sparse ^{19}F distributions using 3D Cartesian compressed sensing, optimal SNR/t is obtained by selecting the minimum number of k-space lines (N_{samp}) that will result in an adequately-resolved reconstructed image, then sampling those k-space lines repeatedly (N_{EX}) to increase SNR to the point where noise is completely suppressed by signal. If SNR is

already sufficiently high, noise is suppressed, and sufficient scan time is available, then increasing the number of samples (N_{samp}) to increase image resolution becomes an appropriate strategy.

7.3 Methods

7.3.1 Simulated CS Reconstruction of ^{19}F Phantom

Compressed sensing reconstruction was tested by simulated k-space undersampling of previously-acquired fluorine phantom data. The fluorine phantom was created by filling 7 glass capillaries with diameters of 1.8, 1.4, 1.1, 0.9, 0.7, 0.4, and 0.3 mm with neat perfluoro-15-crown-5-ether (PCE). Glass capillaries were taped around the circumference of a plastic 50 mL centrifuge tube. A 7 T, 21 cm horizontal bore Bruker AVANCE AV3 system was used to image the phantom using a 128 ×128 resolution and 4 cm field of view. Three pulse sequences were used to generate images with different SNR characteristics: 1) Spin echo pulse sequence with parameters TE/TR=7/1500 ms, slice thickness = 0.5 mm, averages = 1; 2) Gradient echo pulse sequence with parameters TE/TR=7/190 ms, θ=60°, slice thickness = 0.5 mm, averages = 8; and 3) Fast-spin-echo pulse sequence with parameters TE/TR=7/1500 ms, slice thickness = 1 mm, echo train length = 8 echoes, averages = 8. After conventional acquisition, raw k-space data were undersampled by 2×, 4×, 8×, 16×, and 32× using randomly-generated k-space sampling patterns generated by the SparseMRI software package developed by Michael Lustig [141]. Figure 7.1 shows a few of the different compressed sampling schemes used for these simulated reconstructions. Image reconstruction from undersampled k-space data was then done by solving Eq. (7.1) using a nonlinear conjugate gradient descent algorithm with back-tracking line search [141].

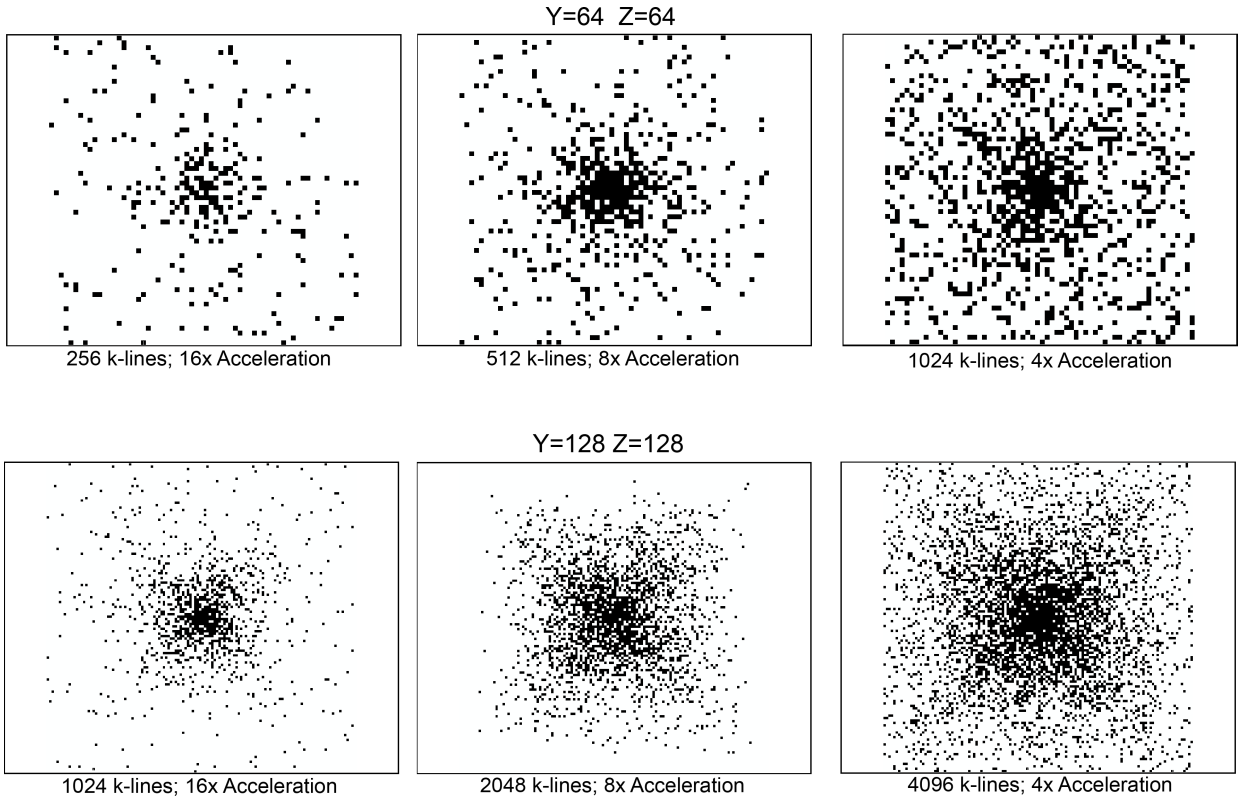

Figure 7.1: Sample undersampling schemes used for 3D compressed sensing acquisition and reconstruction.
Shown are (top row) schemes for images sized Y=64, Z=64 voxels and (bottom row) schemes for images sized Y=128, Z=128 voxels. The readout dimension (X) is fully-sampled and can assume any size. For each image size, sampling schemes for (left) 16× undersampling, (middle) 8× undersampling, and (right) 4× undersampling are shown. Every dark point represents a 3D k-space line that is acquired, while white space represents data not acquired.

7.3.2 CS Acquisition of ^{19}F Phantom and ^{19}F-Labeled Glioma Cells in Rat Brain

Compressed sensing acquisition and reconstruction was applied to the fluorine phantom used for simulations (phantom creation details are above), as well as to a rat brain injected with 9L glioma cells labeled with a PCE emulsion. 9L glioma cells were coincubated with a 7.5 mg/ml PCE emulsion, with cell culture details described elsewhere [75]. Labeled 9L cells (2×10^6) suspended in 10 μl PBS were injected into the right striatum of a female Fischer 344 rat. Unlabeled cells were injected into the contralateral side as a negative control. The rat was sacrificed and perfused transcardially with PBS followed by 4% paraformaldehyde in PBS. The brain was carefully excised and stored in 4% paraformaldehyde overnight for preservation. Additional details for this experimental model are described in Kadayakkara *et al.* [75]. Animal protocols were approved by the Institutional

Animal Care and Use Committee of Carnegie Mellon University and all animals received humane care in compliance with the NIH Guide for the Care and Use of Laboratory Animals. The phantom was imaged using an 11.7 T, 89-mm vertical bore Bruker AVANCE micro-imaging system using a Bruker fast spin echo (RARE) pulse sequence that had been modified to read in a file that detailed a randomly-generated k-space undersampling pattern (shown in Fig. 7.1) and acquire these k-space lines. The phantom was first imaged using a conventional RARE, followed by the custom CS-RARE pulse sequence, undersampling by factors of 2×, 4×, 8×, and 16×. Scan parameters were a resolution of 64×64×64 voxels, TE/TR=7/250 ms, echo train length = 4 echoes, averages = 1. Using the same apparatus and pulse sequence, the rat brain with labeled 9L glioma cells was also imaged using a conventional RARE with 64 averages, then by the custom CS-RARE pulse sequence with a single undersampling factor of 8x and differing numbers of signal averages (64, 16, and 8 averages). The rest of the scan parameters for the rat brain were a resolution of 64×64×64 voxels, TE/TR=7/600 ms, and echo train length = 4 echoes. Image reconstruction for both phantom and rat brain undersampled k-space data was then done by solving Eq. (7.1) using a nonlinear conjugate gradient descent algorithm with back-tracking line search [141].

7.4 Results

In general, images reconstructed using only L1-norm regularization contained noise resembling salt-and-pepper noise spread throughout the image. Images reconstructed using only TV-norm regularization contained blurring artifacts at the edges of signal-containing regions. Images were therefore all reconstructed using a convex combination of L1-norm and TV-norm constraints (TV-L1). Combining these constraints resulted in images with fewer false-positive results by reducing the noise artifact generated by L1-norm reconstruction, as well as alleviated the blurring effect from TV-norm reconstruction.

7.4.1 Simulated CS Reconstruction of ^{19}F Phantom

Compressed sensing reconstruction was tested by simulated k-space undersampling of previously-acquired fluorine phantom data. Figure 7.2 shows these reconstructions for the low-SNR spin echo image (SNR=3), medium-SNR gradient-echo image (SNR=7) and high-SNR fast spin echo

image (SNR=26). For the low-SNR (SNR=3) case, 2× undersampling had a better appearance (Fig. 7.2) than full sampling, allowing 5 capillaries to be resolved. This improved appearance over full sampling is due to the inherent noise-removal properties of the compressed sensing total variation constraint (Eq. (7.1)). 4×, 8×, and 16× undersampling for the low-SNR case resolved only three of the 7 capillaries, and 32 × undersampling presented confounding levels of image noise. For the medium-SNR (SNR=7) case, undersampling by between 2×-16× preserves visibility of 5–6 of 7 capillaries, with capillary edge blurring occurring for 8× and 16× undersampling, and 32× undersampling caused only 4 capillaries to be unambiguously present. For the high-SNR case (SNR=26), undersampling by 2×–16× creates almost perfect reproductions of the fully-sampled case (Fig. 7.2), while capillary edge blurring only occurs as undersampling reaches 32×.

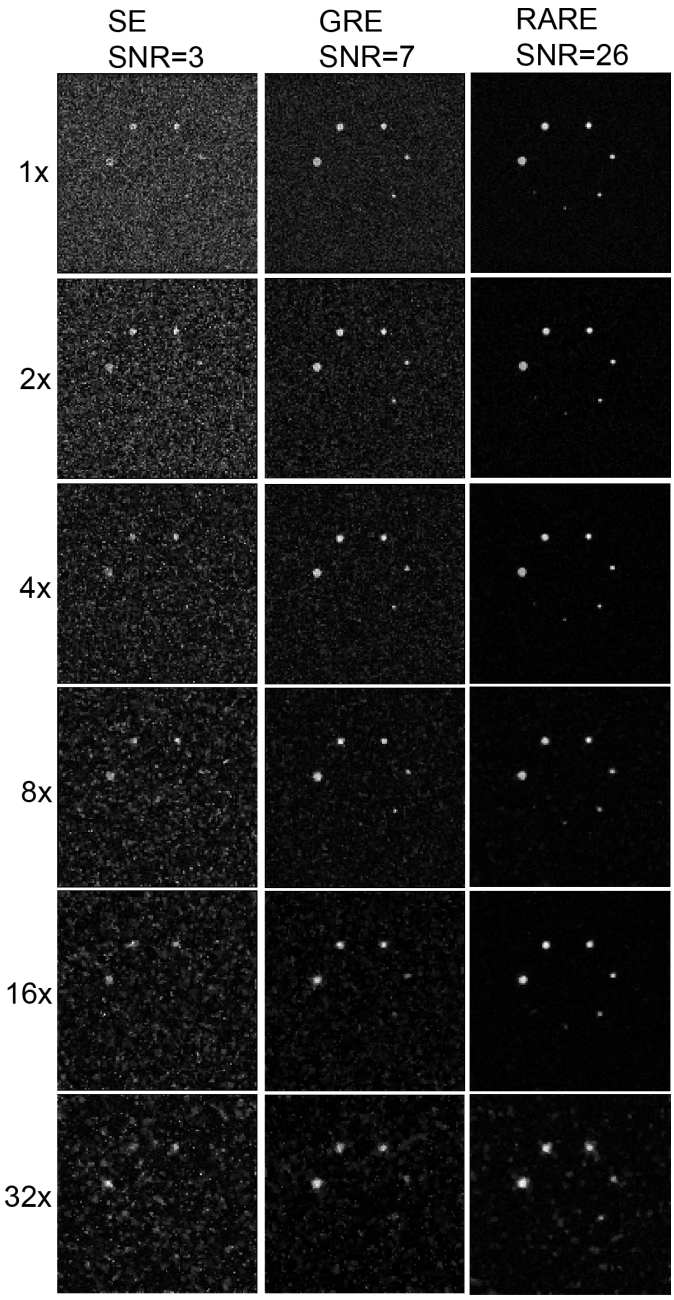

Figure 7.2: Compressed sensing reconstructions of fluorine phantom data by simulated k-space undersampling.

Shown are slices from three fully-acquired MRI scans: (left column) a spin-echo image with SNR=3, (middle column) a gradient echo image with SNR=7, and (right column) a fast spin echo image with SNR=26. The top row for the three scans shows each scans data reconstructed using a conventional 2D Fourier transform. Each successive row shows compressed sensing reconstructions of the three scans using simulated k-space undersampling by a factor of 2×, 4×, 8×, 16×, and 32x×. For the SNR=3 case (left column), 2× undersampling has a better appearance than full sampling, due to compressed sensing's inherent noise-removal properties its total variation constraint. 4×, 8×, and 16x undersampling for this case continue to resolve three capillaries, while 32× presents too much image noise. For the SNR=7 case (middle column), undersampling by 2×-16× preserves five capillaries, capillary edge blurring occurs for 8× and 16× cases, and 32× causes one capillary to be ambiguous. For the SNR=26 case, undersampling by 2×-16× creates almost perfect reproductions of the fully-sampled case, while capillary edge blurring only occurs as undersampling reaches 32×. Image dimensions are 128×128 pixels with a 4 cm image field-of-view.

7.4.2 CS Acquisition of ^{19}F Phantom and ^{19}F-Labeled Glioma Cells in Rat Brain

Compressed sensing acquisition and reconstruction were applied to the fluorine phantom used for simulations, as well as to a rat brain injected with 9L glioma cells labeled with a PCE emulsion. Figure 7.3 shows 3D compressed sensing acquisitions of the fluorine phantom. Panels (top to bottom) show conventional 3D fast spin echo (RARE; SNR $>$ 10) and 2×, 4×, 8×, and 16×-undersampled acquisitions of the same phantom made using the custom compressed sensing fast spin echo sequence (CS-RARE). The 2× and 8× acquisitions maintain an image quality that is qualitatively similar to the RARE acquisition, while the 8× and 16× acquisitions begin to show a blurring artifact in the X-dimension of the image. Because the phantom exhibits high signal and fluorine concentration, the 8× and 16× artifact is likely due to the sampling pattern used (Fig. 7.1), and not prevailing noise levels.

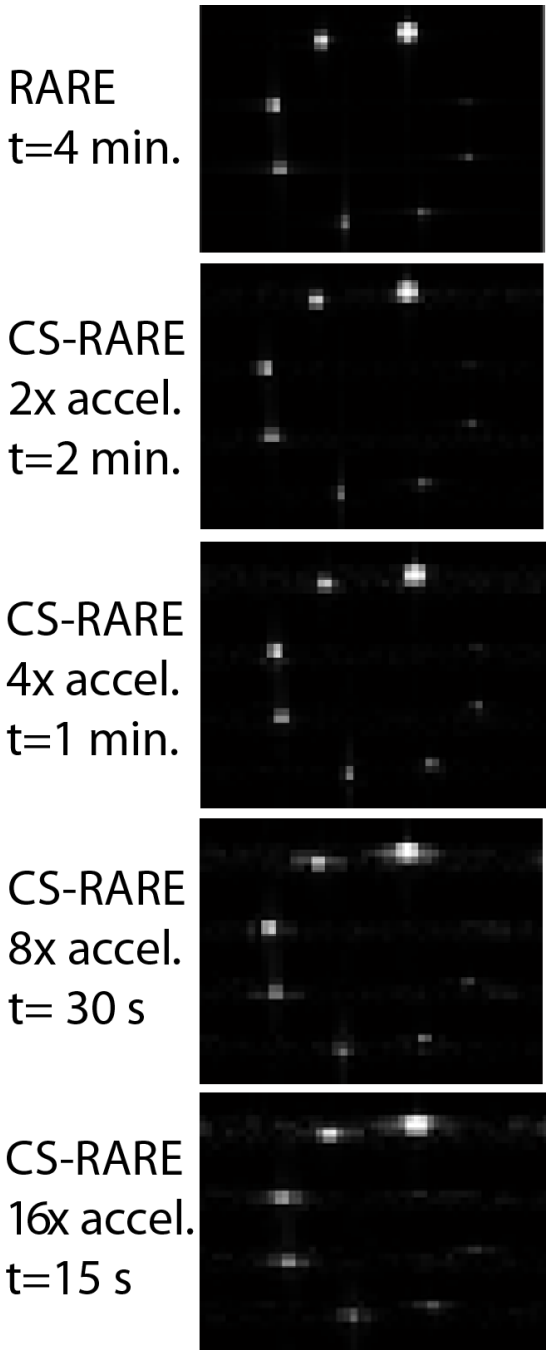

Figure 7.3: 3D compressed sensing acquisitions of fluorine phantom.
The top panel shows the central slice through a conventional 3D fast spin echo (RARE) acquisition of the fluorine phantom, with an SNR > 10. Subsequent panels (top to bottom) show 2×, 4×, 8×, and 16×-undersampled acquisitions of the same phantom made using a compressed sensing fast spin echo sequence (CS-RARE). The 2× and 8× acquisitions maintain an image quality that is qualitatively similar to the RARE acquisition, while the 8× and 16× acquisitions begin to show a blurring artifact in the image X-dimension. Because the phantom exhibits high signal and fluorine concentration, the 8× and 16× artifact is likely due to the sampling pattern used, and not prevailing noise levels (Fig. 7.1). All shown data was acquired in 3D with a resolution of 64×64×64 and isotropic voxels.

Figure 7.4 shows 3D compressed sensing acquisitions of rat brain injected with 2×10^6 9L glioma cells labeled with PCE emulsion. The first two rows in Fig. 7.4 show a 3D conventionally-acquired anatomical proton image and a 3D fast spin echo (RARE) fluorine acquisition (SNR = 4.7) of the same brain slice. Subsequent rows show the same brain acquired using an 8×-undersampled compressed sensing fast spin echo sequence (CS-RARE), using a decreasing number of signal averages. As expected from simulation results with the fluorine phantom, undersampling by 8× using the same number of signal averages produced an image with slight blurring of the fluorine deposit, but increased SNR due to suppression of image noise by the compressed sensing total variation constraint (Eq. (7.1)). Using the 8× undersampled CS-RARE sequence with fewer than 64 averages for this sample (Fig. 7.4) results in increasing incoherent image noise. Remarkably the size and general shape of the fluorine deposit remains intact when acquisition time is 1/60th that required by the conventional 3D fast spin echo acquisition. False-positive signal appears as speckles, reducing the chance it could be mistaken as actual signal clusters.

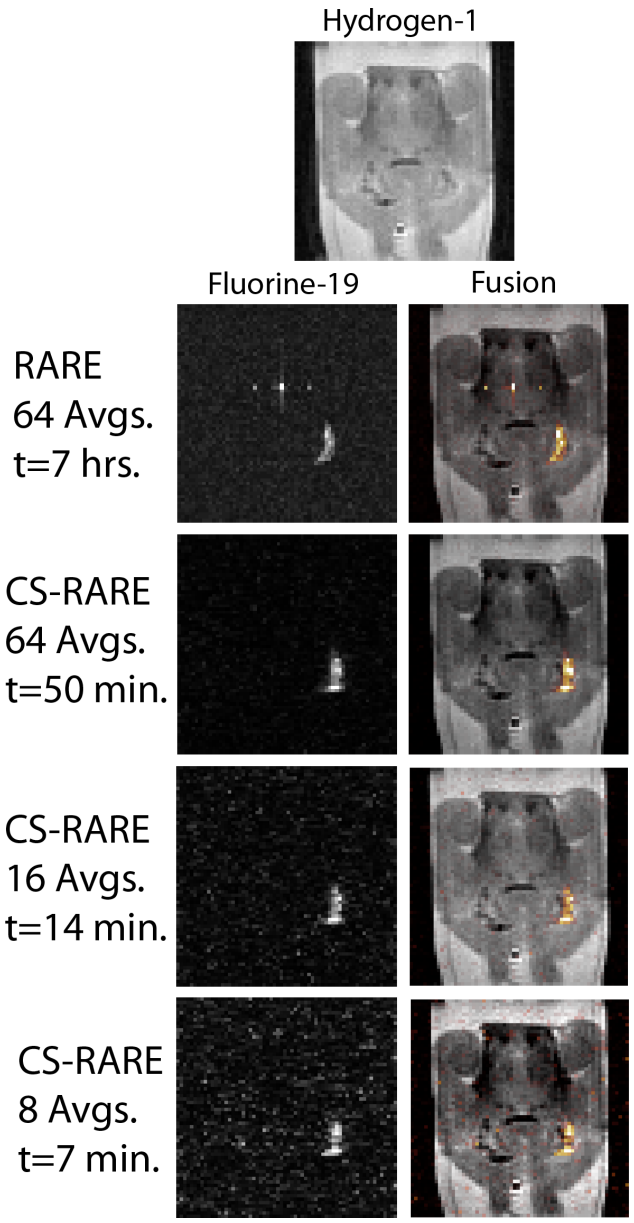

Figure 7.4: 3D compressed sensing acquisitions of rat brain injected with 2×10^6 9L glioma cells labeled with PCE emulsion.

The top panel shows brain anatomy in a conventional 3D proton acquisition. 9L glioma cells labeled with PCE emulsion were injected into the striatum on the right side of this image perspective, while unlabeled cells were injected as a control into the striatum on the left side. The second row shows a conventional 3D fast spin echo (RARE) fluorine acquisition (SNR = 4.7) of the same brain slice, alongside an image that fuses this fluorine image with the anatomical proton image. For 'fusion' images, proton signal is shown in grayscale, while fluorine signal is shown in a red and yellow 'hot' colorscale. Subsequent rows show the same brain acquired using an 8x-undersampled compressed sensing fast spin echo sequence (CS-RARE), using a decreasing number of signal averages. Notably, undersampling by 8× using the same number of signal averages produced an image with slight blurring of the fluorine deposit, but increased SNR due to suppression of image noise by the compressed sensing total variation constraint. The bottom two rows show that using the 8x undersample CS-RARE sequence with fewer than 64 averages for this sample results in increasing, yet incoherent, image noise. Remarkably the size and general shape of the fluorine deposit remains when acquisition time is 1/60th that required by the conventional 3D fast spin echo acquisition. False-positive signal appears as speckles, reducing the chance it could be mistaken as actual signal clusters. All shown data was acquired in 3D with a resolution of 64×64×64 and isotropic voxels of side length 250μm.

Figure 7.5 shows a prominent artifact in a 3D ^{19}F image presumably due to a k-space line contaminated by a constant offset DC receiver voltage. Because compressed sensing reconstruction aggressively undersamples k-space, it relies on correct values. Incorrect k-space values result in artifacts that appear more severe than when imaging using conventional imaging techniques. Therefore, this constant offset DC receiver voltage artifact is much less significant in this dataset's corresponding conventional RARE acquisition, and can be seen in the second row of Figure 7.4.

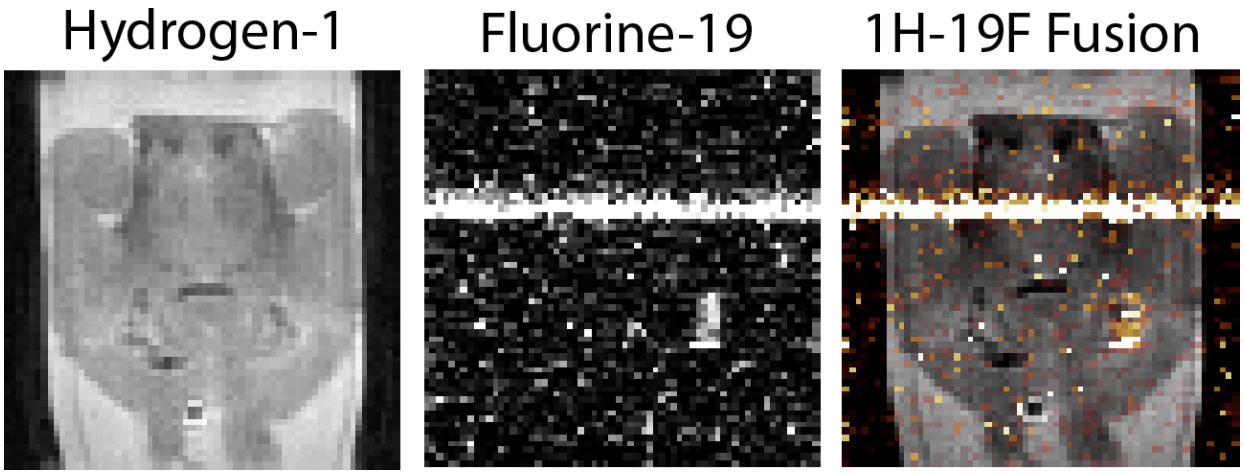

Figure 7.5: Prominent artifact unique to compressed sensing acquisition.
Shown are conventional proton, ^{19}F, and fused ^{1}H-^{19}F images of a rat brain injected with ^{19}F-tracer labeled 9L glioma cells. A central point artifact present in the acquired k-space data, apparently due to a constant offset DC receiver voltage, causes this 3D image reconstructed by compressed sampling to exhibit a prominent artifact. Because this reconstruction technique works by undersampling k-space lines, it is sensitive to incorrect sampled data, and can cause artifacts that are more severe than when imaged with conventional techniques. Notably, this artifact does not appear if reconstructed without the contaminated k-space line. This image data was acquired using the CS-RARE pulse sequence with 16× undersampling, 64×64×64 resolution, isotropic voxels with length 250μm, Averages=64, Acquisition time=50 min.

7.5 Discussion

Using standard compressed sensing acquisition and reconstruction methods greatly increased SNR/t when performing 3D imaging of sparse distributions of neat and intracellular ^{19}F tracer agents. Further improvements can be made at both the signal sampling acquisition stage and the image reconstruction stage. For the signal sampling stage, up to a 2-fold improvement in scan time has been reported through the use of Bayesian methods that compute optimal k-space trajectories for classes of image that exhibit similar characteristics [150]. The fluorine images analyzed here may have similar characteristics that could take advantage of dynamic k-space sampling using Bayesian

or other optimization methods. For the image reconstruction stage, additional constraints can be added, depending on whether they are appropriate for a particular image to be acquired. For images where signal-containing pixels appear in clusters, the use of Markov random fields (MRF) as part of the image reconstruction process been found to require only half the sparse samples relative to conventional L1-norm reconstruction methods [151]. Fluorine-19 images frequently have signal-containing pixels clustered together, making MRF a potentially strong constraint for images containing ^{19}F tracer agents. Another useful type of constraint would be anatomical constraints that model the amount of signal that is lost from the point-spread function, thereby restoring signal in anatomical regions where signal is present while maintaining image structure [152]. Other constraints that may be valuable include: a phase constraint for when phase angle is not expected to vary spatially [144]; object shape constraints such as object length and the total number of pixels the object occupies in an image [143]; object motion constraints, such as maximum allowed changes in position from previous locations in an image [143]; second-derivative total variation (TV2) constraint in order to smooth out the "staircasing" artifacts and patchy appearance of some TV-L1 reconstructed images [153]; and L0 norm minimization to large elements above a user-specified threshold (and regular L1-norm minimization to below-threshold small elements) in order to improve image details and suppress noise and artifacts [154]. Different combinations of these many constraints may accelerate ^{19}F image acquisition and improve reconstructed image quality, depending on the sample being imaged. In general, when fluorine-tracer distribution in an image is completely unknown, a general approach such as the one we demonstrated here would be appropriate, as the addition of constraints that do not represent the underlying signal distribution may result in images of a decreased quality.

When assessing different compressed sensing image reconstruction constraints, image quality metrics are a useful feedback mechanism, especially to computational systems that search for the optimal weighting parameters between these different constraints. The most common error metric when comparing two images is mean squared error (MSE), which calculates the absolute difference between pixel values of two images, regardless of how the images are numerically scaled. MSE has the disadvantage of calculating large errors between images that qualitatively look identical to a human viewer. Therefore, to complement MSE other error metrics have been developed that take into account how the human eye perceives images. One of the most popularly-used metrics in this

class is the structural similarity index (SSI), which computes the difference between two images based on how different structures within the image appear when considering human perception. With the many different possible combinations of available image reconstruction constraints, image quality metrics are poised to be an important component for developing pipelines for compressed sensing MRI.

There are a few additional constraints that may be directly applicable to the case of sparse fluorine tracer imaging. A constraint that prohibits the appearance of signal outside of anatomical boundaries of a subject would aid image reconstruction since such signal would certainly be false-positive signal. A second constraint that factors in foreknowledge about the fraction of pixels that contain signal in 3D ^{19}F images may be valuable, as would constraints that factor in the probability that a pixel contains ^{19}F signal, provided one or more of its neighbors contain signal. Proper and optimal weights for the convex combination of these and other constraints would need to be chosen, so that no one constraint completely obviates others. Finally, the use of non-Cartesian k-space sampling methods such as spiral or radial sampling may offer higher SNR/t than conventional Cartesian methods, since they naturally sample points near the center of 3D k-space with a higher density than points on the edge of k-space, which is how the compressed sensing sampling patterns behave (Fig. 7.1).

7.6 Conclusion

Using standard compressed sensing acquisition and reconstruction methods greatly increased SNR/t when performing 3D imaging of sparse distributions intracellular ^{19}F tracer agents. Increases in SNR/t are subject to subjective evaluation, but here we found that SNR/t improvements of 4× – 8× produced high-quality images when ^{19}F tracer agent was sufficiently sparse in the pixel domain. Future improvements will likely be made through dynamic generation of k-space sampling patterns and the addition of new image reconstruction constraints.

Chapter 8

Conclusion

8.1 Two-Compartment T_2 Contrast Model (T2CM)

Emerging cellular-molecular MRI methods often utilize T_2 contrast agents for *in vivo* detection. We present a general theoretical model to predict minimal contrast agent concentration requirements. This model can be used to aid the development of new generations of contrast agents and their applications, and may be an effective alternative to empirical concentration determinations in phantoms or *in vivo*. It is applicable to a wide range of T_2-type agents and delivery scenarios, requiring only a few readily-evaluated parameters.

8.2 Phase Slope Magnitude Imaging (PSM)

Emerging cellular-molecular MRI applications can benefit from improved sensitivity to paramagnetic CA distributions. The PSM approach generates positive contrast images that help to differentiate CAs from endogenous sources of tissue hypointensity. Unlike many other positive contrast imaging methods, PSM-image generation requires no prior knowledge of magnetic agent strength or distribution, no special pulse or gradient sequences, no extra scan time, and can be applied retrospectively to already-acquired data. Finally, these image generation methods can be made into an automated routine with few or no input parameters.

8.3 Phase Map Cross-Correlation Detection and Quantification (PDQ)

Superparamagnetic MRI contrast agents are increasingly being used to label cells and theranostic vehicles for *in vivo* imaging applications. This study addresses an urgent need in this emerging field which is the analysis and quantification of the resulting MR images. The PDQ algorithm offers great sensitivity by specifically searching for localized SPIO deposits in phase images. After detecting SPIO deposits, PDQ measures their magnetic moment, which is a quantity that can be used to improve detection specificity, reducing false positives and negatives. PDQ-detected dipole locations can be rendered as positive-contrast images for overlaying onto conventional magnitude images to quickly highlight contrast agent deposits. PDQ is capable of detecting single cells and cell clusters *in vivo*, and provides reliable magnetic measurements.

Like other positive contrast methods, PDQ helps differentiate dark areas due to SPIO from other intrinsic sources of hypointensity, but unlike these methods it requires no prior knowledge of agent concentration or distribution, no special imaging pulse sequences, no extra scan time, only a few user-set parameters, and can be applied retrospectively to previously acquired data. PDQ may have future applications for monitoring therapies, measuring cellular iron content, and observing cell behaviors.

8.4 Fluorine-19 Imaging using Compressed Sensing

The use of standard compressed sensing acquisition and reconstruction methods greatly increased SNR/t when performing 3D imaging of sparse distributions of intracellular ^{19}F tracer agents. Image quality is subject to subjective evaluation, but we found that SNR/t improvements of $4\times$ to $8\times$ were achievable while maintaining high-quality 3D images, provided ^{19}F tracer agent was sparse in the pixel domain. Future improvements will likely be made through dynamic generation of optimized k-space sampling patterns during the image acquisition stage and addition of new constraints to the image reconstruction stage.

References

[1] C.A. Castro, A. Ben-Yehudah, J.A. Ozolek, P.H. Mills, C.J. Redinger, J.D. Mich-Basso, D.A. McFarland, S.L. Oliver, E.T. Ahrens, and G.S. Schatten. Semiquantitative histopathology and 3D magnetic resonance microscopy as collaborative platforms for tissue identification and comparison within teratomas derived from pedigreed primate embryonic stem cells. *Stem Cell Res*, 5(3):201–211, Nov 2010.

[2] M. Toppings, C.A. Castro, P.H. Mills, B. Reinhart, G.P. Schatten, E.T. Ahrens, J.R. Chaillet, and J.M. Trasler. Profound phenotypic variation among mice deficient in the maintenance of genomic imprints. *Hum Reprod*, 23(4):807–818, Apr 2008.

[3] K.L. Eagleson, L.J. Schlueter McFadyen-Ketchum, E.T. Ahrens, P.H. Mills, M.D. Does, J. Nickols, and P. Levitt. Disruption of foxg1 expression by knock-in of cre recombinase: effects on the development of the mouse telencephalon. *Neuroscience*, 148(2):385–399, Aug 2007.

[4] N. Muja and J.W.M. Bulte. Magnetic resonance imaging of cells in experimental disease models. *Prog. Nucl. Magn. Reson. Spect.*, 55:61–77, 2009.

[5] W.Liu and J.A.Frank. Detection and quantification of magnetically labeled cells by cellular MRI. *Eur J Radiol*, 70(2):258–264, May 2009.

[6] Jeff W M Bulte. In vivo MRI cell tracking: clinical studies. *Am J Roentgenol*, 193(2):314–325, Aug 2009.

[7] I.J.M. de Vries, W.J. Lesterhuis, J.O. Barentsz, P. Verdijk, J.H. van Krieken, O.C. Boerman, W.J.G. Oyen, J.J. Bonenkamp, J.B. Boezeman, G.J. Adema, J.W.M. Bulte, T.W.J. Scheenen, C.J.A. Punt, A. Heerschap, and C.G. Figdor. Magnetic resonance tracking of dendritic cells in melanoma patients for monitoring of cellular therapy. *Nat Biotechnol*, 23(11):1407–1413, 2005.

[8] B.J. Nieman, J.Y. Shyu, J.J. Rodriguez, A.D. Garcia, A.L. Joyner, and D.H. Turnbull. In vivo MRI of neural cell migration dynamics in the mouse brain. *Neuroimage*, 50(2):456–464, Apr 2010.

[9] T. Ben-Hur, R.B. van Heeswijk, O. Einstein, M. Aharonowiz, R. Xue, E.E. Frost, S. Mori, B.E. Reubinoff, and J.W.M. Bulte. Serial in vivo MR tracking of magnetically labeled neural spheres transplanted in chronic EAE mice. *Magn Reson Med*, 57(1):164–171, Jan 2007.

[10] K.Nohroudi, S.Arnhold, T.Berhorn, K.Addicks, M.Hoehn, and U.Himmelreich. In vivo MRI stem cell tracking requires balancing of detection limit and cell viability. *Cell Transplant*, 19(4):431–441, 2010.

[11] D.A.Kedziorek, N.Muja, P.Walczak, J.Ruiz-Cabello, A.A.Gilad, C.C.Jie, and J.W.M.Bulte. Gene expression profiling reveals early cellular responses to intracellular magnetic labeling with superparamagnetic iron oxide nanoparticles. *Magn Reson Med*, 63(4):1031–1043, Apr 2010.

[12] S.Valable, E.L.Barbier, M.Bernaudin, S.Roussel, C.Segebarth, E.Petit, and C.Remy. In vivo MRI tracking of exogenous monocytes/macrophages targeting brain tumors in a rat model of glioma. *Neuroimage*, 37 Suppl 1:S47–S58, 2007.

[13] Thomas Grobner. Gadolinium–a specific trigger for the development of nephrogenic fibrosing dermopathy and nephrogenic systemic fibrosis? *Nephrol Dial Transplant*, 21(4):1104–1108, Apr 2006.

[14] P. Marckmann, L. Skov, K. Rossen, A. Dupont, M.B. Damholt, J.G. Heaf, and H.S. Thomsen. Nephrogenic systemic fibrosis: suspected causative role of gadodiamide used for contrast-enhanced magnetic resonance imaging. *J Am Soc Nephrol*, 17(9):2359–2362, Sep 2006.

[15] J.Zhu, L.Zhou, and F.Xing-Wu. Tracking neural stem cells in patients with brain trauma. *N Engl J Med*, 355(22):2376–2378, Nov 2006.

[16] E.M.Shapiro, O.Gonzalez-Perez, J.M.Garca-Verdugo, A.Alvarez-Buylla, and A.P.Koretsky. Magnetic resonance imaging of the migration of neuronal precursors generated in the adult rodent brain. *Neuroimage*, 32(3):1150–1157, Sep 2006.

[17] J.W. Bulte, T. Douglas, B. Witwer, S.C. Zhang, E. Strable, B.K. Lewis, H. Zywicke, B. Miller, P. van Gelderen, B.M. Moskowitz, I.D. Duncan, and J.A. Frank. Magnetodendrimers allow endosomal magnetic labeling and in vivo tracking of stem cells. *Nat Biotechnol*, 19(12):1141–1147, Dec 2001.

[18] C.Toso, J-P.Vallee, P.Morel, F.Ris, S.Demuylder-Mischler, M.Lepetit-Coiffe, N.Marangon, F.Saudek, A.M.James Shapiro, D.Bosco, and T.Berney. Clinical magnetic resonance imaging of pancreatic islet grafts after iron nanoparticle labeling. *Am J Transplant*, 8(3):701–706, Mar 2008.

[19] Y.L. Wu, Q. Ye, L.M. Foley, T.K. Hitchens, K. Sato, J.B. Williams, and C. Ho. In situ labeling of immune cells with iron oxide particles: An approach to detect organ rejection by cellular MRI. *Proc Natl Acad Sci U S A*, 103(6):1852–1857, 2006.

[20] J.B.Williams, Q.Ye, T.K.Hitchens, C.L.Kaufman, and C.Ho. MRI detection of macrophages labeled using micrometer-sized iron oxide particles. *J Magn Reson Imaging*, 25(6):1210–1218, Jun 2007.

[21] C.M. Long, H.W.M. van Laarhoven, J.W.M. Bulte, and H.I. Levitsky. Magnetovaccination as a novel method to assess and quantify dendritic cell tumor antigen capture and delivery to lymph nodes. *Cancer Res*, 69(7):3180–3187, Apr 2009.

[22] C. Heyn, C.V. Bowen, B.K. Rutt, and P.J. Foster. Detection threshold of single SPIO-labeled cells with FIESTA. *Magn Reson Med*, 53(2):312–320, 2005.

[23] M.H. Mendoncadias, E. Gaggelli, and P.C. Lauterbur. Paramagnetic contrast agents in nuclear magnetic-resonance medical imaging. *Semin Nuc Med*, 13(4):364–376, 1983.

[24] E.T. Ahrens, M. Feili-Hariri, H. Xu, G. Genove, and P.A. Morel. Receptor-mediated endocytosis of iron-oxide particles provides efficient labeling of dendritic cells for in vivo MR imaging. *Magn Reson Med*, 49(6):1006–1013, 2003.

[25] S. Cerdan, H.R. Lotscher, B. Kunnecke, and J. Seelig. Monoclonal antibody-coated magnetite particles as contrast agents in magnetic-resonance imaging of tumors. *Magn Reson Med*, 12(2):151–163, 1989.

[26] K.G. Go, J.W.M. Bulte, L. Deley, T.H. the, R.L. Kamman, C.E. Hulstaert, E.H. Blaauw, and L.D. Ma. Our approach towards developing a specific tumor-targeted MRI contrast agent for the brain. *European Journal of Radiology*, 16(3):171–175, 1993.

[27] P.W. So, S. Hotee, A.H. Herlihy, and J.D. Bell. Generic method for imaging transgene expression. *Magn Reson Med*, 54(1):218–221, 2005.

[28] C. Ho and T.K. Hitchens. A non-invasive approach to detecting organ rejection by MRI: monitoring the accumulations of immune cells at the transplanted organ. *Curr Pharm Biotechnol*, 5:551–566, 2004.

[29] Y. Anzai, C.W. Piccoli, E.K. Outwater, Stanford W., Bluemke D.A., Nurenberg P., Saini S., Maravilla K.R., Feldman D.E., Schmiedl U.P., Brunberg J.A., Francis I.R., Harms S.E., Som P.M., and Tempany C.M. Evaluation of neck and body metastases to nodes with ferumoxtran 10-enhanced MR imaging: phase III safety and efficacy study. *Radiology*, 228:777–788, 2003.

[30] E.M. Shapiro, S. Skrtic, and A.P. Koretsky. Sizing it up: Cellular MRI using micron-sized iron oxide particles. *Magn Reson Med*, 53(2):329–338, 2005.

[31] J.A. Frank, B.R. Miller, A.S. Arbab, H.A. Zywicke, E.K. Jordan, B.K. Lewis, L.H. Bryant, and J.W.M. Bulte. Clinically applicable labeling of mammalian and stem cells by combining; superparamagnetic iron oxides and transfection agents. *Radiology*, 228(2):480–487, 2003.

[32] P. Walczak, D.A. Kedziorek, A.A. Gilad, S. Lin, and J.W.M. Bulte. Instant MR labeling of stem cells using magnetoelectroporation. *Magn Reson Med*, 54(4):769–774, 2005.

[33] B.Qiu, D.Xie, P.Walczak, X.Li, J.Ruiz-Cabello, S.Minoshima, J.W.M.Bulte, and X.Yang. Magnetosonoporation: instant magnetic labeling of stem cells. *Magn Reson Med*, 63(6):1437–1441, Jun 2010.

[34] J.W.Bulte, S.Zhang, P.van Gelderen, V.Herynek, E.K.Jordan, I.D.Duncan, and J.A.Frank. Neurotransplantation of magnetically labeled oligodendrocyte progenitors: magnetic resonance tracking of cell migration and myelination. *Proc Natl Acad Sci U S A*, 96(26):15256–15261, Dec 1999.

[35] J.Yang, W.Tang, and X.Wang. Superparamagnetic iron oxide nanoparticles may affect endothelial progenitor cell migration ability and adhesion capacity. *Cytotherapy*, 12(2):251–259, Apr 2010.

[36] J. Oca-Cossio, H. Mao, N. Khokhlova, C.M. Kennedy, J.W. Kennedy, C.L. Stabler, E. Hao, A. Sambanis, N.E. Simpson, and L. Constantinidis. Magnetically labeled insulin-secreting cells. *Biochemical and Biophysical Research Communications*, 319(2):569–575, 2004.

[37] E.M. Shapiro, S. Skrtic, K. Sharer, J.M. Hill, C.E. Dunbar, and A.P. Koretsky. MRI detection of single particles for cellular imaging. *Proc Natl Acad Sci U S A*, 101(30):10901–10906, 2004.

[38] E. Pawelczyk, A.S. Arbab, S. Pandit, E. Hu, and J.A. Frank. Expression of transferrin receptor and ferritin following ferumoxides-protamine sulfate labeling of cells: implications for cellular magnetic resonance imaging. *NMR Biomed*, 19:581–592, 2006.

[39] A. Stroh, C. Faber, T. Neuberger, P. Lorenz, K. Sieland, P.M. Jakob, A. Webb, H. Pilgrimm, R. Schober, E.E. Pohl, and C. Zimmer. In vivo detection limits of magnetically labeled embryonic stem cells in the rat brain using high-field (17.6 T) magnetic resonance imaging. *Neuroimage*, 24(3):635–645, 2005.

[40] G. Genove, U. DeMarco, H.Y. Xu, W.F. Goins, and E.T. Ahrens. A new transgene reporter for in vivo magnetic resonance imaging. *Nat Me*, 11(4):450–454, 2005.

[41] B. Cohen, H. Dafni, G. Meir, A. Harmelin, and M. Neeman. Ferritin as an endogenous MRI reporter for noninvasive imaging of gene expression in c6 glioma tumors. *Neoplasia*, 7(2):109–117, 2005.

[42] B. Cohen, K. Ziv, V. Plaks, T. Israely, V. Kalchenko, A. Harmelin, L.E. Benjamin, and M. Neeman. MRI detection of transcriptional regulation of gene expression in transgenic mice. *Nat Med*, 13(4):498–503, 2007.

[43] E.T. Ahrens, W.F. Goins, and C.S. Robison. Genetic approaches for modulating MRI contrast. In J.W.M. Bulte and M. Modo, editors, *Molecular and Cellular MRI*, pages 123–140. CRC Press, San Diego, 2007.

[44] J.P. Basilion, S. Yeon, and R. Botnar. Magnetic resonance imaging: Utility as a molecular imaging modality. *Current Topics in Developmental Biology, Volume 70*, 70, 2005.

[45] R. Weissleder, A. Moore, U. Mahmood, R. Bhorade, H. Benveniste, E.A. Chiocca, and J.P. Basilion. In vivo magnetic resonance imaging of transgene expression. *Nat Med*, 6(3):351–5, 2000.

[46] E.M. Haacke, Y. Xu, Y.C. Cheng, and J.R. Reichenbach. Susceptibility weighted imaging (SWI). *Magn Reson Med*, 52(3):612–8, 2004.

[47] C.H. Cunningham, T. Arai, P.C. Yang, M.V. McConnell, J.M. Pauly, and S.M. Conolly. Positive contrast magnetic resonance imaging of cells labeled with magnetic nanoparticles. *Magn Reson Med*, 53(5):999–1005, 2005.

[48] V. Mani, K.C. Briley-Saebo, V.V. Itskovich, D.D. Samber, and Z.A. Fayad. GRadient echo Acquisition for Superparamagnetic particles with Positive contrast (GRASP): Sequence characterization in membrane and glass superparamagnetic iron oxide phantoms at 1.5T and 3T. *Magn Reson Med*, 55(1):126–135, 2006.

[49] M.Stuber, W.D.Gilson, M.Schr, D.A.Kedziorek, L.V.Hofmann, S.Shah, E.Vonken, J.W.M.Bulte, and D.L.Kraitchman. Positive contrast visualization of iron oxide-labeled stem cells using Inversion-Recovery with ON-resonant water suppression (IRON). *Magn Reson Med*, 58(5):1072–1077, Nov 2007.

[50] J.H. Seppenwoolde, M.A. Viergever, and C.J.G. Bakker. Passive tracking exploiting local signal conservation: The white marker phenomenon. *Magn Reson Med*, 50(4):784–790, 2003.

[51] C.J.G.Bakker, J.Seppenwoolde, and K.L.Vincken. Dephased MRI. *Magn Reson Med*, 55(1):92–97, Jan 2006.

[52] W.S. Warren, S. Ahn, M. Mescher, M. Garwood, K. Ugurbil, W. Richter, R.R. Rizi, J. Hopkins, and J.S. Leigh. MR imaging contrast enhancement based on intermolecular zero quantum coherences. *Science*, 281(5374):247–251, 1998.

[53] M.D. Robson, P.D. Gatehouse, M. Bydder, and G.M. Bydder. Magnetic resonance: An introduction to ultrashort TE (UTE) imaging. *Journal of Computer Assisted Tomography*, 27(6):825–846, 2003.

[54] S.Lai, J.R.Reichenbach, and E.M.Haacke. Commutator filter: a novel technique for the identification of structures producing significant susceptibility inhomogeneities and its application to functional MRI. *Magn Reson Med*, 36(5):781–787, Nov 1996.

[55] Parker H Mills and Eric T Ahrens. Enhanced positive-contrast visualization of paramagnetic contrast agents using phase images. *Magn Reson Med*, 62(5):1349–1355, Nov 2009.

[56] C.J.G.Bakker, H.de Leeuw, K.L.Vincken, E.Vonken, and J.Hendrikse. Phase gradient mapping as an aid in the analysis of object-induced and system-related phase perturbations in MRI. *Phys Med Biol*, 53(18):N349–N358, Sep 2008.

[57] G.McAuley, M.Schrag, P.Sipos, S.Sun, A.Obenaus, J.Neelavalli, E.M.Haacke, B.Holshouser, R.Madcsi, and W.Kirsch. Quantification of punctate iron sources using magnetic resonance phase. *Magn Reson Med*, 63(1):106–115, Jan 2010.

[58] W.T.Dixon, D.J.Blezek, L.A.Lowery, D.E.Meyer, A.M.Kulkarni, B.C.Bales, D.L.Petko, and T.K.Foo. Estimating amounts of iron oxide from gradient echo images. *Magn Reson Med*, 61(5):1132–1136, May 2009.

[59] C.Bos, M.A.Viergever, and C.J.G.Bakker. On the artifact of a subvoxel susceptibility deviation in spoiled gradient-echo imaging. *Magn Reson Med*, 50(2):400–404, Aug 2003.

[60] P.Mowat, F.Franconi, C.Chapon, L.Lemaire, J.Dorat, F.Hindr, J-P.Benoit, P.Richomme, and J-J.Le Jeune. Evaluating SPIO-labelled cell MR efficiency by three-dimensional quantitative T2* MRI. *NMR Biomed*, 20(1):21–27, Feb 2007.

[61] R. Schwarz, M. Schuurmans, J. Seelig, and B. Kunnecke. 19F-MRI of perfluorononane as a novel contrast modality for gastrointestinal imaging. *Magn Reson Med*, 41:80–86, 1999.

[62] A.M.Morawski, P.M.Winter, X.Yu, R.W.Fuhrhop, M.J.Scott, F.Hockett, J.D.Robertson, P.J.Gaffney, G.M.Lanza, and S.A.Wickline. Quantitative "magnetic resonance immunohistochemistry" with ligand-targeted 19-F nanoparticles. *Magn Reson Med*, 52(6):1255–1262, Dec 2004.

[63] A.M. Morawski, P.M. Winter, K.C. Crowder, S.D. Caruthers, R.W. Fuhrhop, M.J. Scott, J.D. Robertson, D.R. Abendschein, G.M. Lanza, and S.A. Wickline. Targeted nanoparticles for quantitative imaging of sparse molecular epitopes with MRI. *Magn Reson Med*, 51(3):480–486, 2004.

[64] S.D.Caruthers, A.M.Neubauer, F.D.Hockett, R.Lamerichs, P.M.Winter, M.J.Scott, P.J.Gaffney, S.A.Wickline, and G.M.Lanza. In vitro demonstration using 19F magnetic resonance to augment molecular imaging with paramagnetic perfluorocarbon nanoparticles at 1.5 Tesla. *Invest Radiol*, 41(3):305–312, Mar 2006.

[65] E.T.Ahrens, R.Flores, H.Xu, and P.A.Morel. In vivo imaging platform for tracking immunotherapeutic cells. *Nat Biotechnol*, 23(8):983–987, Aug 2005.

[66] M.Srinivas, P.A.Morel, L.A.Ernst, D.H.Laidlaw, and E.T.Ahrens. Fluorine-19 MRI for visualization and quantification of cell migration in a diabetes model. *Magn Reson Med*, 58(4):725–734, Oct 2007.

[67] K.C.Partlow, J.Chen, J.A.Brant, A.M.Neubauer, T.E.Meyerrose, M.H.Creer, J.A.Nolta, S.D.Caruthers, G.M.Lanza, and S.A.Wickline. 19F magnetic resonance imaging for stem/progenitor cell tracking with multiple unique perfluorocarbon nanobeacons. *FASEB J*, 21(8):1647–1654, Jun 2007.

[68] T.K.Hitchens, Q.Ye, D.F.Eytan, J.M.Janjic, E.T.Ahrens, and C.Ho. 19F MRI detection of acute allograft rejection with in vivo perfluorocarbon labeling of immune cells. *Magn Reson Med*, Feb 2011.

[69] H.P.Schlemmer, M.Becker, P.Bachert, A.Dietz, V.Rudat, B.Vanselow, P.Wollensack, I.Zuna, M.V.Knopp, H.Weidauer, M.Wannenmacher, and G.van Kaick. Alterations of intratumoral pharmacokinetics of 5-fluorouracil in head and neck carcinoma during simultaneous radiochemotherapy. *Cancer Res*, 59(10):2363–2369, May 1999.

[70] W. Wolf, C. Presant, and V. Waluch. 19F-MRS studies of fluorinated drugs in humans. *Advanced Drug Delivery Reviews*, 41:55–74, 2000.

[71] U.Noth, P.Grohn, A.Jork, U.Zimmermann, A.Haase, and J.Lutz. 19F-MRI in vivo determination of the partial oxygen pressure in perfluorocarbon-loaded alginate capsules implanted into the peritoneal cavity and different tissues. *Magn Reson Med*, 42(6):1039–1047, Dec 1999.

[72] D.K.K.Kadayakkara, J.M.Janjic, L.K.Pusateri, W.Young, and E.T.Ahrens. In vivo observation of intracellular oximetry in perfluorocarbon-labeled glioma cells and chemotherapeutic response in the CNS using fluorine-19 MRI. *Magn Reson Med*, 64(5):1252–1259, Nov 2010.

[73] Y.Fu, D.A.Kedziorek, R.Ouwerkerk, S.M.Shea, N.Azene, A.Arepally, J.W.Bulte, R.Krieg, F.Wacker, and D.L.Kraitchman. Multifunctional perfluorinated microcapsules for mesenchymal stem cell delivery and engraftment tracking using 19F MRI, x-ray, and ultrasound. *Proc Intl Soc Magn Reson Med*, 17:527, 2009.

[74] Jelena M Janjic and Eric T Ahrens. Fluorine-containing nanoemulsions for MRI cell tracking. *Wiley Interdiscip Rev Nanomed Nanobiotechnol*, 1(5):492–501, 2009.

[75] D.K.Kadayakkara, P.L.Beatty, M.S.Turner, J.M.Janjic, E.T.Ahrens, and O.J.Finn. Inflammation driven by overexpression of the hypoglycosylated abnormal mucin 1 (MUC1) links inflammatory bowel disease and pancreatitis. *Pancreas*, 39(4):510–515, May 2010.

[76] P.Brnert, D.G.Norris, H.Koch, W.Dreher, H.Reichelt, and D.Leibfritz. Fast perfluorocarbon imaging using 19F U-FLARE. *Magn Reson Med*, 29(2):226–234, Feb 1993.

[77] H.Lee, R.R.Price, G.E.Holburn, C.L.Partain, M.D.Adams, and W.P.Cacheris. In vivo fluorine-19 MR imaging: relaxation enhancement with Gd-DTPA. *J Magn Reson Imaging*, 4(4):609–613, 1994.

[78] P.Foster-Gareau, C.Heyn, A.Alejski, and B.K.Rutt. Imaging single mammalian cells with a 1.5 T clinical MRI scanner. *Magn Reson Med*, 49(5):968–971, May 2003.

[79] Kenneth S.Krane. *Introductory Nuclear Physics*. John Wiley & Sons, Inc., New York, 1988.

[80] J.F. Schenck. The role of magnetic susceptibility in magnetic resonance imaging: MRI magnetic compatibility of the first and second kinds. *Medical Physics*, 23(6):815–850, 1996.

[81] P. Raghavan. Table of nuclear moments. *Atomic Data and Nuclear Data Tables*, 42:189–291, 1989.

[82] P.T. Callaghan. *Principles of Nuclear Magnetic Resonance Microscopy*. Oxford University Press, 1991.

[83] Z-P. Liang and P.C. Lauterbur. *Principles of Magnetic Resonance Imaging*. SPIE Optical Engineering Press, 2000.

[84] M.L. Wood and F. Wehrli. Principles of magnetic resonance imaging. In D.D. Stark, editor, *Magnetic Resonance Imaging*, volume 1, pages 43–67. Mosby, St.Louis, 3rd. edition, 1999.

[85] N.A. Matwiyoff and W.M. Brooks. Principles of magnetic resonance imaging. In D.D. Stark, editor, *Magnetic Resonance Imaging*, volume 1, pages 43–67. Mosby, St.Louis, 3rd. edition, 1999.

[86] H. Gudbjartsson and S. Patz. The Rician distribution of noisy MRI data. *Magn Reson Med*, 34(6):910–4, 1995.

[87] R.J. Ogg, J.W. Langston, E.M. Haacke, R.G. Steen, and J.S. Taylor. The correlation between phase shifts in gradient-echo MR images and regional brain iron concentration. *Magn Reson Imaging*, 17(8):1141–1148, 1999.

[88] Y. Wang, Y. Yu, D. Li, K.T. Bae, J.J. Brown, W. Lin, and E.M. Haacke. Artery and vein separation using susceptibility-dependent phase in contrast-enhanced MRA. *J Magn Reson Imaging*, 12(5):661–670, 2000.

[89] R. Salomir, B.D. De Senneville, and C.T.W. Moonen. A fast calculation method for magnetic field inhomogeneity due to an arbitrary distribution of bulk susceptibility. *Concepts in Magnetic Resonance Part B-Magnetic Resonance Engineering*, 19B(1):26–34, 2003.

[90] L. Li and J.S. Leigh. Quantifying arbitrary magnetic susceptibility distributions with MR. *Magn Reson Med*, 51(5):1077–1082, 2004.

[91] L. de Rochefort, T. Liu, B. Kressler, J. Liu, P. Spincemaille, V. Lebon, J. Wu, and Y. Wang. Quantitative susceptibility map reconstruction from mr phase data using bayesian regularization: validation and application to brain imaging. *Magn Reson Med*, 63(1):194–206, Jan 2010.

[92] P.W. Kuchel, B.E. Chapman, W.A. Bubb, P.E. Hansen, C.J. Durrant, and M.P. Hertzberg. Magnetic susceptibility: Solutions, emulsions, and cells. *Concepts in Magnetic Resonance Part A*, 18A(1):56–71, 2003.

[93] A. Rauscher, J. Sedlacik, M. Barth, H.J. Mentzel, and J.R. Reichenbach. Magnetic susceptibility-weighted MR phase imaging of the human brain. *Am J Roentgenol*, 26(4):736–742, 2005.

[94] P. Robson and L. Hall. Identifying particles in industrial systems using MRI susceptibifity artefacts. *Aiche Journal*, 51(6):1633–1640, 2005.

[95] R. Cusack and N. Papadakis. New robust 3-D phase unwrapping algorithms: Application to magnetic field mapping and undistorting echoplanar images. *Neuroimage*, 16(3):754–764, 2002.

[96] E. Haacke, R.W. Brown, R.W. Thompson, and R. Venkatesan. Signal, contrast and noise. In E.Mark Haacke, editor, *Magnetic Resonance Imaging*, pages 331–380. John Wiley & Sons, Inc, 1999.

[97] S. Chavez, Q.S. Xiang, and L. An. Understanding phase maps in MRI: A new cutline phase unwrapping method. *IEEE Trans Med Imaging*, 21(8):966–977, 2002.

[98] M. Jenkinson. Fast, automated, N-dimensional phase-unwrapping algorithm. *Magn Reson Med*, 49(1):193–197, 2003.

[99] H.A. Ward, S.J. Riederer, and Jr. Jack, C.R. Real-time autoshimming for echo planar time-course imaging. *Magn Reson Med*, 48(5):771–80, 2002.

[100] L.M. Klassen and R.S. Menon. Robust automated shimming technique using arbitrary mapping acquisition parameters (RASTAMAP). *Magn Reson Med*, 51(5):881–7, 2004.

[101] P.H. Mills and E.T. Ahrens. Theoretical MRI contrast model for exogenous T2 agents. *Magn Reson Med*, 57(2):442–7, 2007.

[102] E.T. Ahrens, U. Rothbacher, R.E. Jacobs, and S.E. Fraser. A model for MRI contrast enhancement using t_1 agents. *Proc Natl Acad Sci USA*, 95:8443–8448, 1998.

[103] R.E. Hendrick. Image contrast and noise. In D.D. Stark, editor, *Magnetic Resonance Imaging*, volume 1, pages 43–67. Mosby, St.Louis, 3rd. edition, 1999.

[104] E.C. Theil. Ferritin - structure, gene-regulation, and cellular function in animals, plants, and microorganisms. *Annual Review of Biochemistry*, 56:289–315, 1987.

[105] R.A. Brooks, J. Vymazal, R.B. Goldfarb, J.W.M. Bulte, and P. Aisen. Relaxometry and magnetometry of ferritin. *Magn Reson Med*, 40(2):227–235, 1998.

[106] S.H. Koenig, R.D. Brown, J.F. Gibson, R.J. Ward, and T.J. Peters. Relaxometry of ferritin solutions and the influence of the Fe-3+ core ions. *Magn Reson Med*, 3(5):755–767, 1986.

[107] J. Vymazal, R.A. Brooks, J.W.M. Bulte, D. Gordon, and P. Aisen. Iron uptake by ferritin: NMR relaxometry studies at low iron loads. *Journal of Inorganic Biochemistry*, 71(3-4):153–157, 1998.

[108] Y. Gossuin, A. Roch, R.N. Muller, and P. Gillis. Relaxation induced by ferritin and ferritin-like magnetic particles: The role of proton exchange. *Magn Reson Med*, 43(2):237–243, 2000.

[109] Z. Gottesfeld and M. Neeman. Ferritin effect on the transverse relaxation of water: NMR microscopy at 9.4 T. *Magn Reson Med*, 35(4):514–520, 1996.

[110] K.P. Whittall, A.L. MacKay, D.A. Graeb, R.A. Nugent, D.K.B. Li, and D.W. Paty. In vivo measurement of T-2 distributions and water contents in normal human brain. *Magn Reson Med*, 37(1):34–43, 1997.

[111] E.T. Ahrens and D.J. Dubowitz. Peripheral somatosensory fMRI in mouse at 11.7 t. *NMR Biomed*, 14(5):318–324, 2001.

[112] M.F. Tweedle. The ProHance story: the making of a novel MRI contrast agent. *European Radiology*, 7:S225–S230, 1997.

[113] A. Tanimoto, K. Oshio, M. Suematsu, D. Pouliquen, and D.D. Stark. Relaxation effects of clustered particles. *J Magn Reson Imaging*, 14(1):72–77, 2001.

[114] Y. Gossuin, R.N. Muller, and P. Gillis. Relaxation induced by ferritin: a better understanding for an improved MRI iron quantification. *NMR Biomed*, 17(7):427–432, 2004.

[115] Teukolsky SA Vetterling WT Press WH, Flannery BP. *Numerical Recipes in C: The Art of Scientific Computing*. Cambridge University Press, 1988-1992.

[116] W. Hanicke and H.U. Vogel. An analytical solution for the SSFP signal in MRI. *Magn Reson Med*, 49(4):771–775, 2003.

[117] J.M.Bonny, W.Laurent, and J.P.Renou. Detection of susceptibility effects using simultaneous T2* and magnetic field mapping. *Magn Reson Imaging*, 18(9):1125–1128, Nov 2000.

[118] H.Dahnke, W.Liu, D.Herzka, J.A.Frank, and T.Schaeffter. Susceptibility gradient mapping (SGM): a new postprocessing method for positive contrast generation applied to superparamagnetic iron oxide particle (SPIO)-labeled cells. *Magn Reson Med*, 60(3):595–603, Sep 2008.

[119] A.P. Koretsky, Y.J. Lin, Schorle H., and Jaenisch R. Genetic control of MRI contrast by expression of the transferrin receptor. *Proc Soc Magn Reson*, 4:54–71, 1996.

[120] G. Girolomoni, M.B. Lutz, S. Pastore, C.U. Assmann, A. Cavani, and P. Ricciardi-Castagnoli. Establishment of a cell line with features of early dendritic cell precursors from fetal mouse skin. *Eur J Immunol*, 25(8):2163–9, 1995.

[121] C.W. Chen and H.A. Zebker. Two-dimensional phase unwrapping with use of statistical models for cost functions in nonlinear optimization. *J Opt Soc Am A*, 18:338–351, 2001.

[122] A. Rauscher, M. Barth, J.R. Reichenbach, R. Stollberger, and E. Moser. Automated unwrapping of MR phase images applied to BOLD MR-venography at 3 Tesla. *J Magn Reson Imaging*, 18(2):175–180, 2003.

[123] P.H. Mills, Y-J.L. Wu, C. Ho, and E.T. Ahrens. Sensitive and automated detection of iron-oxide labeled cells using phase image cross-correlation analysis. *Magn Reson Imaging*, 26(5):618–628, 2008.

[124] B.P. Barnett, A. Arepally, P.V. Karmarkar, D. Qian, W.D. Gilson, P. Walczak, V. Howland, L. Lawler, C. Lauzon, M. Stuber, D.L. Kraitchman, and J.W. Bulte. Magnetic resonance-guided, real-time targeted delivery and imaging of magnetocapsules immunoprotecting pancreatic islet cells. *Nat Med*, 13(8):986–91, 2007.

[125] L.M.Foley, T.K.Hitchens, C.Ho, K.L.Janesko-Feldman, J.A.Melick, H.Bayir, and P.M.Kochanek. Magnetic resonance imaging assessment of macrophage accumulation in mouse brain after experimental traumatic brain injury. *J Neurotrauma*, 26(9):1509–1519, Sep 2009.

[126] N.Beckmann, C.Cannet, A.L.Babin, F.Bl, S.Zurbruegg, R.Kneuer, and V.Dousset. In vivo visualization of macrophage infiltration and activity in inflammation using magnetic resonance imaging. *Wiley Interdiscip Rev Nanomed Nanobiotechnol*, 1(3):272–298, 2009.

[127] E.H.Sinz, P.M.Kochanek, M.P.Heyes, S.R.Wisniewski, M.J.Bell, R.S.Clark, S.T.DeKosky, A.R.Blight, and D.W.Marion. Quinolinic acid is increased in CSF and associated with mortality after traumatic brain injury in humans. *J Cereb Blood Flow Metab*, 18(6):610–615, Jun 1998.

[128] Z.Zhang, M.Artelt, M.Burnet, K.Trautmann, and H.J.Schluesener. Early infiltration of CD8+ macrophages/microglia to lesions of rat traumatic brain injury. *Neuroscience*, 141(2):637–644, Aug 2006.

[129] David J.Griffiths. *Introduction to Electrodynamics*. Upper Saddle River: Prentice Hall, 1999.

[130] S.J. Orfanidis. *Optimum Signal Processing.An Introduction.* Prentice-Hall, Englewood Cliffs, NJ, 2nd edition edition, 1996.

[131] J.P. Lewis. Fast template matching. *Vision Interface*, pages 120–123, 1995.

[132] Q.Ye, Y.L.Wu, L.M.Foley, T.K.Hitchens, D.F.Eytan, H.Shirwan, and C.Ho. Longitudinal tracking of recipient macrophages in a rat chronic cardiac allograft rejection model with noninvasive magnetic resonance imaging using micrometer-sized paramagnetic iron oxide particles. *Circulation*, 118(2):149–156, Jul 2008.

[133] M.A.Banks, D.W.Porter, W.H.Pailes, D.Schwegler-Berry, W.G.Martin, and V.Castranova. Taurine content of isolated rat alveolar type I cells. *Comp Biochem Physiol B*, 100(4):795–799, 1991.

[134] O. Bomati-Miguel, M.P. Morales, P. Tartaj, J. Ruiz-Cabello, P. Bonville, M. Santos, X. Zhao, and S. Veintemillas-Verdaguer. Fe-based nanoparticulate metallic alloys as contrast agents for magnetic resonance imaging. *Biomaterials*, 26:5695–5703, 2005.

[135] T.Shen, R.Weissleder, M.Papisov, A.Bogdanov, and T.J.Brady. Monocrystalline iron oxide nanocompounds (MION): physicochemical properties. *Magn Reson Med*, 29(5):599–604, May 1993.

[136] S.Schlatt, D.M.de Kretser, and M.P.Hedger. Mitosis of resident macrophages in the adult rat testis. *J Reprod Fertil*, 116(2):223–228, Jul 1999.

[137] M.J.Evans, L.J.Cabral, R.J.Stephens, and G.Freeman. Cell division of alveolar macrophages in rat lung following exposure to NO2. *Am J Pathol*, 70(2):199–208, Feb 1973.

[138] U.Gamper, P.Boesiger, and S.Kozerke. Compressed sensing in dynamic MRI. *Magn Reson Med*, 59(2):365–373, Feb 2008.

[139] M.Doneva, P.Brnert, H.Eggers, C.Stehning, J.Sngas, and A.Mertins. Compressed sensing reconstruction for magnetic resonance parameter mapping. *Magn Reson Med*, 64(4):1114–1120, Oct 2010.

[140] J.Paulsen, V.S.Bajaj, and A.Pines. Compressed sensing of remotely detected MRI velocimetry in microfluidics. *J Magn Reson*, 205(2):196–201, Aug 2010.

[141] M. Lustig, D. Donoho, and J.M. Pauly. Sparse MRI: The application of compressed sensing for rapid MR imaging. *Magn Reson Med*, 58(6):1182–1195, 2007.

[142] J.Yerly, M.L.Lauzon, H.S.Chen, and R.Frayne. A simulation-based analysis of the potential of compressed sensing for accelerating passive MR catheter visualization in endovascular therapy. *Magn Reson Med*, 63(2):473–483, Feb 2010.

[143] C.O.Schirra, S.Weiss, S.Krueger, S.F.Pedersen, R.Razavi, T.Schaeffter, and S.Kozerke. Toward true 3D visualization of active catheters using compressed sensing. *Magn Reson Med*, 62(2):341–347, Aug 2009.

[144] Y.Kim, S.S.Narayanan, and K.S.Nayak. Accelerated three-dimensional upper airway MRI using compressed sensing. *Magn Reson Med*, 61(6):1434–1440, Jun 2009.

[145] S.Ajraoui, K.J.Lee, M.H.Deppe, S.R.Parnell, J.Parra-Robles, and J.M.Wild. Compressed sensing in hyperpolarized 3He lung MRI. *Magn Reson Med*, 63(4):1059–1069, Apr 2010.

[146] T.Kampf, A.Fischer, T.C.Basse-Lsebrink, G.Ladewig, F.Breuer, G.Stoll, P.M.Jakob, and W.R.Bauer. Application of compressed sensing to in vivo 3D 19F CSI. *J Magn Reson*, 207(2):262–273, Dec 2010.

[147] D.Liang, B.Liu, J.Wang, and L.Ying. Accelerating SENSE using compressed sensing. *Magn Reson Med*, 62(6):1574–1584, Dec 2009.

[148] E. Candes, N. Braun, and M. Wakin. Sparse signal and image recovery from compressive samples. In *Proc.4th IEEE Int.Symp.Biomedical Imaging: From Nano to Macro ISBI 2007*, pages 976–979, 2007.

[149] J. Romberg. Imaging via compressive sampling. 25(2):14–20, 2008.

[150] M.Seeger, H.Nickisch, R.Pohmann, and B.Schlkopf. Optimization of k-space trajectories for compressed sensing by Bayesian experimental design. *Magn Reson Med*, 63(1):116–126, Jan 2010.

[151] V.Cevher, M.F.Duarte, C.Hegde, and R.G.Baraniuk. Sparse signal recovery using markov random fields. *Proceedings of the Workshop on Neural Information Processing Systems*, December, 2008.

[152] J.P.Haldar, D.Hernando, S.Song, and Z.Liang. Anatomically constrained reconstruction from noisy data. *Magn Reson Med*, 59(4):810–818, Apr 2008.

[153] F.Knoll, K.Bredies, T.Pock, and R.Stollberger. Second order total generalized variation (TGV) for MRI. *Magn Reson Med*, 65(2):480–491, Feb 2011.

[154] D.Liang and L.Ying. A hybrid L0-L1 minimization algorithm for compressed sensing MRI. *Proc Intl Soc Magn Reson Med*, 2010.

Appendix 1

Source Code

9.1 PSM - Phase Slope Magnitude Imaging

9.1.1 PSM.m

```
%%%%%%%%%%%%%%%%%%%%%%%%%%%%%%%%%%%%%%%%%%%%%%%%%%%%%%%%%%%%%%%%%%%%%%%%%%%%%%%%
% @file PSM.m
% @author Parker Mills, Ahrens Lab, Carnegie Mellon
% @brief Creates phase slope magnitude (PSM), angle (PSA), Angle Coherence (AC)
%        and Composite images based on provided phase image. 2nd and 3rd derivatives
%        were not found to be useful for analysis of phase changes in MR images, but
%        perhaps trying it with other image types or biological samples my prove of use.
%
% ========================= INPUT PARAMETERS ==========================
% @param     image              (2D/3D Float)     Phase-unwrapped, optionally high-pass filtered image
% @param     dimensionality     (String)          '2d': Calculation performed slicewise in 2D
%                                                 '3d': Calculation performed in full 3D
%
% ========================= RETURNED DATA =============================
%
% ====Conventional PSM Products (Magnitude, x-,y-,z-components) ====
% @return  PSMrun.PSM.mag         (2D/3D Float)  Phase slope magnitude image   (*Main product* - Magnitude
    of phase change over space)
%          PSMrun.PSM.x           (2D/3D Float)  X-direction phase slope magnitude image   (X-component of
    phase change over space (1st derivative))
%          PSMrun.PSM.y           (2D/3D Float)  Y-direction phase slope magnitude image   (Y-component of
    phase change over space (1st derivative))
%          PSMrun.PSM.z           (2D/3D Float)  Z-direction phase slope magnitude image   (Z-component of
    phase change over space (1st derivative))
%
% ====Unpublished/Experimental PSM Products (Phase slope angle, angle coherence, and composite images)====
% @return  PSMrun.PSA         (2D/3D Float)  Phase slope angle image       (The angle (in radians) of the
    direction in which phase is changing over space)
% @return  PSMrun.AC          (2D/3D Float)  Phase angle coherence image   (Measure of how consistent the
    phase slope angle (PSA) is in a 3x3 pixel region. Calculated only for x-y plane, and not for z.)
% @return  PSMrun.Composite   (2D/3D Float)  Composite image               (Product of PSM.mag and AC
    images (PSM .* AC). In theory, highlights rapid spatial changes in phase that are all happening in the
     same direction!)
%
%
% ========================= ASSUMPTIONS ===============================
% @assume Input data is phase data that has been unwrapped ([0, 2*pi] boundaries removed), and optionally
    high-pass filtered
%
% ========================= DEPENDENCIES ==============================
% @depend myfun.m
% @depend
%
% ========================= EXAMPLE USAGE =============================
% PSMrun = PSM(image, dimensionality)
% PSMrun = PSM(unwrapped_phase, '2d')
% PSMrun = PSM(unwrapped_phase, '3d')
%
%%%%%%%%%%%%%%%%%%%%%%%%%%%%%%%%%%%%%%%%%%%%%%%%%%%%%%%%%%%%%%%%%%%%%%%%%%%%%%%%


function PSMrun = PSM(image, dimensionality)


%% Preferences
```

```
pref_diff_level = 1; %Which derivative to calculate (1 = first derivative, 2 = 2nd derivative, etc.)
pref_calculate_experimental = 0; % Calculating experimental images computationally intensive for large 3D
    volumes


%% Gather information and perform sanity checks

% Get dimensions
[x_dim y_dim z_dim] = size(image);

% If 2D image is given and user requested 3D PSM
if(ndims(image) == 2 && strcmp(dimensionality,'3d'))
    error('PSM: 3D computation requested for 2D image. Quitting.');
end

% Ensure dimensionality is either 2D or 3D
if(~strcmp(dimensionality,'2d') && ~strcmp(dimensionality,'3d'))
    error('PSM: dimensionality must be "2d" or "3d". Quitting.');
end



%% Compute difference (first derivative by default preferences) between neighboring voxels in 2D or 3D
% Also reduces floating point precision from double to single
PSMrun.PSM.x = single(diff(image, pref_diff_level, 1));
PSMrun.PSM.y = single(diff(image, pref_diff_level, 2));
if(strcmp(dimensionality,'3d'))
    PSMrun.PSM.z = single(diff(image, pref_diff_level, 3));
end



%% Preallocate results
if(strcmp(dimensionality,'2d'))
    PSMrun.PSM.mag   = ones(x_dim-pref_diff_level, y_dim-pref_diff_level, z_dim);
    PSMrun.PSA       = ones(x_dim-pref_diff_level, y_dim-pref_diff_level, z_dim);
    PSMrun.AC        = ones(x_dim-pref_diff_level, y_dim-pref_diff_level, z_dim);
    PSMrun.Composite = ones(x_dim-pref_diff_level, y_dim-pref_diff_level, z_dim);
else
    PSMrun.PSM.mag   = ones(x_dim-pref_diff_level, y_dim-pref_diff_level, z_dim - pref_diff_level);
    PSMrun.PSA       = ones(x_dim-pref_diff_level, y_dim-pref_diff_level, z_dim - pref_diff_level);
    PSMrun.AC        = ones(x_dim-pref_diff_level, y_dim-pref_diff_level, z_dim - pref_diff_level);
    PSMrun.Composite = ones(x_dim-pref_diff_level, y_dim-pref_diff_level, z_dim - pref_diff_level);
end



%% Compute magnitude and angle for each row, filling [mag, angle]
for j1 = 1:x_dim - pref_diff_level
    for j2 = 1:y_dim - pref_diff_level

        if(strcmp(dimensionality,'3d'))
            for j3 = 1:z_dim - pref_diff_level
                PSMrun.PSM.mag(j1,j2,j3) = sqrt( PSMrun.PSM.x(j1,j2,j3).^2 + PSMrun.PSM.y(j1,j2,j3).^2 +
                    PSMrun.PSM.z(j1,j2,j3).^2 );
            end
            PSMrun.PSA(j1,j2,:) = atan2(PSMrun.PSM.x(j1,j2,1:z_dim-pref_diff_level), PSMrun.PSM.y(j1,j2,1:
                z_dim-pref_diff_level)); % Angle is only done for X-Y plane and doesn't factor in Z
        else
            PSMrun.PSM.mag(j1,j2,:) = sqrt( PSMrun.PSM.x(j1,j2,1:z_dim).^2 + PSMrun.PSM.y(j1,j2,1:z_dim)
                .^2);
            PSMrun.PSA(j1,j2,:) = atan2(PSMrun.PSM.x(j1,j2,1:z_dim), PSMrun.PSM.y(j1,j2,1:z_dim)); % Angle
                is only done for X-Y plane and doesn't factor in Z
        end

    end
end



%% Compute Angle Coherence (AC) and Composite images
if(pref_calculate_experimental)
    if(strcmp(dimensionality,'3d'))
        for j3 = 1:z_dim - pref_diff_level
            PSMrun.AC(:,:,j3) = -nlfilter(PSMrun.PSA(:,:,j3), [3 3], @neighbor_differences);
        end
    else
        for j3 = 1:z_dim
            PSMrun.AC(:,:,j3) = -nlfilter(PSMrun.PSA(:,:,j3), [3 3], @neighbor_differences);
        end
    end
    PSMrun.Composite = PSMrun.PSM.mag .* PSMrun.AC;
end


%%%%%%%%%%%%%%%
%     EOF
%%%%%%%%%%%%%%%%%
```

9.2 PDQ - Phase Cross-Correlation Detection and Quantification

9.2.1 PDQ.m

```
%%%%%%%%%%%%%%%%%%%%%%%%%%%%%%%%%%%%%%%%%%%%%%%%%%%%%%%%%%%%%%%%%%%%%%%%%%%%%%%%
% @file PDQ.m
% @brief Runs entire PDQ operation on an MRIdata object
% @author Parker Mills, Ahrens Lab, Carnegie Mellon 2009
%
% ========== INPUT PARAMETERS ==========
% @param MRIdata                (MRIdata)       MRI dataset to be analyzed by PDQ (see README.txt for
    datatype details)
% @param CHI_background         (Float)         Magnetic susceptibility of background material
    surrounding SPIO deposits.
%                                               Necessary for accurate determination of dipole's
    susceptibility and magnetic dipole moment
%
% @param orientation            (Float)         OPTIONAL Orientation axis, if already known beforehand
% @param user_radius            (Float)         OPTIONAL Estimated radius range of sphere of SPIO. 2
    element vector if upper-bound and lower-bound known
%                                                       3 element vector if optimal_radius also known:
     [lower_bound upper_bound] -OR- [lower_bound upper_bound optimal_radius]
%
% @param dual_gaussian          (Float)         OPTIONAL
%
% ========== RETURNED DATA ==========
% @return MRIdata               (MRIdata)           PDQ result (see README.txt)
%
% ========== ASSUMPTIONS ==========
% @assume If a data item is already present in the MRIdata structure, PDQ will not re-calculate those
    items.
%         You must delete them in order for them to be recalculated.
%         For example, "MRIdata = rmfield(MRIdata, 'PDQ');" will erase all PDQ results so they may be
    calculated from scratch.
%
% ========== EXAMPLE USAGE ==========
% MRIdata = PDQ(MRIdata, CHI_background, orientation, user_radius, dual_gaussian);
% jhu_gel3 = PDQ(jhu_gel3, -9.035e-6, 1, [65 540], 0);
% lesleybrain0 = PDQ(lesleybrain0, -9.035e-6, 1, [0 60 32], 0);
%%%%%%%%%%%%%%%%%%%%%%%%%%%%%%%%%%%%%%%%%%%%%%%%%%%%%%%%%%%%%%%%%%%%%%%%%%%%%%%%

function MRIdata = PDQ(MRIdata, CHI_background, orientation, user_radius, dual_gaussian)


%% Preferences
platform = 'unix';  % Set to either 'windows' or 'unix'. On unix, automatic phase-unwrapping will be
    attempted. On windows,
                    % phase maps will be exported for manual unwrapping

xcorr_cutoff = 0.3; % Dipoles with XCORR similarity values below this threshold are ignored.
                    % Typically set to 0.3 (30% similar). Must be between [0.0 1.0] (positive similarity).
                    % Setting below 0.1 is a false-positive disaster. Setting below 0.3 causes a moderatly
                        -dense class of false-positive results.

xcorr_cutoff_multiradii = 0.6; % Dipoles with XCORR values below this threshold are not include in the
    dipole radii fit.
                               % Typically set to 0.6, meaning dipoles with < 60% resemblance to the
                                   template won't be fit
                               % This is because we assume that any dipole with <60% resemblance will get
                                   an inaccurate radius fit

maximum_unwrap_hours = 24;      % At most we want to wait this many hours for a phase dataset to be
    unwrapped by PRELUDE. This may result in
                               % some phase unwrapping errors, but it keeps the maximum time down

pref_run_phase_ramp = 0;   % Run PDQ on phase-ramp-removed data. Worth doing to seeing how results differ
    from high-passed
                           % phase if ramp is very homogenous. But of course, takes twice as long.


% Technical Parameters
peak_detection_threshold = 0.0; % Peaks in XCORR similariry below this value will not be considered. We
    only desire peaks
                                % with a positive similarity, so this is set to 0.0
pref_phase_std = 0.0;           % When generating mask, threshold out phase incoherence below this
    threshold (default is 0.0)
pref_default_noise_std = 1.0;   % When generating mask, this is the default sigma value for eliminated
    noise
pref_num_of_radii = 50;  % When it comes to fitting dipole radius, how many would you like to test?
pref_template_shift = sqrt(3)/4.0;      % What fraction of a pixel do you want to shift the templates for
    detecting off-center dipoles?
                                        % This value is approximately 0.433 (sqrt(3)/4.0)
                                        % Choose this number to be irrational may reduce chance of
                                            artifacts.


%% Initializations
```

```
% Reboot matlab pool, if available, to allow for parallel function execution
disp('PDQ: Initializing');
matlabpool close force
matlabpool open

% Add PDQ field to MRIdata, if not present
if(~isfield(MRIdata,'PDQ'))
    MRIdata.PDQ = [];
end

% Store dimensions
[x_dim y_dim z_dim] = size(MRIdata.mag);
MRIdata.PDQ.xcorr_cutoff = xcorr_cutoff;

% Prompt user for key variables, if not given in function call
if(~exist('orientation','var'))
    if(isfield(MRIdata,'unwrapped'))
        fig1 = images(MRIdata.unwrapped); title('MRI data raw phase image');
    else
        fig1 = images(MRIdata.phase); title('MRI data raw phase image');
    end
    orientation = input('What direction is B0?   1: Up-Down   2: In-Out   3: Left-Right  [1-3]: ');
    close(fig1);
end
if(~exist('user_radius','var'))
    user_radius = input('What is estimated radius range of SPIO spheres? [microns microns]: ');
end



%% Calculate mask from magnitude image
disp('PDQ: Calculating masks');
if(~isfield(MRIdata,'mask'))

    % Establish whether the dataset is a single or dual-Gaussian image
    if(~exist('dual_gaussian','var'))
        dual_gaussian = 0;
        reply_dual_gaussian = input('Is this a dual-Gaussian image (e.g., sample in liquid)? y/n [n]:', 's
            ');
        if(strcmp(reply_dual_gaussian,'y'))
            dual_gaussian = 1;
        end
    end

    MRIdata.mask = generate_mask(MRIdata, pref_default_noise_std, pref_phase_std, dual_gaussian,1);
end



%% Unwrap phase images
disp('PDQ: Unwrapping phase images');
if(~isfield(MRIdata,'unwrapped'))
    MRIdata = unwrap_phase_image(MRIdata, platform, maximum_unwrap_hours);
    if(strcmp(platform,'windows'))
        error('PDQ: You are using Windows. Data has been exported using prelude_export. You must manually
            unwrap your images using PRELUDE. Data saved to disc as MRIdata.mat. Quitting.');
    end
end



%% If phase images were unwrapped in 2D, normalize phase through 3rd dimension
if(strcmp(MRIdata.k_space_type, '2d'))
    MRIdata.unwrapped = Normalize3Dunwrap(MRIdata.unwrapped,MRIdata.mag);

    % Prompt user for sanity check
    images(reshape(MRIdata.unwrapped(:,ceil(y_dim/2),:),x_dim,z_dim)); title('Normalized volume'); % Show
        normalized volume as sanity check
    reply = input('Stack Normalization OK? Y/N [Y]: ', 's');
    if strcmp(reply,'n')
        error('PDQ: Stack normalization failed - requires some sort of user intervention. Quitting.');
    end
end



%% Calculate high-passed, Rausher, and ramp-removed phase images
disp('PDQ: Removing low-frequency phase changes from phase images');
if(~isfield(MRIdata,'high_pass')) MRIdata.high_pass = hp(MRIdata.unwrapped); end
if(pref_run_phase_ramp)
    if(~isfield(MRIdata,'ramp')) MRIdata = phase_ramp_remove(MRIdata, 1); end
end


% Temporary Checkpoint
save PDQ_checkpoint MRIdata;



%% Generate templates for large range of radii and template shifts
disp('PDQ: Generating templates spanning range of radii based on user-estimate');
approx_template = PDQ_generate_template(MRIdata.resolution, orientation, mean(user_radius), MRIdata.B0,
```

```
    MRIdata.TE, 1.0e-5, [0 0 0]);
if(~isfield(MRIdata,'template_spectrum'))
    MRIdata.template_spectrum = PDQ_generate_template_spectrum(approx_template, pref_num_of_radii,
        user_radius, pref_template_shift);
end

% Temporary Checkpoint
save PDQ_checkpoint MRIdata;


%% Run dipole search using the 'approximate template', using it to create the 'detection template'
disp('PDQ: Performing preliminary dipole search based on user-provided estimates');
if(~isfield(MRIdata.PDQ,'detection_template'))
    if(length(user_radius) == 3)
        MRIdata.PDQ.detection_template =PDQ_generate_template(MRIdata.resolution, orientation, user_radius
            (3), MRIdata.B0, MRIdata.TE, 7.0e-5, [0 0 0]);
    else
        x_correlate_hp = real(normxcorr3(approx_template.template, MRIdata.high_pass, 'same')) .* MRIdata.
            mask; % Command ordering: (template, image, shape)
        raw_peaks_hp = logical(peaks3d(x_correlate_hp, peak_detection_threshold)) .* x_correlate_hp;
        dipoles = PDQ_dipole_analysis(MRIdata.high_pass, raw_peaks_hp, xcorr_cutoff, approx_template,
            CHI_background);
        disp('PDQ: Generating optimized dipole detection template from preliminary search results');
        MRIdata.PDQ.detection_template = PDQ_generate_optimal_template(dipoles, approx_template, MRIdata.
            template_spectrum);
    end
end


%% Calculate 3D XCORR volumes and find peaks for high-passed phase and (optionally) ramp-removed phase
% High-pass (default)
if(~isfield(MRIdata.PDQ,'dipoles_hp'))
    disp('PDQ: Performing dipole search on high-passed phase using optimized dipole detection template');
    x_correlate_hp = real(normxcorr3(MRIdata.PDQ.detection_template.template, MRIdata.high_pass, 'same'))
        .* MRIdata.mask; % Command ordering: (template, image, shape)
    raw_peaks_hp = logical(peaks3d(x_correlate_hp, peak_detection_threshold)) .* x_correlate_hp;
    disp('PDQ: Calculating susceptibility of high-passed dipoles, assuming fixed radius');
    MRIdata.PDQ.dipoles_hp = PDQ_dipole_analysis(MRIdata.high_pass, raw_peaks_hp, xcorr_cutoff, MRIdata.
        PDQ.detection_template, CHI_background);
end

% Ramp
if(pref_run_phase_ramp)
    if(~isfield(MRIdata.PDQ,'dipoles_ramp'))
        disp('PDQ: Performing dipole search on ramp-removed phase using optimized dipole detection
            template');
        x_correlate_ramp = real(normxcorr3(MRIdata.PDQ.detection_template.template, MRIdata.ramp, 'same'))
            .* MRIdata.mask; % Command ordering: (template, image, shape)
        raw_peaks_ramp = logical(peaks3d(x_correlate_ramp, peak_detection_threshold)) .* x_correlate_ramp;
        disp('PDQ: Calculating susceptibility of ramp-removed dipoles, assuming fixed radius');
        MRIdata.PDQ.dipoles_ramp = PDQ_dipole_analysis(MRIdata.ramp, raw_peaks_ramp, xcorr_cutoff, MRIdata
            .PDQ.detection_template);
    end
end


%% Check to see if any dipoles were found. If not, return!
if(isempty(MRIdata.PDQ.dipoles_hp))
   return
end


%% Find neighbors of dipoles (within template dimensions, which are significant pixels if they overlap)
disp('PDQ: Finding neighbors for each dipole');
if(~isfield(MRIdata.PDQ,'neighbor_consensus'))
    [MRIdata.PDQ.dipoles_hp neighbor_consensus_hp] = PDQ_calculate_neighbors(MRIdata.PDQ.dipoles_hp);
    if(pref_run_phase_ramp)
        [MRIdata.PDQ.dipoles_ramp neighbor_consensus_ramp] = PDQ_calculate_neighbors(MRIdata.PDQ.
            dipoles_ramp);
    end
    MRIdata.PDQ.neighbor_consensus = neighbor_consensus_hp; % Consensus result comes from high-passed
        phase
end


%% Calculate Radii and Chi for non-fixed radii
disp('PDQ: Calculating susceptibility of dipoles, assuming variable radii');
if(~isfield(MRIdata.PDQ,'dipoles_multiradii_hp'))
    MRIdata.PDQ.dipoles_multiradii_hp = PDQ_calculate_radii_and_chi(MRIdata.PDQ.detection_template,
        MRIdata.PDQ.dipoles_hp, xcorr_cutoff_multiradii, MRIdata.template_spectrum, CHI_background);
end
if(pref_run_phase_ramp)
    if(~isfield(MRIdata.PDQ,'dipoles_multiradii_ramp'))
        MRIdata.PDQ.dipoles_multiradii_ramp = PDQ_calculate_radii_and_chi(MRIdata.PDQ.detection_template,
            MRIdata.PDQ.dipoles_ramp, xcorr_cutoff_multiradii,MRIdata.template_spectrum, CHI_background);
    end
end
```

```
%% If ROIs (regions of interest) are specified, count dipoles within each region, and determine distance
     of dipoles outside of regions
disp('PDQ: Calculating statistics for user-specified ROIs (regions of interest)');
if(isfield(MRIdata,'regions'))
    MRIdata = PDQ_process_regions(MRIdata, xcorr_cutoff_multiradii);
end


%% Display minimal output from PDQ Run
disp('PDQ: ###### Finished ######');
disp(['PDQ result: ',num2str(length(MRIdata.PDQ.dipoles_hp)), ' dipoles found in high-passed phase with
     XCORR greater than ',num2str(xcorr_cutoff)]);
disp(['PDQ result: Optimal fixed radius was found to be ',num2str(MRIdata.PDQ.detection_template.radius),'
      microns']);
disp(['PDQ result: ',num2str(length(MRIdata.PDQ.dipoles_multiradii_hp)), ' dipoles found in high-passed
     phase with XCORR greater than ',num2str(xcorr_cutoff_multiradii)]);


%% Close worker pool
matlabpool close force


%%%%%%%%%%%%%
% EOF
%%%%%%%%%%%%%
```

9.2.2 PDQ_calc_volume.m

```
%% Calculates volume of MRIdata from resolution and mask data fields

function volume = PDQ_calc_volume(MRIdata, suppress_output)

volume_cubic_microns = MRIdata.resolution(1) * MRIdata.resolution(2) * MRIdata.resolution(3) * sum(sum(sum
     (MRIdata.mask)));
volume_cc = volume_cubic_microns * 1e-12;

if(~exist('suppress_output','var'))
    disp(['calc_volume: Dataset mask has volume of ',num2str(volume_cc),' cubic centimeters.']);
end

volume = volume_cc;

%%%%%%%%%%%%%
%     EOF
%%%%%%%%%%%%%
```

9.2.3 PDQ_calculate_neighbors.m

```
function [dipoles neighbor_consensus] = PDQ_calculate_neighbors(dipoles)

%% Initialize
num_dipoles = length(dipoles);
template_dims = size(dipoles(1).phase);
x_dim_template = template_dims(1);
y_dim_template = template_dims(2);
z_dim_template = template_dims(3);


%% Go through dipole list to find neighbors of each dipole
for i = 1:num_dipoles

    % Determine range as half-template size
    low_x  = dipoles(i).x - (x_dim_template-1)/2;
    high_x = dipoles(i).x + (x_dim_template-1)/2;

    % Go through list for comparison with other dipoles
    num_neighbors = 0;
    for k = 1:num_dipoles
        neigh_location_x = dipoles(k).x;

        % Time-reduction sanity check (checks x-dimension first)
        if((neigh_location_x > low_x) && (neigh_location_x < high_x))

            low_y  = dipoles(i).y - (y_dim_template-1)/2;
            high_y = dipoles(i).y + (y_dim_template-1)/2;
```

```
            low_z  = dipoles(i).z - (z_dim_template-1)/2;
            high_z = dipoles(i).z + (z_dim_template-1)/2;

            % If the alternate dipole is unique, and within a template-sized region of the first dipole
            if((i ~= k) && (dipoles(k).y > low_y) && (dipoles(k).y < high_y)  && (dipoles(k).z > low_z) &&
                (dipoles(k).z < high_z)  )
                % Neighbor found! Put this dipole's index into the original dipoles index list
                num_neighbors = num_neighbors + 1;
                dipoles(i).neighbors(num_neighbors) = k;
            end
            dipoles(i).num_neighbors = num_neighbors;
        end


    end % All comparison dipoles

    % Put in blank neighbors field if has no neighbors
    if(~isfield(dipoles(i),'neighbors'))
       dipoles(i).neighbors = 0;
    end

end % All dipoles

% Put in blank neighbors field if has no neighbors


%% Generate consensus
num_bins = max([dipoles.num_neighbors])+1;
sum_xcorr_per_bin = zeros(1,num_bins);
sum_dipoles_per_bin = zeros(1,num_bins);
neighbor_consensus = single(zeros(x_dim_template, y_dim_template, z_dim_template, num_bins));

for j_7 = 1:num_dipoles
    temp_num_neighbors = dipoles(j_7).num_neighbors+1; %Offset by one to avoid zero-indexing
    sum_dipoles_per_bin(temp_num_neighbors) = sum_dipoles_per_bin(temp_num_neighbors) + 1;
    neighbor_consensus(:,:,:,temp_num_neighbors) = neighbor_consensus(:,:,:,temp_num_neighbors) + dipoles(
        j_7).phase;
    sum_xcorr_per_bin(temp_num_neighbors) = sum_xcorr_per_bin(temp_num_neighbors) + dipoles(j_7).xcorr;
end
for j_8=1:length(sum_xcorr_per_bin)
    sum_xcorr_per_bin(j_8) = sum_xcorr_per_bin(j_8) / sum_dipoles_per_bin(j_8);
    neighbor_consensus(:,:,:,j_8) = neighbor_consensus(:,:,:,j_8) / sum_dipoles_per_bin(j_8);
end


%%%%%%%%%%%%%
%     EOF
%%%%%%%%%%%%%
```

9.2.4 PDQ_calculate_radii_and_chi.m

```
%%%%%%%%%%%%%%%%%%%%%%%%%%%%%%%%%%%%%%%%%%%%%%%%%%%%%%%%%%%%%%%%%%%%%%%%%%%%%%%
% @name calclulate_radii_and_chi.m
% @author Parker Mills, Ahrens Lab, Carnegie Mellon 2009
% @brief Calculates radii and chi for all dipoles in PDQ dipole list above xcorr_cutoff
% @trusted yes
% @robust no
% @commented no
% @optimized no
% @parallelized no
%
% ========================= INPUT PARAMETERS ==========================
% @param template            (Template)       Original template used to create the list of dipoles
% @param dipoles             (1D Dipole)      List of dipoles to be analyzed
% @param xcorr_cutoff        (Float)          Radii/susceptibility will not be calculated for dipoles with
    XCORR below this value
% @param template_spectrum   (3D Template)    3D matrix filled with Template datatypes, for comparison with
    detected dipoles
%
% ========================= RETURNED DATA =============================
% @return dipole_list        (1D Dipole_multiradii)      List of dipoles for all radii
%
% ========================= ASSUMPTIONS ===============================
% @assume
%
% ========================= EXAMPLE USAGE =============================
% dipole_list = calculate_radii_and_chi(template, dipoles, xcorr_cutoff, template_spectrum)
%
%%%%%%%%%%%%%%%%%%%%%%%%%%%%%%%%%%%%%%%%%%%%%%%%%%%%%%%%%%%%%%%%%%%%%%%%%%%%%%%


function dipole_list = PDQ_calculate_radii_and_chi(template, dipoles, xcorr_cutoff, template_spectrum,
    CHI_background)


%% Preferences

pref_radii_bottom_threshold = 0.02; % Percent of lowest radii in template_spectrum that are not considered
```

```
%% Initializations

% Dipole structure
dipole_list = struct('index',{},'xcorr',{}, 'radius',{}, 'suscept_sphere',{}, 'suscept_core', {}, '
    m_sphere',{}, 'm_core', {}, 'm_vol_sphere', {}, 'm_vol_core',{}, 'shift',{}, 'spectrum',{},'verified
    ',{});



%% If a dipole is above the xcorr_cutoff, and has no neighbors
parfor i = 1:length(dipoles)
    if( (dipoles(i).xcorr > xcorr_cutoff) && (~dipoles(i).num_neighbors) )

        %% Fit dipole
        % Go through radii
        xcorr_list = zeros(3,3,3, length(template_spectrum(2,2,2,:)));
        index_start = ceil(pref_radii_bottom_threshold * length(template_spectrum(2,2,2,:)));
        for x_shift = 1:3
            for y_shift = 1:3
                for z_shift = 1:3
                    for radii = index_start:length(template_spectrum(2,2,2,:))
                        xcorr_list(x_shift, y_shift, z_shift, radii) = normxcorr3(dipoles(i).phase,
                            template_spectrum(x_shift, y_shift, z_shift, radii).template, 'valid');
                    end
                end
            end
        end

        % Find optimal shifts
        [optimal_radius_xcorr_1, optimal_index_1] = max(xcorr_list); % Find maximum x_shift
        [optimal_radius_xcorr_2, optimal_index_2] = max(optimal_radius_xcorr_1); % Find maximum y_shift
        [optimal_radius_xcorr_3, optimal_index_3] = max(optimal_radius_xcorr_2); % Find maxiumum z_shift
        [optimal_radius_xcorr, optimal_index_4] = max(optimal_radius_xcorr_3); % Find optimal radius!

        % Find optimal index for the optimal shift
        matrix_index_4 = optimal_index_4;
        matrix_index_3 = optimal_index_3(:, :, :, matrix_index_4);
        matrix_index_2 = optimal_index_2(:, :, matrix_index_3,matrix_index_4);
        matrix_index_1 = optimal_index_1(:, matrix_index_2,matrix_index_3,matrix_index_4);

        optimal_template = template_spectrum(matrix_index_1, matrix_index_2, matrix_index_3,
            matrix_index_4);



        %% Store dipole and its various properties

        % Index, XCORR, etc.
        dipole = struct;
        dipole.index = i;
        dipole.xcorr = optimal_radius_xcorr;
        dipole.radius = optimal_template.radius;

        % Magnetic properties
        radius_3 = (dipole.radius * 1e-6)^3.0;
        volume = 4/3 * pi * radius_3;
        dipole.suscept_sphere = (optimal_template.d_Chi .* minsumsquares(dipoles(i).phase,
            optimal_template.template))   +   CHI_background;
        dipole.suscept_core   = (optimal_template.d_Chi .* minsumsquares(dipoles(i).phase,
            optimal_template.template))                    ;
        dipole.m_sphere = 1e7 * (optimal_template.B0/3) * radius_3 * dipole.suscept_sphere / (1 + dipole.
            suscept_sphere);
        dipole.m_core   = 1e7 * (optimal_template.B0/3) * radius_3 * dipole.suscept_core   / (1 + dipole.
            suscept_core  );
        dipole.m_vol_sphere = dipole.m_sphere / volume;
        dipole.m_vol_core   = dipole.m_core / volume;

        % Dipole radius fit information
        dipole.shift = [matrix_index_1 matrix_index_2 matrix_index_3];
        dipole.spectrum = reshape(xcorr_list(matrix_index_1, matrix_index_2, matrix_index_3,:),1,length(
            template_spectrum(2,2,2,:)));

        % Verification flag
        dipole.verified = 0;

        % Append to vector
        dipole_list = [dipole_list dipole];

    end
end


%%%%%%%%%%%%%%%
%       EOF
%%%%%%%%%%%%%%%
```

9.2.5 PDQ_dipole_analysis.m

```
%%%%%%%%%%%%%%%%%%%%%%%%%%%%%%%%%%%%%%%%%%%%%%%%%%%%%%%%%%%%%%%%%%%%%%%%%%%%%%%
```

```
% @name dipole_analysis.m
% @author Parker Mills, Ahrens Lab, Carnegie Mellon 2009
% @brief Analyzes XCORR peaks found throughout a phase volume, creating a list of dipoles
% @trusted yes
% @commented yes
% @optimized probably
% @parallelized yes
%
% ========== INPUT PARAMETERS ==========
% @param phase            (2D/3D Float)       Phase dataset
% @param raw_peaks        (2D/3D Float)       Peaks found in phase dataset
% @param xcorr_cutoff     (Float)             Cutoff value for a peak to be considered to be a dipole
% @param template         (Template)          Template used to form the raw peaks
%
% ========== RETURNED DATA ==========
% @return dipoles         (1D Dipole)         List of dipoles found in volume
%
% ========== ASSUMPTIONS ==========
% @assume
%
% ========== EXAMPLE USAGE ==========
% optimal_template = dipole_analysis(phase, raw_peaks, xcorr_cutoff, template)
%
%%%%%%%%%%%%%%%%%%%%%%%%%%%%%%%%%%%%%%%%%%%%%%%%%%%%%%%%%%%%%%%%%%%%%%%%%%%%%%%


function dipoles = PDQ_dipole_analysis(phase, raw_peaks, xcorr_cutoff, template, CHI_background)


%% Initializations

%TEMPORARY PREF
template_shift = sqrt(3)/4.0;

% Dimensions
phase_dims = size(phase);
template_dims = size(template.template);

% Dipole structure
dipoles = struct('x',{},'y',{},'z',{},'radius',{},'phase',{},'xcorr',{},'suscept_sphere',{},'suscept_core
    ',{},'m_sphere',{},'m_core',{},'m_vol_sphere',{},'m_vol_core',{},'verified',{});

%Create shifted templates
for z_shift = 1:3
    for y_shift = 1:3
        for x_shift = 1:3
            optimal_templates(x_shift,y_shift,z_shift) = PDQ_generate_template(template.resolution,
                template.orientation, template.radius, template.B0, template.TE, template.d_Chi, [
                template_shift*(x_shift-2) template_shift*(y_shift-2)  template_shift*(z_shift-2)]);
        end
    end
end

%% Go through all peaks, adding them as dipoles to the dipole structure
%for j_1 = 1:phase_dims(1)
for j_1 = 1:phase_dims(1) %doesn't work with optimal templates matrix
    for j_2 = 1:phase_dims(2)
        for j_3 = 1:phase_dims(3)
            if( raw_peaks(j_1,j_2,j_3) > xcorr_cutoff ) % If peak magnitude (dipole) is over xcorr_cutoff
                threshold

                %Determine boundary coordinates of peak (dipole)
                low_x  = j_1  -  (template_dims(1) - 1)/2;
                high_x = j_1  +  (template_dims(1) - 1)/2;
                low_y  = j_2  -  (template_dims(2) - 1)/2;
                high_y = j_2  +  (template_dims(2) - 1)/2;
                low_z  = j_3  -  (template_dims(3) - 1)/2;
                high_z = j_3  +  (template_dims(3) - 1)/2;

                % Only address peaks (dipoles) that are not perched on the edge of the dataset
                if((low_x > 0)  &&  (low_y > 0)  &&  (low_z > 0)  &&  (high_x <= phase_dims(1))  &&  (
                    high_y <= phase_dims(2))  &&  (high_z <= phase_dims(3)))

                    % Find optimal shift
                    best_xcorr = -1.0;
                    for z_shift = 1:3
                        for y_shift = 1:3
                            for x_shift = 1:3
                                current_xcorr = real(normxcorr3(optimal_templates(x_shift,y_shift,z_shift)
                                    .template, phase(low_x:high_x, low_y:high_y, low_z:high_z), 'valid'));
                                if(current_xcorr > best_xcorr)
                                    template_optimal = optimal_templates(x_shift,y_shift,z_shift);
                                    best_xcorr = current_xcorr;
                                end
                            end
                        end
                    end



                    % Store information about this dipole in dipole listing
                    dipole = struct;
```

```
                    dipole.x = j_1;
                    dipole.y = j_2;
                    dipole.z = j_3;
                    dipole.radius = template_optimal.radius;
                    dipole.phase = phase(low_x:high_x, low_y:high_y, low_z:high_z); % Store dipole phase
                        impression
                    dipole.xcorr = best_xcorr; % Store XCORR value

                    % Calculate dipole's magnetic properties
                    radius_3 = (dipole.radius * 1e-6)^3.0;
                    volume = 4/3 * pi * radius_3;
                    dipole.suscept_sphere = (template_optimal.d_Chi * minsumsquares(phase(low_x:high_x,
                        low_y:high_y, low_z:high_z), template_optimal.template))   +   CHI_background;
                    dipole.suscept_core   = (template_optimal.d_Chi * minsumsquares(phase(low_x:high_x,
                        low_y:high_y, low_z:high_z) ,template_optimal.template))                        ;
                    dipole.m_sphere = 1e7 * (template_optimal.B0/3) * radius_3 * dipole.suscept_sphere /
                        (1 + dipole.suscept_sphere);
                    dipole.m_core   = 1e7 * (template_optimal.B0/3) * radius_3 * dipole.suscept_core   /
                        (1 + dipole.suscept_core  );
                    dipole.m_vol_sphere = dipole.m_sphere / volume;
                    dipole.m_vol_core   = dipole.m_core / volume;

                    % Verification structure
                    dipole.verified = 0;

                    % Append this dipole to dipole vector
                    dipoles = [dipoles dipole];
                end
            end
        end
    end
end


%%%%%%%%%%%%%
%     EOF
%%%%%%%%%%%%%
```

9.2.6 PDQ_generate_optimal_template.m

```
%%%%%%%%%%%%%%%%%%%%%%%%%%%%%%%%%%%%%%%%%%%%%%%%%%%%%%%%%%%%%%%%%%%%%%%%%%%%%%%
% @name generate_optimal_template.m
% @author Parker Mills, Ahrens Lab, Carnegie Mellon 2009
% @brief Generates an optimal PDQ template based on dipole list and the template used to generate the
    dipole list
% @trusted yes
% @robust yes
% @commented yes
% @optimized yes
% @parallelized yes
%
% ========== INPUT PARAMETERS ==========
% @param dipoles            (1D dipole)        List of dipoles
% @param template           (template)         Template used to form dipole list
%
% ========== RETURNED DATA ==========
% @return optimal_template   (template)         The optimal template
%
% ========== ASSUMPTIONS ==========
% @assume
%
% ========== EXAMPLE USAGE ==========
% optimal_template = generate_optimal_template(dipoles, template)
%%%%%%%%%%%%%%%%%%%%%%%%%%%%%%%%%%%%%%%%%%%%%%%%%%%%%%%%%%%%%%%%%%%%%%%%%%%%%%%


function optimal_template = PDQ_generate_optimal_template(dipoles, template, template_spectrum)


%% Preferences

pref_min_dipoles = 10; % Minimum number of dipoles allowed as candidates for the optimal template
pref_max_dipoles = 100; % Maximum number of dipoles allowed as candidates for the optimal template

pref_xcorr_increment = 0.025; % Value by which xcorr_cutoff is incremented/decremented in order to
                        % reach a number of dipoles between [pref_min_dipoles pref_max_dipoles]

pref_radii_bottom_threshold = 0.02; % Percent of lowest radii in template_spectrum that are not considered
                                    %


%% Initialize

% Set a starting cutoff value. Value doesn't matter since it is soon optimized
xcorr_cutoff = 0.7;

% If there are more than pref_max_dipoles dipoles at this xcorr_cutoff value, make cutoff more strict
while( sum(   [dipoles.xcorr] > xcorr_cutoff   ) > pref_max_dipoles && (xcorr_cutoff < 1.0))
    xcorr_cutoff = xcorr_cutoff + pref_xcorr_increment;
```

```
end

% If there are fewer than pref_min_dipoles at this xcorr_cutoff value, loosen things up!
while( sum(  [dipoles.xcorr] > xcorr_cutoff  ) < pref_min_dipoles )
   xcorr_cutoff = xcorr_cutoff - pref_xcorr_increment;
   if(xcorr_cutoff < 0.3)
       warning(['generate_optimal_template: Need to find more than ',num2str(pref_min_dipoles), ' dipoles.
            Try a different estimate. Returning same template.']);
       optimal_template = template;
       return;
   end
end


%% Find dipoles with XCORR greater than the established cutoff.
num_dipoles = length(dipoles);
great_dipole_count = sum([dipoles.xcorr] > xcorr_cutoff);
great_dipoles = zeros(great_dipole_count, 1);
great_dipole_xcorr = zeros(great_dipole_count, great_dipole_count);
great_dipole_index = 0;
for j1 = 1:num_dipoles
    if(dipoles(j1).xcorr > xcorr_cutoff)
        great_dipole_index = great_dipole_index + 1;
        great_dipoles(great_dipole_index) =  j1;
    end
end


%% Xcorr each 'great dipole' with every other 'great dipole'. Store results.
for j1 = 1:great_dipole_count
    for j2 = j1:great_dipole_count
        great_dipole_xcorr(j1,j2) = normxcorr3(dipoles(great_dipoles(j1)).phase, dipoles(great_dipoles(j2)
            ).phase,'valid');
    end
end


%% Find top 3 pairs and combine each pair to create "top 3 template types"

% Sort pairs
[mm,im] = max(great_dipole_xcorr);
[ss,is] = sort(mm);

% First, Second, and Third place pairs
firstpair = dipoles(great_dipoles(im(length(ss)  ))).phase + dipoles(great_dipoles(is(length(ss)  ))).
    phase;
secondpair = dipoles(great_dipoles(im(length(ss)-1))).phase + dipoles(great_dipoles(is(length(ss)-1))).
    phase;
thirdpair = dipoles(great_dipoles(im(length(ss)-2))).phase + dipoles(great_dipoles(is(length(ss)-2))).
    phase;

% Normalize each dipole pair, since they were added together
firstpair = firstpair ./ 2.0;
secondpair = secondpair ./ 2.0;
thirdpair = thirdpair ./ 2.0;
combined = (firstpair + secondpair + thirdpair) ./ 3.0;
images(combined); title('Top three dipole pairs, combined into one template');


%% Fit the top 3 pairs using the dipole generation engine
value_spectrum = [];
index_start = ceil(pref_radii_bottom_threshold * length(template_spectrum(2,2,2,:)));
parfor radii = index_start:length(template_spectrum(2,2,2,:))
    value = normxcorr3(combined, template_spectrum(2,2,2,radii).template, 'valid');
    value_spectrum = [value_spectrum value];
end

[optimal_radius_xcorr, optimal_index] = max(value_spectrum);
optimal_radius = template_spectrum(2,2,2, optimal_index + index_start - 1).radius;


%% Create optimal template with desired radius
optimal_template = PDQ_generate_template(template.resolution, template.orientation, optimal_radius,
    template.B0, template.TE, 1.0e-5, [0 0 0]);


end

%%%%%%%%%%%%%%%%%
%     EOF
%%%%%%%%%%%%%%%%%
```

9.2.7 PDQ_generate_template.m

```
%%%%%%%%%%%%%%%%%%%%%%%%%%%%%%%%%%%%%%%%%%%%%%%%%%%%%%%%%%%%%%%%%%%%%%%%%%%%
```

```
% @name generate_PDQ_template.m
% @author Parker Mills, Ahrens Lab, Carnegie Mellon 2009
% @brief Creates 3D matrix of magnetic dipole phase impression
% @trust yes
% @robust yes
% @commented yes
% @optimized no (oversampling size may be too large)
% @parallelized no
%
% ==================== INPUT PARAMETERS ====================
%
% @param    resolution     (1D Float)      Pixel resolution (microns): [x_res y_res z_res]
% @param    orientation    (Float)         Direction of B0:  1=Up-down (Along X-axis (MATLAB))
%                                                           2=In-out  (Along Z-axis)
%                                                           3=Left-right (Along Y-axis (MATLAB))
%
% @param    radius         (Float)         Spheroid radius (microns)
% @param    B0             (Float)         Field strength (Tesla or MHz)
% @param    TE             (Float)         Echo time (ms)
% @param    d_Chi          (Float)         Volume magnetic susceptibility of spheroid's material,
    surrounded by background media (unitless)
% @param    shift          (1D Float)      [x_shift y_shift z_shift] Shift, in pixels, of dipole from
    center of template
%                                          Typically, shifts are <= 0.5, since a shift of more than that
    would mean the dipole is at a location one pixel away
%
% ==================== RETURNED DATA ====================
% @return   template           (template)      The desired template (for Template data structure see
    README.txt)
%
% ==================== ASSUMPTIONS ====================
% @assume   B0 is assumed to be in:  Tesla if B0 <= pref_tesla_mhz_decision
%                                    MHz   if B0  > pref_tesla_mhz_decision
%
% @assume   Gyromagnetic ratio is for Hydrogen, not 19F or some other nucleus
%
% ==================== DISPLAYED PRODUCTS ====================
% @product
%
% ==================== SAMPLE USAGE ====================
% template = generate_PDQ_template(resolution, orientation, radius, B0,  TE, d_Chi,      shift);
% template = generate_PDQ_template([51 51 98],           3, 300,    11.7, 11, 1.03e-4,  [0 0 0]);
%
%%%%%%%%%%%%%%%%%%%%%%%%%%%%%%%%%%%%%%%%%%%%%%%%%%%%%%%%%%%%%%%%%%%%%%%%%%%%%%%%%%%%%%%%%%%%%%%%%%%%


function template = PDQ_generate_template(resolution, orientation, radius, B0, TE, d_Chi, shift)


%% User-set preferences
pref_gridsize = 7; % Size of dipole template, in pixels (e.g. default is 7, resulting in template sized 7
    x7x7)
% Usually set to N=7 or N=9, as dipole impression falls off like r^3. Should be set to
% smallest reasonable value so that the template doesn't factor in phase perturbations in other areas!

pref_invert_dipole_template = 1; % For some reason, the entire dipole template must be inverted.

pref_samples = 10000; % Samples per pixel in template. 25,000 for excellent sampling. 10,000 is decent.
    2,500 is good for rough sampling. Assuming gridsize of 7x7x7, total_samples = 343 * pref_samples;

pref_print_magnetic_information = 0; % Print out template's magnetic specifications

pref_display_figures = 0; % Visualize template by showing figures for user

pref_model_inside = 'nothing'; % Model Bz inside the sphere of SPIO? Set to 'griffiths' or 'nothing'
% Signal is usually too low inside dipoles to model their inside.
% Also, this is set only if the material is homogeneous.

gamma = 2 * pi * 42576000; % Gyromagnetic ratio (Default is for Hydrogen = 42,576,000 (2*pi*Hz)/T )
gamma_2pi = 42576000; % Gyromagnetic ratio (Default is for Hydrogen = 42,576,000 Hz/T )


% Technical settings
pref_tesla_mhz_decision = 24; % B0 assumed to be in Tesla if below this value, MHz if above this value



%% Set physical constants
mu_0 = 4 * pi * 1e-7; % Permeability of free space (Tesla * meter / Amp)



%% Sanity checks
if(size(resolution)~=3) % Check resolution
    error('generate_PDQ_template: Resolution must be vector with 3 elements. Quitting.');
end

% Check a, B0, TE, d_Chi are provided
if(~exist('radius','var'))
    error('generate_PDQ_template: radius must be provided. Quitting');
end
if(~exist('B0','var'))
```

```
    error('generate_PDQ_template: B0 (MHz or T) must be provided. Quitting');
end
if(~exist('TE','var'))
    error('generate_PDQ_template: TE (milliseconds) must be provided. Quitting');
end
if(~exist('d_Chi','var'))
    error('generate_PDQ_template: d_Chi must be provided. Quitting');
end



%% Convert all units into meters, seconds, Tesla
resolution = resolution ./ 1e6; % Convert resolution from microns to meters
TE = TE ./ 1000.0; % Convert TE from milliseconds into seconds
radius = radius ./ 1e6; % Convert radius from microns to meters

% If B0 is in MHz, convert it to Tesla.
if(abs(B0) > pref_tesla_mhz_decision)
    B0 = B0 .* 1e6 ./ gamma_2pi;
end

% If we want to invert the dipole
if(pref_invert_dipole_template)
    if(B0 > 0.0)
        B0 = -B0;
    end
end



%% Perform magnetic calculations related to template and its surrounding environment
volume = (4.0 / 3.0) * pi * radius ^ 3.0; % Calculate volume of a sphere (m^3)
mdm = 1e7 * B0 * (radius^3.0 / 3) * (d_Chi /(1 + d_Chi)); % Magnetic Dipole Moment (Amp * meter^2)
M_vol  = mdm / volume; % ASSUMES CHI_BACKGROUND = 0. Bulk magnetization, magnetic dipole moment per unit
    volume, (A/m)



%% If preferred, print out all the magnetic calculations
if(pref_print_magnetic_information)
    disp('You have created a dipole with:');
    disp(['Volume susceptibility (dimensionless SI units): ',num2str(d_Chi)]);
    disp(['Volume: ',num2str(volume),' (m^3) or ', num2str(volume * 1e18),' (microns^3)']);
    disp(['Bulk magnetization: ',num2str(M_vol),' A/m']);
    disp(['Magnetic dipole moment: ',num2str(mdm),' A*m^2']);
    disp(' ');
end



%% Create grid representing dipole in space. X, Y, Z values are in meters
% For each voxel, generate a high-resolution grid containing 'pref_sampling_multiplier' points, then
    average to make template
lower_bound_x = ((-pref_gridsize + 2.0 * shift(1)) * resolution(1)) / 2.0;
lower_bound_y = ((-pref_gridsize + 2.0 * shift(2)) * resolution(2)) / 2.0;
lower_bound_z = ((-pref_gridsize + 2.0 * shift(3)) * resolution(3)) / 2.0;



%% Calculate magnetic field inside sphere (OBSOLETE FOR THIS PROJECT, MAY BE OF VALUE IN FUTURE)
% Math note:
% Bz = (2/3) * mu_0 * M     (Griffiths, SI units)

% Set Bz inside of sphere to user preference
switch pref_model_inside
    case 'griffiths'
        inside_Bz = mu_0 .* (2/3) .* M_vol;   % Bz inside of sphere if it was a homogeneous media (Tesla)
    case 'nothing'
        inside_Bz = 0.0;
end

template.template = zeros(pref_gridsize, pref_gridsize, pref_gridsize); % Allocate template
for j_1 = 1:pref_gridsize
    x_min = lower_bound_x + (j_1 - 1) * resolution(1);
    for j_2 = 1:pref_gridsize
        y_min = lower_bound_y + (j_2 - 1) * resolution(2);
        for j_3 = 1:pref_gridsize
            z_min = lower_bound_z + (j_3 - 1) * resolution(3);

            samples = ceil(pref_samples / (abs(j_1 -3.5)*abs(j_2 -3.5)*abs(j_3 -3.5)));

            for j_4 = 1:samples
                x = x_min + rand * resolution(1);
                y = y_min + rand * resolution(2);
                z = z_min + rand * resolution(3);
                radius2 = x^2 + y^2 + z^2;
                % Does not yet factor in ANYTHING about the material (e.g., dCHI, B0, 1/3, or a^3)
                % Math note:
                % r = sqrt(x.^2 + y.^2 + z.^2)
                % cos(theta).^2 = z.^2 / r.^2
                dipole = (3 * ((z^2)/radius2) - 1) / ( sqrt(radius2)^3 );
```

```
                spin = gamma * TE * dipole * d_Chi * (radius .^ 3.0) * B0 / 3.0;
                switch orientation
                    case 1
                        if(sqrt(radius2) >= radius )%&& abs(spin) < 4*pi)
                            template.template(j_3,j_2,j_1) = template.template(j_3,j_2,j_1) + spin;
                        else
                            template.template(j_3,j_2,j_1) = template.template(j_3,j_2,j_1) + gamma * TE *
                                inside_Bz; % Units: 1/(T*s) * s * T
                        end
                    case 2
                        if(sqrt(radius2) >= radius )%&& abs(spin) < 4*pi)
                            template.template(j_1,j_2,j_3) = template.template(j_1,j_2,j_3) + spin;
                        else
                            template.template(j_1,j_2,j_3) = template.template(j_1,j_2,j_3) + gamma * TE *
                                inside_Bz; % Units: 1/(T*s) * s * T
                        end
                    otherwise
                        if(sqrt(radius2) >= radius )%&& abs(spin) < 4*pi)
                            template.template(j_1,j_3,j_2) = template.template(j_1,j_3,j_2) + spin;
                        else
                            template.template(j_1,j_3,j_2) = template.template(j_1,j_3,j_2) + gamma * TE *
                                inside_Bz; % Units: 1/(T*s) * s * T
                        end
                end
            end

            switch orientation
                case 1
                    template.template(j_3,j_2,j_1) = template.template(j_3,j_2,j_1) ./ samples;
                case 2
                    template.template(j_1,j_2,j_3) = template.template(j_1,j_2,j_3) ./ samples;
                otherwise
                    template.template(j_1,j_3,j_2) = template.template(j_1,j_3,j_2) ./ samples;
            end

            % ADVANCED: Possible future feature: If susceptibility is WELL-KNOWN, then one can normalize
                for phase unwrapping (i.e., can't have phase unwrapped beyond 2*pi)
            %               template.template = template.template + 2 * pi;
            %               template.template = mod(template.template, 4*pi);
            %               template.template = template.template - 2 * pi;
            %template.template(4,4,4) = 0;
        end
    end
end


%% Export template and template metadata so its parameters are known
% Convert back to microns, milliseconds from meters, seconds
template.template = single(template.template);
template.resolution = resolution .* 1e6;
template.orientation = orientation;
template.radius = radius .* 1e6; % Convert meters back into microns
if(pref_invert_dipole_template) % Correct for inversion
    template.B0 = -B0;
else
    template.B0 = B0;
end
template.TE = TE .* 1000;
template.d_Chi = d_Chi;
template.model_inside = pref_model_inside;


%% Visualize high-resolution dipole model and central slice of template
if(pref_display_figures)
    % 2D Visualization
    images(template.template(:,:,4));

    % 3D Visualization
    %     figure;
    %     p1 = patch(isosurface(template.template,-max(max(max(template.template)))/20.0),'FaceColor','
        black','EdgeColor','none');
    %     p2 = patch(isosurface(template.template, max(max(max(template.template)))/20.0),'FaceColor
        ',[0.95,0.95,0.95],'EdgeColor','none');
    %     isonormals(template.template,p1);
    %     isonormals(template.template,p2);
    %     view(2); % Set view in 2D plane so user can see dipole orientation clearly
    %     axis tight; axis equal; camlight; camlight(-80,-10); lighting phong; title('Dipole'); % Axis
        stuff
end


%%%%%%%%%%%
% EOF
%%%%%%%%%%%
```

9.2.8 PDQ_inspect.m

```
%%%%%%%%%%%%%%%%%%%%%%%%%%%%%%%%%%%%%%%%%%%%%%%%%%%%%%%%%%%%%%%%%%%%%%%%%%%%%%%
% @name PDQ_inspect.m
```

```
% @author Parker Mills, Ahrens Lab, Carnegie Mellon 2010
% @brief Allows user to manually verify dipoles in tissue volume.
%
% ======================= INPUT PARAMETERS ========================
% @param    XXXXXXXXXXXXXXX
%
% ======================= RETURNED DATA ===========================
% @return  MRIdata with dipole list 'verity' field with following values:
%                   'unverified': Dipole unverified (Default after running PDQ)
%                   'probable'  : Dipole automatically determined to be probable dipole
%                   'genuine'   : Dipole manually verified as genuine
%                   'invalid'   : Dipole automatically or manually determined to be invalid
%
% ======================= ASSUMPTIONS =============================
% @assume
%
% ======================= DISPLAYED PRODUCTS ======================
%
% ======================= EXAMPLE USAGE ===========================
% MRIdata = PDQ_inspect(XXXXXXXXXXXXXXXXXXXXXXX)
%%%%%%%%%%%%%%%%%%%%%%%%%%%%%%%%%%%%%%%%%%%%%%%%%%%%%%%%%%%%%%%%%%%%%%%%%%%%%%%%


function MRIdata = PDQ_inspect(MRIdata, xcorr_cutoff, mdm_range_cutoff, inspect_every_dipole, full_screen)

%% Hard-coded preferences
border_validity = 2; % if dipole within this many pixels from border, it is declared invalid


%% Initializations
data_size = size(MRIdata.high_pass);
dipole_list_length = length(MRIdata.PDQ.dipoles_hp);
multiradii_dipole_list_length = length(MRIdata.PDQ.dipoles_multiradii_hp);


%% Mark all dipoles as 'unverified'
for i = 1:dipole_list_length
    MRIdata.PDQ.dipoles_hp(i).verity = 'unverified';
end


%% Go through dipole list, performing automatic disqualifications
for i = 1:dipole_list_length
    current_dipole = MRIdata.PDQ.dipoles_hp(i);

    % Disqualify dipoles on borders of anatomy
    within_tissue = 1;

    % Mark as not within tissue if close to border
    for j=current_dipole.x - border_validity:current_dipole.x + border_validity
        for k=current_dipole.y - border_validity:current_dipole.y + border_validity
            for l=current_dipole.z - border_validity:current_dipole.z + border_validity
                if(~MRIdata.mask(min(abs(j)+1,data_size(1)),min(abs(k)+1,data_size(2)),min(abs(l)+1,
                    data_size(3))))
                    within_tissue = 0;
                end
            end
        end
    end

    % Mark dipole as invalid if not within tissue
    if (~within_tissue)
        MRIdata.PDQ.dipoles_hp(i).verity = 'invalid';

        % Also mark dipole in the high-quality dipole list
        for j=1:multiradii_dipole_list_length
            if(MRIdata.PDQ.dipoles_multiradii_hp(j).index == i)
                MRIdata.PDQ.dipoles_multiradii_hp(j).verity = 'invalid';
            end
        end

        % Otherwise mark dipole as probable
    else
        MRIdata.PDQ.dipoles_hp(i).verity = 'probable';
        for j=1:multiradii_dipole_list_length
            if(MRIdata.PDQ.dipoles_multiradii_hp(j).index == i)
                MRIdata.PDQ.dipoles_multiradii_hp(j).verity = 'probable';
            end
        end
    end


    %% Disqualify dipoles that neighbor another dipole (discard the one of the pair with lower XCORR value
        )
    % Gather XCORR values for all neighbors
    neighboring_xcorrs = zeros(current_dipole.num_neighbors+1,1);
    neighboring_xcorrs(1) = current_dipole.xcorr;
    if(current_dipole.num_neighbors)
        for j = 2:current_dipole.num_neighbors+1
```

```
            neighboring_xcorrs(j) = MRIdata.PDQ.dipoles_hp(current_dipole.neighbors(j-1)).xcorr;
        end
    end

    % Determine which neighbor has the highest XCORR value
    [max_xcorr max_xcorr_index] = max(neighboring_xcorrs);

    % If the original dipole is not the largest, label it as invalid -- the largest one will later be
        marked valid
    if (max_xcorr_index ~= 1)
        MRIdata.PDQ.dipoles_hp(i).verity = 'invalid';
    end



    %% Disqualify dipoles that have too small XCORR values
    if (current_dipole.xcorr < xcorr_cutoff)
        MRIdata.PDQ.dipoles_hp(i).verity = 'invalid';
    end



    %% Disqualify dipoles that have MDM values that are out-of-bounds
    if(  (current_dipole.m_core < mdm_range_cutoff(1))   ||   (current_dipole.m_core > mdm_range_cutoff(2)
        ) )
        MRIdata.PDQ.dipoles_hp(i).verity = 'invalid';
    end


end



%% Go through dipole list and ask user to verify dipoles that haven't been automatically eliminated
if (inspect_every_dipole)
    for i = 1:dipole_list_length

        current_dipole = MRIdata.PDQ.dipoles_hp(i);

        % If  current dipole hasn't been labeled invalid, present it to user for manual inspection
        if(~strcmp(MRIdata.PDQ.dipoles_hp(i).verity, 'invalid'))

            % Show slice for current dipole
            inspection_figure = PDQ_visualize_slice(MRIdata, current_dipole.z, 1, xcorr_cutoff,
                mdm_range_cutoff, full_screen);

            % Prompt user to verify current dipole's validity
            valid = input(['Is dipole #',num2str(i),' valid? (y/n) [Y]: '], 's');
            if isempty(valid)
                valid = 'y';
            end

            % Store result
            if(strcmp(valid,'y'))
                MRIdata.PDQ.dipoles_hp(i).verity = 'genuine';
            else
                MRIdata.PDQ.dipoles_hp(i).verity = 'invalid';
            end

            close(inspection_figure);

        end
    end

end


%%%%%%%%%%%
%   EOF
%%%%%%%%%%%
```

9.2.9 PDQ_process_regions.m

```
%%%%%%%%%%%%%%%%%%%%%%%%%%%%%%%%%
% Calculates statistics on regions, if specified
%%%%%%%%%%%%%%%%%%%%%%%%%%%%%%%%%

function MRIdata = PDQ_process_regions(MRIdata, xcorr_cutoff)

%% Preferences
pref_num_random_points = 9000; % Number of random points selected for calculating distance from ROI

%% Initialize

% Extract information from MRIdata file
regions_dims = size(MRIdata.regions(1).mask);
num_regions = length(MRIdata.regions);
num_dipoles = length([MRIdata.PDQ.dipoles_hp]);
```

```
% Create coordinate grid
coordinate_grid_x = 1:regions_dims(1);
coordinate_grid_y = 1:regions_dims(2);
coordinate_grid_z = 1:regions_dims(3);


%% For each region, perform analysis
for curr_region = 1:num_regions

    % Invert the region's mask
    warning off MATLAB:divideByZero
    inverted_mask = 1./MRIdata.regions(curr_region).mask;
    warning on MATLAB:divideByZero


    %% Generate random grid of points in sample volume for later normalization
    if(~isfield(MRIdata.regions, 'random_grid'))
        % Create random x,y,z coordinate points
        random_points_x = round(  rand(pref_num_random_points, 1) .* (regions_dims(1) - 1)  ) + 1;
        random_points_y = round(  rand(pref_num_random_points, 1) .* (regions_dims(2) - 1)  ) + 1;
        random_points_z = round(  rand(pref_num_random_points, 1) .* (regions_dims(3) - 1)  ) + 1;

        % For each random point
        for jj = 1:pref_num_random_points

            % If the point is within entire MRIdata's mask, but not in current region
            if(MRIdata.mask(random_points_x(jj),random_points_y(jj),random_points_z(jj)) && ~MRIdata.
                regions(curr_region).mask(random_points_x(jj),random_points_y(jj),random_points_z(jj)))

                % Generate 3D distance grid for this specific point
                x_dist = ((coordinate_grid_x - random_points_x(jj)).^2)'* ones(1, regions_dims(1));
                y_dist = rot90((   (coordinate_grid_y - random_points_y(jj)).^2)'* ones(1, regions_dims(2)
                    ) );
                z_dist = (coordinate_grid_z - random_points_z(jj)).^2;
                xy_dist = x_dist + y_dist;
                for j_4 = 1:regions_dims(3) % Z-dim
                    random_points_xyz_dist(:,:,j_4) = sqrt(xy_dist + z_dist(j_4));
                end

                % Find this point's minimum distance to the current region
                distance_masked = random_points_xyz_dist .* inverted_mask;
                MRIdata.regions(curr_region).random_grid(jj) = min(min(min(distance_masked)));

            end
        end
    end


    %% Go through all dipoles, counting those located within this region
    if(~isfield(MRIdata.regions, 'dipole_min_dist'))

        % Set counts to zero
        MRIdata.regions(curr_region).dipole_count = 0;
        dipole_not_in_region = 0;

        for curr_dipole = 1:num_dipoles

            % Give status report
            if(mod(curr_dipole,100)==0)
                disp([num2str(curr_dipole),' Dipoles analyzed. (',num2str(curr_dipole/num_dipoles * 100)
                    ,'% done with Region ',num2str(curr_region),') '])
            end

            % If current dipole is above xcorr_cutoff
            if (MRIdata.PDQ.dipoles_hp(curr_dipole).xcorr > xcorr_cutoff)
                location = [MRIdata.PDQ.dipoles_hp(curr_dipole).x    MRIdata.PDQ.dipoles_hp(curr_dipole).y
                        MRIdata.PDQ.dipoles_hp(curr_dipole).z];

                % If within region, just add one to the dipole count for this dipole and visualize that
                    slice, since it's interesting
                if(MRIdata.regions(curr_region).mask(location(1),location(2),location(3)))
                    MRIdata.regions(curr_region).dipole_count = MRIdata.regions(curr_region).dipole_count
                        + 1;
                    %%%PDQ_visualize_slice(MRIdata, MRIdata.PDQ.dipoles_hp(curr_dipole).z, 0, xcorr_cutoff
                        , 1);
                    %%%images(MRIdata.mag(:,:,MRIdata.PDQ.dipoles_hp(curr_dipole).z));

                    % If not within region, increment and determin distance of this dipole to the region
                else
                    dipole_not_in_region = dipole_not_in_region + 1;

                    % Generate 3D distance grid
                    x_dist = ((coordinate_grid_x - location(1)).^2)'* ones(1,regions_dims(1));
                    y_dist = rot90((   (coordinate_grid_y - location(2)).^2)'* ones(1,regions_dims(2)) );
                    z_dist = (coordinate_grid_z - location(3)).^2;
                    xy_dist = x_dist+y_dist;
                    for j_4 = 1:regions_dims(3)
                        xyz_dist(:,:,j_4) = sqrt(xy_dist + z_dist(j_4));
```

```
                    end

                    % Find nearest distance to other regions
                    distance_masked = xyz_dist .* inverted_mask;
                    MRIdata.regions(curr_region).dipole_min_dist(dipole_not_in_region) = min(min(min(
                        distance_masked)));

                end
            end
        end
    end

    % Prepare vectors by removing zeros
    MRIdata.regions(curr_region).random_grid = vectorize_and_remove_zeros(MRIdata.regions(curr_region).
        random_grid);

    % Visualize
    random_grid_hist = hist([zeros(1,999) MRIdata.regions(1).random_grid max(regions_dims).*ones(1,999)],
        30);
    distribution_grid_hist = hist([zeros(1,1) MRIdata.regions(1).dipole_min_dist max(regions_dims).*ones
        (1,1)], 30);
    figure; bar(distribution_grid_hist ./ random_grid_hist);

    random_grid_hist = hist([zeros(1,999) MRIdata.regions(1).random_grid max(regions_dims).*ones(1,999)],
        20);
    distribution_grid_hist = hist([zeros(1,1) MRIdata.regions(1).dipole_min_dist max(regions_dims).*ones
        (1,1)], 20);
    figure; bar(distribution_grid_hist ./ random_grid_hist);

    random_grid_hist = hist([zeros(1,999) MRIdata.regions(1).random_grid max(regions_dims).*ones(1,999)],
        10);
    distribution_grid_hist = hist([zeros(1,1) MRIdata.regions(1).dipole_min_dist max(regions_dims).*ones
        (1,1)], 10);
    figure; bar(distribution_grid_hist ./ random_grid_hist);

end % End for each region


%%%%%%%%%%%%%%%%%
%     EOF
%%%%%%%%%%%%%%%%%
```

9.2.10 PDQ_register.m

```
%%%%%%%%%%%%%%%%%%%%%%%%%%%%%%%%%%%%%%%%%%%%%%%%%%%%%%%%%%%%%%%%%%%%%%%%%%%%%%%
% @name PDQ_register.m
% @author Parker Mills, Ahrens Lab, Carnegie Mellon 2010
% @author T. Kevin Hitchens, Pittsburgh NMR Center for Biomedical Research, Carnegie Mellon 2010
% @brief Performs rigid registration, dipole registration, and dipole movement measurement on a set of MRI
    datasets
% @trusted no
% @robust no
% @commented no
% @optimized no
% @parallelized no
%
% ========================= INPUT PARAMETERS ==========================
% @param MRIdataSeries          (1D MRIdata)        Datasets to be registered across time
% @param max_speed              (Float)             Maximum speed moved in microns/hour
%                                                   (e.g., 40 microns/hour = 960 microns/day)
% @param max_mdm_change         (Float)             Cutoff in maximum mdm change
%                                                   (e.g., Found to be 0.4e-12 A m^2 for in vivo mouse
    brains at 256x190x190 resoluton)
%
% ========================= RETURNED DATA =============================
% @return registered            (1D MRIdata)        Series of co-registered datasets
% @return registration_data     (Registration)      Structure containing registration information between
    datasets
%
% ========================= ASSUMPTIONS ===============================
% @assume 3D volumes are already roughly registered
% @assume 3D volumes have same dimensions
% @assume All MRIdata files must contain a field entitled 'date', which is in units of hours
%
% ========================= EXAMPLE USAGE =============================
% [TBI_brains_registered reg_data] = PDQ_register(TBI_brains,50, 0.4e-12); % 50 microns/hour
% [registered reg_data] = PDQ_register([data1 data2], 35, 0.4e-12);
%%%%%%%%%%%%%%%%%%%%%%%%%%%%%%%%%%%%%%%%%%%%%%%%%%%%%%%%%%%%%%%%%%%%%%%%%%%%%%%

function [registered registration_data] = PDQ_register(MRIdataSeries, max_speed, max_mdm_change)

%% Checks & Initializations

% Start parallelization
%matlabpool close force
if(matlabpool('size') == 0)
    matlabpool open
end
```

```
% Hard-Coded Preferences
pref_show_registration_steps = 0;
pref_registration_basis = 'magnitude'; % 'magnitude' for registration to be on mag images, 'mask' for it
    to be done on image masks

% Global Vars
timepoints = length(MRIdataSeries);


%% Sanity Checks

% Check there's more than one dataset in the series
if(timepoints < 2)
    error('PDQ_register: Require more than one dataset. Quitting.');
end

% Compare different timepoints
for i=1:timepoints-1

    % Check datasets have same dimensions
    if(size(MRIdataSeries(i).mag) ~= size(MRIdataSeries(i+1).mag))
        error('PDQ_register: Input MRIdata datasets have different image dimensions. Quitting.');
    end

    % Check datasets have same resolutions
    if(MRIdataSeries(i).resolution ~= MRIdataSeries(i+1).resolution)
        error('PDQ_register: Input MRIdata datasets have different image resolutions. Quitting.');
    end

    % Check datasets have different time stamps
    if(MRIdataSeries(i).date == MRIdataSeries(i+1).date)
        error('PDQ_register: Input MRIdata datasets have same time stamp. Quitting.');
    end

    % Check datasets have dipole verity field marked
    if(~isfield(MRIdataSeries(i).PDQ.dipoles_hp,'verity'))
        error('PDQ_register: Input MRIdata datasets need dipole verity set. Run PDQ_inspect first.');
    end
end



%% Perform rigid transformations registration between dataset pairs, going from first dataset to last
    dataset
registered(1) = MRIdataSeries(1);
for i = 2:timepoints
    registered(i) = register(registered(i-1), MRIdataSeries(i), pref_registration_basis,
        pref_show_registration_steps);
end


%% Disqualify dipoles outside of anatomy
for i = 1:timepoints
    registered(i) = PDQ_inspect(registered(i),0.3,[0 3e-12],0,0);
end



%% Prepare dipoles to be registered
for timepoint = 1:timepoints-1

    % Initialize distance matrices
    distance_matrix_size = max(length(registered(timepoint).PDQ.dipoles_hp), length(registered(timepoint
        +1).PDQ.dipoles_hp));
    empty_distance_matrix = inf .* ones(distance_matrix_size, distance_matrix_size);
    theta = empty_distance_matrix;
    phi = empty_distance_matrix;
    r = empty_distance_matrix;
    mdm_change = empty_distance_matrix;
    xcorr_change = empty_distance_matrix;

    for i = 1:length(registered(timepoint).PDQ.dipoles_hp) % Early Dipoles
        for j = 1:length(registered(timepoint+1).PDQ.dipoles_hp) % Late Dipoles
            p1 = registered(timepoint).PDQ.dipoles_hp(i);
            p2 = registered(timepoint+1).PDQ.dipoles_hp(j);

            % Calculate and store all changes ("distances")
            spatial_change.x = (p2.x - p1.x) * registered(1).resolution(1);
            spatial_change.y = (p2.y - p1.y) * registered(1).resolution(2);
            spatial_change.z = (p2.z - p1.z) * registered(1).resolution(3);
            % tbi_initial_distance(i,j) = sqrt((tbi_p(1)-p1.x)^2 + (tbi_p(2)-p1.y)^2 + (tbi_p(3)-p1.z)^2);
            % tbi_final_distance(i,j) = sqrt((tbi_p(1)-p2.x)^2 + (tbi_p(2)-p2.y)^2 + (tbi_p(3)-p2.z)^2);
            % tbi_movement(i,j) = tbi_final_distance(i,j) - tbi_initial_distance(i,j);
            mdm_change(i,j) = p2.m_core - p1.m_core;
            xcorr_change(i,j) = p2.xcorr - p1.xcorr;
            [theta_p, phi_p, r_p] = cart2sph(spatial_change.x, spatial_change.y, spatial_change.z);
            theta(i,j) = theta_p;
            phi(i,j) = phi_p;

            % Disqualify distant dipoles
```

```
            max_distance = max_speed * (registered(timepoint+1).date - registered(timepoint).date);
            if(r_p > max_distance)
                r(i,j) = inf;
            else
                r(i,j) = r_p;
            end

            % Disqualify dipoles with large mdm changes
            if (abs(mdm_change(i,j)) > max_mdm_change)
                mdm_change(i,j) = inf;
            end

            % Disqualify invalid dipoles
            if(strcmp(p1.verity,'invalid') || strcmp(p2.verity,'invalid'))
                r(i,j) = inf;
            end

        end
    end

    weighted_dist_matrix = r/max_distance + mdm_change/max_mdm_change;

    % Reverse sign of distance matrix for processing by Hungarian Algorithm, since it tries to maximize,
        not minimize
    weighted_dist_matrix = -weighted_dist_matrix;

    % Feed distance matrix to Hungarian Algorithm to find matching dipoles
    matches = libmaxmatching(weighted_dist_matrix);



    %% Print out results for interpretation by user
    export_matrix = zeros(max(length(registered(timepoint).PDQ.dipoles_hp),length(registered(timepoint+1).
        PDQ.dipoles_hp)));
    for i=1:length(registered(timepoint).PDQ.dipoles_hp) % Early Dipoles
        for j=1:length(registered(timepoint+1).PDQ.dipoles_hp) % Late Dipoles

            % Mark dipole as not matched if the distance equals infinity
            if(matches(i,j) && (r(i,j) ~= inf))
                disp(['Dipole ',num2str(j),' matches Early Dipole ',num2str(i),'. Movement (microns): ',
                    num2str(r(i,j)),...
                    ', Theta: ',num2str(theta(i,j)),', Phi: ',num2str(phi(i,j)),...
                    ', mdm_change: ',num2str(1e12 * abs(mdm_change(i,j))),', xcorr_change: ',num2str(abs(
                        xcorr_change(i,j)))]);
                export_matrix(i,1:3) = [registered(timepoint).PDQ.dipoles_hp(i).x registered(timepoint).
                    PDQ.dipoles_hp(i).y registered(timepoint).PDQ.dipoles_hp(i).z];
                export_matrix(i,4:6) = [registered(timepoint+1).PDQ.dipoles_hp(j).x registered(timepoint
                    +1).PDQ.dipoles_hp(j).y registered(timepoint+1).PDQ.dipoles_hp(j).z];
                export_matrix(i,7) = registered(timepoint).PDQ.dipoles_hp(i).m_core;
            end
        end
    end
    csvwrite(['PDQ',num2str(timepoint),'.csv'], export_matrix);



    %% Store results in Registration structure
    registration_data(timepoint).matches = matches;
    registration_data(timepoint).theta = theta;
    registration_data(timepoint).phi = phi;
    registration_data(timepoint).r = r;
    registration_data(timepoint).mdm_change = mdm_change;
    registration_data(timepoint).xcorr_change = xcorr_change;
    registration_data(timepoint).dipoles = matches .* (r ~= inf);
end

curr_point = 1;
outline = abs(diff(registered(1).mask,1,1));
for i = 1:1:size(registered(1).mask,1)-1
for j = 1:5:size(registered(1).mask,2)-1
for k = 1:5:size(registered(1).mask,3)-1
if(outline(i,j,k))
points(curr_point,1) = i;
points(curr_point,2) = j;
points(curr_point,3) = k;
curr_point = curr_point + 1;
end
end
end
end
csvwrite('mask.csv',points)


% Discover which dipoles were registered across all three datasets
%[x y] = find(registration_data(1).dipoles)
% [x y] = find(registration_data(1).dipoles)
% across3=[];
% for(i=1:length(y))
% for(j=1:length(x2))
% if(y(i) == x2(j))
% across3 = [across3 y(i)]
% end
```

```
% end
% end

%%%%%%%%%%%%%
%    EOF
%%%%%%%%%%%%%
```

9.2.11 PDQ_visualize.m

```
%%%%%%%%%%%%%%%%%%%%%%%%%%%%%%%%%%%%%%%%%%%%%%%%%%%%%%%%%%%%%%%%%%%%%%%%%%%%%%%
% @name PDQ_visualize.m
% @author Parker Mills, Ahrens Lab, Carnegie Mellon 2009
% @brief Visualizes the results of an MRIdata that has been processed by PDQ
% @trusted no
% @robust no
% @commented no
% @optimized no
% @parallelized no
%
% ========== INPUT PARAMETERS ==========
% @param MRIdata                (1D MRIdata)      MRI dataset(s) to be visualized by PDQ (see README.txt
    for datatype details)
%
% ========== RETURNED DATA ==========
% @return
%
% ========== ASSUMPTIONS ==========
% @assume If a vector of MRIdata is provided, visualize_PDQ will visualize all datasets TOGETHER\
% @assume PDQ results for high-passed phase are used, not ramp-removed phase results or other phase
    product results
%
% ========== EXAMPLE USAGE ==========
% visualize_PDQ(MRIdata)
%
%%%%%%%%%%%%%%%%%%%%%%%%%%%%%%%%%%%%%%%%%%%%%%%%%%%%%%%%%%%%%%%%%%%%%%%%%%%%%%%

function PDQ_visualize(MRIdata, fixed_xcorr_cutoff, var_xcorr_cutoff, fixed_mdm_range, var_mdm_range,
    just_count)


%% Preferences
pref_fixed_xcorr_cutoff_default = 0.3;
pref_var_xcorr_cutoff_default = 0.6;
pref_fixed_mdm_range_default = [-inf inf];
pref_var_mdm_range_default = [-inf inf];
pref_display_gaussian_fits = 1;


%% Initializations and sanity-checks

% If xcorr_cutoff values are not specified, set them to default
if(~exist('fixed_xcorr_cutoff','var'))
    warning(['Fixed XCORR cutoff not specified, setting to default of ',num2str(
        pref_fixed_xcorr_cutoff_default)]);
    fixed_xcorr_cutoff = pref_fixed_xcorr_cutoff_default;
end
if(~exist('var_xcorr_cutoff','var'))
    warning(['Variable XCORR cutoff not specified, setting to default of ',num2str(
        pref_fixed_xcorr_cutoff_default)]);
    var_xcorr_cutoff = pref_var_xcorr_cutoff_default;
end
if(~exist('fixed_mdm_range','var'))
    warning(['Range of acceptable fixed-radius mdm values not specified. Setting default to ',num2str(
        pref_fixed_mdm_range_default)]);
    fixed_mdm_range = pref_fixed_mdm_range_default;
end
if(~exist('var_mdm_range','var'))
    warning(['Range of acceptable variable-radius mdm values not specified. Setting default to ',num2str(
        pref_var_mdm_range_default)]);
    var_mdm_range = pref_var_mdm_range_default;
end
if(~exist('just_count','var'))
    just_count = 0;
end

% Check to see if this is a single MRIdata, or multiple MRIdata
num_datasets = length(MRIdata);

% Check to see if fixed radii are consistent
fixed_radius = MRIdata(1).PDQ.detection_template.radius;
all_fixed_radii_equal = 1;
% for i=1:num_datasets
%     if(fixed_radius ~= MRIdata(i).PDQ.detection_template.radius)
%         all_fixed_radii_equal = 0;
%     end
% end

% For each MRIdata, check to ensure they've been analyzed by PDQ already
```

```
for i = 1:num_datasets
    if(~isfield(MRIdata(i),'PDQ'))
        error('visualize_PDQ: Provided MRIdata has no PDQ field. PDQ needs to be run first. Quitting.');
    end
end

% Append all PDQ vectors
dipoles = [];
dipoles_multiradii = [];
for i = 1:num_datasets
    dipoles = [dipoles MRIdata(i).PDQ.dipoles_hp];
    dipoles_multiradii = [dipoles_multiradii MRIdata(i).PDQ.dipoles_multiradii_hp];
end

% Remove dipoles from both lists that are below xcorr_cutoffs, and those that aren't in mdm range
dipoles            = vectorize_and_remove_zeros(dipoles,            'dipoles', fixed_xcorr_cutoff,
    fixed_mdm_range);
dipoles_multiradii = vectorize_and_remove_zeros(dipoles_multiradii, 'dipoles', var_xcorr_cutoff,
    var_mdm_range);

% Store lengths, sizes, and screen size
num_dipoles = length(dipoles);
num_dipoles_multiradii = length(dipoles_multiradii);
scrsz = get(0,'ScreenSize');


%% If there's only one dataset, show spatial distribution of dipoles
if(~just_count)
    if(num_datasets == 1)
        data_dims = size(MRIdata(1).mask);
        x_dim = data_dims(1);
        y_dim = data_dims(2);
        z_dim = data_dims(3);

        [aa bb cc] = ndgrid(1:x_dim,1:y_dim,1:z_dim);
        x_grid = aa .* MRIdata.mask;
        y_grid = bb .* MRIdata.mask;
        z_grid = cc .* MRIdata.mask;

        warning off MATLAB:divideByZero
        % Volume sampling for normalization purposes
        [sample_dist_x sdx] = hist([vectorize_and_remove_zeros(x_grid(:                    , 1:ceil(y_dim
            /10):y_dim, 1:ceil(z_dim/10):z_dim)) ones(1,1e4) x_dim * ones(1,1e4)], 30);
        [sample_dist_y sdy] = hist([vectorize_and_remove_zeros(y_grid(1:ceil(x_dim/10):x_dim, :
                                , 1:ceil(z_dim/10):z_dim)) ones(1,1e4) y_dim * ones(1,1e4)], 30);
        [sample_dist_z sdz] = hist([vectorize_and_remove_zeros(z_grid(1:ceil(x_dim/10):x_dim, 1:ceil(y_dim
            /10):y_dim, :                    )) ones(1,1e4) z_dim * ones(1,1e4)], 30);

        % Dipole sampling
        [dipole_dist_x ddx] = hist([dipoles.x 1 x_dim], 30);
        [dipole_dist_y ddy] = hist([dipoles.y 1 y_dim], 30);
        [dipole_dist_z ddz] = hist([dipoles.z 1 z_dim], 30);

        % Create figures
        figure('Position',[10 scrsz(4)/2 scrsz(3)/2.2 scrsz(4)/2.5]);
        bar(sdx, dipole_dist_x ./ sample_dist_x);
        title('Dipole distribution in x-dimension'); xlabel('X Coordinate'); ylabel('# of dipoles with X
            Coordinate');

        figure('Position',[10 scrsz(4)/2 scrsz(3)/2.2 scrsz(4)/2.5]);
        bar(sdy, dipole_dist_y ./ sample_dist_y);
        title('Dipole distribution in y-dimension'); xlabel('Y Coordinate'); ylabel('# of dipoles with Y
            Coordinate');

        figure('Position',[10 scrsz(4)/2 scrsz(3)/2.2 scrsz(4)/2.5]);
        bar(sdz, dipole_dist_z ./ sample_dist_z);
        title('Dipole distribution in z-dimension'); xlabel('Z Coordinate'); ylabel('# of Dipoles with Z
            Coordinate');

        warning on MATLAB:divideByZero
    end
end

if(~just_count && all_fixed_radii_equal)
    %% If all datasets share the same radius, show fixed_radius visuals
    % XCORR
    figure('Position',[10 20 scrsz(3)/2.2 scrsz(4)/2.5]);
    hist([dipoles.xcorr],  30);
    title(['XCORR value for fixed radius of ',num2str(fixed_radius),' microns']); xlabel('XCORR (unitless)
        '); ylabel('# of Dipoles');

    % MDM SPHERE
    figure('Position',[10 20 scrsz(3)/2.2 scrsz(4)/2.5]);
        export_m_sphere = [dipoles.m_sphere]';
        save export_m_sphere export_m_sphere
    hist([dipoles.m_sphere],   30);
    title(['Sphere magnetic dipole moment for fixed radius of ',num2str(fixed_radius),' microns']); xlabel
        ('Magnetic dipole moment (A*m^2)'); ylabel('# of Dipoles');

    % MDM CORE
    figure('Position',[10 20 scrsz(3)/2.2 scrsz(4)/2.5]);
```

```
    export_m_core = [dipoles.m_core]';
    save export_m_core export_m_core
    hist(export_m_core,   30);
    title(['Core magnetic dipole moment for fixed radius of ',num2str(fixed_radius),' microns']); xlabel('
        Magnetic dipole moment (A*m^2)'); ylabel('# of Dipoles');

    % SUSCEPT SPHERE
    figure('Position',[10 20 scrsz(3)/2.2 scrsz(4)/2.5]);
    hist([dipoles.suscept_sphere],  30);
    title(['Sphere magnetic susceptibility for fixed radius of ',num2str(fixed_radius),' microns']);
        xlabel('Susceptibility (unitless)'); ylabel('# of Dipoles');

    % SUSCEPT CORE
    figure('Position',[10 20 scrsz(3)/2.2 scrsz(4)/2.5]);
    hist([dipoles.suscept_core],  30);
    title(['Core magnetic susceptibility for fixed radius of ',num2str(fixed_radius),' microns']); xlabel
        ('Susceptibility (unitless)'); ylabel('# of Dipoles');

    % VOLUME MAGNETIZATION SPHERE
    figure('Position',[10 20 scrsz(3)/2.2 scrsz(4)/2.5]);
    hist([dipoles.m_vol_sphere],  60);
    title(['Sphere volume magnetization for fixed radius of ',num2str(fixed_radius),' microns']); xlabel('
        Volume Magnetization (A/m)'); ylabel('# of Dipoles');

    % VOLUME MAGNETIZATION CORE
    figure('Position',[10 20 scrsz(3)/2.2 scrsz(4)/2.5]);
    hist([dipoles.m_vol_core],  60);
    title(['Core volume magnetization for fixed radius of ',num2str(fixed_radius),' microns']); xlabel('
        Volume Magnetization (A/m)'); ylabel('# of Dipoles');

    % MDM vs XCORR SPHERE
    figure('Position',[10 20 scrsz(3)/2.2 scrsz(4)/2.5]);
    scatter([dipoles.xcorr], [dipoles.m_sphere],'.','blue');
    title(['Fixed radius (',num2str(fixed_radius),' microns): Sphere magnetic dipole moment VS XCORR value
        ']); xlabel('XCORR (0.0, 1.0)'); ylabel('Magnetic dipole moment (A*m^2)');

    % MDM vs XCORR CORE
    figure('Position',[10 20 scrsz(3)/2.2 scrsz(4)/2.5]);
    export_xcorr = [dipoles.xcorr];
    scatter([dipoles.xcorr], [dipoles.m_core],'.','blue');
    title(['Fixed radius (',num2str(fixed_radius),' microns): Core magnetic dipole moment VS XCORR value
        ']); xlabel('XCORR (0.0, 1.0)'); ylabel('Magnetic dipole moment (A*m^2)');
    save export_xcorr export_xcorr

end


%% Fixed radius Calculations
if(all_fixed_radii_equal && ~just_count)
    [fixed_m_sphere_mean        fixed_m_sphere_std]       = gaussian_fit([dipoles.m_sphere],        30,
        pref_display_gaussian_fits);
    [fixed_m_core_mean          fixed_m_core_std]         = gaussian_fit([dipoles.m_core],          30,
        pref_display_gaussian_fits);
    [fixed_suscept_sphere_mean fixed_suscept_sphere_std] = gaussian_fit([dipoles.suscept_sphere], 30,
        pref_display_gaussian_fits);
    [fixed_suscept_core_mean    fixed_suscept_core_std]   = gaussian_fit([dipoles.suscept_core],    30,
        pref_display_gaussian_fits);
    [fixed_m_vol_sphere_mean    fixed_m_vol_sphere_std]   = gaussian_fit([dipoles.m_vol_sphere],    30,
        pref_display_gaussian_fits);
    [fixed_m_vol_core_mean      fixed_m_vol_core_std]     = gaussian_fit([dipoles.m_vol_core],      30,
        pref_display_gaussian_fits);
end

if(~just_count && (~isempty([dipoles_multiradii])))
    %% Variable radius visuals
    % RADIUS
    figure('Position',[scrsz(3)/2 20 scrsz(3)/2.2 scrsz(4)/2.5]);
    hist([dipoles_multiradii.radius],        20);
    title('Sphere estimated radius'); xlabel('Radius (microns)'); ylabel('# of Dipoles');

    % XCORR
    figure('Position',[scrsz(3)/2 20 scrsz(3)/2.2 scrsz(4)/2.5]);
    hist([dipoles_multiradii.xcorr],  30);
    title('XCORR for variable radius'); xlabel('XCORR (unitless)'); ylabel('# of Dipoles');

    % MDM SPHERE
    figure('Position',[scrsz(3)/2 20 scrsz(3)/2.2 scrsz(4)/2.5]);
    hist([dipoles_multiradii.m_sphere],    40);
    title('Sphere magnetic dipole moment for variable radius'); xlabel('Magnetic dipole moment  (A*m^2)');
         ylabel('# of Dipoles');

    % MDM CORE
    figure('Position',[scrsz(3)/2 20 scrsz(3)/2.2 scrsz(4)/2.5]);
    hist([dipoles_multiradii.m_core],    40);
    title('Core magnetic dipole moment for variable radius'); xlabel('Magnetic dipole moment (A*m^2)');
        ylabel('# of Dipoles');

    % SUSCEPT SPHERE
    figure('Position',[scrsz(3)/2 20 scrsz(3)/2.2 scrsz(4)/2.5]);
    hist([dipoles_multiradii.suscept_sphere],  60);
    title('Sphere magnetic susceptibility for variable radius'); xlabel('Susceptibility (unitless)');
        ylabel('# of Dipoles');
```

```
    % SUSCEPT CORE
    figure('Position',[scrsz(3)/2 20 scrsz(3)/2.2 scrsz(4)/2.5]);
    hist([dipoles_multiradii.suscept_core], 60);
    title('Core magnetic susceptibility for variable radius'); xlabel('Susceptibility (unitless)'); ylabel
        ('# of Dipoles');

    % VOLUME MAGNETIZATION SPHERE
    figure('Position',[scrsz(3)/2 20 scrsz(3)/2.2 scrsz(4)/2.5]);
    hist([dipoles_multiradii.m_vol_sphere], 60);
    title(['Sphere volume magnetization for variable radius']); xlabel('Volume Magnetization (A/m)');
        ylabel('# of Dipoles');

    % VOLUME MAGNETIZATION CORE
    figure('Position',[scrsz(3)/2 20 scrsz(3)/2.2 scrsz(4)/2.5]);
    hist([dipoles_multiradii.m_vol_core], 60);
    title(['Core volume magnetization for variable radius']); xlabel('Volume Magnetization (A/m)'); ylabel
        ('# of Dipoles');

    % MDM vs RADIUS
    figure('Position',[scrsz(3)/2 20 scrsz(3)/2.2 scrsz(4)/2.5]);
    scatter([dipoles_multiradii.radius], [dipoles_multiradii.m_core], '.','blue');
    title('Variable radius: Core magnetic dipole moment VS radius'); xlabel('Radius (microns)'); ylabel('
        Magnetic dipole moment (A*m^2)');

    % Sphere MDM vs XCORR
    figure('Position',[scrsz(3)/2 20 scrsz(3)/2.2 scrsz(4)/2.5]);
    scatter([dipoles_multiradii.xcorr], [dipoles_multiradii.m_sphere],'.','blue');
    title('Variable radius: Sphere magnetic dipole moment VS XCORR value'); xlabel('XCORR value [0.0,
        1.0]'); ylabel('Magnetic dipole moment  (A*m^2)');

    % Core MDM vs XCORR
    figure('Position',[scrsz(3)/2 20 scrsz(3)/2.2 scrsz(4)/2.5]);
    scatter([dipoles_multiradii.xcorr], [dipoles_multiradii.m_core],'.','blue');
    title('Variable radius: Core magnetic dipole moment VS XCORR value'); xlabel('XCORR value [0.0, 1.0]')
        ; ylabel('Magnetic dipole moment  (A*m^2)');

    % RADIUS vs XCORR
    figure('Position',[scrsz(3)/2 20 scrsz(3)/2.2 scrsz(4)/2.5]);
    scatter([dipoles_multiradii.xcorr], [dipoles_multiradii.radius],'.','blue');
    title('Variable radius: Radius VS XCORR value'); xlabel('XCORR value (0.0, 1.0)'); ylabel('Radius (
        microns)');
end


%% Variable radius calculations
if(~just_count && (~isempty([dipoles_multiradii])))
    [var_radius_mean          var_radius_std]          = gaussian_fit([dipoles_multiradii.radius],
        30, pref_display_gaussian_fits);
    [var_xcorr_mean           var_xcorr_std]           = gaussian_fit([dipoles_multiradii.xcorr],
        30, pref_display_gaussian_fits);
    [var_mdm_mean             var_mdm_std]             = gaussian_fit([dipoles_multiradii.m_sphere],
        30, pref_display_gaussian_fits);
    [var_m_core_mean          var_m_core_std]          = gaussian_fit([dipoles_multiradii.m_core],
        30, pref_display_gaussian_fits);
    [var_suscept_sphere_mean var_suscept_sphere_std] = gaussian_fit([dipoles_multiradii.suscept_sphere],
        30, pref_display_gaussian_fits);
    [var_suscept_core_mean    var_suscept_core_std]    = gaussian_fit([dipoles_multiradii.suscept_core],
        30, pref_display_gaussian_fits);
    [var_m_vol_sphere_mean    var_m_vol_sphere_std]    = gaussian_fit([dipoles_multiradii.m_vol_sphere],
        30, pref_display_gaussian_fits);
    [var_m_vol_core_mean      var_m_vol_core_std]      = gaussian_fit([dipoles_multiradii.m_vol_core],
        30, pref_display_gaussian_fits);
end


%% Neighbor-related Visualization
if(~just_count)
    figure('Position',[scrsz(3)/2 scrsz(4)/2 scrsz(3)/2.2 scrsz(4)/2.5]);
    scatter([dipoles.num_neighbors] + 1,[dipoles.xcorr]);
    hold on
    %plot(sum_xcorr_per_bin)
    xlabel('Number of Neighbors INCLUDING self'); ylabel('Average XCORR value');
    hold off

    % (Histogram)  X_neighbors VS num_dipoles_with_X_neighbors
    % (Image)      Consensus dipoles from different numbers of neighbors
    if(max([dipoles.num_neighbors]))
        figure('Position',[scrsz(3)/2 scrsz(4)/2 scrsz(3)/2.2 scrsz(4)/2.5]);
        hist([dipoles.num_neighbors], max([dipoles.num_neighbors])); xlabel('X Neighbors'); ylabel('Number
            of Dipoles with X Neighbors within Template Dimensions');
    end

    if(num_datasets == 1)
        for i = 1:max([dipoles.num_neighbors])
            images(MRIdata.PDQ.neighbor_consensus(:,:,:,i)); title(['Consensus of All Dipoles with ',
                num2str(i),' Neighbors.']);
        end
    end
end
```

```
%% Mahalanobis Furthest-Distance Clustering
% max_clusts = 7;
% x_dim_template = template_dims(1);
% y_dim_template = template_dims(2);
% z_dim_template = template_dims(3);
%
% % Calculate mahalanobis distances
% %distance_mahal = pdist( [[dipoles_multiradii.radius]; ([dipoles_multiradii.m_sphere])].', 'mahalanobis
    ');
% distance_mahal = pdist( [dipoles_multiradii.m_sphere ]  .', 'mahalanobis');
%
% % Create linkage based on distances
% linkage_mahal_complete = linkage(distance_mahal, 'complete');
%
% % Create clusters from linkages
% for i = 2:max_clusts
%     clusts(:,i) = cluster(linkage_mahal_complete,'maxclust',i);
% end
%
% % Store clusters into dipole data structure
% for i = 1:min(length(dipoles), length(clusts(:,2)) )
%     dipoles_multiradii(i).cluster_2 = clusts(i,2);
%     dipoles_multiradii(i).cluster_3 = clusts(i,3);
%     dipoles_multiradii(i).cluster_4 = clusts(i,4);
%     dipoles_multiradii(i).cluster_5 = clusts(i,5);
%     dipoles_multiradii(i).cluster_6 = clusts(i,6);
%     dipoles_multiradii(i).cluster_7 = clusts(i,7);
% end

% Prepare
% cluster_consensus_2 = single(zeros(x_dim_template, y_dim_template, z_dim_template, 2));
% cluster_consensus_3 = single(zeros(x_dim_template, y_dim_template, z_dim_template, 3));
% cluster_consensus_4 = single(zeros(x_dim_template, y_dim_template, z_dim_template, 4));
% cluster_consensus_5 = single(zeros(x_dim_template, y_dim_template, z_dim_template, 5));
%
% for i = 1:2
%     count = 0;
%     for j = 1:length(dipoles)
%         if (dipoles(j).cluster_2 == i)
%             cluster_consensus_2(:,:,:,i) = cluster_consensus_2(:,:,:,i) + dipoles(j).phase;
%             count = count + 1;
%         end
%     end
%     cluster_consensus_2(:,:,:,i) = cluster_consensus_2(:,:,:,i)/count;
%     images(cluster_consensus_2(:,:,:,i)); title(['2-Cluster Furthest-Distance Mahalanobis. Dipole
    consensus from ',num2str(count),' Dipoles in Cluster #',num2str(i)]);
% end
%
% for i = 1:3
%     count = 0;
%     for j = 1:length(dipoles)
%         if (dipoles(j).cluster_3 == i)
%             cluster_consensus_3(:,:,:,i) = cluster_consensus_3(:,:,:,i) + dipoles(j).phase;
%             count = count + 1;
%         end
%     end
%     cluster_consensus_3(:,:,:,i) = cluster_consensus_3(:,:,:,i)/count;
%     images(cluster_consensus_3(:,:,:,i)); title(['3-Cluster Furthest-Distance Mahalanobis. Dipole
    consensus from ',num2str(count),' Dipoles in Cluster #',num2str(i)]);
% end
% for i = 1:4
%     count = 0;
%     for j = 1:length(dipoles)
%         if (dipoles(j).cluster_4 == i)
%             cluster_consensus_4(:,:,:,i) = cluster_consensus_4(:,:,:,i) + dipoles(j).phase;
%             count = count + 1;
%         end
%     end
%     cluster_consensus_4(:,:,:,i) = cluster_consensus_4(:,:,:,i)/count;
%     images(cluster_consensus_4(:,:,:,i)); title(['4-Cluster Furthest-Distance Mahalanobis. Dipole
    consensus from ',num2str(count),' Dipoles in Cluster #',num2str(i)]);
% end
% for i = 1:5
%     count = 0;
%     for j = 1:length(dipoles)
%         if (dipoles(j).cluster_5 == i)
%             cluster_consensus_5(:,:,:,i) = cluster_consensus_5(:,:,:,i) + dipoles(j).phase;
%             count = count + 1;
%         end
%     end
%     cluster_consensus_5(:,:,:,i) = cluster_consensus_5(:,:,:,i)/count;
%     images(cluster_consensus_5(:,:,:,i)); title(['5-Cluster Furthest-Distance Mahalanobis. Dipole
    consensus from ',num2str(count),' Dipoles in Cluster #',num2str(i)]);
% end

% % Display dendrogram
% figure('Position',[scrsz(3)/2 scrsz(4)/2 scrsz(3)/2.2 scrsz(4)/2.5]);
% dendrogram(linkage_mahal_complete,5);
%
% % For each set of clusters
% for i = 1:7
%     figure('Position',[scrsz(3)/2 scrsz(4)/2 scrsz(3)/2.2 scrsz(4)/2.5]);
```

```
%     scatter([dipoles_multiradii.radius]' .* (clusts(:,i)==1), ([dipoles_multiradii.m_sphere])' .* (
    clusts(:,i)==1) ,'r.');
%     title(['Mahalanobis Farthest-Distance Clustering: ', num2str(i), ' clusters']); xlabel('Radius');
    ylabel('mdm (A*m^2)');
%     hold on
%     scatter([dipoles_multiradii.radius].' .* (clusts(:,i)==2), ([dipoles_multiradii.m_sphere]).' .* (
    clusts(:,i)==2),'g.');
%     scatter([dipoles_multiradii.radius].' .* (clusts(:,i)==3), ([dipoles_multiradii.m_sphere]).' .* (
    clusts(:,i)==3),'b.');
%     scatter([dipoles_multiradii.radius].' .* (clusts(:,i)==4), ([dipoles_multiradii.m_sphere]).' .* (
    clusts(:,i)==4),'k.');
%     scatter([dipoles_multiradii.radius].' .* (clusts(:,i)==5), ([dipoles_multiradii.m_sphere]).' .* (
    clusts(:,i)==5),'c.');
%     scatter([dipoles_multiradii.radius].' .* (clusts(:,i)==6), ([dipoles_multiradii.m_sphere]).' .* (
    clusts(:,i)==6),'y.');
%     scatter([dipoles_multiradii.radius].' .* (clusts(:,i)==7), ([dipoles_multiradii.m_sphere]).' .* (
    clusts(:,i)==7),'m.');
%     hold off
% end


%% Region Visualizations
% for curr_region = 1:num_regions
%     disp(['Dipoles in Region ',num2str(curr_region), ' = ', num2str(MRIdata.regions(curr_region).
    dipole_count)]);
% end
%
% volume_distribution = hist(MRIdata.random_grid,50);
% dipole_distribution = hist(MRIdata.regions.dipole_min_dist,50);
% figure; plot(dipole_distribution./volume_distribution);


%% Print dipole counts and statistics
disp('############################## Counting Result ##############################');
disp(['Analyzed volume: ', num2str(PDQ_calc_volume(MRIdata(1),1 )), ' cc']);
disp([num2str(length(dipoles)),                ' dipoles found with: XCORR > ', num2str(fixed_xcorr_cutoff), '
     & ', num2str(fixed_mdm_range(1)), ' < mdm < ', num2str(fixed_mdm_range(2))]);
disp([num2str(length(dipoles_multiradii)), ' dipoles found with: XCORR > ', num2str(var_xcorr_cutoff),    '
     & ', num2str(var_mdm_range(1)), ' < mdm < ', num2str(var_mdm_range(2))]);
disp('#############################################################################');
disp(' ');
disp(' ');
if(~just_count)
    if(all_fixed_radii_equal)
        disp(['######## Magnetic Properties, Assuming fixed radius of ',num2str(fixed_radius), ' microns
            ##########']);
        disp(['# XCORR: ', num2str(mean([dipoles.xcorr])), ' +/- ', num2str(std([dipoles.xcorr]))]);
        disp(['#### Assuming Background Susceptibility Value = User-Provided Value ####']);
        disp(['# Magnetic Dipole Moment (m): ', num2str(fixed_m_sphere_mean*1e12), ' +/- ', num2str(
            fixed_m_sphere_std*1e12)]);
        disp(['# Susceptibility: (chi): ', num2str(fixed_suscept_sphere_mean*1e6), ' +/- ', num2str(
            fixed_suscept_sphere_std*1e6)]);
        disp(['# Volume Magnetization (M): ', num2str(fixed_m_vol_sphere_mean), ' +/- ', num2str(
            fixed_m_vol_sphere_std)]);
        disp('#');
        disp(['#### Assuming Background Susceptibility = 0.0 ##']);
        disp(['# Magnetic Dipole Moment (m): ', num2str(fixed_m_core_mean*1e12), ' +/- ', num2str(
            fixed_m_core_std*1e12)]);
        disp(['# Susceptibility: (chi): ', num2str(fixed_suscept_core_mean*1e6), ' +/- ', num2str(
            fixed_suscept_core_std*1e6)]);
        disp(['# Volume Magnetization (M): ', num2str(fixed_m_vol_core_mean), ' +/- ', num2str(
            fixed_m_vol_core_std)]);
        disp('#############################################################################');
        disp(' ');
        disp(' ');
    end
    if((~isempty([dipoles_multiradii])))
    disp(['########## Magnetic Properties, Allowing variable radius ##########']);
    disp(['# XCORR: ', num2str(var_xcorr_mean), ' +/- ', num2str(var_xcorr_std)]);
    disp(['# Radius: ', num2str(var_radius_mean), ' +/- ', num2str(var_radius_std)]);
    disp(['#### Assuming Background Susceptibility Value = User-Provided Value ####']);
    disp(['# Magnetic Dipole Moment (m): ', num2str(var_mdm_mean*1e12), ' +/- ', num2str(var_mdm_std*1e12)
        ]);
    disp(['# Susceptibility: (chi): ', num2str(var_suscept_sphere_mean*1e6), ' +/- ', num2str(
        var_suscept_sphere_std*1e6)]);
    disp(['# Volume Magnetization (M): ', num2str(var_m_vol_sphere_mean), ' +/- ', num2str(
        var_m_vol_sphere_std)]);
    disp('#');
    disp(['#### Assuming Background Susceptibility = 0.0 ##']);
    disp(['# Magnetic Dipole Moment (m): ', num2str(var_m_core_mean*1e12), ' +/- ', num2str(var_m_core_std
        *1e12)]);
    disp(['# Susceptibility: (chi): ', num2str(var_suscept_core_mean*1e6), ' +/- ', num2str(
        var_suscept_core_std*1e6)]);
    disp(['# Volume Magnetization (M): ', num2str(var_m_vol_core_mean), ' +/- ', num2str(
        var_m_vol_core_std)]);
    disp('#############################################################################');
    end
    end
```

```
%%%%%%%%%%%%%%
%    EOF
%%%%%%%%%%%%%%
```

9.2.12 PDQ_visualize_slice.m

```
%%%%%%%%%%%%%%%%%%%%%%%%%%%%%%%%%%%%%%%%%%%%%%%%%%%%%%%%%%%%%%%%%%%%%%%%%%%%%%%
% @name PDQ_visualize_slice.m
% @author Parker Mills, Ahrens Lab, Carnegie Mellon 2009
% @brief Visualizes a specified slice from 3D phase volume, marking
%        the location and susceptibility of each dipole present in
%        the slice.
%
% ========================= INPUT PARAMETERS ==========================
% @param    dataset          (MRIdata)     Volumetric phase dataset
% @param    slice            (1D Float)     Slice to be visualized
% @param    slice_thickness (1D Float)     Maximum distance, in slices, that a dipole can be from
%                                          currently visualized slice in order for it to be displayed.
%                                          Default is half template size (i.e., half dipole size)
%
% @param    xcorr_cutoff     (1D Float)     Cross-correlation quality threshold value; [0.0 1.0]
% @param    full_screen      (1D Float)     1: Full screen view of stuff, 0: Normal window
%
% ========================= RETURNED DATA ==========================
% @return   fig         (Float)        Figure handle
%
% ========================= ASSUMPTIONS ==========================
% @assume
%
% ========================= DISPLAYED PRODUCTS ==========================
%
% ========================= EXAMPLE USAGE ==========================
% fig1 = PDQ_visualize_slice(MRIdata, slice, slice_thickness, xcorr_cutoff);
% fig1 = PDQ_visualize_slice(MRIdata, 16, 2, 0.3);
%
%%%%%%%%%%%%%%%%%%%%%%%%%%%%%%%%%%%%%%%%%%%%%%%%%%%%%%%%%%%%%%%%%%%%%%%%%%%%%%%

function fig1 = PDQ_visualize_slice(MRIdata, slice, slice_thickness, xcorr_cutoff, mdm_range, full_screen)



%% Determine what phase image is being used for visualization

if(exist('MRIdata.rauscher','var'))
    backdrop = MRIdata.rauscher;
else
    backdrop = MRIdata.high_pass;
end

[x_dim y_dim z_dim] = size(backdrop);

%% Sanity checks
if(slice < 1 || slice > z_dim)
        error(['visualize_PDQ_slice_slice: Selected slice number, ',num2str(slice),', is outside of volume
            ']);
end

%% Show the desired slice
if (full_screen)
   fig1 = images(backdrop(:,:,slice),[-1 1],'fullscreen');
else
    fig1 = images(backdrop(:,:,slice),[-1 1]);
end

% If slice thickness not provided, set default: half dipole's diameter
if(~exist('slice_thickness','var'))
    slice_thickness = floor(max(size(MRIdata.PDQ.dipoles_hp(1).phase))/2);
else
   if (isempty(slice_thickness))
       slice_thickness = floor(max(size(MRIdata.PDQ.dipoles_hp_hp(1).phase))/2);
   end
end

% Go through all dipoles
for j_1 = 1:length(MRIdata.PDQ.dipoles_hp)

        % If dipole within "z-depth" of user-selected slice, label it!
        if(  (MRIdata.PDQ.dipoles_hp(j_1).z >= (slice - slice_thickness))...
                    && (MRIdata.PDQ.dipoles_hp(j_1).z <= (slice + slice_thickness))...
                    && (MRIdata.PDQ.dipoles_hp(j_1).xcorr > xcorr_cutoff)...
            && (MRIdata.PDQ.dipoles_hp(j_1).m_core > mdm_range(1)))

                arrow_x = [(MRIdata.PDQ.dipoles_hp(j_1).y + rand*30-15) MRIdata.PDQ.dipoles_hp(j_1).y];
                arrow_y = [(x_dim+1)-(MRIdata.PDQ.dipoles_hp(j_1).x + rand*30-15) (x_dim+1)-MRIdata.PDQ.
                    dipoles_hp(j_1).x];
                [arrow_x,arrow_y] = dsxy2figxy(gca, arrow_x, arrow_y);
```

```
                annotation(fig1,'textarrow', arrow_x, arrow_y,...
                        'TextEdgeColor','none',...
                        'TextLineWidth',2,...
                        'TextColor',[1 0 0],...
                        'FontSize',10,...
            'String',{...
            strcat('#'      ,num2str(j_1)                                    ),...
            strcat('xcorr=',num2str(MRIdata.PDQ.dipoles_hp(j_1).xcorr  ,2)),...
            strcat('mdm='   ,num2str(MRIdata.PDQ.dipoles_hp(j_1).m_core,2))...
            },'LineWidth',1,...
            'Color',[1 0 0]);
        end
end

%%%%%%%%%%
% EOF
%%%%%%%%%%
```